DESY 09-093
June 2009

ISSN 0418-9833

Diffractive Electroproduction of ρ and ϕ Mesons at HERA

H1 Collaboration

Abstract

Diffractive electroproduction of ρ and ϕ mesons is measured at HERA with the H1 detector in the elastic and proton dissociative channels. The data correspond to an integrated luminosity of $51\ \mathrm{pb}^{-1}$. About 10500 ρ and 2000 ϕ events are analysed in the kinematic range of squared photon virtuality $2.5 \leq Q^2 \leq 60\ \mathrm{GeV}^2$, photon-proton centre of mass energy $35 \leq W \leq 180$ GeV and squared four-momentum transfer to the proton $|t| \leq 3\ \mathrm{GeV}^2$. The total, longitudinal and transverse cross sections are measured as a function of Q^2, W and $|t|$. The measurements show a transition to a dominantly "hard" behaviour, typical of high gluon densities and small $q\bar{q}$ dipoles, for Q^2 larger than 10 to $20\ \mathrm{GeV}^2$. They support flavour independence of the diffractive exchange, expressed in terms of the scaling variable $(Q^2+M_V^2)/4$, and proton vertex factorisation. The spin density matrix elements are measured as a function of kinematic variables. The ratio of the longitudinal to transverse cross sections, the ratio of the helicity amplitudes and their relative phases are extracted. Several of these measurements have not been performed before and bring new information on the dynamics of diffraction in a QCD framework. The measurements are discussed in the context of models using generalised parton distributions or universal dipole cross sections.

Submitted to *JHEP*

F.D. Aaron[5,49], M. Aldaya Martin[11], C. Alexa[5], K. Alimujiang[11], V. Andreev[25], B. Antunovic[11], A. Asmone[33], S. Backovic[30], A. Baghdasaryan[38], E. Barrelet[29], W. Bartel[11], K. Begzsuren[35], A. Belousov[25], J.C. Bizot[27], V. Boudry[28], I. Bozovic-Jelisavcic[2], J. Bracinik[3], G. Brandt[11], M. Brinkmann[12], V. Brisson[27], D. Bruncko[16], A. Bunyatyan[13,38], G. Buschhorn[26], L. Bystritskaya[24], A.J. Campbell[11], K.B. Cantun Avila[22], F. Cassol-Brunner[21], K. Cerny[32], V. Cerny[16,47], V. Chekelian[26], A. Cholewa[11], J.G. Contreras[22], J.A. Coughlan[6], G. Cozzika[10], J. Cvach[31], J.B. Dainton[18], K. Daum[37,43], M. Deák[11], Y. de Boer[11], B. Delcourt[27], M. Del Degan[40], J. Delvax[4], E.A. De Wolf[4], C. Diaconu[21], V. Dodonov[13], A. Dossanov[26], A. Dubak[30,46], G. Eckerlin[11], V. Efremenko[24], S. Egli[36], A. Eliseev[25], E. Elsen[11], A. Falkiewicz[7], L. Favart[4], A. Fedotov[24], R. Felst[11], J. Feltesse[10,48], J. Ferencei[16], D.-J. Fischer[11], M. Fleischer[11], A. Fomenko[25], E. Gabathuler[18], J. Gayler[11], S. Ghazaryan[38], A. Glazov[11], I. Glushkov[39], L. Goerlich[7], N. Gogitidze[25], M. Gouzevitch[11], C. Grab[40], T. Greenshaw[18], B.R. Grell[11], G. Grindhammer[26], S. Habib[12,50], D. Haidt[11], C. Helebrant[11], R.C.W. Henderson[17], E. Hennekemper[15], H. Henschel[39], M. Herbst[15], G. Herrera[23], M. Hildebrandt[36], K.H. Hiller[39], D. Hoffmann[21], R. Horisberger[36], T. Hreus[4,44], M. Jacquet[27], M.E. Janssen[11], X. Janssen[4], L. Jönsson[20], A.W. Jung[15], H. Jung[11], M. Kapichine[9], J. Katzy[11], I.R. Kenyon[3], C. Kiesling[26], M. Klein[18], C. Kleinwort[11], T. Kluge[18], A. Knutsson[11], R. Kogler[26], P. Kostka[39], M. Kraemer[11], K. Krastev[11], J. Kretzschmar[18], A. Kropivnitskaya[24], K. Krüger[15], K. Kutak[11], M.P.J. Landon[19], W. Lange[39], G. Laštovička-Medin[30], P. Laycock[18], A. Lebedev[25], G. Leibenguth[40], V. Lendermann[15], S. Levonian[11], G. Li[27], K. Lipka[11], A. Liptaj[26], B. List[12], J. List[11], N. Loktionova[25], R. Lopez-Fernandez[23], V. Lubimov[24], L. Lytkin[13], A. Makankine[9], E. Malinovski[25], P. Marage[4], Ll. Marti[11], H.-U. Martyn[1], S.J. Maxfield[18], A. Mehta[18], A.B. Meyer[11], H. Meyer[11], H. Meyer[37], J. Meyer[11], V. Michels[11], S. Mikocki[7], I. Milcewicz-Mika[7], F. Moreau[28], A. Morozov[9], J.V. Morris[6], M.U. Mozer[4], M. Mudrinic[2], K. Müller[41], P. Murín[16,44], Th. Naumann[39], P.R. Newman[3], C. Niebuhr[11], A. Nikiforov[11], G. Nowak[7], K. Nowak[41], M. Nozicka[11], B. Olivier[26], J.E. Olsson[11], S. Osman[20], D. Ozerov[24], V. Palichik[9], I. Panagoulias[l,11,42], M. Pandurovic[2], Th. Papadopoulou[l,11,42], C. Pascaud[27], G.D. Patel[18], O. Pejchal[32], E. Perez[10,45], A. Petrukhin[24], I. Picuric[30], S. Piec[39], D. Pitzl[11], R. Plačakytė[11], B. Pokorny[12], R. Polifka[32], B. Povh[13], T. Preda[5], V. Radescu[11], A.J. Rahmat[18], N. Raicevic[30], A. Raspiareza[26], T. Ravdandorj[35], P. Reimer[31], E. Rizvi[19], P. Robmann[41], B. Roland[4], R. Roosen[4], A. Rostovtsev[24], M. Rotaru[5], J.E. Ruiz Tabasco[22], Z. Rurikova[11], S. Rusakov[25], D. Šálek[32], D.P.C. Sankey[6], M. Sauter[40], E. Sauvan[21], S. Schmitt[11], L. Schoeffel[10], A. Schöning[14], H.-C. Schultz-Coulon[15], F. Sefkow[11], R.N. Shaw-West[3], L.N. Shtarkov[25], S. Shushkevich[26], T. Sloan[17], I. Smiljanic[2], Y. Soloviev[25], P. Sopicki[7], D. South[8], V. Spaskov[9], A. Specka[28], Z. Staykova[11], M. Steder[11], B. Stella[33], G. Stoicea[5], U. Straumann[41], D. Sunar[4], T. Sykora[4], V. Tchoulakov[9], G. Thompson[19], P.D. Thompson[3], T. Toll[12], F. Tomasz[16], T.H. Tran[27], D. Traynor[19], T.N. Trinh[21], P. Truöl[41], I. Tsakov[34], B. Tseepeldorj[35,51], J. Turnau[7], K. Urban[15], A. Valkárová[32], C. Vallée[21], P. Van Mechelen[4], A. Vargas Trevino[11], Y. Vazdik[25], S. Vinokurova[11], V. Volchinski[38], M. von den Driesch[11], D. Wegener[8], Ch. Wissing[11], E. Wünsch[11], J. Žáček[32], J. Zálešák[31], Z. Zhang[27], A. Zhokin[24], T. Zimmermann[40], H. Zohrabyan[38], F. Zomer[27], and R. Zus[5]

[1] *I. Physikalisches Institut der RWTH, Aachen, Germany*[a]

[2] *Vinca Institute of Nuclear Sciences, Belgrade, Serbia*

[3] *School of Physics and Astronomy, University of Birmingham, Birmingham, UK*[b]

[4] *Inter-University Institute for High Energies ULB-VUB, Brussels; Universiteit Antwerpen, Antwerpen; Belgium*[c]
[5] *National Institute for Physics and Nuclear Engineering (NIPNE) , Bucharest, Romania*
[6] *Rutherford Appleton Laboratory, Chilton, Didcot, UK*[b]
[7] *Institute for Nuclear Physics, Cracow, Poland*[d]
[8] *Institut für Physik, TU Dortmund, Dortmund, Germany*[a]
[9] *Joint Institute for Nuclear Research, Dubna, Russia*
[10] *CEA, DSM/Irfu, CE-Saclay, Gif-sur-Yvette, France*
[11] *DESY, Hamburg, Germany*
[12] *Institut für Experimentalphysik, Universität Hamburg, Hamburg, Germany*[a]
[13] *Max-Planck-Institut für Kernphysik, Heidelberg, Germany*
[14] *Physikalisches Institut, Universität Heidelberg, Heidelberg, Germany*[a]
[15] *Kirchhoff-Institut für Physik, Universität Heidelberg, Heidelberg, Germany*[a]
[16] *Institute of Experimental Physics, Slovak Academy of Sciences, Košice, Slovak Republic*[f]
[17] *Department of Physics, University of Lancaster, Lancaster, UK*[b]
[18] *Department of Physics, University of Liverpool, Liverpool, UK*[b]
[19] *Queen Mary and Westfield College, London, UK*[b]
[20] *Physics Department, University of Lund, Lund, Sweden*[g]
[21] *CPPM, CNRS/IN2P3 - Univ. Mediterranee, Marseille, France*
[22] *Departamento de Fisica Aplicada, CINVESTAV, Mérida, Yucatán, México*[j]
[23] *Departamento de Fisica, CINVESTAV, México*[j]
[24] *Institute for Theoretical and Experimental Physics, Moscow, Russia*[k]
[25] *Lebedev Physical Institute, Moscow, Russia*[e]
[26] *Max-Planck-Institut für Physik, München, Germany*
[27] *LAL, Univ Paris-Sud, CNRS/IN2P3, Orsay, France*
[28] *LLR, Ecole Polytechnique, IN2P3-CNRS, Palaiseau, France*
[29] *LPNHE, Universités Paris VI and VII, IN2P3-CNRS, Paris, France*
[30] *Faculty of Science, University of Montenegro, Podgorica, Montenegro*[e]
[31] *Institute of Physics, Academy of Sciences of the Czech Republic, Praha, Czech Republic*[h]
[32] *Faculty of Mathematics and Physics, Charles University, Praha, Czech Republic*[h]
[33] *Dipartimento di Fisica Università di Roma Tre and INFN Roma 3, Roma, Italy*
[34] *Institute for Nuclear Research and Nuclear Energy, Sofia, Bulgaria*[e]
[35] *Institute of Physics and Technology of the Mongolian Academy of Sciences , Ulaanbaatar, Mongolia*
[36] *Paul Scherrer Institut, Villigen, Switzerland*
[37] *Fachbereich C, Universität Wuppertal, Wuppertal, Germany*
[38] *Yerevan Physics Institute, Yerevan, Armenia*
[39] *DESY, Zeuthen, Germany*
[40] *Institut für Teilchenphysik, ETH, Zürich, Switzerland*[i]
[41] *Physik-Institut der Universität Zürich, Zürich, Switzerland*[i]

[42] *Also at Physics Department, National Technical University, Zografou Campus, GR-15773 Athens, Greece*
[43] *Also at Rechenzentrum, Universität Wuppertal, Wuppertal, Germany*
[44] *Also at University of P.J. Šafárik, Košice, Slovak Republic*
[45] *Also at CERN, Geneva, Switzerland*

[46] *Also at Max-Planck-Institut für Physik, München, Germany*
[47] *Also at Comenius University, Bratislava, Slovak Republic*
[48] *Also at DESY and University Hamburg, Helmholtz Humboldt Research Award*
[49] *Also at Faculty of Physics, University of Bucharest, Bucharest, Romania*
[50] *Supported by a scholarship of the World Laboratory Björn Wiik Research Project*
[51] *Also at Ulaanbaatar University, Ulaanbaatar, Mongolia*

[a] *Supported by the Bundesministerium für Bildung und Forschung, FRG, under contract numbers 05 H1 1GUA /1, 05 H1 1PAA /1, 05 H1 1PAB /9, 05 H1 1PEA /6, 05 H1 1VHA /7 and 05 H1 1VHB /5*
[b] *Supported by the UK Science and Technology Facilities Council, and formerly by the UK Particle Physics and Astronomy Research Council*
[c] *Supported by FNRS-FWO-Vlaanderen, IISN-IIKW and IWT and by Interuniversity Attraction Poles Programme, Belgian Science Policy*
[d] *Partially Supported by Polish Ministry of Science and Higher Education, grant PBS/DESY/70/2006*
[e] *Supported by the Deutsche Forschungsgemeinschaft*
[f] *Supported by VEGA SR grant no. 2/7062/ 27*
[g] *Supported by the Swedish Natural Science Research Council*
[h] *Supported by the Ministry of Education of the Czech Republic under the projects LC527, INGO-1P05LA259 and MSM0021620859*
[i] *Supported by the Swiss National Science Foundation*
[j] *Supported by CONACYT, México, grant 48778-F*
[k] *Russian Foundation for Basic Research (RFBR), grant no 1329.2008.2*
[l] *This project is co-funded by the European Social Fund (75%) and National Resources (25%) - (EPEAEK II) - PYTHAGORAS II*

1 Introduction

Diffractive scattering is characterised, in high energy hadron interactions, by final states consisting of two systems well separated in rapidity, which carry the quantum numbers of the initial state hadrons. The process is related through unitarity to inelastic scattering and governs the high energy behaviour of total cross sections. It is described in Regge theory [1] by the exchange of the vacuum singularity, called the "pomeron", and may be interpreted as the differential absorption of the various virtual components of the interacting systems [2]. It is a challenge for Quantum Chromodynamics (QCD) to explain diffraction in terms of quark and gluon interactions.

Most diffractive phenomena – which include elastic scattering – are governed by large distance, "soft" processes, which in general are not accessible to perturbative QCD (pQCD) calculations. However, for short distance processes, the presence of a "hard" scale offers the possibility to use perturbative techniques to calculate diffractive amplitudes. Alternatively, at high energy the interaction properties of colour fields are invoked in models which characterize the incident particles as a superposition of colour dipoles with various size to calculate diffractive and total cross sections.

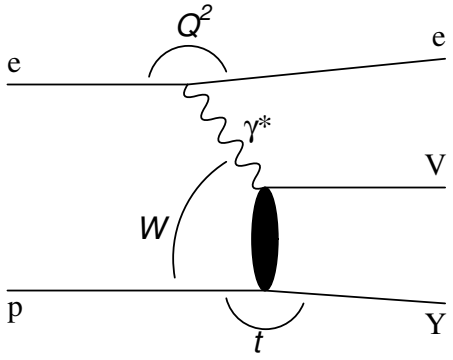

Figure 1: Diffractive vector meson electroproduction.

An important testing ground for calculations in diffraction is provided by the study of exclusive vector meson (VM) production $e + p \rightarrow e + V + Y$. This process is illustrated in Fig. 1: the intermediate photon of four-momentum q converts into a diffractively scattered VM (ρ, ω, ϕ, J/ψ, ...) of mass M_V, while the incoming proton is scattered into a system Y of mass M_Y, which can be a proton ("elastic" scattering) or a diffractively excited system ("proton dissociation"). In VM production, a hard scale can be provided by the photon virtuality Q, with $Q^2 = -q^2$, the four-momentum transfer $\sqrt{|t|}$ from the proton, or by the quark mass (for heavy VM production). The reaction energy is defined by the photon-proton centre of mass energy W, with $W^2 \simeq Q^2/x$, where x is the Bjorken scaling variable. The high energy electron-proton collider HERA offers access to all these scales, over a wide range of values.

The present publication is devoted to the study of the diffractive electroproduction of ρ and ϕ mesons, both for elastic and proton dissociative scattering. The data were taken at HERA with the H1 detector in the period from 1996 to 2000. A common analysis of the four channels

is performed. Measurements of the production cross sections and of the spin density matrix elements, which give access to the helicity amplitudes, are presented as a function of the kinematic variables Q^2 (including the Q^2 dependence of the polarised cross sections), W, t and, for ρ mesons, the dipion mass.

The measurement of kinematic dependences and the comparison between different VMs provide tests of a large spectrum of predictions. The data cover the interesting transition from the low Q^2 domain, dominated by soft diffraction, to the domain of $(Q^2+M_V^2)/4$ above 3 to 5 GeV^2, where hard diffraction is expected to be dominant. This offers the opportunity to test the relevance of soft physics features present in the photon and VM wave function, and to study the development of hard features predicted by pQCD calculations. Quantitative tests of pQCD and colour dipole calculations are provided by the comparison with the data of various model predictions. Two important aspects of diffraction are tested: the flavour independence of the diffractive process and the factorisation of the process into a hard scattering contribution at the photon vertex and soft diffractive scattering at the proton vertex ("Regge factorisation"). In addition, valuable information is provided by precise measurements of empirical parameters, in particular the Q^2 and t dependences of the cross sections and the ratio of the proton dissociative to elastic cross sections, as well as the contributions of various backgrounds.

The present studies confirm with increased precision previous H1 measurements on ρ [3–6] and ϕ [6,7] electroproduction, mainly in the elastic channel but also in proton dissociation [5,6]. The samples analysed here include data taken in 1996 and 1997, and the present results supersede those presented in [4, 5, 7]. Thanks to the larger statistics, the scope of the investigation is significantly extended.

This analysis complements other H1 measurements of exclusive diffractive processes: production of real photons, in photoproduction ($Q^2 \simeq 0$) at large $|t|$ [8] and in electroproduction at small $|t|$ (deeply virtual Compton scattering – DVCS) [9], production of ρ mesons in photoproduction at low [10] and large $|t|$ [11], of J/ψ mesons in photo- and electroproduction at low [12] and large $|t|$ [13], of $\psi(2s)$ [14] and Υ [15] mesons in photoproduction.

The ZEUS collaboration at HERA has performed measurements of DVCS [16], ρ [17–20], ω [21, 22], ϕ [20, 23, 24], J/ψ [20, 25–27] and Υ [28] production. Results at lower energy have been published, in particular for ρ electroproduction, by the DESY-Glasgow [29], CHIO [30], NMC [31], E665 [32] and HERMES [33] collaborations. The experimental and theoretical status of diffractive VM production before the high energy fixed target and HERA experiments is presented in detail in the review [34].

The paper is organised as follows. The theoretical context and the models which will be compared to the data are presented in section 2. The H1 detector and the event selection criteria are summarised in section 3, where the kinematic and angular variables are defined. The various signal samples are defined in section 4, which also contains a detailed discussion of the backgrounds, a description of the Monte Carlo (MC) simulations used for the analyses and a discussion of the systematic errors affecting the measurements. In section 5, the measurements of the VM line shapes and of the elastic and proton dissociative cross sections are presented, and VM universality and proton vertex factorisation are discussed. Section 6 is devoted to the polarisation characteristics of the reactions and their kinematic dependence. A summary of the results and conclusions are given in section 7.

2 Theoretical Context

Since the first observation of high Q^2 inclusive diffraction [35] and of VM production at HERA, a large number of theoretical studies has been published on diffractive VM production (see e.g. [36–63]). Reviews of theoretical predictions confronted by the data have been published recently [64, 65].

2.1 Cross section calculations

Calculations are performed following two main approaches, sketched in Fig. 2. The approach based on collinear factorisation, illustrated in Fig. 2(a), describes VM production using the parton content of the proton, in the presence of a hard scale. The colour dipole picture of Fig. 2(b) provides a complementary way to describe high energy scattering.

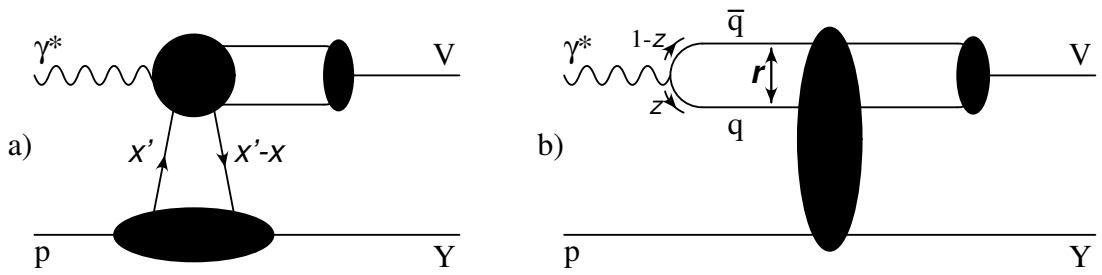

Figure 2: Representative diagrams for diffractive VM electroproduction: a) the collinear factorisation, GPD approach; b) the high energy, low x colour dipole approach.

Collinear factorisation In a pQCD framework, a collinear factorisation theorem [36] has been proven for the production of longitudinally polarised VMs in the kinematic domain with $W^2 \gg M_V^2$, $Q^2 \gg \Lambda^2_{QCD}$ and $|t| \lesssim \Lambda^2_{QCD}$, for leading powers of Q and for all values of x. The longitudinal amplitude, sketched in Fig. 2(a), is given by

$$T_L^{\gamma^\star p \to Vp}(x;t) = \Sigma_{i,j} \int_0^1 \mathrm{d}z \int \mathrm{d}x' \; f_{i/p}(x', x'-x, t; \mu) \cdot H_{i,j}(Q^2 x'/x, Q^2, z; \mu) \cdot \Psi_j^V(z;\mu), \quad (1)$$

where $f_{i/p}(x', x'-x, t; \mu)$ is the generalised parton distribution function (GPD) for parton i in the proton and μ is the factorisation and renormalisation scale, of the order of Q. The GPDs (see e.g. [66]), which are an extension of ordinary parton distribution functions (PDF), include correlations between partons with longitudinal momenta x and x' and transverse momenta t; they describe the off-diagonal kinematics ($x' \neq x$) implied by the different squared four-momenta of the incoming photon and outgoing VM. The $H_{i,j}$ matrix elements describe the hard scattering from the parton i in the proton to the parton j in the meson with wave function $\Psi_j^V(z;\mu)$, where z is the fraction of the photon longitudinal momentum carried by one of the quarks. The scale evolution is calculated, in the HERA kinematic domain, using the DGLAP equations, and higher order corrections have been calculated [57, 58, 63]. Collinear factorisation holds for heavy VMs [36], and its validity is extended to transverse amplitudes at sufficiently high Q^2 (see e.g. [36, 45, 48, 65]).

Dipole approach At high energy (small x) and small $|t|$, VM production is conveniently studied in the proton rest frame, for all values of Q^2. It is described as three factorising contributions, characterised by widely different time scales [67, 68], as illustrated in Fig. 2(b): the fluctuation of the virtual photon into a $q\bar{q}$ colour dipole, with a coupling depending only on the quark charge, the dipole-proton scattering (either elastic or proton dissociative scattering), and the $q\bar{q}$ recombination into the final state VM. The amplitude is

$$T^{\gamma^\star p \to Vp}(x;t) = \int_0^1 \mathrm{d}z \int \mathrm{d}^2\mathbf{r}\; \Psi^\gamma(z,\mathbf{r}) \cdot \sigma^{q\bar{q}-p}(x,\mathbf{r};t) \cdot \Psi^V(z,\mathbf{r}), \tag{2}$$

where $\mathbf{r}$ is the transverse distance between the quark and the antiquark, and $\Psi^\gamma(z,\mathbf{r})$ and $\Psi^V(z,\mathbf{r})$ are the photon and the VM wave functions, respectively. The diffractive dipole-proton cross section $\sigma^{q\bar{q}-p}(x,\mathbf{r};t)$ is expected to be flavour independent and to depend only on the dipole transverse size (the impact parameter between the dipole and the proton is integrated over). Photons with large virtuality and fluctuations into heavy quarks are dominated by dipoles with small transverse size. In this case, the two quarks tend at large distance to screen each other's colour ("colour transparency" [69]), which explains the small cross section. In several models [38, 43], the convolution of the VM wave function with the dipole is expected to play a significant role in VM production, by selecting specific dipoles. It can be noted that the Generalised Vector Meson Dominance model [34, 50] is related to the dipole approach.

Dipole-proton scattering is modeled at lowest order (LO) in pQCD through the exchange of a gluon pair in a colour singlet state [70], and in the leading logarithm approximation (LL $1/x$) as the exchange of a BFKL-type gluon ladder. In a $(z,\mathbf{k}_t)$ representation, where $\mathbf{k}_t$ represents the gluon momentum component transverse to the photon direction, k_t-unintegrated gluon distribution functions are used. The contributions of gluons with small k_t are of a non-perturbative nature, whereas at large k_t they can be obtained from the Q^2 logarithmic derivative of the usual, integrated, gluon distribution, $G(x,Q^2)$. In the LO and LL $1/x$ approximations both gluons emitted from the proton carry the same fraction x of the proton longitudinal momentum and the cross section is proportional to the square of the gluon density [41, 42]. Calculations beyond the LL $1/x$ approximation take into account the difference between the longitudinal momentum fractions carried by the two gluons ("skewing" effects) [46, 65, 71].

At low x, VM production can be calculated [52, 56, 59, 62], in the absence of a hard scale, using universal dipole-proton cross sections obtained from deep inelastic scattering (DIS) measurements [72]. This approach automatically incorporates soft, non-perturbative contributions. Such models often involve parton saturation effects, expected from the recombination of high density gluons [73, 74] as inferred from the observation of geometric scaling [62, 74]. DGLAP evolution can also be included, for instance in the model [59].

2.2 Kinematic dependences and σ_L/σ_T

The photon-proton cross section can be decomposed into a longitudinal and transverse part, σ_L and σ_T, respectively. At LO and for $t = 0$, the dependences $\sigma_L \propto 1/Q^6$ and $\sigma_T \propto 1/Q^8$ are predicted [42], and the ratio $R \equiv \sigma_L/\sigma_T$ is predicted to be $R = Q^2/M_V^2$. Modifications to these dependences are expected (see e.g. [43]), due to the Q^2 dependence of the gluon density, the

quark transverse movement (Fermi motion) and quark virtuality [49], and the Q^2 dependence of the strong coupling constant α_s.

In the dipole approach, the square of the scale μ of the interaction is

$$\mu^2 \simeq z(1-z)Q^2 + k_t^2 + m_q^2 \simeq z(1-z)(Q^2 + M_V^2), \tag{3}$$

m_q being the current quark mass. It is related to the inverse of the relevant "scanning radius" [38, 43, 65] in the dipole-proton interaction.

For longitudinally polarised photons or for heavy quark production, the $q\bar{q}$ wave function $\Psi^\gamma(z, \mathbf{r})$ is concentrated around $z \simeq 1 - z \simeq 1/2$. A universal hard scale μ, following from the transverse size of the dominant dipoles, is thus given by $\mu^2 \simeq (Q^2 + M_V^2)/4$. For transverse photons fluctuating into light quarks, in contrast, the wave function is non-zero at the end-points $z \simeq 0$ or 1. These contributions correspond to small k_t values of the quarks forming the dipole, and hence to a large transverse distance between them. The scale μ is therefore damped to smaller values than for longitudinal photons with the same virtuality, soft contributions may be significant and formal divergences appear in pQCD calculations for $z \to 0, 1$ [43, 44, 65]. For moderate Q^2 values, the z distribution of light quark pairs from longitudinal photons can present a non-negligible smearing around the value $z = 1/2$, which results in a contamination of soft, "finite size" effects [64]. It is estimated that the fully perturbative QCD regime is reached for light VM production by longitudinal photons for Q^2 above 20 to 30 GeV^2 [64, 65].

The W dependence of VM production is governed by the $x^{-\lambda}$ evolution of the gluon distribution, with λ increasing from 0.16 for $Q^2 = 2\ \mathrm{GeV}^2$ to 0.26 for $Q^2 = 20\ \mathrm{GeV}^2$, as measured in the total DIS cross sections at HERA [75]. For heavy VMs and for longitudinally polarised light VMs at sufficiently high Q^2, a strong ("hard") W dependence of the cross section is thus expected, fixed for all VMs by the scale $(Q^2 + M_V^2)/4$. In contrast, the W dependence of the transverse cross section is expected to be milder than for longitudinal photons, since the λ parameter is taken at a smaller value of the effective scale. This may result in a W dependence of the cross section ratio $R = \sigma_L/\sigma_T$. In the frame of Regge theory, the existence of two pomerons [76] is postulated to describe both the soft and hard behaviours of the cross section [53].

At low $|t|$ ($|t| \lesssim 0.5 - 0.6\ \mathrm{GeV}^2$ for elastic scattering), the t dependence of VM production is well described by an exponentially falling distribution with slope b, $\mathrm{d}\sigma/\mathrm{d}t \propto e^{-b|t|}$ (predictions for the $|t|$ dependence are also given e.g. in [49,54,62]). In an optical model approach, the slope b is given by the sum of the transverse sizes of the scattered system Y, of the $q\bar{q}$ dipole and of the exchanged system, with possibly in addition a VM form factor. Neglecting the latter, the t slopes for heavy VMs and for light VM production by longitudinally polarised photons are expected to take universal values, depending only on $(Q^2 + M_V^2)/4$, whereas the production of light VMs by transverse photons, which is dominated by dipoles with larger transverse size, is expected to exhibit steeper t distributions [43, 56]. This may result in a t dependence of σ_L/σ_T.

2.3 Helicity amplitudes

The helicity amplitudes $T_{\lambda_V \lambda_\gamma}$, where λ_V and λ_γ are the VM and photon helicities, respectively, have been calculated in perturbative QCD for the electroproduction of light VMs with

$|t| \ll Q^2$ [48, 49, 62, 65]. In this domain, the dominant amplitude is the s-channel helicity conserving (SCHC) T_{00} amplitude, which describes the transition from a longitudinal photon to a longitudinal VM. Other amplitudes are damped by powers of Q. Those leading to the production of a transverse VM, of which the SCHC T_{11} amplitude is largest, contain an additional factor $\propto 1/Q$. SCHC violation implies for single helicity flip amplitudes an additional factor $\propto \sqrt{|t|}/Q$, to be squared for the double flip T_{-11} amplitude. This leads, in the kinematic range studied here, to the following hierarchy of amplitude intensities (assuming natural parity exchange): $|T_{00}| > |T_{11}| > |T_{01}| > |T_{10}|, |T_{-11}|$.

2.4 Comparison of models with the data

Predictions for VM production are available from a large number of models. Quantitative calculations generally imply the choice of PDF or GPD parameterisations or, in colour dipole models, of dipole-proton cross section parameterisations. Model calculations also generally imply the choice of VM wave function parameterisations, often taken as following a Gaussian shape, with several variants [39, 40, 44, 56, 65, 72]. In view of the large number of models, no attempt is made in this paper to provide exhaustive comparisons to the data. Instead, a few models and parameterisations, representative of recent approaches, are compared to various choices of observables.

- The GPD model of Goloskokov and Kroll (GK [61]) provides predictions within the handbag factorisation scheme for the longitudinal and transverse amplitudes in the SCHC approximation. Soft physics is described by a GPD parameterisation of the proton structure, constructed from standard PDFs with adequate skewing features and t dependences. The end-point singularities are removed with the aid of a specific model for the VM wave function. Error bands are provided with the model predictions.

- The model of Martin, Ryskin and Teubner (MRT [45]) for ρ meson production is based on parton-hadron duality. Open $q\bar{q}$ production is calculated in an appropriate spin-angular state and in a specific invariant mass interval, which is then assumed to saturate ρ production, thus neglecting any VM wave function effects. The Q^2 dependence of the gluon density, described by the anomalous dimension γ with $G(x, Q^2) \propto (Q^2/Q_0^2)^\gamma$, is used to calculate the longitudinal and transverse cross sections. Skewing effects are parameterised [46, 71] without explicit use of GPDs. Predictions using two alternative PDFs are compared with the present data: CTEQ6.5M [77] and MRST-2004-NLO [78].

- The model presented in the review of Ivanov, Nikolaev and Savin (INS [65]) is framed in the k_t-factorisation dipole approach. The helicity amplitudes are calculated perturbatively and then extended into the soft region by constructing parameterisations of the off-forward unintegrated gluon density. The Q^2 and W dependences of the cross sections and the full set of spin density matrix elements are predicted. Two wave function models, "compact" and "large", are used for ρ mesons, corresponding to two extreme cases for describing the $\rho \to e^+e^-$ decay width.

- The k_t-factorisation calculations of Ivanov and Kirschner (IK [48]) provide predictions for the full set of helicity amplitudes, including helicity flip transitions. Similar to the

MRT approach, the relevance of pQCD for transverse amplitude calculations is justified by the scale behaviour $\propto (Q^2/Q_0^2)^\gamma$ of the gluon distribution, which avoids divergences for $z \to 0, 1$.

- The dipole approach of Kowalski, Motyka and Watt (KMW [59]) uses an impact parameter dependent description of the dipole cross section in the non-forward direction [79], within the saturation models of Golec-Biernat and Wüsthoff (GW [73]) and of Iancu *et al.* (Colour Glass Condensate – CGC [74]). The Q^2 and W dependences of the SCHC longitudinal and transverse amplitudes are predicted using the DGLAP evolution equations for $|t| \lesssim 0.5\ \mathrm{GeV}^2$.

- The dipole approach of Marquet, Peschanski and Soyez (MPS [62]) proposes an extension of the saturation model [74], geometric scaling being extended to non-forward amplitudes with a linear t dependence of the saturation scale. The exponential t dependence at the proton vertex is parameterised with a universal slope obtained from previous VM measurements.

3 Experimental Conditions and Variable Definitions

The diffractive production and decay of ρ and ϕ mesons is identified using the following reactions:

$$\begin{aligned} e + p &\to e + V + Y, \\ \rho &\to \pi^+ + \pi^- \quad (\mathcal{BR} \simeq 100\%), \\ \phi &\to K^+ + K^- \quad (\mathcal{BR} = 49.2 \pm 0.6\%). \end{aligned} \tag{4}$$

The events are selected by requiring the detection of the scattered electron and of a pair of oppositely charged particles, and by requiring the absence of additional activity in the detector, except in the region close to the outgoing proton beam, where proton dissociation can contribute.

The kinematic domain of the measurements is:

$$\begin{aligned} 2.5 \le\ & Q^2 \le 60\ \mathrm{GeV}^2, \\ 35 \le\ & W \le 180\ \mathrm{GeV}, \\ & |t| \le 3\ \mathrm{GeV}^2, \\ & M_Y < 5\ \mathrm{GeV}. \end{aligned} \tag{5}$$

The large values of W^2 compared to Q^2, M_Y^2, M_V^2 and $|t|$ ensure that the process is diffractive, i.e. due to pomeron exchange. The variable $x_{I\!P} = (Q^2 + M_V^2 + |t|)/(W^2 + Q^2 - M_Y^2)$, which corresponds to the proton energy loss, is always smaller than 10^{-2}.

3.1 Data sets

The data studied here were taken with 27.5 GeV energy electrons or positrons colliding with 820 or 920 GeV protons (in the rest of this paper the term "electron" is used generically to refer to both electrons and positrons). The data sets are summarised in Table 1, where $\sqrt{s}$ is the ep centre of mass energy and the lepton beam type is specified. The integrated luminosity of $51\ \mathrm{pb}^{-1}$ corresponds to running periods with all relevant parts of the detector fully operational. The periods with high prescaling of the triggers relevant for the present analyses are discarded. The published results with $1 \leq Q^2 \leq 2.5\ \mathrm{GeV}^2$ [4, 7] are also presented in Table 1 ("H1 SV"). They were obtained in 1995 in a special run of $125\ \mathrm{nb}^{-1}$, with the ep interaction point shifted by $70\ \mathrm{cm}$ in the outgoing p beam direction. This data set is not re-analysed in the present publication.

Data taking year	lepton beam	proton energy (GeV)	$\sqrt{s}$ (GeV)	luminosity (pb^{-1})
1995 (SV)	e^+	820	300	0.125
1996	e^+	820	300	4.0
1997	e^+	820	300	9.8
1999	e^-	920	320	4.8
1999	e^+	920	320	4.6
2000	e^+	920	320	28.1

Table 1: Characteristics of the data taken in 1995 with a shifted vertex (SV) and of the data sets used in the present paper (1996-2000).

3.2 The H1 detector and triggers

A detailed description of the H1 detector can be found in [80]. Only the components essential to the present analysis are described here. The origin of the H1 coordinate system is the nominal ep interaction point, with the positive z–axis (forward direction) along the direction of the proton beam. The polar angles θ and the particle transverse momenta are defined with respect to this axis, and the pseudorapidity is $\eta = -\log\tan(\theta/2)$.

A system of two large coaxial cylindrical drift chambers (CJC) of $2\ \mathrm{m}$ length and $0.85\ \mathrm{m}$ external radius, with wires parallel to the beam direction, is located in a $1.16\ \mathrm{T}$ uniform magnetic field. This provides a measurement of the transverse momentum of charged particles with resolution $\Delta p_t/p_t \simeq 0.006\ p_t \oplus 0.015$ (p_t measured in GeV), for particles emitted from the nominal interaction point with polar angle $20 \leq \theta \leq 160^\circ$. Drift chambers with wires perpendicular to the beam direction, located inside the inner CJC and between the two CJC chambers, provide measurements of z coordinates. Track measurements are improved by the use of the central silicon tracker [81] (from 1997 onward). The interaction vertex is reconstructed from the tracks.

The liquid argon (LAr) calorimeter, located inside the magnet and surrounding the central tracker, covers the angular range $4 \leq \theta \leq 154^\circ$. The backward electromagnetic calorimeter

Spacal ($153 \leq \theta \leq 177.5^{\circ}$) is used to identify scattered electrons. In front of the Spacal, the backward drift chambers (BDC) provide a precise electron direction measurement.

The "forward detectors" are sensitive to energy flow close to the outgoing proton beam direction. They consist of the proton remnant tagger (PRT), a set of scintillators placed $24\ \mathrm{m}$ downstream of the interaction point and covering the angles $0.06 \leq \theta \leq 0.17^{\circ}$, and the forward muon detector (FMD), a system of drift chambers covering the angular region $3 \leq \theta \leq 17^{\circ}$. The PRT and the three layers of the FMD situated closer to the main calorimeter detect secondary particles produced in interactions with the beam collimators or the beam pipe walls of elastically scattered protons at large $|t|$ and of decay products of diffractively excited systems Y with $M_Y \gtrsim 1.6\ \mathrm{GeV}$.

For the data collected in 1996 and 1997, events with $Q^2 \geq 2.5\ \mathrm{GeV}^2$ were selected by inclusive triggers requesting an electromagnetic energy deposit in the Spacal. For the years 1999 and 2000, diffractive VM events with $Q^2 \geq 5\ \mathrm{GeV}^2$ were registered using several inclusive triggers; in addition, a special trigger was dedicated to elastic ϕ production with $Q^2 > 2\ \mathrm{GeV}^2$.

To reduce the data recording rate to an acceptable level, data selected by certain triggers have been dowscaled. In the following, the accepted events are weighted accordingly.

3.3 Event selection

For the present analyses, events are selected on the basis of the following requirements.

The scattered electron candidate is identified as an electromagnetic cluster with energy larger than 17 GeV reconstructed in the Spacal calorimeter. This energy threshold reduces to a negligible level the background of photoproduction events with a wrongly identified electron candidate in the Spacal. The electron direction is calculated from the position of the measured interaction vertex and from the BDC signals, when their transverse distance to the cluster barycentre is less than $3\ \mathrm{cm}$; if no such BDC signal is registered, the cluster centre is used.

The VM candidate selection requires the reconstruction in the central tracking detector of the trajectories of two oppositely charged particles. They must originate from a common vertex lying within $30\ \mathrm{cm}$ in z of the nominal ep interaction point, and must have transverse momenta larger than $0.15\ \mathrm{GeV}$ and polar angles within the interval $20 \leq \theta \leq 160^{\circ}$. This ensures a difference in pseudorapidity of at least two units between the most forward track and the most forward cell of the LAr calorimeter. The VM momentum is calculated as the vector sum of the two charged particle momenta.

The existence of a gap in rapidity between the VM and the forward system Y is further ensured by two veto conditions: that there is in the central tracker no additional track, except if it is associated to the electron candidate, and that there is in the LAr calorimeter no cluster with energy above noise level, $E > 400$ MeV, unless it is associated to the VM candidate. These requirements reduce to negligible level the contamination from non-diffractive DIS interactions, which are characterised by the absence of a significant gap in rapidity in the fragmentation process. They imply that the mass of the diffractively excited proton system is restricted to $M_Y \lesssim 5\ \mathrm{GeV}$. They also contribute to the suppression of backgrounds due to the diffractive production of systems subsequently decaying into a pair of charged particles and additional

neutral particles. Energy deposits unrelated to the VM event and noise in the calorimeter are monitored from randomly triggered readouts of the detector. The energy threshold of 400 MeV leads to an average loss of $13^{+3}_{-5}\%$ of the diffractive VM events.

A cut is applied to the difference between the sum of energies and the sum of longitudinal momenta of the scattered electron and VM candidate, $\Sigma(E - p_z) > 50$ GeV. For events where all particles except the forward going system Y are detected, this quantity is close to twice the incident electron beam energy, 55 GeV. The cut reduces the QED radiation and background contributions in which additional particles remain undetected.

3.4 Kinematic and angular variables

To optimise measurements in the selected domain, the kinematic variables are reconstructed from the measured quantities following the algorithms detailed in [4]. In addition to the nominal beam energies, they make use of well measured quantities in the H1 detector: the electron and VM directions and the VM momentum.

The variable Q^2 is reconstructed from the polar angles of the electron and of the VM ("double angle" method [82]). The modulus of the variable t is to very good precision equal to the square of the transverse momentum of the scattered system Y, which is calculated as the vector sum $\vec{p}_{t,miss} = -(\vec{p}_{t,V} + \vec{p}_{t,e})$ of the transverse momenta of the VM candidate and of the scattered electron[1]. The electron transverse momentum, $\vec{p}_{t,e}$, is determined using the electron energy obtained from the "double angle" method. The variable W is reconstructed from the VM energy and longitudinal momentum [83]. The electron energy measured in the Spacal is used only for the calculation of the variable $\Sigma(E - p_z)$.

Three angles characterise VM electroproduction and two-body decay (Fig. 3). In the helicity frame used for the present measurements, they are chosen as follows. The azimuthal angle ϕ is defined in the hadronic centre of mass system as the angle between the electron scattering plane and the VM production plane, which is formed by the directions of the virtual photon and the VM. The two other angles, which describe VM decay, are chosen in the VM rest frame as the polar angle θ and the azimuthal angle φ of the positively charged decay particle, h^+, the quantization axis being opposite to the direction of the outgoing system Y.

4 Data Analysis

This section first defines the analysis samples. The backgrounds are then discussed, the Monte Carlo simulations used to extract the signals are introduced, and the predictions are compared to the distributions of the hadronic invariant mass and of other observables. Finally, systematic uncertainties are discussed.

[1] More precisely, the quantity $|\vec{p}_{t,miss}|^2$ is a measure of $t' = |t| - |t|_{min}$, where $|t|_{min}$ is the minimum value of $|t|$ kinematically required for the VM and the system Y to be produced on shell through longitudinal momentum transfer. At HERA energies and for the relevant values of M_V and M_Y, $|t|_{min}$ is negligibly small compared to $|t|$. In the following the notations $|t|$ is used for t'.

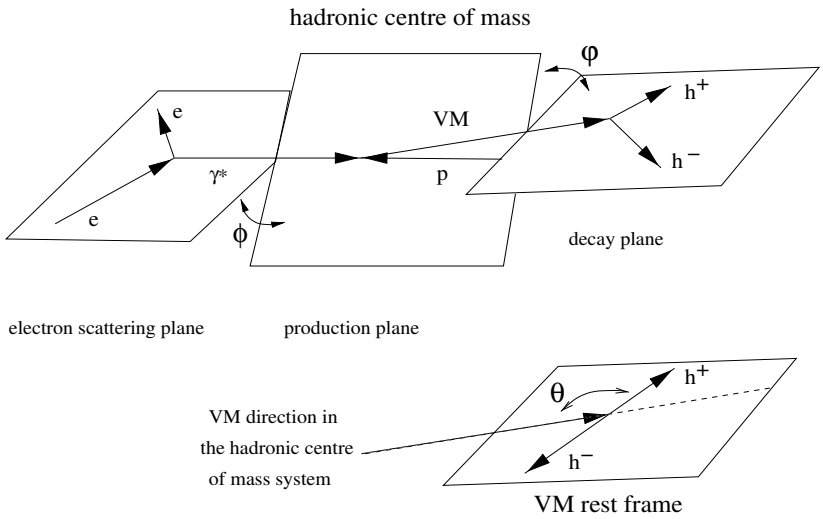

Figure 3: Definition of the angles characterising diffractive VM production and decay in the helicity system.

4.1 Analysis samples

Four event samples, which correspond approximately to the four processes studied in this paper, are selected following the conditions summarised in Tables 2 and 3. These conditions are chosen to minimize background contributions.

Vector meson	mass range
ρ sample	$0.6 \leq m_{\pi\pi} \leq 1.1$ GeV
ϕ sample	$1.00 \leq m_{KK} \leq 1.04$ GeV

Table 2: Sample definition for the two VM selection.

The VM identification relies on the invariant mass of the two particles with trajectories reconstructed in the central tracker; no decay particle identification is performed. For the ρ sample, the mass $m_{\pi\pi}$ calculated under the pion mass hypothesis is required to lie in the range $0.6 \leq m_{\pi\pi} \leq 1.1$ GeV. For the ϕ sample, the range $1.00 \leq m_{KK} \leq 1.04$ GeV is selected, the invariant mass m_{KK} being calculated under the kaon hypothesis.

Diffractive process	forward detector selection	t range
notag sample	no signal above noise	$\lvert t\rvert \leq 0.5$ GeV^2
tag sample	signal detected above noise	$\lvert t\rvert \leq 3.0$ GeV^2

Table 3: Sample definition for the two diffractive processes.

The events in the ρ and ϕ samples are further classified in two categories, "notag" and "tag", according to the absence or the presence of activity above noise levels in the forward detectors, respectively. Elastic production is studied in the notag sample with $|t| \leq 0.5$ GeV^2 whereas the tag sample with $|t| \leq 3$ GeV^2 is used for proton dissociative studies.

Year	VM	Q^2 range (GeV^2)	W range (GeV)
1995 - SV	ρ, ϕ	$1.0 \leq Q^2 \leq 2.5$	$40 \leq W \leq 140$
1996-1997	ρ, ϕ	$2.5 \leq Q^2 < 4.9$	$35 \leq W \leq 100$
		$4.9 \leq Q^2 < 9.8$	$40 \leq W \leq 120$
		$9.8 \leq Q^2 < 15.5$	$50 \leq W \leq 140$
		$15.5 \leq Q^2 < 27.3$	$50 \leq W \leq 150$
		$27.3 \leq Q^2 \leq 60.0$	$60 \leq W \leq 150$
1999-2000	ϕ notag	$2.5 \leq Q^2 < 4.9$	$35 \leq W \leq 100$
	ρ, ϕ	$4.9 \leq Q^2 < 9.8$	$40 \leq W \leq 120$
		$9.8 \leq Q^2 < 15.5$	$50 \leq W \leq 140$
		$15.5 \leq Q^2 < 27.3$	$50 \leq W \leq 160$
		$27.3 \leq Q^2 \leq 60.0$	$60 \leq W \leq 180$

Table 4: Kinematic range of the measurements.

The kinematic domain of the measurements is summarised in Table 4. It is determined by the detector geometry, the beam energies and the triggers, with the requirement of a reasonably uniform acceptance. The accepted Q^2 range depends on the data taking period; for the notag ϕ sample in 1999-2000 it extends to smaller values than for the tag ϕ sample and for the ρ samples, due to the special elastic ϕ trigger. For W, the regions with good acceptance are determined by the track requirement; the accepted W values increase with Q^2 and with $\sqrt{s}$.

The acceptance increases with Q^2, mostly because of the non-uniform geometric acceptance of the electron trigger for $Q^2 \lesssim 20$ GeV^2. Monte Carlo studies show that the total acceptance increases from 15% (18%) for ρ (ϕ) elastic production at $Q^2 = 2.5$ GeV^2 to about 50% at $Q^2 = 8$ (6) GeV^2 and to more than 60% for $Q^2 = 12$ (10) GeV^2, and that they are essentially independent of W in the measurement domain.

The raw numbers of events selected in the four samples defined by Tables 2-4 are given in Table 5, together with the numbers weighted to account for the downscaling applied to certain triggers.

Numbers of events	ρ sample		ϕ sample	
	raw	weighted	raw	weighted
notag sample	7793	11775	1574	1976
tag sample	2760	3824	416	495

Table 5: Events in the different data samples: raw numbers and numbers weighted to account for the downscaling applied to certain triggers.

	ρ notag $\lvert t\rvert \leq 0.5$ GeV^2	ρ tag $\lvert t\rvert \leq 3$ GeV^2	ϕ notag $\lvert t\rvert \leq 0.5$ GeV^2	ϕ tag $\lvert t\rvert \leq 3$ GeV^2
p. diss. events	$10.7 \pm 0.3\%$	$-$	$9.7 \pm 0.7\%$	$-$
el. events	$-$	$13.1 \pm 0.5\%$	$-$	$11.8 \pm 1.5\%$
$\pi^+\pi^-$	$-$	$-$	$6.3 \pm 0.5\%$	$4.7 \pm 0.9\%$
$\phi \rightarrow 3\,\pi$	$0.3 \pm 0.1\%$	$0.4 \pm 0.1\%$	$-$	$-$
ω	$0.6 \pm 0.1\%$	$0.7 \pm 0.1\%$	$1.7 \pm 0.3\%$	$2.8 \pm 0.7\%$
ρ'	$4.0 \pm 0.2\%$	$7.7 \pm 0.4\%$	$3.6 \pm 0.4\%$	$9.2 \pm 1.3\%$

Table 6: Background contributions to the four data samples defined in Tables 2-4. The quoted errors are the statistical errors from the MC samples.

4.2 Backgrounds

Several background processes, which affect differently the four data samples and depend on the kinematic domain, are discussed in this section. Their contributions are summarised in Table 6. The non-resonant $\pi\pi$ contribution to the ρ signal, which contributes essentially through interference, is discussed separately in section 5.2.1. The e^+e^- and $\mu^+\mu^-$ backgrounds were found, using the GRAPE simulation [85], to be completely negligible.

4.2.1 Cross-contaminations between the elastic and proton dissociative processes

The notag and tag samples correspond roughly to the elastic and proton dissociative processes, respectively. However, cross-contaminations occur, due to the limited acceptance and efficiency of the forward detectors and to the presence of noise. The response of these detectors is modeled using independent measurements, by comparing signals in the various PRT and FMD planes.

The cross-contaminations are determined for each VM species without *a priori* assumptions on the relative production rates of elastic and inelastic events. In a first step, the contaminations are calculated from the numbers of tag and notag events and from the probabilities for elastic and proton dissociative events to deposit a signal in the forward detectors as obtained from the MC simulations. The crossed backgrounds are then determined in an iterative procedure from the simulations, after final tunings to the data.

Proton dissociative backgrounds in the notag samples Proton dissociative events produce a background to the elastic signals in the notag samples when the mass of the excited baryonic system is too low to give a signal in the forward detectors ($M_Y \lesssim 1.6$ GeV) or because of inefficiencies of these detectors. The background fraction increases strongly with $|t|$, because the proton dissociative cross sections have a shallower $|t|$ distribution than the elastic cross sections. In the notag samples with $|t| \leq 0.5$ GeV^2, the proton dissociative background amounts to 10.5%.

Elastic backgrounds in the tag samples Conversely, elastic background in the proton dissociative samples of tag events is due to unrelated signal or noise in the forward detectors. For $|t| \leq 3$ GeV^2, it amounts to 12.5%, with larger contributions for small $|t|$ values where the elastic to proton dissociative cross section ratio is larger. In addition, when $|t|$ is large enough for the scattered proton to hit the beam pipe walls or adjacent material ($|t| \gtrsim 0.75$ GeV^2), elastic events may give signal in the forward detectors.

4.2.2 Cross-contaminations between ρ and ϕ samples

For ρ production, the contribution from the $\phi \to K^+K^-$ channel is removed by the requirement $m_{\pi\pi} \geq 0.6$ GeV, which also suppresses the contribution of the $\phi \to K^0_S K^0_L$ channel ($\mathcal{BR} = 34\%$) with the K^0_S meson decaying into a pion pair close to the emission vertex and the K^0_L being undetected in the calorimeter.

The largest background in the selected ϕ samples is due to the low mass tail of $\pi^+\pi^-$ pair production extending under the ϕ peak. It amounts to 6% and depends on Q^2. The shape of the $\pi^+\pi^-$ distribution corresponding to small values of m_{KK} is discussed in section 4.3.

4.2.3 $\phi \to 3\,\pi$ and ω backgrounds

A small ϕ contamination in the ρ samples is due to the channel $\phi \to \pi^+\pi^-\pi^0$ ($\mathcal{BR} = 15\%$) when each photon from the π^0 decay remains undetected because it is emitted outside the LAr calorimeter acceptance, because the energy deposit in the LAr calorimeter does not pass the 400 MeV threshold, or because it is associated with one of the charged pions. This background contributes to the $m_{\pi\pi}$ distribution mostly below the selected mass range; it amounts to 0.3% of the selected ρ notag sample with $|t| \leq 0.5$ GeV^2 and 0.4% of the tag sample with $|t| \leq 3$ GeV^2. The background rate increases with $|t|$ because the non-detection of the π^0 decay photons leads in general to an overestimate of the p_t imbalance of the event, $\vec{p}_{t,miss}$, which mimics a large $|t|$ value. The $\phi \to 3\,\pi$ contribution below the $\phi \to KK$ signal is negligible.

Similarly, the diffractive production of ω mesons decaying in the mode $\omega \to \pi^+\pi^-\pi^0$ ($\mathcal{BR} = 89\%$) gives background contributions to the ρ and ϕ samples when the π^0 decay photons escape detection. In addition, the $\omega \to \pi^+\pi^-$ ($\mathcal{BR} = 1.7\%$) channel gives an irreducible background to the ρ signal. The background due to ω production contributes 0.6% to the elastic and 0.7% to the proton dissociative ρ samples, and 1.7 and 2.8% for the ϕ samples, respectively. The non-detection of photons leads to large reconstructed $|t|$ values for these contributions. Note that for the cross sections quoted below, as for results in previous HERA papers, the $\omega - \rho$ interference is neglected: its contribution is small and cancels when integrated over the mass range.

4.2.4 ρ' background

The largest background to the ρ signal and the second largest background to the ϕ signal is due to diffractive ρ' production[2]. The ρ' mesons decay mostly into a ρ meson and a pion pair, leading to

[2]The detailed mass structure [84] of the states described in the past as the $\rho'(1600)$ meson is not relevant for the present study. The name ρ' is used for all VM states with mass in the range $1.3 - 1.7$ GeV.

final states with four charged pions ($\rho' \to \rho^0\pi^+\pi^-$) or with two charged and two neutral pions ($\rho' \to \rho^\pm\pi^\mp\pi^0,\ \rho^\pm \to \pi^\pm\pi^0$). The $\pi^+\pi^-\pi^0\pi^0$ events can mimic large $|t|$ ρ or ϕ production when the photons from the π^0 decays escape detection, which induces a p_t imbalance in the event and a distortion of the t distribution, similarly to the $\phi \to 3\,\pi$ and $\omega \to 3\,\pi$ backgrounds. At high $|t|$, this background affects mostly the notag samples. It is indeed distributed between the notag and tag samples following the elastic to proton dissociative production cross section ratio, whereas genuine high $|t|$ ρ and ϕ mesons are essentially produced with proton dissociation and thus contribute mainly to the tag samples.

No cross section measurement of diffractive ρ' production has been published in the relevant Q^2 range. The ρ' contribution to the ρ signal is thus determined from the data themselves, using a method presented in the H1 analysis of high $|t|$ ρ electroproduction [5]. The distribution of the variable ζ, which is the cosine of the angle between the transverse components of the ρ candidate momentum, $\vec{p}_{t,\rho}$, and of the event missing momentum, $\vec{p}_{t,miss}$, is sensitive to the relative amounts of ρ signal and ρ' background. The ρ' contribution gives a peak at $\zeta = +1$ and a negligible contribution at $\zeta = -1$, since the ρ and the missing π^0's are all emitted roughly in the direction of the ρ'. In contrast, the ρ signal gives peaks at $\zeta = +1$ and $\zeta = -1$. However, for genuine ρ production, ζ is also correlated to the angle ϕ between the ρ production plane and the electron scattering plane, which is distributed according to the a priori unknown value of the combinations of spin density matrix elements $r^5_{00} + 2r^5_{11}$ and $r^1_{00} + 2r^1_{11}$ (Eq. (41), Appendix A).

An iterative procedure is used to determine simultaneously the amounts of ρ' background in the notag and tag samples, the matrix element combinations $r^5_{00} + 2r^5_{11}$ and $r^1_{00} + 2r^1_{11}$ (assumed to be identical for elastic and proton dissociative scattering), and the $|t|$ distributions of ρ elastic and proton dissociative production. It is found to converge after a few steps. The results are also used to calculate the ρ' background to the ϕ signal.

The ρ' background is estimated to contribute 4% to the notag samples with $|t| \leq 0.5\ \mathrm{GeV}^2$, and 8% to the tag samples with $|t| \leq 3\ \mathrm{GeV}^2$.

4.3 Monte Carlo simulations

Monte Carlo simulations based on the DIFFVM program are used to describe ρ, ω, ϕ and ρ' VM production and decay, detector response (acceptances, efficiencies and variable reconstruction) and radiative effects.

The DIFFVM program [86] is based on Regge theory and Vector Meson Dominance [87]. The M_Y diffractive mass distribution for proton dissociative events contains an explicit simulation of baryonic resonance production for $M_Y < 1.9\ \mathrm{GeV}$ and a dependence $\mathrm{d}\sigma/\mathrm{d}M_Y^2 \propto 1/M_Y^{2.16}$ for larger masses [88], with quark and diquark fragmentation simulated using the JETSET programme [89].

The ρ and ϕ MC samples are reweighted according to the measurements of the Q^2, W and $|t|$ differential cross sections and of the angular VM production and decay distributions: the angle θ is distributed according to the measurements of the r^{04}_{00} matrix element (Eq. (39)), the angle ϕ to those of the $r^5_{00} + 2r^5_{11}$ and $r^1_{00} + 2r^1_{11}$ combinations (Eq. (41)), and the angle φ to those of the $\cos\delta$ parameter, which in the SCHC approximation fixes the $\psi = \phi - \varphi$ distribution (Eq. (47)).

For the ω and ρ' backgrounds, the cross section dependences on the kinematic variables Q^2, W and $|t|$ are taken to be the same as for ρ mesons at the same $(Q^2+M_V^2)/4$ value. For the two-body ω decay, the angular distributions are taken as for ρ mesons. For three-body ω and ϕ decays, the angular distributions are chosen to follow ϕ and $\cos\theta$ distributions described by the same values of the matrix elements as for two-body decays. For ρ' decays[3], the parameters $M_1(00)$ and $M_1(10)$ describe the angular distributions [90]. The values $|M_1(00)|^2 = 0.5, |M_1(10)|^2 = 0.5$ are chosen for the present simulations.

The ratio of proton dissociative to elastic cross sections is taken from the present ρ analysis and assumed to be the same for all VMs. All kinematic and angular distributions are taken to be identical for elastic and proton dissociative scattering, as supported by the present data, except for the $|t|$ dependence of the cross sections.

The ϕ to ρ cross section ratio is set to that measured in this analysis. The ω to ρ ratio is taken from ZEUS measurements [21, 22]. For ρ' production, a ρ' to ρ ratio of 1.12 is used[4], as a result of the procedure described in the previous section.

For ρ, ϕ and ω mesons, the particle mass, width and decay branching ratios are taken from the PDG compilation [84]. The mass and width of the ρ' resonance are taken as $1450\ \mathrm{MeV}$ and $300\ \mathrm{MeV}$, respectively. For ρ and ϕ meson decays into two pseudoscalar mesons, the mass distributions are described by a relativistic Breit-Wigner function $BW(m)$ with momentum dependent width, as described in section 5.2. In addition, the ρ mass shape is skewed according to the parameterisation of Ross and Stodolsky [91],

$$\frac{\mathrm{d}N(m_{\pi\pi})}{\mathrm{d}m_{\pi\pi}} \propto BW_\rho(m_{\pi\pi}) \left(\frac{m_\rho}{m_{\pi\pi}}\right)^n, \tag{6}$$

with the Q^2 dependent value of n measured in this analysis.

The $\pi\pi$ background in the ϕ mass region is taken from the skewed Breit-Wigner distribution for ρ mesons, modified for $m_{\pi\pi} < 0.6\ \mathrm{GeV}$ according to the empirical form

$$\frac{\mathrm{d}N(m_{\pi\pi})}{\mathrm{d}m_{\pi\pi}} \propto BW_\rho(m_{\pi\pi}) \cdot \left(\frac{m_\rho}{0.6}\right)^n \cdot \left[1 + \kappa\sqrt{0.6 - m_{\pi\pi}}\,\right], \tag{7}$$

with masses expressed in GeVand the parameter κ being taken to be 1.5. This parameterisation describes the low mass $m_{\pi\pi}$ distribution well, as shown in Figs. 4, 5 and 9, where the cut $m_{KK} > 1.04\ \mathrm{GeV}$ is applied to suppress genuine ϕ production.

Radiative effects are calculated using the HERACLES program [92]. Corrections for these effects in the selected kinematic range with $\Sigma(E - p_z) > 50$ GeV are of the order of 1%.

[3]In the dominant $\rho' \to \rho\pi\pi$ decay mode, the two pions do not form a ρ resonance and can be assumed to be in a spin 0 state. The angular decay distribution thus includes the two possible polarisation states of the ρ meson, with the squared amplitude $|M_1(00)|^2$ ($|M_1(10)|^2$) corresponding to the probability that it is longitudinally (transversely) polarised, giving in the SCHC approximation, with the notations of Appendix A:
$W(\theta,\psi) = \frac{3}{4\pi}\,\frac{1}{1+\varepsilon R}\left\{|M_1(00)|^2\ \left[\ \frac{1}{2}\sin^2\theta + \varepsilon R\cos^2\theta - \frac{K}{2}\sin 2\theta\cos\psi\cos\delta + \frac{\varepsilon}{2}\sin^2\theta\cos 2\psi\ \right]\right.$
$\left. + |M_1(10)|^2\ \left[\ \frac{1}{2}(1 + \cos^2\theta + \varepsilon R\sin^2\theta + \frac{K}{2}\sin 2\theta\cos\psi\cos\delta - \frac{\varepsilon}{2}\sin^2\theta\cos 2\psi\ \right]\right\}$, where $K = \sqrt{2\varepsilon R(1+\varepsilon)}$.

[4]This number does not constitute a ρ' cross section measurement, but it is used as an empirical parameterisation for describing the ρ' background contribution under the ρ peak, for the ρ' mass and width chosen in the simulation; as a consequence, varying the latter values has negligible influence on the background subtraction.

All generated events are processed through the full GEANT [93] based simulation of the H1 apparatus and are reconstructed using the same program chain as for the data. Of particular relevance to the present analysis is the description of the forward detector response; the activity in these detectors, not related to VM production, is obtained from data taken independently of physics triggers, and is superimposed on generated events in the MC simulations.

4.4 Mass distributions

The $m_{\pi\pi}$ and m_{KK} mass distributions are shown in Figs. 4 to 6, separately for the notag and tag samples. The results of the Monte Carlo simulations, comprising signal and backgrounds, are also shown. They are reweighted and normalised to the data as described in the previous section.

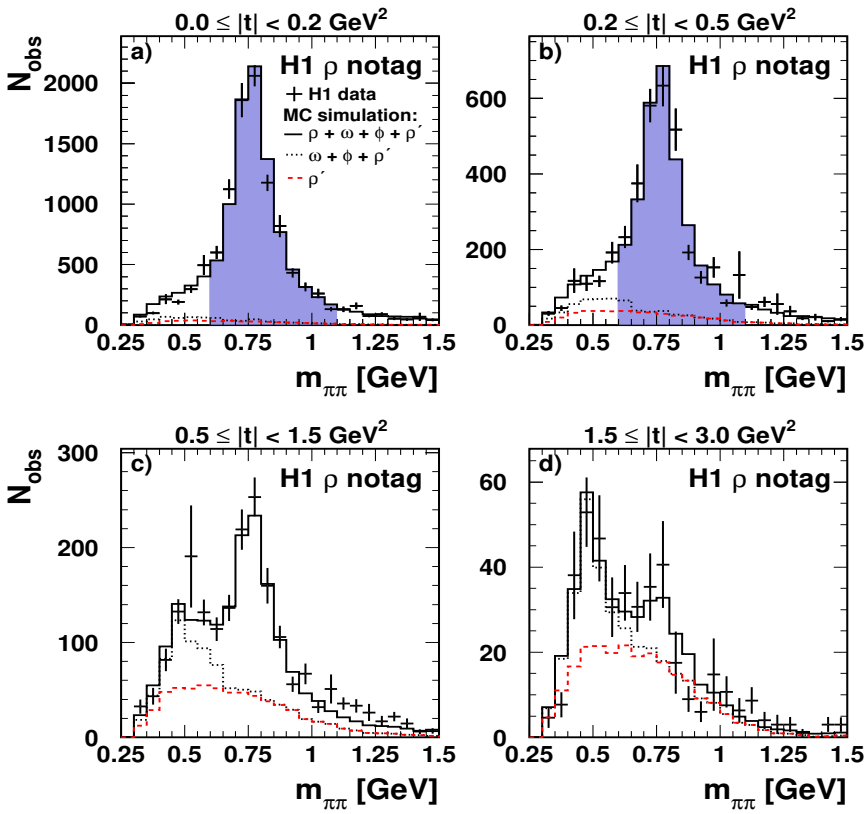

Figure 4: Distributions of the invariant mass $m_{\pi\pi}$ (with the cut $m_{KK} > 1.04$ GeV to reject the $\phi \to KK$ signal) in four domains in $|t|$, for the notag sample. The dashed histograms show the MC predictions for the ρ' background, the dotted histograms the sum of the ρ', ω and ϕ backgrounds, and the full histograms the ρ signal (including interference with $\pi\pi$ non-resonant production) and the sum of all backgrounds. The mass and $|t|$ domain where the cross section measurements are performed is shaded.

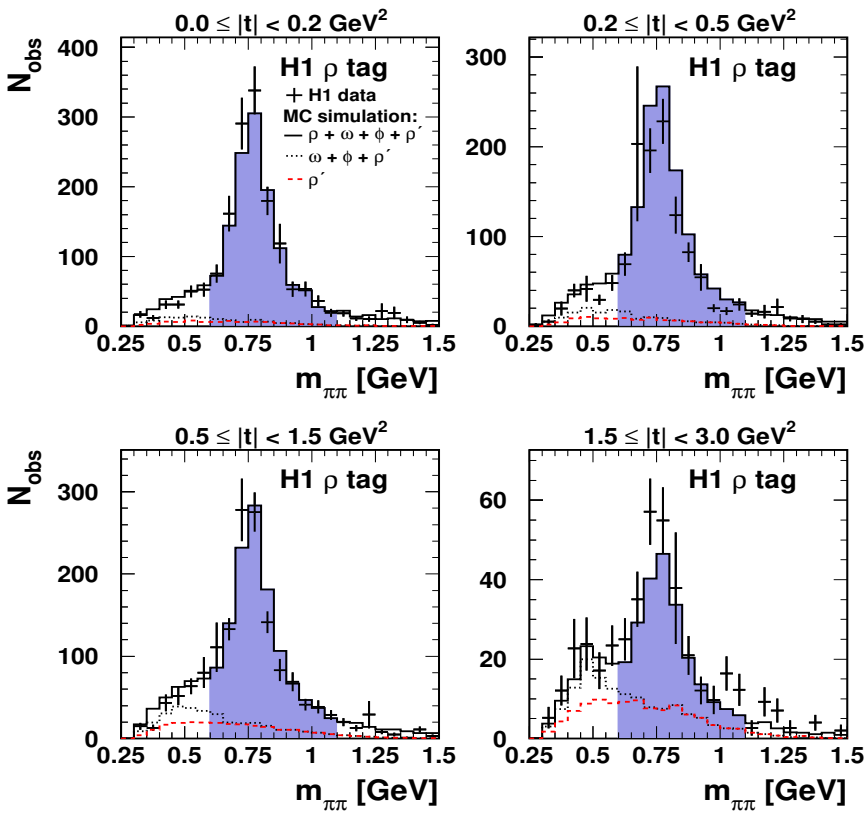

Figure 5: Same as in Fig. 4, for the tag sample.

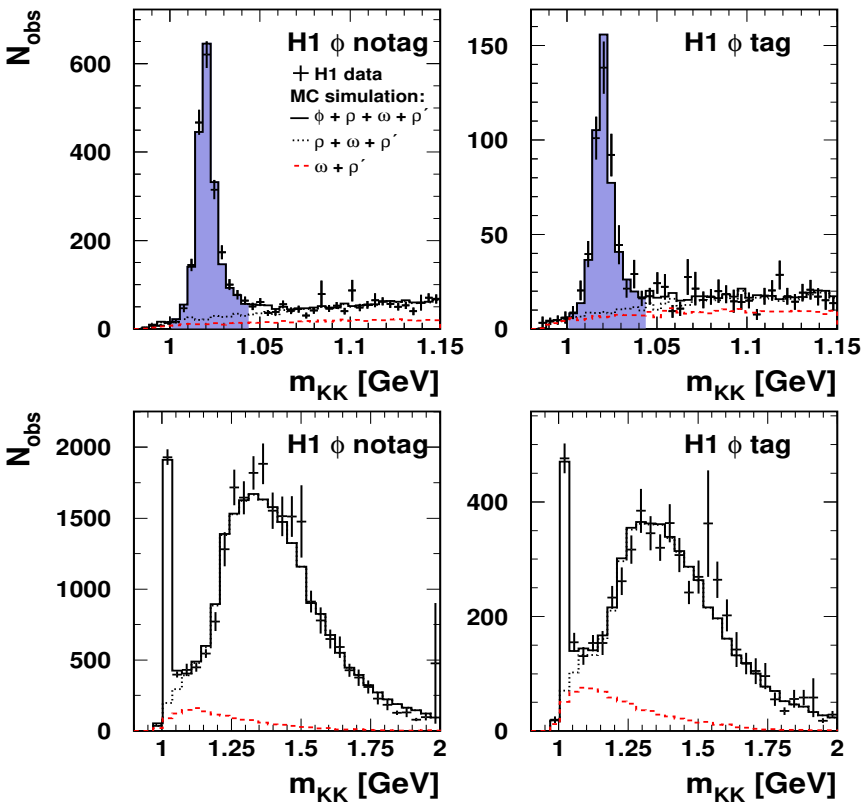

Figure 6: Distributions of the invariant mass m_{KK}: (upper plots) in the ϕ mass region, for the notag and tag samples separately; (lower plots) over an extended mass range, showing the ϕ signal and the reflection of ρ production and the backgrounds. The dashed histograms show the sum of the ρ', ω and $\phi \rightarrow 3\,\pi$ backgrounds, the dotted histograms show in addition the ρ and non-resonant $\pi\pi$ backgrounds, and the full histograms the $\phi \rightarrow KK$ signal and the sum of all backgrounds. In (a) and (b), the mass domain where the cross section measurements are performed is shaded.

The mass spectra are presented from threshold to masses well above the actual measurement ranges defined in Table 2. The $m_{\pi\pi}$ spectra in Figs. 4 and 5 are presented in four bins in $|t|$, with the cut $m_{KK} > 1.04$ GeV. The m_{KK} spectra in Fig. 6 exhibit the reflection of ρ production and of backgrounds.

The $m_{\pi\pi}$ mass distributions are well described from the threshold at $2m_\pi$ up to 1.5 GeV. The backgrounds are small in the mass ranges selected for the physics analyses, shown as the shaded regions in the figures, but their contributions can be distinctly identified outside these domains. In the $m_{\pi\pi}$ distributions, they are particularly visible at low mass and, as expected, they contribute mostly at large $|t|$, especially in the notag sample with $|t| > 0.5$ GeV^2 of Fig. 4. A decrease of the background with increasing Q^2 for the same ranges in $|t|$ is also observed (not shown here), which is explained by the larger transverse momentum of the virtual photon, resulting in larger p_t values of the decay photons which thus pass the detection threshold and lead to the rejection of the events.

In view of the small ρ' background in the final selected samples, an analysis of only the mass spectrum, performed in the restricted mass range $0.6 \leq m_{\pi\pi} \leq 1.1$ GeV, is not sufficient to constrain the ρ' contribution. Controlling this background is crucial for the measurements of the $|t|$ slope and of the r_{00}^{04} matrix element. In the present analysis, the amount of ρ' background is obtained from the distribution of the variable ζ (defined in section 4.2.4). The value determined within the mass range $0.6 \leq m_{\pi\pi} \leq 1.1$ GeV also gives a good description of the mass range $2m_\pi < m_{\pi\pi} < 0.6$ GeV, below the actual measurement. This demonstrates the reliability of the background estimate.

The m_{KK} mass distribution shown in Fig. 6 is also very well described. The $\pi\pi$ background under the ϕ peak, which contains a ρ' contribution obtained from the ρ analysis, is small[5].

4.5 Kinematic and angular distributions

Figures 7 and 8 present several kinematic and angular variable distributions for the samples selected as defined in Tables 2-4. They demonstrate that the simulations, taking into account the detector acceptance and response and the background contributions, correctly describe the data.

Figure 7 shows kinematic variable distributions of the ρ and ϕ notag samples. The structure observed in the electron polar angle distribution (a) results from the different kinematic range selections for the different years. The dip in the distribution (b) of the laboratory azimuthal angle ϕ_e of the electron is due to an asymmetric electron trigger acceptance. The p_t distributions of the decay mesons (e), (i) reflect the VM mass and the decay angular distributions. The good description of the difference between the azimuthal angles of the decay kaons in the ϕ sample (f) indicates that the reconstruction of pairs of tracks with small differences in azimuthal angles is under control. A description of similar quality is obtained for the tag samples.

[5]For the notag sample with $|t| \leq 0.5$ GeV^2, the background under the ϕ peak amounts to 20.5% for $Q^2 = 2.5$ GeV^2 (10% from the $\pi^+\pi^-$ low mass tail, 3% from ω and 7.5% from ρ' production), and to 5.5% for $Q^2 = 13$ GeV^2 (2.5%, 0.5% and 2.5%, respectively). An empirical description of the background by ZEUS, using a simple power law shape, is in agreement with these detailed findings: it amounts to 18% for $Q^2 = 2.5$ GeV^2 and 5% for $Q^2 = 13$ GeV^2 [24].

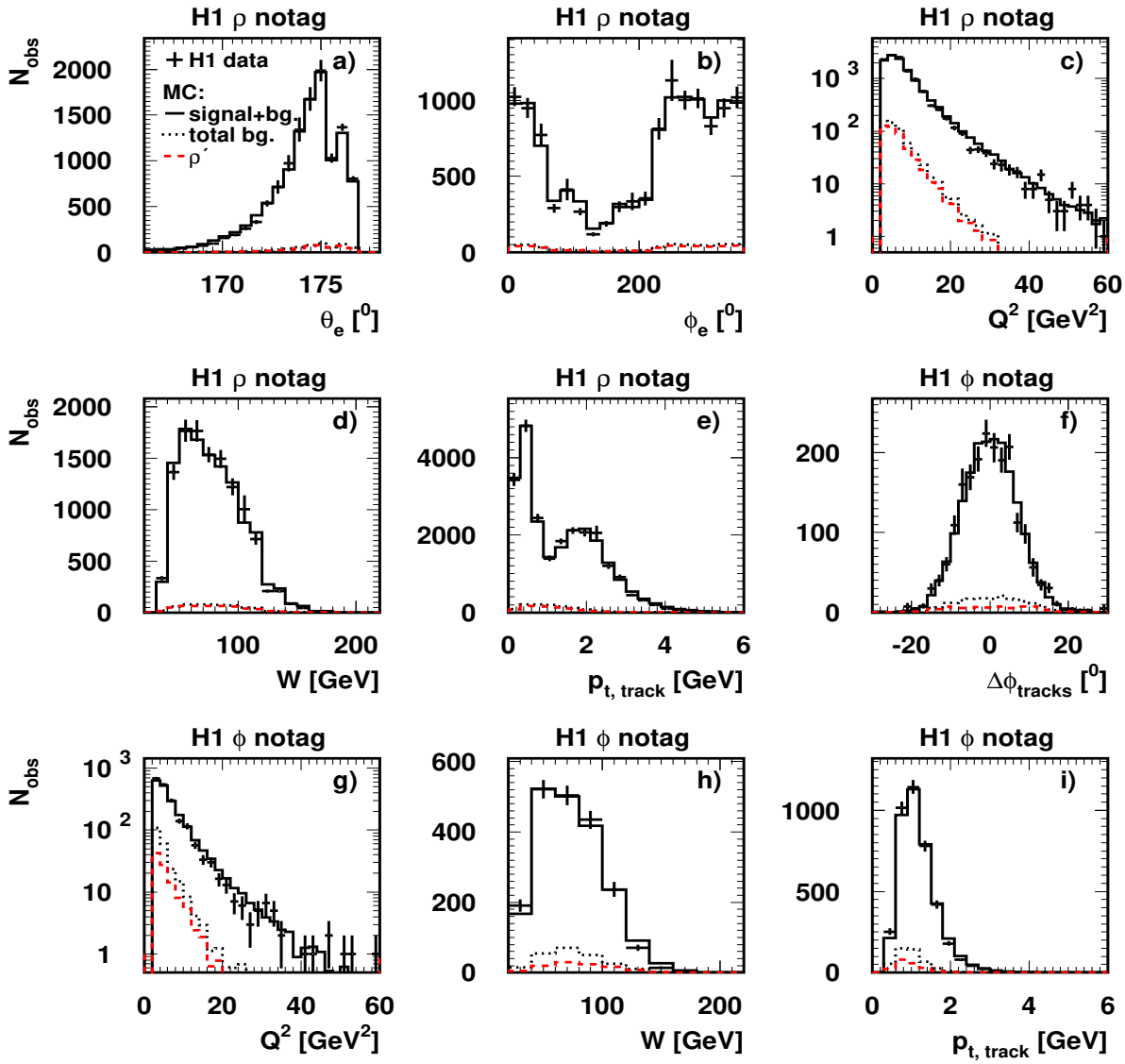

Figure 7: Distributions of the polar angle θ_e (a) and azimuthal angle ϕ_e (b) of the scattered electron, of the Q^2 (c) and W (d) variables, and of the transverse momenta of the decay mesons (e), for the ρ notag sample; distributions of the difference between the azimuthal angles ϕ of the decay kaons (f) and, in (g)-(i), of the same observables as in (c)-(e), for the ϕ notag sample. In panels (a)-(e), the dashed histograms present the MC predictions for the distributions of the ρ' background, the dotted histograms in addition for the ω and ϕ backgrounds, and the full histograms for the ρ signal and the sum of all backgrounds; in panels (f)-(i), the dashed histograms describe the ρ' and ω backgrounds, the dotted histograms in addition the $\pi\pi$ background, and the full histograms the ϕ signal and the sum of all backgrounds.

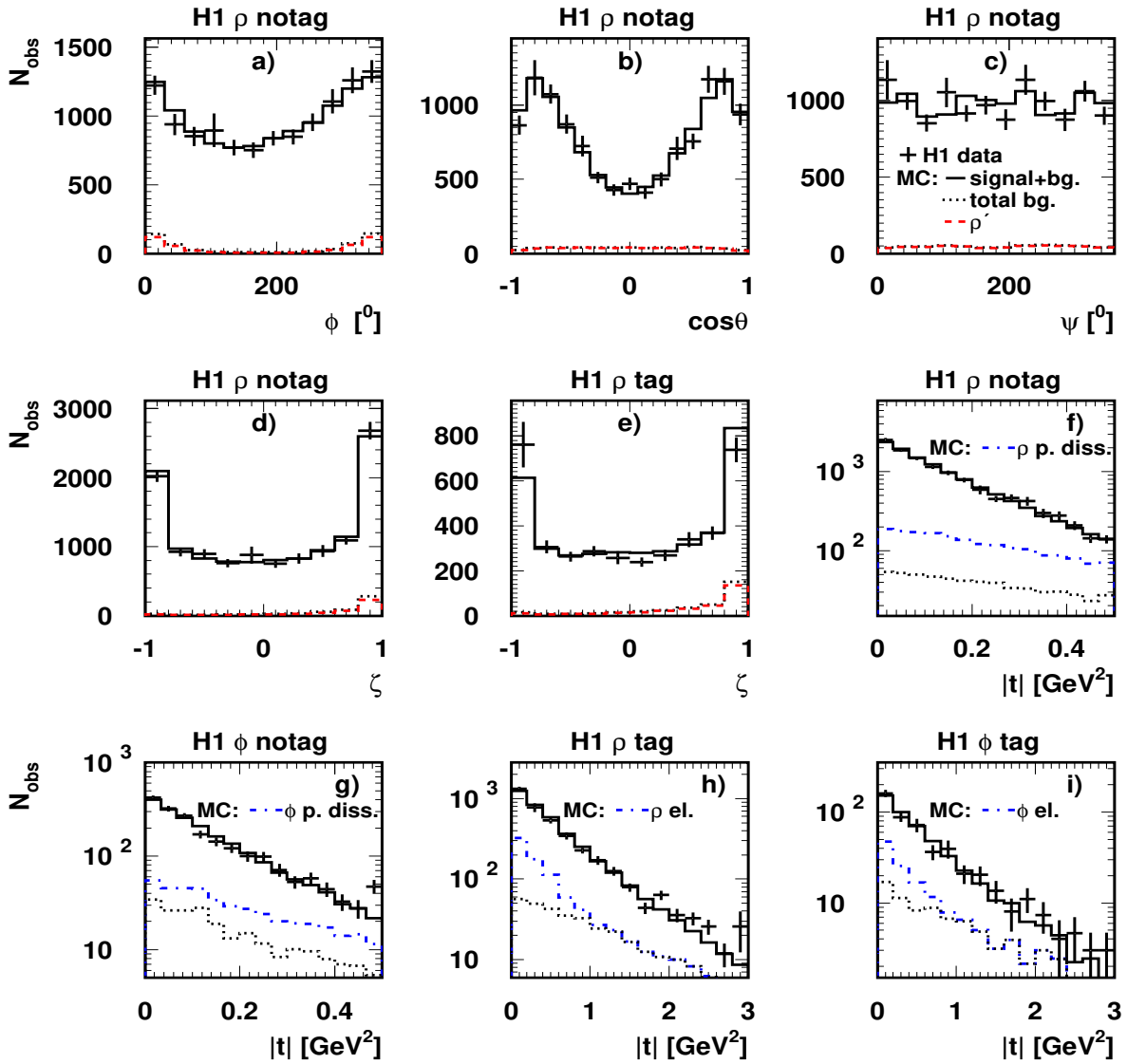

Figure 8: Distributions of the VM production and decay angles ϕ (a), $\cos\theta$ (b) and $\psi = \phi - \varphi$ (c) for the ρ notag sample; of the ζ variable for the ρ notag (d) and tag (e) samples; of the $|t|$ variable for the ρ (f) and ϕ (g) notag samples and for the tag samples (h)-(i). In panels (a)-(e), the dashed histograms present the MC predictions for the distributions of the ρ' background, the dotted histograms show in addition the ω and ϕ backgrounds, and the full histograms the ρ signal and the sum of all backgrounds; in panels (f)-(i), the dotted histograms show the sum of the various VM backgrounds (ρ', ω, ϕ or $\rho + \pi\pi$), the dash-dotted histograms show in addition the diffractive background (proton dissociation in panels (f)-(g) and elastic production in panels (h)-(i)), and the full histograms the signal and the sum of all backgrounds.

Figures 8(a)-(c) present distributions related to the spin density matrix elements. The ζ distributions (d)-(e) are sensitive to the values of the matrix element combinations $r^5_{00} + 2r^5_{11}$ and $r^1_{00} + 2r^1_{11}$ and to the amount of ρ' background especially at high $|t|$ as discussed in section 4.2.4. The $|t|$ distributions (f)-(i) are sensitive to the amount of diffractive backgrounds (proton dissociation for the notag sample, elastic scattering for the tag sample) and to the values assumed for the exponential t slopes.

4.6 Systematic errors

Uncertainties on the detector response and background contributions are listed in Table 7. They are estimated by varying the MC parameters in the limits indicated in the table, which are in most cases determined from the data. Global normalisation errors are given separately.

The error on the electron polar angle θ_e, which affects the Q^2 measurements and the acceptance calculations, is due to the uncertainty on the absolute positioning of the BDC with respect to the CJC chambers, the uncertainty on the electron beam direction in the interaction region and the error on the z position of the interaction vertex.

The uncertainty on the energy scale of the Spacal calorimeter affects the cross section measurements through the electron energy threshold of 17 GeV and the $\Sigma(E - p_z)$ cut.

The uncertainty on losses due to the rejection of events affected by noise in the LAr calorimeter or containing energy deposits unrelated to the diffractive event is estimated by varying the energy threshold, both in the data and in the simulation (where data taken from random triggers are directly superimposed to the simulated events).

The uncertainties on the simulated cross section dependences on Q^2, W and $|t|$ affect the bin-to-bin migrations and the extrapolations from the average value of the kinematic variables in a bin to the position where they are presented ("bin centre corrections").

An absolute error of ± 0.10 is used for the ratio of the proton dissociative (with $M_Y < 5$ GeV) to elastic cross sections, which corresponds to about 20% relative error. It is estimated by varying by ± 0.15 the parameter n in the simulated dissociative mass distribution $\mathrm{d}\sigma/\mathrm{d}M_Y^2 \propto 1/M_Y^{2n}$, by varying the slope parameters of the exponential $|t|$ distributions of elastic and proton dissociative events within the experimental limits, and by calculating the cross section ratio using only the PRT or only the FMD. The latter covers uncertainties in the inefficiencies of these detectors.

For the ρ cross section measurements, the error due to the extraction of the non-resonant $\pi\pi$ background is estimated through the variation of the Q^2 dependent skewing parameter n of the Ross-Stodolsky parameterisation of Eq. (6).

The errors on the various cross section ratios are taken from the present analysis for the ϕ to ρ and ρ' to ρ ratios, and from the ZEUS measurements of the ω/ρ ratio [22].

The errors due to the uncertainty on the ρ' decay angular distribution are estimated by considering the two extreme cases $|M_1(00)|^2 = 1, |M_1(10)|^2 = 0$ and $|M_1(00)|^2 = 0, |M_1(10)|^2 = 1$ of the pair of variables defined in [90].

MC parameter	functional dependence	VM	variation
Detector effects			
electron polar angle θ_e		all VM	± 1 mrad
Spacal energy scale		all VM	$\pm 1\%$
noise threshold in LAr		all VM	± 100 MeV
Cross section dependences			
$\mathrm{d}\sigma/\mathrm{d}Q^2$	$(Q^2+M^2)^{-n}$	all VM	$n \pm 0.15$
$\mathrm{d}\sigma/\mathrm{d}W$	W^{δ}	all VM	$\delta \pm 25\%$
$\mathrm{d}\sigma/\mathrm{d}t$	$e^{-b\|t\|}$, b in GeV^{-2}	ρ	el. : $b \pm 0.5$ GeV^{-2}
			p. diss. : $b \pm 0.3$ GeV^{-2}
		ϕ, ρ', ω	el. : $b \pm 1.0$ GeV^{-2}
			p. diss. : $b \pm 0.7$ GeV^{-2}
Backgrounds			
proton dissoc. / elastic		all VM	± 0.10 ($\approx \pm 20\%$)
ρ shape skewing	$(m_\rho/m_{\pi\pi})^n$	ρ	$n \pm 0.15$
VM cross sections		ω/ρ	± 0.02 ($\approx \pm 20\%$)
		ϕ/ρ	± 0.03 ($\approx \pm 15\%$)
		ρ'/ρ	± 0.40 ($\approx \pm 35\%$)
ρ' decay	$M_1(00)$ and $M_1(10)$	ρ'	see text
ρ and ϕ angular decay distributions			
r^{04}_{00}	$f(Q^2)$	ρ, ϕ	$\pm 15\%$
$r^5_{00}+2r^5_{11}$, $r^1_{00}+2r^1_{11}$	$f(\|t\|)$	ρ, ϕ	$\pm 30\%$
$\cos\delta$		ρ, ϕ	± 0.05
Global normalisation			
luminosity		all VM	$\pm 1.5\%$
trigger efficiency		all VM	$\pm 1.0\%$
track rec. eff. (per track)		all VM	$\pm 2\%$
width of rel. B.-W.	see text	ρ	$\pm 2\%$
$\phi \to KK$ $\mathcal{BR}$	see [84]	ϕ	$\pm 1.2\%$
$\pi\pi$ under ϕ peak (κ param.)		ϕ	$\pm 100\%$
$\mathrm{d}\sigma/\mathrm{d}M_Y^2$	$1/M_Y^{2n}$	all p. diss.	$n \pm 0.15$

Table 7: Parameter variation in MC simulations for the estimation of systematic uncertainties. Numbers between parentheses indicate the relative variations.

The uncertainty on the angular distributions are described by varying the values of the matrix element r_{00}^{04} (for the angle θ), of the combinations $r_{00}^{5} + 2r_{11}^{5}$ and $r_{00}^{1} + 2r_{11}^{1}$ (for the angle ϕ) and of the $\cos\delta$ parameter (for the angle $\psi = \phi - \varphi$).

The uncertainty on the choice of the momentum dependent width of ρ mesons results in normalisation uncertainties of 2% (see section 5.2).

For ϕ production, the uncertainty on the $\pi\pi$ background under the signal is estimated by varying the parameter κ globally from 0 to 3 (Eq. (7) in section 4.3), leading to a normalisation error of $\pm 3\%$ on the cross section measurements.

For the proton dissociative cross sections, the error on the correction for the smearing through the experimental cut $M_Y < 5$ GeV is estimated by varying the parameter n of the M_Y distribution ($\mathrm{d}\sigma/\mathrm{d}M_Y^2 \propto 1/M_Y^{2n}$, with $n \pm 0.15$), which leads to an additional normalisation error of $\pm 2.4\%$ on the proton dissociative cross section measurement.

The uncertainties on the luminosity measurement, on the triggers and on the track reconstruction efficiency are assumed to affect globally the normalisation only.

Systematic errors due to limited MC statistics are negligible compared to the statistical precision of the measurements (the generated samples correspond to at least ten times the data integrated luminosity).

All systematic errors on the measurements presented in the rest of this paper are calculated from separate quadratic sums of positive and negative effects of the variations listed in Table 7. In all figures, measurements are shown with statistical errors (inner error bars) and statistical and systematic errors added in quadrature (full error bars). In tables, the errors are given separately: first the statistical, second the systematic errors. Overall normalisation errors are not included in the error bars but are quoted in the relevant captions.

5 Cross Section Results

In this section, measurements of the ρ and ϕ line shapes are presented first. The elastic and proton dissociative cross sections are then measured as a function of Q^2 (total and polarised cross sections), W and t (total cross sections); results for different VMs are compared. Finally, elastic and proton dissociative scatterings are compared, including tests of proton vertex factorisation. Model predictions are compared to the data.

5.1 Measurement of cross sections

The cross sections for ρ and ϕ production presented in this paper are extracted from the numbers of events in the mass ranges $0.6 \leq m_{\pi\pi} \leq 1.1$ GeV and $1.00 \leq m_{KK} \leq 1.04$ GeV, respectively. They are corrected for all backgrounds, including for ρ mesons the non-resonant dipion diffractive production (see section 5.2.1). They include all corrections for detector acceptance and response. When quoted at a fixed value of a kinematic variable, the cross sections are evolved from the average value in the bin using dependences measured in this analysis.

The cross sections are quoted for the full resonance mass range from the two particle threshold up to the nominal mass plus five times the resonance width:

$$\begin{aligned} 2\,m_\pi \le m_{\pi\pi} \le m_\rho + 5\,\Gamma_\rho \;&\simeq 1501\ \mathrm{MeV}, \\ 2\,m_K \le m_{KK} \le m_\phi + 5\,\Gamma_\phi \;&\simeq 1041\ \mathrm{MeV}. \end{aligned} \tag{8}$$

For ϕ mesons, the cross sections take into account the branching ratio to the K^+K^- channel.

Elastic and proton dissociative cross sections are given at the Born level (i.e. they are corrected for QED radiation effects) in terms of $\gamma^\star p$ cross sections (except for the mass shapes, which are given in terms of ep cross sections). The $\gamma^\star p$ cross sections are extracted from the ep cross sections in the Weizsäcker-Williams equivalent photon approximation [94] using the definition

$$\sigma(\gamma^* + p \to V + Y) = \frac{1}{\Gamma} \cdot \frac{\mathrm{d}^2\sigma(e + p \to e + V + Y)}{\mathrm{d}y\ \mathrm{d}Q^2} \tag{9}$$

where the flux Γ of virtual photons [95] and the inelasticity y are given by

$$\Gamma = \frac{\alpha_{em}}{\pi}\ \frac{1 - y + y^2/2}{y\,Q^2}, \qquad y = \frac{p \cdot q}{p \cdot k}, \tag{10}$$

α_{em} being the fine structure constant and p and k the four-momenta of the incident proton and electron, respectively.

5.2 Vector meson line shapes

The distribution of the invariant mass m of the VM decay particles is analysed assuming the relativistic Breit-Wigner distribution $BW(m)$ with momentum dependent width $\Gamma(m)$ [96]:

$$BW(m) \;=\; \frac{m\,M_V\,\Gamma(m)}{(M_V^2 - m^2)^2 + M_V^2\,\Gamma(m)^2}, \tag{11}$$

$$\Gamma(m) \;=\; \Gamma_V \left(\frac{q^*}{q_0^*}\right)^3 \frac{M_V}{m}, \tag{12}$$

where M_V and Γ_V are the nominal VM resonance mass and width, q^* is the momentum of the decay particles in the rest frame of the pair with mass m, and q_0^* is the value taken by q^* when $m = M_V$.

For ρ mesons, the mass extrapolation from the measurement domain $0.6 \le m_{\pi\pi} \le 1.1$ GeV to the full range given by Eq. (8), including the correction for skewing effects, implies a correction factor of 1.15 with a systematic error of 2% due to the theoretical uncertainty on the choice of the momentum dependent width [96]. For ϕ production, a very small extrapolation outside the measurement domain is required, with negligible related error.

5.2.1 ρ mesons

Distributions of the $m_{\pi\pi}$ mass in the range $2\,m_\pi \le m_{\pi\pi} \le 1.5$ GeV, with the cut $m_{KK} > 1.04$ GeV applied to suppress the ϕ signal at low mass, are shown in Fig. 9 for elastically produced events in four ranges in Q^2, after subtraction of the proton dissociative, ϕ, ω and ρ' backgrounds and corrections for detector and QED radiation effects. The mass resolution in the ρ mass range, determined with the MC simulation, is about 10 MeV.

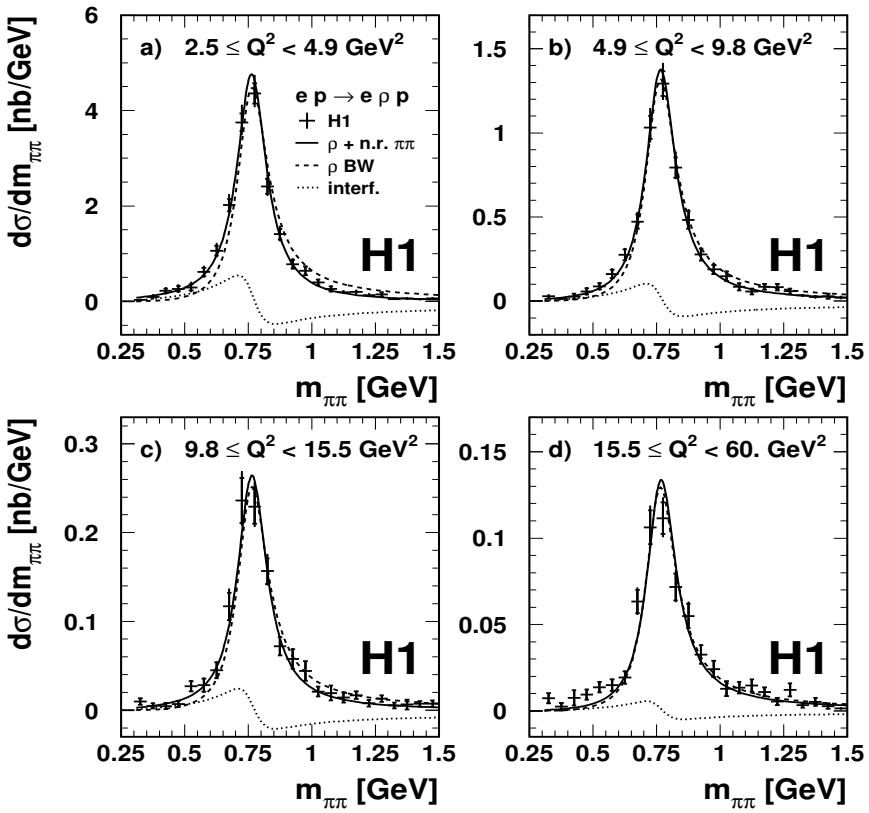

Figure 9: Distributions of the $m_{\pi\pi}$ mass for elastic ρ production with $|t| < 0.5\ \mathrm{GeV}^2$, expressed as ep cross sections, after experimental corrections and background subtraction, for four ranges in Q^2 and in the W domains defined in Table 4. The solid curves show the results of fits to the data in the mass range $0.6 \leq m_{\pi\pi} \leq 1.1\ \mathrm{GeV}$ of the relativistic Breit-Wigner function with momentum dependent width defined in Eqs. (11-12), with skewing of the mass distribution following the Söding parameterisation given by Eq. (13); the dashed curves correspond to a non-skewed relativistic Breit-Wigner function and the dotted curves to the interference between resonant and non-resonant amplitudes.

Skewing The mass distributions are skewed towards small masses, especially at low Q^2. According to Söding's analysis [97], this is due to the interference of the ρ meson with background from p-wave Drell-type non-resonant $\pi\pi$ pair production, with positive interference for $m_{\pi\pi} < m_\rho$ and negative interference for $m_{\pi\pi} > m_\rho$.

Following one of the forms of skewing proposed in [17], the ρ mass shape is described as

$$\frac{\mathrm{d}N(m_{\pi\pi})}{\mathrm{d}m_{\pi\pi}} \propto \left| \frac{\sqrt{m_{\pi\pi}\, m_\rho\, \Gamma(m_{\pi\pi})}}{m_\rho^2 - m_{\pi\pi}^2 + i\, m_\rho \Gamma(m_{\pi\pi})} + \frac{f_I}{2} \right|^2 , \tag{13}$$

where resonant and non-resonant $\pi\pi$ production are supposed to be in phase. The interference is proportional to f_I, which is taken to be independent of the $m_{\pi\pi}$ mass; the very small purely non-resonant contribution is given by $f_I^2/4$. Figure 9 shows that the ρ mass shape is well described by Eqs. (11-13) over the full range $2m_\pi \leq m_{\pi\pi} \leq 1.5$ GeV, with the skewing parameters fitted in the range $0.6 \leq m_{\pi\pi} \leq 1.1$ GeV. No indication is found for significant additional backgrounds, also outside the mass domain used for the measurements. The ρ skewing effect is also often conveniently parameterised in the form proposed by Ross and Stodolsky [91], given by Eq. (6).

For a fit over the whole Q^2 range with the parameterisation of Ross and Stodolsky, the values of the resonance mass and width are $769 \pm 4\,(\mathrm{stat.})$ MeV and $162 \pm 8\,(\mathrm{stat.})$ MeV, respectively. The Söding parameterisation gives similar values, with larger errors. This is in agreement with the world average values as obtained in photoproduction [84]: $m_\rho = 768.5 \pm 1.1$ MeV and $\Gamma_\rho = 150.7 \pm 2.9$ MeV. Within errors, no difference is observed between the elastic and proton dissociative samples.

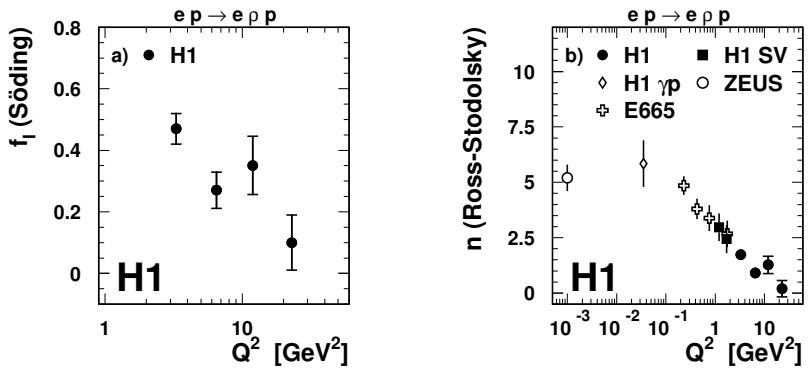

Figure 10: Q^2 dependence (a) of the Söding skewing parameter f_I defined in Eq. (13); (b) of the Ross-Stodolsky parameter n defined in Eq. (6), for ρ elastic production. Measurements from H1 [10] and ZEUS [17] in photoproduction and E665 [32] in electroproduction are also shown. The present measurements are given in Table 14.

Figure 10 presents the Q^2 dependence of the fitted values of the skewing parameters for elastic ρ production[6], the mass and width of the resonance being fixed to the PDG values [84].

[6]The values of the parameters f_I and n slightly depend on the fit mass range. At low mass, this is related to the shape uncertainties reflected by the uncertainty in the parameterisation of Eq. (7). For higher masses, the mass limit dependence may be due to additional interference of ρ mesons with heavier (ρ') resonances [98].

The skewing effects decrease with increasing Q^2, showing that the non-resonant amplitude decreases faster with Q^2 than the resonant amplitude, as expected on theoretical grounds [99]. No significant dependence of the skewing parameters is observed as a function of W or $|t|$.

5.2.2 ϕ mesons

The mass distribution for elastically produced kaon pairs is shown in Fig. 11, after background subtraction and corrections for detector and QED radiation effects. It is well described by the convolution of the Breit-Wigner function defined by Eqs. (11-12) with a Gaussian distribution of width $\sigma = 2$ MeV describing the mass resolution, as determined using the MC simulation. The mass and width of the resonance, fitted over the interval $1.006 \leq m_{KK} \leq 1.040$ GeV, are 1018.9 ± 0.2 (stat.) MeV and 3.1 ± 0.2 (stat.) MeV, respectively, reasonably close to the world average values of 1019.46 ± 0.02 MeV and 4.26 ± 0.04 MeV [84]. Conversely, when the ϕ mass and width are fixed to the nominal values, the fitted resolution is 1.0 ± 0.1 MeV, slightly smaller than the resolution obtained from simulations. As expected [98], no indication is found for skewing effects due to interference with non-resonant K^+K^- production.

5.3 Q^2 dependence of the total cross sections

5.3.1 Cross section measurements

The measurements of the $\gamma^* p$ cross sections for ρ and ϕ meson elastic and proton dissociative production are presented in Fig. 12 as a function of the scaling variable $(Q^2+M_V^2)$. They are quoted for $W = 75$ GeV using the W dependences parameterised as a function of Q^2 following the measurements of section 5.5.2. Using the fits of the Q^2 dependence presented below, it is verified that the normalisations of the 1995 (SV) cross section measurement [4] and of the present measurement are in good agreement for ρ mesons (the ratio is 1.01 ± 0.10). For the ϕ data, the 1995 SV measurement is slightly lower than extrapolated from the present result (the ratio is 0.84 ± 0.11). This difference is attributed to the different treatments of the backgrounds. ZEUS measurements of ρ and ϕ electroproduction are also shown in Fig. 12. Whereas the ρ measurements agree well, ϕ measurements of ZEUS are a factor 1.20 above the present data. When an improved estimation of the proton dissociative background, investigated for the latest ZEUS ρ production study [19], is used to subtract this background in their ϕ analysis, the cross section ratio of the two experiments is reduced to 1.06, which is within experimental errors [100].

The total cross sections roughly follow power laws of the type $1/(Q^2+M_V^2)^n$ with values of n, fitted over the domain $1 \leq Q^2 \leq 60$ GeV^2, given in Table 8(a). These values are compatible for elastic and proton dissociative scattering. They are also similar for ρ and ϕ mesons, which supports the relevance of the scaling variable $(Q^2+M_V^2)$.

The generally poor values of $\chi^2/\mathrm{d.o.f.}$ for fits with constant values of n confirms the observation of [4]: compared to a simple power law, the cross section dependence is damped for small values of $(Q^2+M_V^2)$ and steepens for larger values. An empirical parameterisation $n = c_1 + c_2\,(Q^2+M_V^2)$ provides a significant improvement of the fit and a good description of

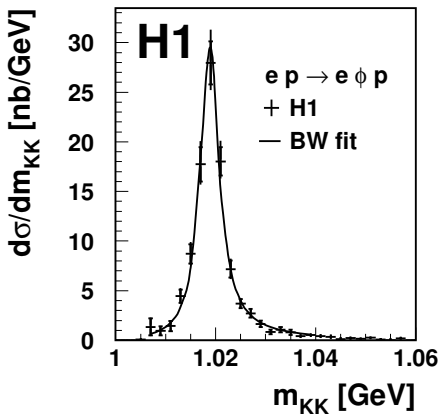

Figure 11: Distribution of the m_{KK} mass for elastic ϕ production with $|t| < 0.5$ GeV^2, expressed as ep cross section, after experimental corrections and background subtraction, for the Q^2 and W domains defined in Table 4. The solid curve shows the result of a fit to the data in the mass range $1.00 \leq m_{KK} \leq 1.04$ GeV of a relativistic Breit-Wigner function with momentum dependent width defined in Eqs. (11-12), convoluted with the experimental resolution.

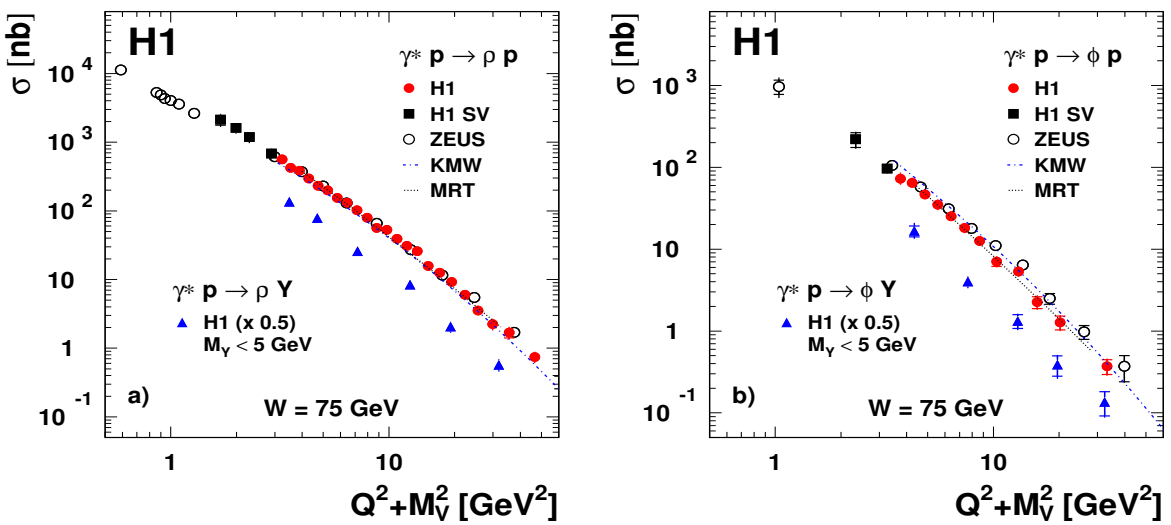

Figure 12: $(Q^2+M_V^2)$ dependence of the $\gamma^* p$ cross sections for $W = 75$ GeV: (a) ρ meson production; (b) ϕ production. The upper points are for the elastic processes, the lower points for proton dissociative diffraction, divided by a factor 2 to improve the readability of the figures. Overall normalisation errors of 3.9% (4.6%) for elastic (proton dissociative) ρ production and 4.7% (5.3%) for ϕ production are not included in the error bars. ZEUS measurements [17–19, 23, 24] are also presented; when needed, they were translated to $W = 75$ GeV using the measured W dependence. The superimposed curves are from the KMW model [59] with GW saturation [73] (dash-dotted lines) and from the MRT model [45] with CTEQ6.5M PDFs [77] (dotted lines). The present measurements are given in Tables 15-18.

(a) n constant		
	ρ el.	ρ p. diss.
n	$2.37 \pm 0.02\ ^{+0.06}_{-0.06}$	$2.45 \pm 0.06\ ^{+0.10}_{-0.09}$
χ^2/d.o.f.	$40.4/25$	$13.7/4$
	ϕ el.	ϕ p. diss.
n	$2.40 \pm 0.07\ ^{+0.07}_{-0.07}$	$2.40 \pm 0.31\ ^{+0.14}_{-0.10}$
χ^2/d.o.f.	$11.3/13$	$0.67/3$

(b) $n = c_1 + c_2\,(Q^2 + M_V^2)$		
	ρ el.	ρ p. diss.
c_1	$2.09 \pm 0.07\ ^{+0.06}_{-0.07}$	$2.18 \pm 0.23\ ^{+0.13}_{-0.12}$
c_2 (10^{-2} GeV^{-2})	$0.73 \pm 0.18\ ^{+0.09}_{-0.08}$	$0.72 \pm 0.60\ ^{+0.12}_{-0.08}$
χ^2/d.o.f.	$17.1/24$	$8.0/3$
	ϕ el.	ϕ p. diss.
c_1	$2.15 \pm 0.14\ ^{+0.10}_{-0.11}$	$2.45 \pm 0.52\ ^{+0.29}_{-0.20}$
c_2 (10^{-2} GeV^{-2})	$0.74 \pm 0.40\ ^{+0.23}_{-0.19}$	$0.11 \pm 1.04\ ^{+0.27}_{-0.39}$
χ^2/d.o.f.	$4.2/12$	$0.65/2$

Table 8: $(Q^2+M_V^2)$ dependence of the cross sections for ρ and ϕ elastic and proton dissociative production, parameterised in the form $1/(Q^2+M_V^2)^n$, with (a) n constant and (b) n parameterised as $n = c_1 + c_2\,(Q^2+M_V^2)$. The 1995 (SV) measurements are normalised to those of 1996-2000.

the data (Table 8(b)). It is interesting to note that the fitted values of the parameter c_1 are close to the value 2 expected in the Vector Meson Dominance model [87] for the exponent n when $Q^2 \to 0$.

5.3.2 Comparison with models

Predictions of the KMW dipole model [59] with GW saturation [73] are compared to the data in Fig. 12. The shape of the ρ elastic cross section measurement is well described. The normalisation of the prediction is low by 10%, while the overall normalisation error in the present measurement is of 4%. Predictions using CGC saturation [74] (not shown) are nearly indistinguishable, except for the highest bins in Q^2 where, however, the limited precision of the data does not allow to discriminate. The MRT model [45] does not provide normalisation predictions, because of the uncertainty on the quark pair invariant mass window corresponding to the meson recombination. For this reason, the predictions for different PDF parameterisations are normalised to the data at $Q^2 = 6$ GeV^2. Both the CTEQ6.5M [77] and the MRST 2004 NLO PDFs [78] (not shown) lead to predictions which are compatible with the Q^2 dependence of the data. It should however be noted that the normalisation factors required to fit the data are about 1.1 for CTEQ6.5M but larger than 2 for the MRST04 NLO PDF. This surprisingly large factor suggests that the gluon contribution in the MRST04 NLO PDFs is underestimated.

For elastic ϕ production, the KMW predictions describe the shape of the distribution well, but are higher than the data by 25%. The MRT model gives a good description of the Q^2 dependence of the cross section, with normalisation factors similar to those for ρ mesons.

5.3.3 Vector meson cross section ratios

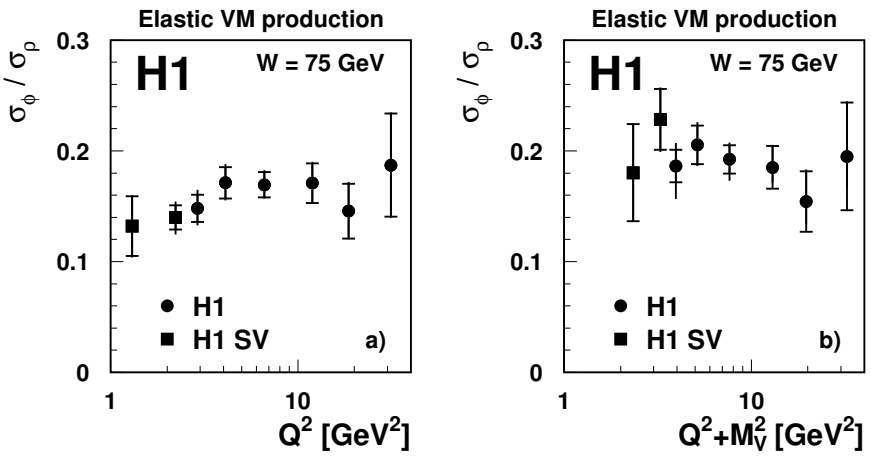

Figure 13: Ratio of the ϕ to ρ elastic production cross sections for $W = 75$ GeV: (a) as a function of Q^2; (b) as a function of $(Q^2+M_V^2)$. The overall normalisation errors on the ratios, which are not included in the error bars, are 4.0%. The present measurements are given in Table 19.

Figures 13(a) and (b) present as a function of Q^2 and $(Q^2+M_V^2)$, respectively, the ratio of the ϕ to ρ elastic cross sections, for which several uncertainties cancel, in particular those related to the subtraction of the proton dissociative background. The ratios are different because the same value of Q^2 corresponds to different values of $(Q^2+M_V^2)$ for ρ and ϕ mesons, in view of the mass difference. A slight increase of the ratio with Q^2 is observed for $Q^2 \lesssim 4$ GeV^2, whereas the ratio is consistent with being constant when plotted as a function of $(Q^2+M_V^2)$. Similar behaviours (not shown) are obtained for proton dissociative production.

The cross section ratios for $W = 75$ GeV are

$$\begin{aligned}
\frac{\sigma(\phi)}{\sigma(\rho)}(\text{el.}) &= 0.191 \pm 0.007\ (\text{stat.})\ ^{+0.008}_{-0.006}\ (\text{syst.}) \pm 0.008\ (\text{norm.}) \\
&\qquad (Q^2+M_V^2 \geq 2\ \text{GeV}^2), \\
\frac{\sigma(\phi)}{\sigma(\rho)}(\text{p. diss.}) &= 0.178 \pm 0.015\ (\text{stat.})\ ^{+0.007}_{-0.010}\ (\text{syst.}) \pm 0.008\ (\text{norm.}) \\
&\qquad (Q^2+M_V^2 \geq 3.5\ \text{GeV}^2), \qquad (14)
\end{aligned}$$

where the ratio of elastic cross sections includes the 1995 SV measurements ($1 \leq Q^2 \leq 2.5$ GeV^2). The measurements are close to the value expected from quark charge counting $\phi/\rho = 2:9$, but they tend to be slightly lower.

Qualitatively, the behaviour of the ratio is consistent with the dipole model. At small Q^2, the influence of the meson mass on the transverse size of the $q\bar{q}$ pair is larger, which implies that colour screening is expected to be larger for ϕ mesons than for ρ mesons. In contrast, for $Q^2 \gg M_V^2$, the transverse size of the dipole is given essentially by Q^2 and symmetry is expected to be restored.

The dipole size effect also explains the strong increase with Q^2 of the J/ψ to ρ ratio, scaled according to the quark charge content $J/\psi : \rho = 8 : 9$, as presented in Fig. 14(a), and the fact that the ratio is nearly constant and close to unity when studied as a function of $(Q^2+M_V^2)$, as shown in Fig. 14(b) (note the different vertical scales).

Although striking, the agreement with SU(4) universality is however only qualitative, with the scaled ϕ to ρ cross section ratios slightly below 1 and the scaled J/ψ to ρ ratios slightly above 1. Scaling factors obtained from the VM electronic decay widths [43,44,65] are expected to encompass wave function and soft effects; the use of the factors given in [65] modifies the scaled ϕ to ρ ratio very little and brings the scaled J/ψ to ρ ratio slightly below 1.

5.4 Q^2 dependence of the polarised cross sections

The separate study of the polarised (longitudinal and transverse) cross sections sheds light on the dynamics of the process and on the Q^2 dependence of the total cross section. Soft physics contributions, related to large transverse dipoles, are predicted to play a significant role in transverse cross sections, whereas hard features should be significant in longitudinal amplitudes. At

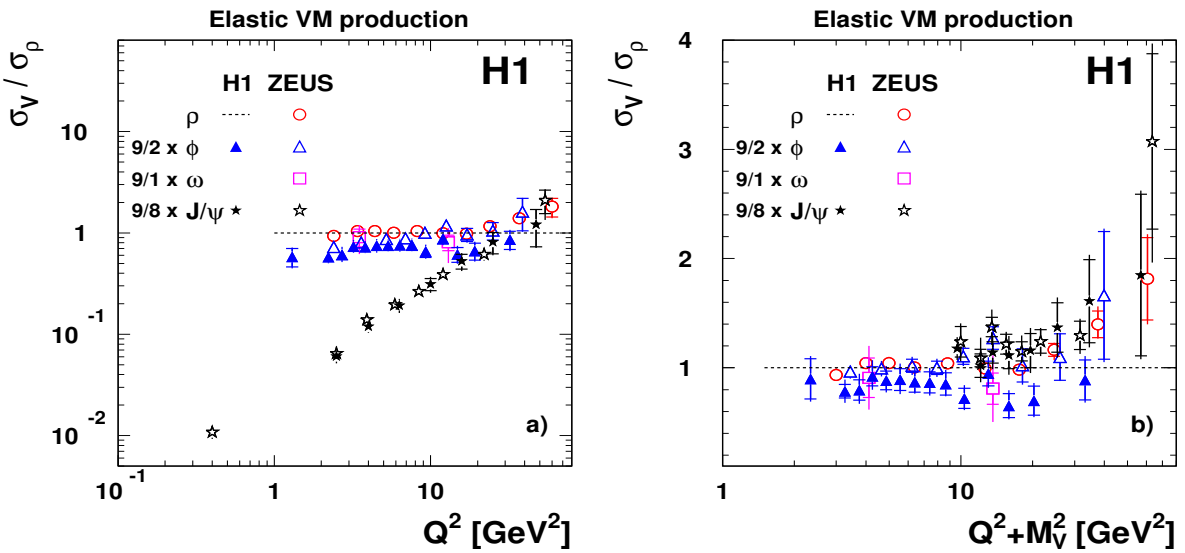

Figure 14: Ratios of ω, ϕ and J/ψ to ρ elastic production cross sections as parameterised in Table 8(b), scaled according to the quark charge contents, $\rho : \omega : \phi : J/\psi = 9 : 1 : 2 : 8$, plotted as a function of (a) Q^2; (b) $(Q^2+M_V^2)$. The ratios are determined for the H1 ϕ (this analysis) and J/ψ [12] measurements, and from the ZEUS ρ [19], ω [22], ϕ [24] and J/ψ [25,26] studies.

relatively low values of the scale, $(Q^2+M_V^2)/4 \lesssim 3$ GeV^2, soft, "finite size" effects are however expected to also affect longitudinal cross sections.

The extraction of the polarised cross sections presented in this section implies the use of the measurement of the cross section ratio $R = \sigma_L/\sigma_T$, which is performed using angular distributions and is discussed in section 6.3.

5.4.1 Cross section measurements

The total $\gamma^* p$ cross section can be expressed as the sum of the contributions of transversely and longitudinally polarised virtual photons:

$$\sigma_{tot}(\gamma^* + p \to V + Y) = \sigma_T + \varepsilon\sigma_L = \sigma_T\,(1 + \varepsilon\, R), \tag{15}$$

where ε is the photon polarisation parameter, $\varepsilon \simeq (1-y)/(1-y+y^2/2)$, with $0.91 < \varepsilon < 1.00$ and $\langle\varepsilon\rangle = 0.98$ in the kinematic domain corresponding to the present measurement.

The polarised cross sections, obtained from the measurements of the total cross sections and of R, with the value of ε for the relevant Q^2, are presented in Fig. 15 for elastic ρ and ϕ production, as a function of $(Q^2+M_V^2)$.

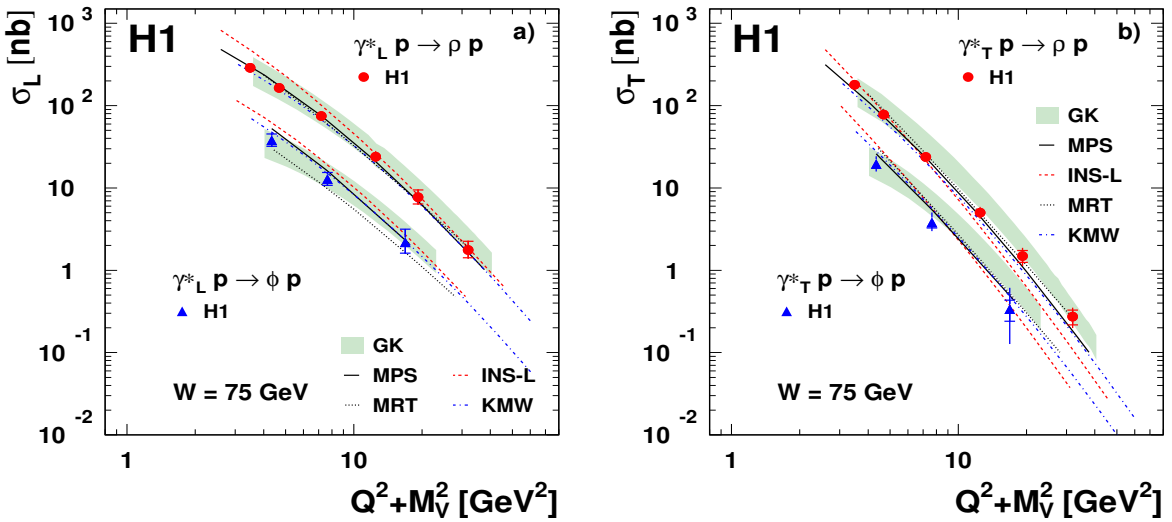

Figure 15: $(Q^2+M_V^2)$ dependence of (a) longitudinal and (b) transverse $\gamma^* p$ cross sections for elastic ρ and ϕ meson production with $W = 75$ GeV. Overall normalisation errors of 3.9% for ρ and 4.6% for ϕ mesons are not included in the error bars. The superimposed curves are model predictions: GK [61] (shaded bands), MPS [62] (solid lines), INS with large wave function [65] (dashed lines), MRT [45] with CTEQ6.5M PDFs [77] and the same normalisation as in Fig. 12 (dotted lines) and KMW [59] with GW saturation [73] (dash-dotted lines). The measurements are given in Tables 20-21.

n constant	
$\sigma_L(\rho)$	$\sigma_T(\rho)$
$2.17 \pm 0.09^{+0.07}_{-0.07}$	$2.86 \pm 0.07^{+0.11}_{-0.12}$
$\sigma_L(\phi)$	$\sigma_T(\phi)$
$2.06 \pm 0.49^{+0.09}_{-0.09}$	$2.97 \pm 0.52^{+0.14}_{-0.16}$

Table 9: $(Q^2+M_V^2)$ dependence of the longitudinal and transverse cross sections for ρ and ϕ meson elastic production, parameterised in the form $1/(Q^2+M_V^2)^n$ with n constant.

Results of power law fits with constant exponents are presented in Table 9 (the fit quality does not improve with a $(Q^2+M_V^2)$ dependent value of n). The fit values differ from the results $n = 3$ for the longitudinal and $n = 4$ for the transverse cross sections, obtained from a LO calculation of two gluon exchange [42].

Model predictions for σ_L and σ_T are compared to the data in Fig. 15. The GPD predictions of the GK model [61] are slightly too flat, both for σ_L and for σ_T, but the global normalisations are within the theoretical and experimental errors, which suggests that higher order effects, not included in the model, are weak. The KMW model [59] describes well the shapes of the σ_L and σ_T measurement and the absolute normalisation of σ_L, whereas the normalisation is too low for σ_T; this is the reflection of the good description of the shape for σ_{tot} and of the prediction for R which is systematically too high (see Fig. 40 in section 6.3). The MRT [45] predictions for the ρ polarised cross sections are reasonable, but for ϕ production they are too low for σ_L and too high for σ_T, which reflects the fact that the predictions for R are too low (Fig. 40). The INS k_t-unintegrated model with the compact wave function [65] gives predictions which are significantly too high both for σ_L and for σ_T, and too steep for σ_T (not shown); the predictions with the large wave function have better absolute predictions but are too steep for σ_L and for σ_T. The MPS dipole saturation model [62] describes the data rather well.

The same data and model predictions are presented in Fig. 16, where the longitudinal cross sections are divided by Q^2 and the transverse cross sections by M_V^2, all being in addition multiplied by the scaling factors $(Q^2+M_V^2)^4$ to remove trivial kinematic dependences [101]. The breaking of the formal expectations ($n = 3$, $n = 4$) for the $1/(Q^2+M_V^2)^n$ dependence of the longitudinal and transverse cross sections is manifest in this presentation. This is expected from the fast increase with Q^2 of the gluon density at small x. Note that the cross sections in Fig. 16 are given for a fixed value of W and thus correspond to different values of x. The increase with Q^2 of the scaled longitudinal cross section is slower than that of the scaled transverse cross section. This is reflected in the Q^2 dependence of the cross section ratio $R = \sigma_L/\sigma_T$, which is slower than Q^2/M_V^2 (see section 6.3, Figs. 40 and 41).

5.4.2 Vector meson polarised cross section ratios

Figure 17 shows the ϕ to ρ and J/ψ to ρ polarised cross section ratios, scaled according to the quark charge content of the VM (J/ψ longitudinal cross sections are affected by very large errors due to the measurement errors on R and are not shown).

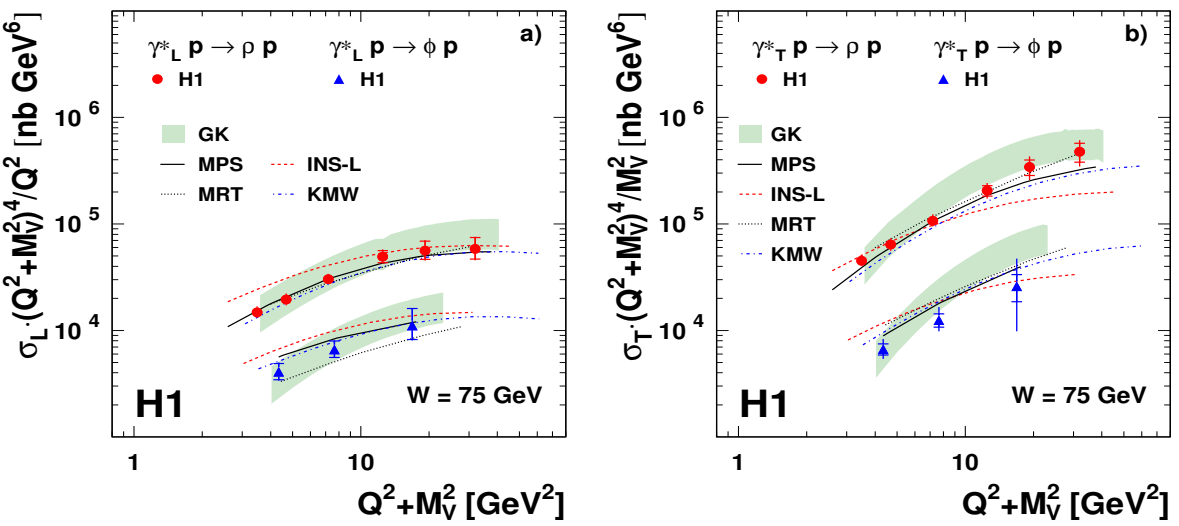

Figure 16: $(Q^2+M_V^2)$ dependences of the $\gamma^* p$ cross sections for ρ and ϕ elastic production with $W = 75$ GeV: (a) longitudinal cross sections, multiplied by the scaling factor $(Q^2 + M_V^2)^4/Q^2$; (b) transverse cross sections, multiplied by $(Q^2 + M_V^2)^4/M_V^2$. The superimposed model predictions are the same as in Fig. 15.

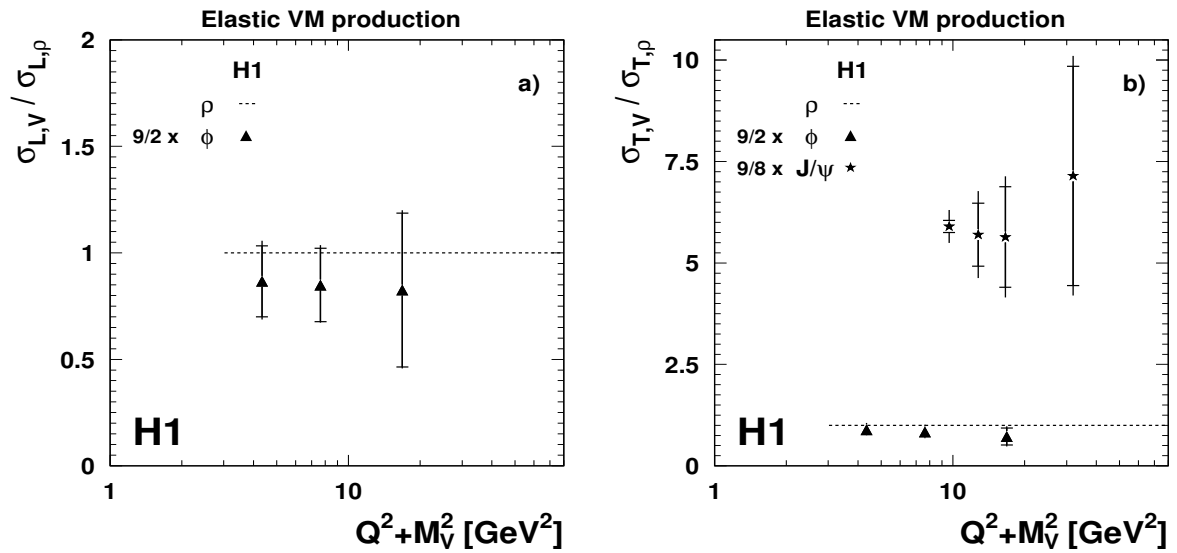

Figure 17: Polarised cross sections for the elastic production of ϕ (present measurements) and J/ψ [12] mesons, divided by the parameterisations of the ρ elastic polarised cross sections and scaled according to the quark charge contents, $\rho : \phi : J/\psi = 9 : 2 : 8$; in (a) longitudinal; (b) transverse cross sections.

The ratios of the ϕ to ρ polarised production cross sections are within uncertainties independent of $(Q^2+M_V^2)$ and close to the ratio of the total cross sections (Fig. 14), suggesting little effect of the wave functions. In contrast, the ratios of the J/ψ to ρ transverse cross sections are very different from 1. This is because the polarisation states for ρ and ϕ mesons on the one hand and for J/ψ mesons on the other hand are very different for the same $(Q^2+M_V^2)$ value, in view of the Q^2 dependence of R. The fact that the cross section ratios are consistent with being independent of $(Q^2+M_V^2)$ thus indicates that, within the present errors, no large difference is found between the small dipoles involved in transverse J/ψ production and the dipoles involved in transverse ρ production, for $(Q^2+M_V^2) \gtrsim 10$ GeV^2.

5.5 W dependences

5.5.1 Cross section measurements

Figure 18 displays the W dependence of the $\gamma^* p$ cross sections for the production of ρ and ϕ mesons, for several values of Q^2. For the first time, measurements are performed for both the elastic and the proton dissociative channels.

The W dependence of the cross sections is well described by power laws of the form

$$\sigma(\gamma^* + p \to V + Y) \propto W^{\delta}, \tag{16}$$

represented by the straight lines in Fig. 18. This parameterisation is inspired by the Regge description of hadron interactions at high energy, with

$$\delta(t) = 4\,(\alpha_{I\!P}(t) - 1), \tag{17}$$

$$\alpha_{I\!P}(t) = \alpha_{I\!P}(0) + \alpha' \cdot\ t. \tag{18}$$

In hadron interactions, typical values for the intercept and the slope of the pomeron trajectory are $\alpha_{I\!P}(0) = 1.08$ to 1.11 [102] and $\alpha' = 0.25$ GeV^{-2} [103], respectively.

5.5.2 Hardening of the W distributions with Q^2

The W dependence of the cross sections is presented in Fig. 19 in the form of the intercept of the effective pomeron trajectory, $\alpha_{I\!P}(0)$, to allow comparison between different channels with different t dependences. The values of $\alpha_{I\!P}(0)$ are calculated for the present ρ and ϕ meson production from the W dependences following Eqs. (16-18), using the measured values of $\langle t \rangle$ and the measurements of α' for ρ production given in Table 11; the latter are derived from the evolution with t of the W dependence of the cross section. The measurements of $\alpha_{I\!P}(0)$ are presented as a function of the scale $\mu^2 = (Q^2+M_V^2)/4$ for ρ, ϕ and J/ψ production, and as a function of $\mu^2 = Q^2$ for DVCS.

Up to $(Q^2+M_V^2)/4$ values of the order of 3 GeV^2, the W dependence of the elastic cross section for both ρ and ϕ production is slightly harder than the soft behaviour characteristic of hadron interactions and photoproduction (Fig. 19(a)). For the higher $(Q^2+M_V^2)/4$ range, higher values of $\alpha_{I\!P}(0)$ are reached, of the order of 1.2 to 1.3, compatible with J/ψ measurements. This evolution is related to the hardening of the gluon distribution with the scale of the interaction. Consistent results are obtained in the proton dissociative channel, but with larger uncertainties (Fig. 19(b)).

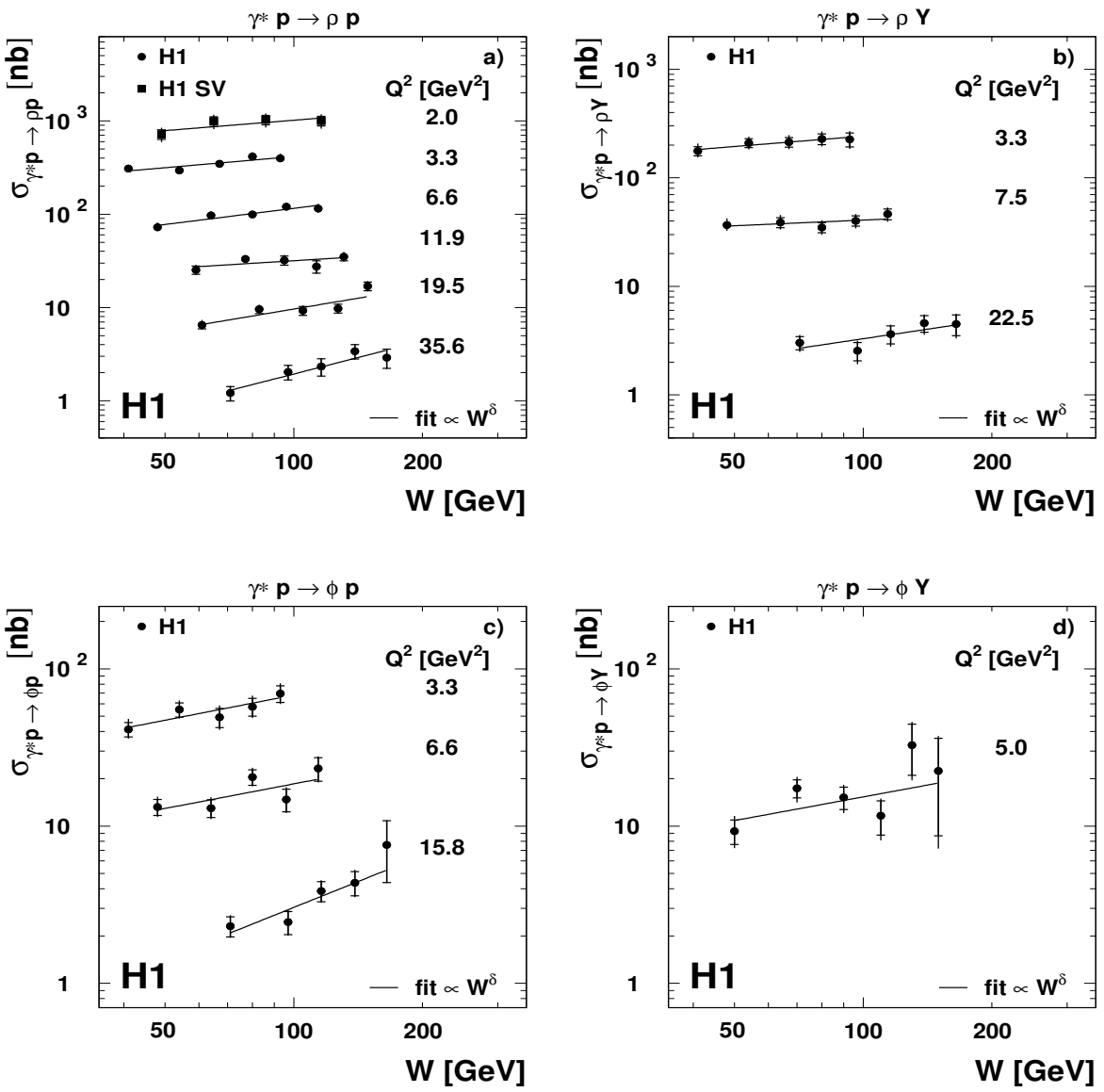

Figure 18: W dependence of the $\gamma^* p$ cross sections for elastic (a)-(c) and proton dissociative (b)-(d) production for several values of Q^2: (a)-(b) ρ meson production; (c)-(d) ϕ production. The overall normalisation errors, not included in the error bars, are the same as in Fig. 12. The lines are the results of power law fits. The present measurements are given in Tables 22-25.

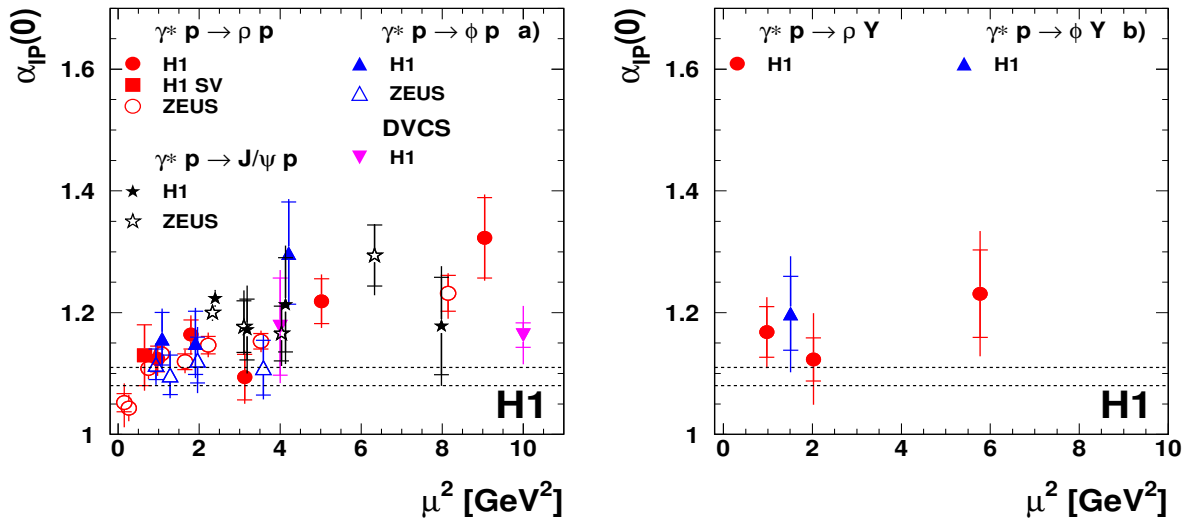

Figure 19: Evolution with the scale $\mu^2 = (Q^2 + M_V^2)/4$ of the intercept of the effective pomeron trajectory, $\alpha_{I\!P}(0)$, for ρ and ϕ production: (a) elastic production; (b) proton dissociation. H1 measurements of DVCS [9] and J/ψ production [12] and ZEUS measurements of ρ [17, 19] (for the low Q^2 points, the value of α' in [17] is used), ϕ [24] and J/ψ production [25, 26] are also shown. For DVCS, the scale is taken as $\mu^2 = Q^2$. The values 1.08 and 1.11 [102], typical for soft diffraction, are indicated by the dotted lines. The present measurements are given in Table 26.

5.5.3 Comparison with models

In principle, the W dependence of VM production can put constraints on gluon distributions, including effects like saturation at very low x and large W values. All models predict a hardening of the W distribution with increasing Q^2, following from the steepening of the gluon distributions. As examples, predictions are given in Fig. 20 for the GK GPD model [61], the INS k_t-unintegrated model with the large wave function [65] and the KMW dipole [59] with GW saturation [73]. The MPS saturation model [62] (not shown) gives predictions for ρ production nearly identical to those of KMW. In general, relatively small differences are found between the model predictions for the W dependence, and the present data do not provide significant discrimination. Differences in normalisation between models in Fig. 20 reflect differences in the predicted Q^2 dependence of the cross sections.

5.6 *t* dependences

5.6.1 Cross section measurements

The differential cross sections as a function of $|t|$ for ρ and ϕ elastic and proton dissociative production are presented in Fig. 21 for different ranges in Q^2. They are well described by empirical exponential laws of the type $\mathrm{d}\sigma/\mathrm{d}t \propto e^{-b|t|}$.

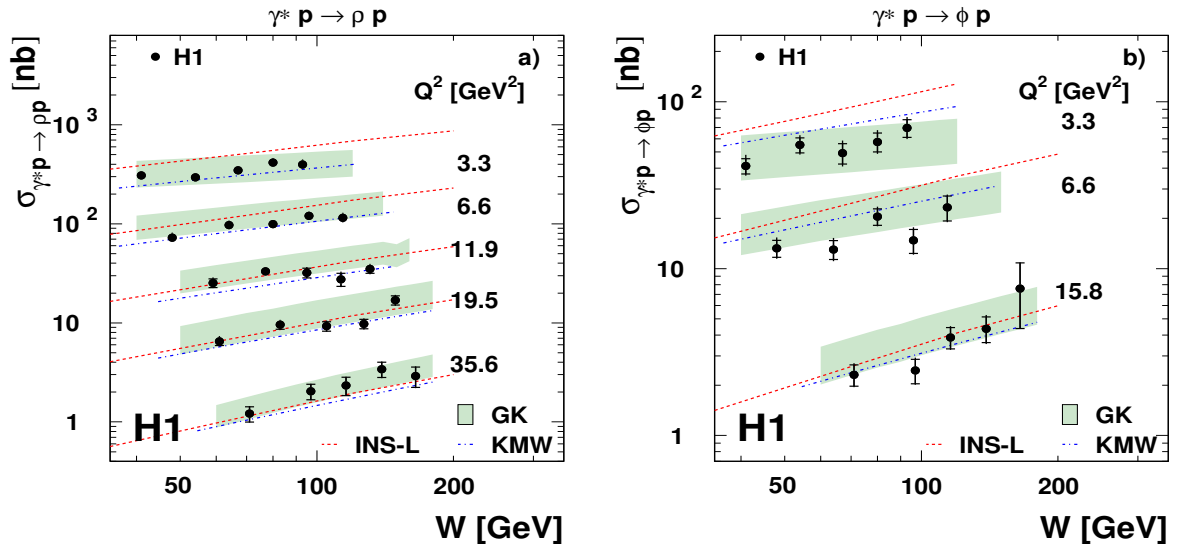

Figure 20: Comparison with models of the W dependences of the $\gamma^* p$ cross sections given in Figs. 18(a) and (c), for the elastic production of (a) ρ mesons; (b) ϕ mesons. The superimposed curves are model predictions: GK [61] (shaded bands), INS with large wave function [65] (dashed lines) and KMW [59] with GW saturation [73] (dash-dotted lines).

The slope parameters b extracted from exponential fits in the range $|t| \leq 0.5$ GeV^2 for elastic scattering and $|t| \leq 3$ GeV^2 for proton dissociation are presented in Fig. 22 as a function of the scale $\mu^2 = (Q^2 + M_V^2)/4$. The measurements of the proton dissociative slopes are the first precise determination at HERA for light VM in electroproduction; they constitute an important ingredient for the extraction of the elastic b slopes. In Fig. 22, ρ and ϕ measurements by ZEUS and J/ψ measurements are also presented as a function of $(Q^2 + M_V^2)/4$, together with DVCS measurements (with $\mu^2 = Q^2$).

The present measurements of the b slopes for $(Q^2 + M_V^2)/4 \lesssim 5$ GeV^2 are higher than those of ZEUS [19] and also than those of a previous H1 measurement [4]. Two sources of systematic experimental differences are identified. The first is related to the estimation of the proton dissociative background, both in size and in shape. The subtraction of a smaller amount of proton dissociative background and the use of a steeper proton dissociative slope lead to shallower $|t|$ distributions of the elastic cross section and to smaller b slope measurements. The use of a central value of 2.5 GeV^{-2} for the proton dissociative slope, as assumed in [4], compared to the values measured here (Fig. 22(b)), leads to a decrease of the elastic slope determination by 0.1 GeV^{-2}, and a variation by $\pm 20\%$ of the amount of proton dissociative background induces a change of the elastic slope measurement by ± 0.2 GeV^{-2} for $Q^2 = 5$ GeV^2 and ± 0.1 GeV^{-2} for $Q^2 = 20$ GeV^2. The second – and major – source of discrepancy, for both VMs, is in the treatment of the ω, ϕ and mostly ρ' backgrounds discussed in section 4.2.4. Because of the non-detection of the decay photons, these backgrounds exhibit effective $|t|$ distributions which are much flatter than their genuine distributions and than the signal. Neglecting completely the presence of the ρ' background would lead in the present analysis to a decrease of the measurement of the elastic b slope by 0.4 GeV^{-2} for $Q^2 = 3$ GeV^2 and 0.2 GeV^{-2} for $Q^2 = 20$ GeV^2.

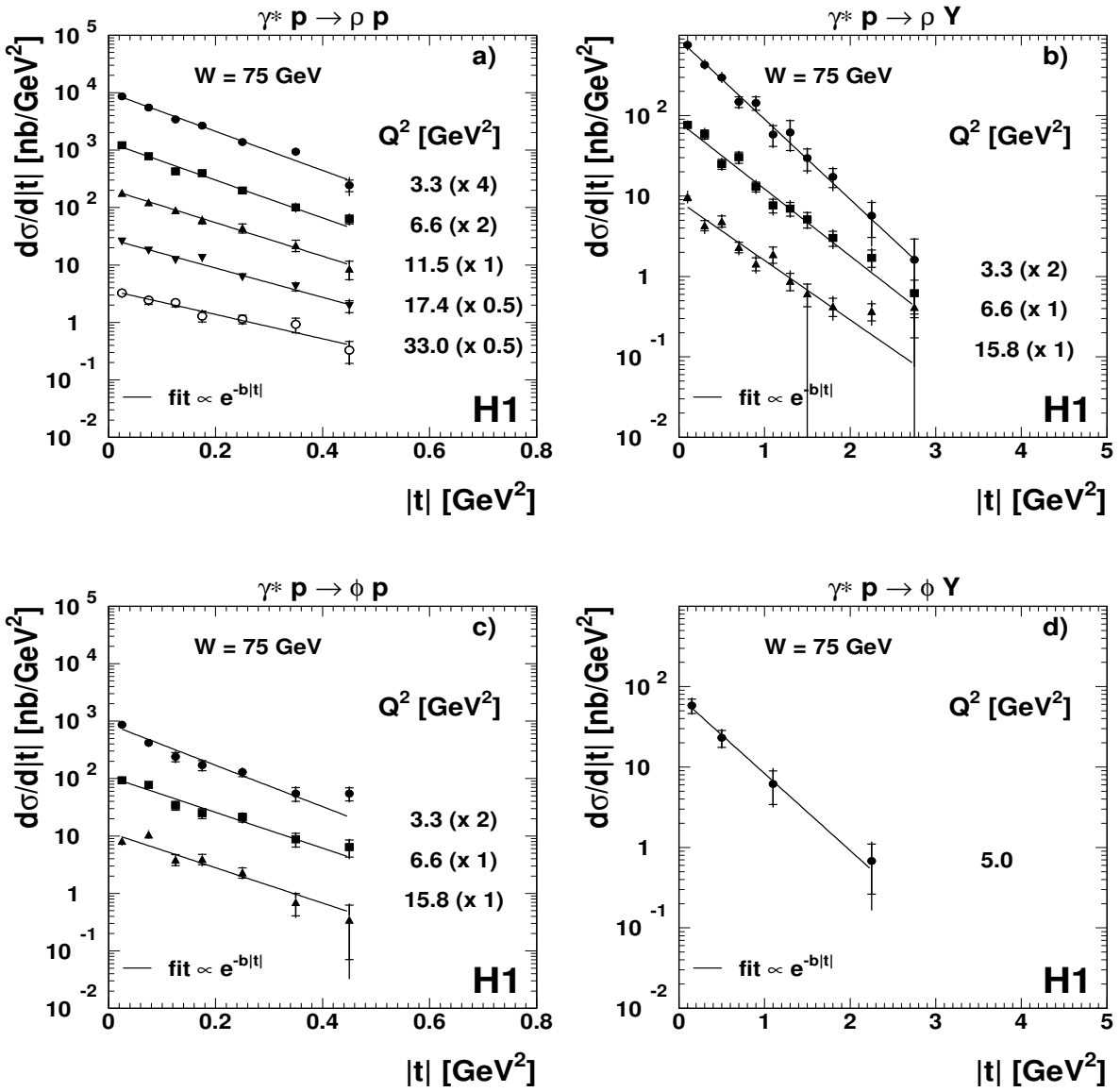

Figure 21: t dependence of the $\gamma^* p$ elastic (a)-(c) and proton dissociative (b)-(d) production cross sections for several values of Q^2: (a)-(b) ρ production; (c)-(d) ϕ production. Some distributions are multiplied by constant factors to improve the readability of the figures. The overall normalisation errors, not included in the error bars, are the same as in Fig. 12. The superimposed lines correspond to exponential fits. The measurements are given in Tables 27-30.

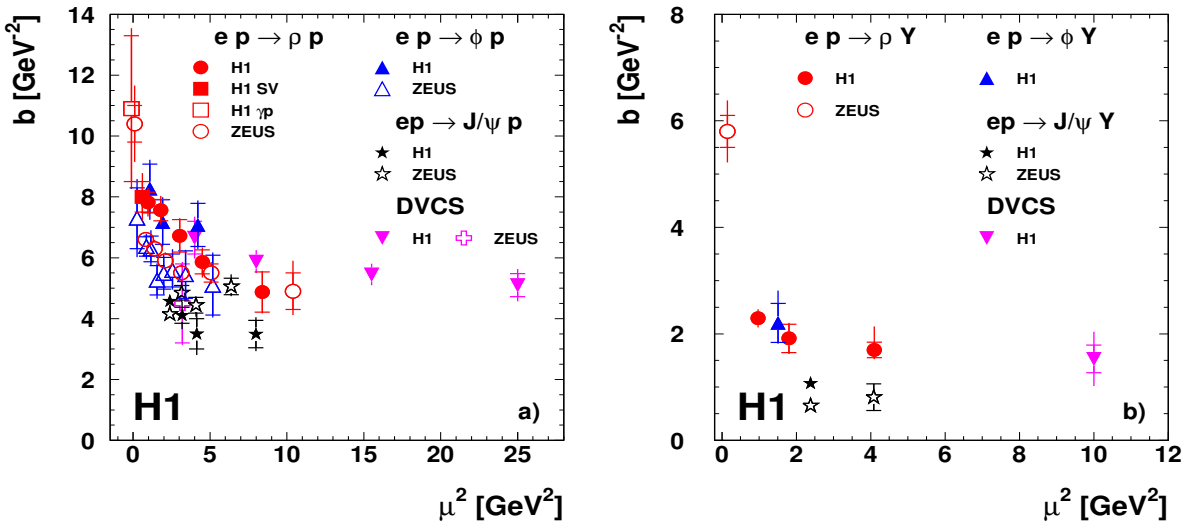

Figure 22: Evolution with the scale $\mu^2 = (Q^2+M_V^2)/4$ of the slope parameters b of the exponentially falling $|t|$ distributions of ρ and ϕ electroproduction: (a) elastic scattering; (b) proton dissociation. H1 data for DVCS [9], ρ photoproduction [10] and J/ψ production [12, 14] and ZEUS data for ρ [17, 19], ϕ [23, 24] and J/ψ [25, 26] production are also presented. For DVCS, the scale is taken as $\mu^2 = Q^2$. The present measurements are given in Table 31.

5.6.2 Universality of *t* slopes and hard diffraction

In an optical model inspired approach, the t slopes for DVCS and VM production result from the sum of terms describing the form factors due to the transverse sizes of the scattered system Y (b_Y), of the $q\bar{q}$ dipole pair ($b_{q\bar{q}}$) and of the exchange ($b_{I\!P}$). An additional form factor reflecting the VM transverse size may also give a contribution, b_V, to the t slope for light VM production in models where the wave function plays an important role in the process, while being negligible for DVCS and for J/ψ. The value of the slope can thus be decomposed as:

$$b = b_Y + b_{q\bar{q}} + b_{I\!P} + b_V. \tag{19}$$

In elastic scattering, the slope $b_Y = b_p$ reflects the colour distribution in the proton. For baryonic excited states with size larger than that of the proton, larger slopes (i.e. steeper t distributions) than for elastic scattering may be expected. In contrast, when the proton is disrupted in the diffractive scattering, no form factor arises from the Y system and b_Y is expected to be $\simeq 0$. The $b_{I\!P}$ contribution of the exchange is generally believed to be small and independent of Q^2. There is indeed a priori no relation between Q^2 and the transverse size of the exchange, at least for $|t| \ll Q^2$ and for α_s taken to be constant (LL BFKL).

It is visible in Fig. 22 that, already for $(Q^2+M_V^2)/4 \gtrsim 0.5$ GeV^2, the elastic b slopes for light VM electroproduction are significantly lower than in photoproduction, showing a departure from purely soft diffraction and a decrease of the relevant $q\bar{q}$ dipole transverse size. Until the scale $(Q^2+M_V^2)/4$ reaches values $\gtrsim 5$ GeV^2, light VM slopes are however significantly

larger than for J/ψ. This indicates the presence of dipoles with relatively large transverse sizes for light VMs in this Q^2 domain. This is expected in the transverse amplitudes and also in longitudinal amplitudes until the fully hard regime is reached ("finite size" effects). Light VM and DVCS slopes are compatible when plotted as a function of the scales $(Q^2+M_V^2)/4$ and Q^2, respectively. For large scale values, they are consistent with the J/ψ data, although they may be slightly higher. All these features confirm that the present Q^2 domain covers the transition from the regime where soft diffraction dominates light VM production to the regime where hard diffraction dominates. The comparable values of the slopes for ρ, ϕ and J/ψ production in the harder regime suggests that light VM form factors are small.

For proton dissociative diffraction, the t slopes shown in Fig. 22(b) have significantly smaller values than for elastic scattering. This is expected for Y systems above the nucleon resonance region, with vanishing values of b_Y. The proton dissociative slopes for ρ and ϕ mesons are similar at the same $(Q^2+M_V^2)/4$ value, but remain larger than for J/ψ, confirming the presence of large dipoles for $(Q^2+M_V^2)/4 \lesssim 5$ GeV^2 or, alternatively, leaving room for a light VM form factor.

5.6.3 Comparison with models

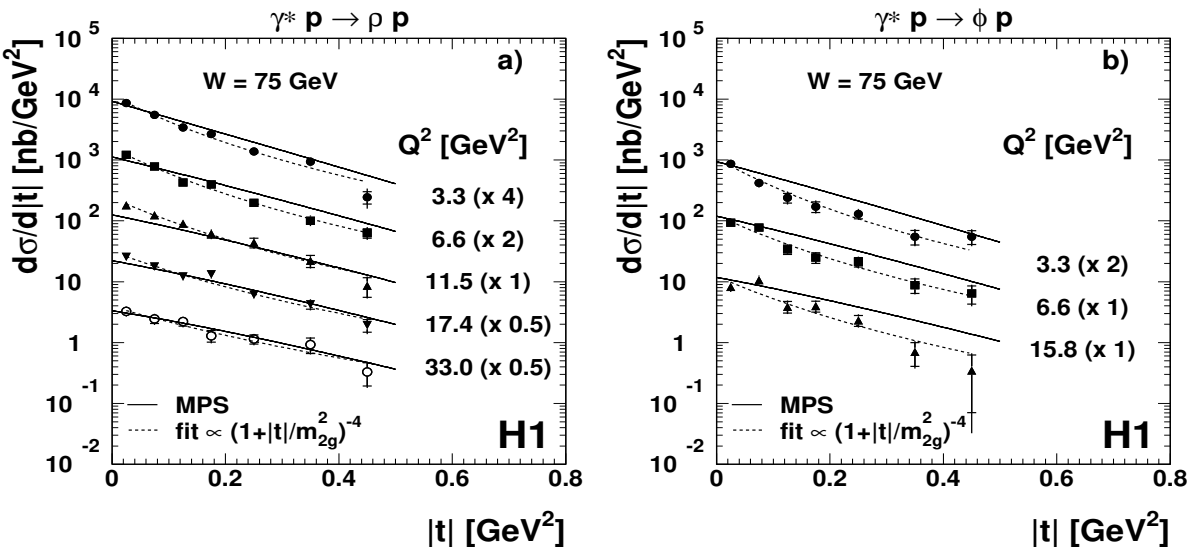

Figure 23: Comparison with models of the t dependences of the $\gamma^* p$ cross sections given in Figs. 21(a) and (c), for the elastic production of (a) ρ mesons; (b) ϕ mesons. The superimposed curves are predictions from the MPS model [62] (solid lines) and fits of Eq. (20) parameterising the two-gluon form factor in the FS model [54] (dashed lines). Some distributions are multiplied by constant factors to improve the readability of the figures.

Figure 23 shows predictions of the MPS saturation model [62] for the t dependence of the cross sections, superimposed on the elastic measurements. The data fall faster with $|t|$ than

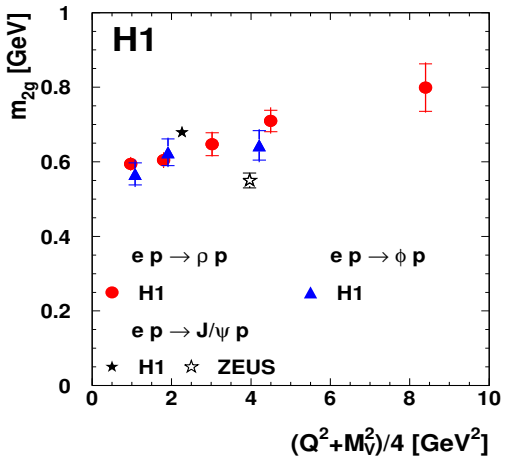

Figure 24: Dependence on the scale $(Q^2+M_V^2)/4$ of the parameter m_{2g} of the two-gluon form factor of the FS model [54], extracted from fits of Eq. (20) to the t distributions of ρ and ϕ elastic production cross sections. The J/ψ measurements by H1 in photoproduction [12] and by ZEUS in electroproduction [26] are also presented. The present measurements are given in Table 32.

predicted by the model, especially at small Q^2. The discrepancy is particularly significant for ϕ production.

A dipole function with a t dependent two-gluon form factor has been proposed by Frankfurt and Strikman (FS) [54], with

$$\mathrm{d}\sigma/\mathrm{d}t \propto (1+|t|/m_{2g}^2)^{-4}, \tag{20}$$

which tends to $e^{-b|t|}$ for $t \to 0$, with $b = 4/m_{2g}^2$. Fits of this parameterisation to the data for ρ and ϕ elastic production in several bins in Q^2 are shown in Fig. 23, superimposed on the measurements. The fit quality is good, similar to the exponential fits. Figure 24 presents the extracted values of the parameter m_{2g} as a function of $(Q^2+M_V^2)/4$ for the ρ and ϕ elastic channels. The parameter increases with $(Q^2+M_V^2)/4$, from about 0.6 GeV at 5 GeV^2 to about 0.8 GeV at 35 GeV^2. A measurement in J/ψ photoproduction is also shown.

5.6.4 Slope of the effective pomeron trajectory

The W dependences in four bins in $|t|$ of the $\gamma^* p$ cross sections for ρ meson production are presented in Fig. 25 for two values of Q^2. The notag ($|t| \leq 0.5$ GeV^2) and tag ($|t| \leq 3$ GeV^2) samples are combined in order to extend the measurement lever arm in $|t|$. It was checked that, using only the notag events, compatible values of α' are obtained, although with much larger errors. The combination is also supported by the fact that the values of $\alpha_{I\!P}(0)$ for the elastic and proton dissociative processes are compatible (see Fig. 19).

The W dependences, which are observed to depend on $|t|$, are parameterised following the power law of Eq. (16). The extracted values of $\alpha_{I\!P}(t) = \delta(t)/4 + 1$ are presented in

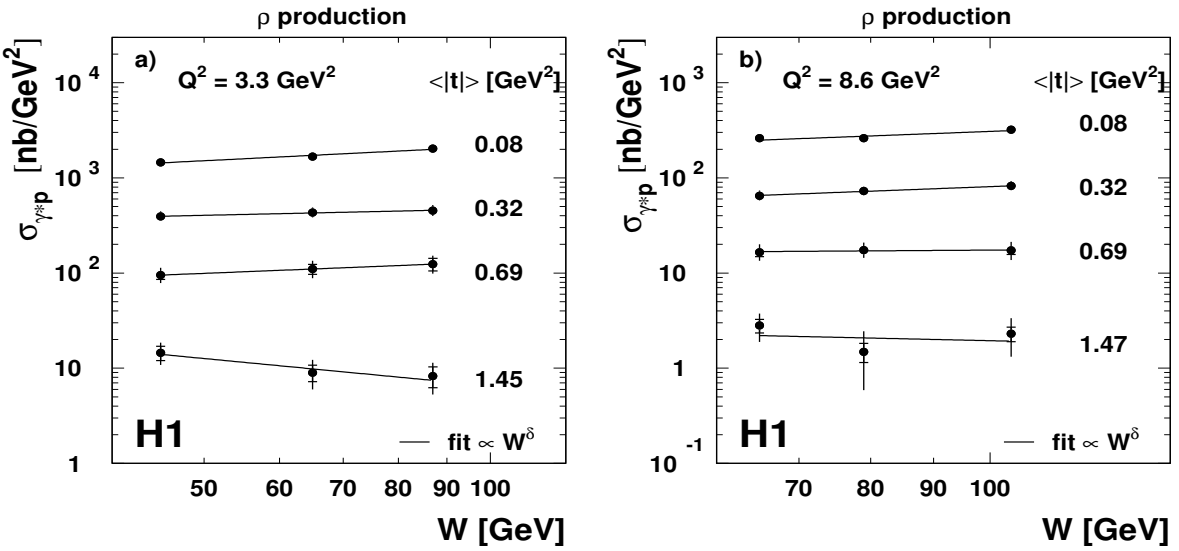

Figure 25: W dependence of the $\gamma^* p$ cross sections for ρ meson production in four bins in $|t|$, for (a) $Q^2 = 3.3$ GeV^2 and (b) $Q^2 = 8.6$ GeV^2. The lines are the results of power law fits. The notag ($|t| \leq 0.5$ GeV^2) and tag ($|t| \leq 3$ GeV^2) samples are combined. The measurements are given in Table 33.

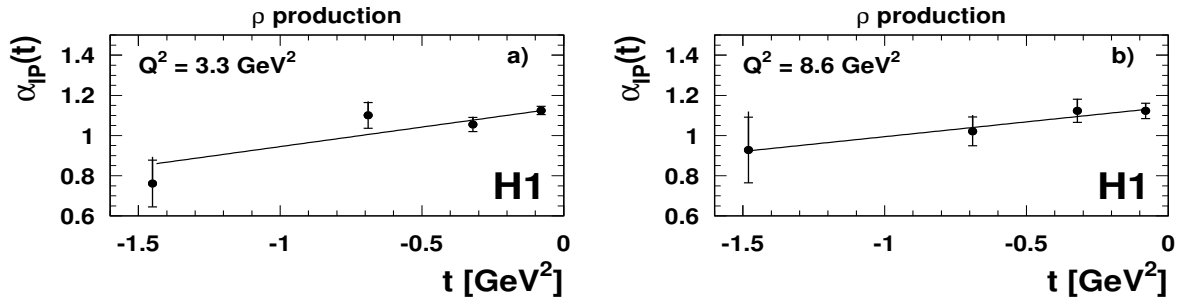

Figure 26: t dependence of the values of the $\alpha_{I\!P}(t) = \delta(t)/4 + 1$ parameters obtained from the linear fits to the W dependences shown in Fig. 25 (ρ production), for (a) $Q^2 = 3.3$ GeV^2; (b) $Q^2 = 8.6$ GeV^2. The lines are the results of linear fits of the form of Eq. (18). The measurements are given in Table 34.

Fig. 26. Linear fits to the t dependence of $\alpha_{I\!P}(t)$, following Eq. (18), give the measurements of the slope α' of the effective pomeron trajectory reported in Table 10. Values slightly smaller than 0.25 GeV^{-2} and higher than 0 are obtained.

In soft diffraction, the non-zero value of the slope α' of the pomeron trajectory ($\alpha' \simeq 0.25$ GeV^{-2}) explains the shrinkage of the forward diffractive peak with increasing W:

$$\begin{aligned} \frac{\mathrm{d}\sigma}{\mathrm{d}t}(W) &= \frac{\mathrm{d}\sigma}{\mathrm{d}t}(W_0) \left(\frac{W}{W_0}\right)^{\delta} \propto e^{b_0 t} \left(\frac{W}{W_0}\right)^{4(\alpha_{I\!P}(0)+\alpha' t-1)} , \\ b &= b_0 + 4\,\alpha'\,t\,\ln(W/W_0)\,. \end{aligned} \tag{21}$$

Q^2 (GeV^2)	α' (GeV^{-2})	
	$\|t\|$ evolution of W^δ fits	W evolution of $\|t\|$ slopes
3.3	$0.19 \pm 0.07\ ^{+0.03}_{-0.04}$	$0.21 \pm 0.25\ ^{+0.13}_{-0.15}$
8.6	$0.15 \pm 0.09\ ^{+0.07}_{-0.06}$	$0.31 \pm 0.45\ ^{+0.22}_{-0.15}$

Table 10: Measurement of the slope of the effective pomeron trajectory α' for ρ production, from the $|t|$ evolution of the W dependence of the ρ cross section presented in Fig. 26, using Eqs. (16-18), and from the evolution with W of the exponential $|t|$ slopes for elastic ρ production with $|t| \leq 0.5$ GeV^2, using Eq. (21), for $Q^2 = 3.3$ and 8.6 GeV^2.

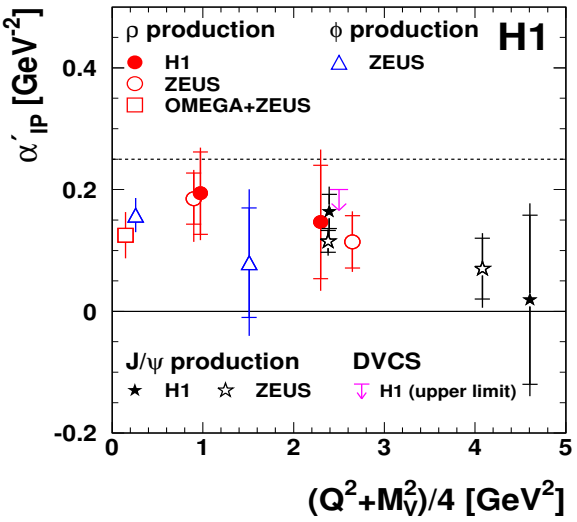

Figure 27: Slope of the effective pomeron trajectory α', presented as a function of the scale $\mu^2 = (Q^2 + M_V^2)/4$, together with measurements by H1 [9, 12] and ZEUS [17, 19, 24–26] for DVCS (upper limit 95% $C.L.$, with the scale $\mu^2 = Q^2$) and ρ, ϕ and J/ψ in photo- and electroproduction with $|t| \lesssim 1.5$ GeV^2. The line $\alpha' = 0.25$ GeV^{-2} represents a typical value in hadron-hadron interactions.

The parameter α' can thus also be obtained from the evolution with W of the exponential $|t|$ slopes for elastic ρ production with $|t| \leq 0.5$ GeV^2, Eq. (21). This measurement, which is affected by the large errors on the b measurements, is given for information in Table 10.

Figure 27 and Table 11 summarise α' measurements by H1 and ZEUS for DVCS and in photo- and electroproduction of ρ, ϕ and J/ψ mesons. The α' measurement for ρ photoproduction [17], which combines the ZEUS data at high energy with OMEGA results [104] at low energy, is $\alpha' = 0.12 \pm 0.04$ GeV^{-2}, which is lower than the value 0.25 typical for soft hadronic diffraction and is similar, within errors, to values of α' in electroproduction. Measurements of α' at large $|t|$ are consistent with 0, with small errors on the J/ψ measurements [12, 25, 26].

	t range (GeV^2)	$\langle Q^2 \rangle$ (GeV^2)	α' (GeV^{-2})			
DVCS	$\lvert t\rvert < 1$	$\simeq 10$	< 0.20 (95% C.L.)			H1 [9]
ρ	$\lvert t\rvert \lesssim 1.5$	$\ll 1$	0.125	± 0.038		ZEUS [17]
		3.3	0.19	± 0.07	$^{+0.03}_{-0.04}$	H1
		3	0.185	± 0.042	$^{+0.022}_{-0.057}$	ZEUS [19]
		8.6	0.15	± 0.09	$^{+0.07}_{-0.06}$	H1
		10	0.114	± 0.043	$^{+0.026}_{-0.024}$	ZEUS [19]
ϕ	$\lvert t\rvert \lesssim 1.5$	$\ll 1$	0.158	± 0.028		ZEUS [17]
		5.3	0.08	± 0.09	$^{+0.08}_{-0.08}$	ZEUS [24]
J/ψ	$\lvert t\rvert \lesssim 1.5$	0.05	0.164	± 0.028	± 0.030	H1 [12]
		$\ll 1$	0.115	± 0.018	$^{+0.008}_{-0.015}$	ZEUS [25]
		8.9	0.019	± 0.139	± 0.076	H1 [12]
		6.8	0.07	± 0.05	$^{+0.03}_{-0.04}$	ZEUS [26]
ρ	$1 \leq \lvert t\rvert \leq 12$	$\ll 1$	-0.02	± 0.05	$^{+0.04}_{-0.08}$	ZEUS [20]
ϕ	$1 \leq \lvert t\rvert \leq 12$	$\ll 1$	-0.06	± 0.12	$^{+0.05}_{-0.09}$	ZEUS [20]
J/ψ	$2 \leq \lvert t\rvert \leq 30$	0.06	-0.014	± 0.007	± 0.005	H1 [13]
	$2 \leq \lvert t\rvert \leq 20$	$\ll 1$	-0.014	± 0.007	$^{+0.004}_{-0.005}$	ZEUS [27]

Table 11: Measurements by the H1 and ZEUS experiments of the slope of the effective pomeron trajectory α' for DVCS and VM photo- and electroproduction, at small and large $|t|$ values.

In the BFKL description of hard scattering, the value of α', which reflects the average transverse momentum k_t of partons along the diffractive ladder, is expected to be small. In Regge theory, the reggeon trajectories are fixed by the resonance positions, and slopes do not depend on Q^2. Evolutions of the effective pomeron trajectories with Q^2 or $|t|$ are thus an indication of additional effects, e.g. multiple exchanges and rescattering processes.

5.7 Comparison of proton dissociative and elastic cross sections

This section presents comparisons of the proton dissociative and elastic channels, for both ρ and ϕ meson production. Measurements of the t integrated cross section ratios are first presented, providing empirical information useful for experimental studies. The factorisation of VM production amplitudes into photon vertex and proton vertex contributions, which can be disentangled by comparing elastic and proton dissociative scatterings, is then discussed: the photon vertex contributions govern the Q^2 dependence and the relative strenght of the various helicity amplitudes, whereas proton vertex form factors govern the t dependence. Proton vertex factorisation ("Regge factorisation") has been observed to hold, within experimental uncertainties, for inclusive diffraction [105]. Factorisation is tested here through the study of the Q^2 independence of the VM production cross section ratios at $t = 0$ and through the measurement of the difference $b_{el.} - b_{p.\ diss.}$ between the elastic and the proton dissociative exponential t slopes.

5.7.1 Q^2 dependence of the cross section ratios

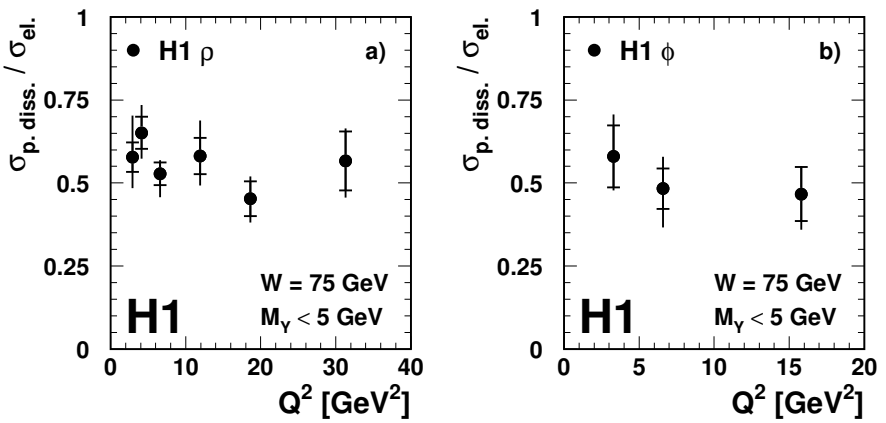

Figure 28: Q^2 dependence of the ratio of proton dissociative ($M_Y < 5$ GeV) to elastic $\gamma^* p$ cross sections for $W = 75$ GeV: (a) ρ meson production; (b) ϕ production. The overall normalisation error on the ratios, which is not included in the error bars, is 2.4%. The measurements are given in Tables 35 and 36.

Figure 28 presents, as a function of Q^2, the ratio of the proton dissociative to elastic $\gamma^* p$ cross sections, for ρ and ϕ mesons. In the ratio, several systematic uncertainties cancel, in

particular those related to meson reconstruction. No significant dependence of the ratios on Q^2 is observed.

The average ratios of proton dissociative (with $M_Y < 5$ GeV) to elastic cross sections, integrated over t, are:

$$\begin{aligned}
\frac{\sigma^{\mathrm{M_Y<5\ GeV}}_{tot,\mathrm{p.\ diss.}}}{\sigma_{tot,\mathrm{el.}}}(\rho) &= 0.56 \pm 0.02\ (\mathrm{stat.})\ ^{+0.03}_{-0.05}\ (\mathrm{syst.}) \pm 0.01\ (\mathrm{norm.})\ , \\
\frac{\sigma^{\mathrm{M_Y<5\ GeV}}_{tot,\mathrm{p.\ diss.}}}{\sigma_{tot,\mathrm{el.}}}(\phi) &= 0.50 \pm 0.04\ (\mathrm{stat.})\ ^{+0.06}_{-0.08}\ (\mathrm{syst.}) \pm 0.01\ (\mathrm{norm.})\ . \qquad (22)
\end{aligned}$$

Within uncertainties, the values for the two VMs are compatible. Using the DIFFVM model to estimate the contributions of proton dissociative scattering with $M_Y > 5$ GeV, the ratio of the proton dissociative cross section for the full M_Y mass range to the elastic cross section is found to be close to 1. This value is used e.g. in [105].

5.7.2 Cross section ratios for $t = 0$

If the same object (e.g. a gluon ladder) is exchanged in proton dissociative and elastic scattering, proton vertex factorisation should be manifest through the Q^2 independence of the cross section ratio for $t = 0$.

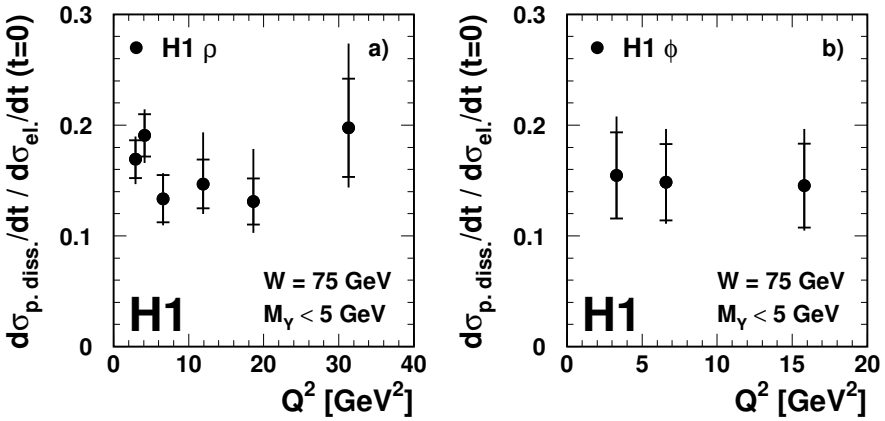

Figure 29: Q^2 dependence of the ratio of the proton dissociative (with $M_Y < 5$ GeV) to the elastic $\gamma^* p$ cross sections at $t = 0$ and $W = 75$ GeV, $\frac{\mathrm{d}\sigma_{\mathrm{p.\ diss.}}/\mathrm{d}t}{\mathrm{d}\sigma_{\mathrm{el.}}/\mathrm{d}t}(\mathrm{t} = 0)$, for (a) ρ meson production; (b) ϕ production. The overall normalisation errors, not included in the error bars, are the same as in Fig. 28. The measurements are given in Tables 35-36.

For exponentially falling t distributions, the cross section ratio at $t = 0$ is obtained from the total cross sections and the b slopes as

$$\frac{\mathrm{d}\sigma_{\mathrm{p.\ diss.}}/\mathrm{d}t}{\mathrm{d}\sigma_{\mathrm{el.}}/\mathrm{d}t}(\mathrm{t} = 0) = \frac{\sigma_{tot,\mathrm{p.\ diss.}}}{\sigma_{tot,\mathrm{el.}}} \cdot \frac{b_{\mathrm{p.\ diss.}}}{b_{\mathrm{el.}}}\ . \qquad (23)$$

Figure 29 presents, as a function of Q^2, the cross section ratios at $t = 0$ for ρ and ϕ production, as obtained from the total cross section ratios presented in Fig. 28 and the b slopes given in Fig. 22.

The average ratios for both VMs are measured as:

$$\begin{aligned}
\frac{\mathrm{d}\sigma^{\mathrm{M_Y<5\ GeV}}_{\mathrm{p.\ diss.}}/\mathrm{d}t}{\mathrm{d}\sigma_{\mathrm{el.}}/\mathrm{d}t}(\mathrm{t}=0)(\rho) &= 0.159 \pm 0.009\ (\mathrm{stat.})\ ^{+0.011}_{-0.025}\ (\mathrm{syst.}) \pm 0.004\ (\mathrm{norm.})\ , \\
\frac{\mathrm{d}\sigma^{\mathrm{M_Y<5\ GeV}}_{\mathrm{p.\ diss.}}/\mathrm{d}t}{\mathrm{d}\sigma_{\mathrm{el.}}/\mathrm{d}t}(\mathrm{t}=0)(\phi) &= 0.149 \pm 0.021\ (\mathrm{stat.})\ ^{+0.035}_{-0.036}\ (\mathrm{syst.}) \pm 0.003\ (\mathrm{norm.})\ .
\end{aligned} \tag{24}$$

The ratios are observed to be independent of Q^2 and consistent for the two VMs, which supports proton vertex factorisation.

The ratios of the proton dissociative to elastic b slopes are also independent of Q^2, with average values of

$$\begin{aligned}
b_{p.\ diss.}\ /\ b_{el.}(\rho) &= 0.28 \pm 0.01\ (\mathrm{stat.})\ ^{+0.01}_{-0.02}\ (\mathrm{syst.})\ , \\
b_{p.\ diss.}\ /\ b_{el.}(\phi) &= 0.27 \pm 0.05\ (\mathrm{stat.})\ ^{+0.06}_{-0.01}\ (\mathrm{syst.})\ .
\end{aligned} \tag{25}$$

This empirical observation is consistent with the Q^2 independence of the total cross section ratios (Fig. 28) and of the cross section ratios at $t = 0$ (Fig. 29).

5.7.3 Difference in *t* slope between elastic and proton dissociative scattering

In the optical model approach of Eq. (19), assuming pomeron universality, the difference between the elastic and proton dissociative b slopes, $b_{el.} - b_{p.\ diss.}$, is related only to the proton size and independent of the interaction scale at the photon vertex and of the VM species.

Figure 30 presents the slope difference $b_{el.} - b_{p.\ diss.}$ for ρ and ϕ meson production, as a function of $(Q^2 + M_V^2)/4$. Within errors, Q^2 independent values for the slope differences are found, with consistent average values of

$$\begin{aligned}
b_{el.} - b_{p.\ diss.}(\rho) &= 5.31 \pm 0.28\ (\mathrm{stat.})\ ^{+0.29}_{-0.24}\ (\mathrm{syst.})\ , \\
b_{el.} - b_{p.\ diss.}(\phi) &= 5.81 \pm 1.14\ (\mathrm{stat.})\ ^{+0.14}_{-0.74}\ (\mathrm{syst.})\ .
\end{aligned} \tag{26}$$

These observations support proton vertex factorisation, with a proton form factor contribution of about $5.5\ \mathrm{GeV}^{-2}$.

Measurements of J/ψ photo- and electroproduction are also presented in Fig. 30. They are consistent with Q^2 independence, with $b_{el.} - b_{p.\ diss.} = 3.50 \pm 0.07\ \mathrm{GeV}^{-2}$, a value significantly smaller than for ρ and ϕ production; for DVCS [9], the measurement is $3.88 \pm 0.61\ \mathrm{GeV}^{-2}$. The difference observed between light and heavy VMs is difficult to understand in the optical model, since the contributions to the slopes of the $q\bar{q}$ dipole form factors and of possible VM form factors should cancel in the difference. It may indicate that the hard regime is not reached for ρ and ϕ mesons in the present kinematic domain.

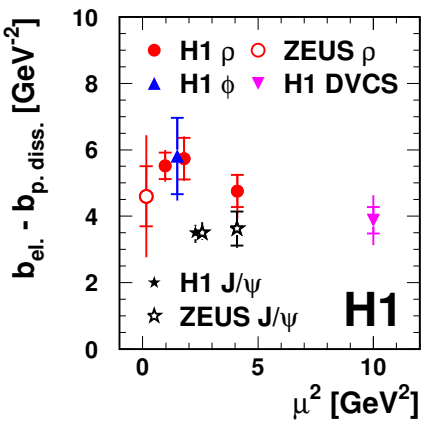

Figure 30: Slope differences $b_{el.} - b_{p.\ diss.}$ between elastic and proton dissociative scattering for ρ and ϕ meson production, as a function of $(Q^2+M_V^2)/4$. Results of H1 for DCVS [9] and J/ψ photoproduction [12, 14] and of ZEUS for ρ [17] and J/ψ [25, 26] photo- and electroproduction are also shown. The present measurements are given in Table 37.

6 Polarisation Measurements

Information on the spin and parity properties of the exchange and on the contribution of the various polarisation amplitudes are accessed in diffractive VM production through the distributions of the angles θ, φ and ϕ defined in Fig. 3. The present section presents, successively, the measurements of the spin density matrix elements, a discussion of the nature of the exchange (NPE and SCHC), measurements of the longitudinal over transverse cross section ratio R, and measurements of the ratios and relative phases of the helicity amplitudes. The results are compared with QCD models.

6.1 Spin density matrix elements

6.1.1 Measurement procedure

In the formalism of Shilling and Wolf [106], summarised in the Appendix, the angular distributions allow the measurement of spin density matrix elements given in the form r^i_{jk}, which are normalised bilinear combinations of the complex helicity amplitudes $T_{\lambda_V \lambda_{N'},\lambda_\gamma \lambda_N}$, λ_γ and λ_V being the helicities of the virtual photon and of the VM, respectively, and λ_N and $\lambda_{N'}$ those of the incoming proton and of the outgoing baryonic system Y.

At HERA, the proton beam is not polarised and the helicity of the outgoing baryonic system Y is not measured; the helicities λ_N and $\lambda_{N'}$ are thus integrated over. For the electron beam, transverse polarisation builds up progressively over the running period through the Sokolov-Ternov effect but the related matrix elements are measurable only for $Q^2 \approx m_e^2$, where m_e is the electron mass, and are not accessible in electroproduction. The electron beam is thus treated here as unpolarised.

In these conditions, a total of 15 independent components of the spin density matrix remain accessible to measurement. They are expressed in terms of the helicity amplitudes, as given in Appendix B. Under natural parity exchange (NPE) in the t channel[7], five $T_{\lambda_V \lambda_\gamma}$ amplitudes are independent: two helicity conserving amplitudes (T_{00} and T_{11}), two single helicity flip amplitudes (T_{01} and T_{10}) and one double flip amplitude (T_{-11}).

The 15 matrix elements enter the normalised angular distribution $W(\theta, \varphi, \phi)$ which is given in Eq. (38) of Appendix A. They are measured as projections of the $W(\theta, \varphi, \phi)$ distribution onto 15 orthogonal functions of the θ, φ and ϕ angles, listed in Appendix C of [106]. In practice, each matrix element is given by the average value of the corresponding (θ, φ, ϕ) function, calculated over the relevant data sample. For ρ production, the ω, ϕ and ρ' background contributions to the angular distributions are subtracted following the results of the Monte Carlo simulations; no correction is performed for the interfering non-resonant $\pi\pi$ channel but this is expected to have a small effect since the interference contribution is small, decreases with Q^2 and changes sign at the resonance mass value, so that it largely cancels when integrated over the selected mass range (see Fig. 9). For ϕ production, the ω, ρ' and dipion backgrounds are subtracted. Kinematic and angular distributions are corrected for detector acceptance and migration effects. The systematic errors on the measurements are estimated by varying the MC simulations according to the list given in Table 7. In addition, a systematic error related to the binning is assigned to the acceptance correction used for determining the average value of the projection functions; it is quantified by varying the number of bins in the θ, φ and ϕ angular variables.

For both ρ and ϕ mesons, the matrix element measurements for the elastic and proton dissociative channels are found to be compatible within experimental errors. In order to improve the statistical significance of the measurements and to reach higher $|t|$ values, the notag and tag samples with $|t| \leq 0.5$ GeV^2 and $|t| \leq 3$ GeV^2, respectively, are combined. The large $|t|$ notag sample is not used because of the large ρ' background, as shown in Figs. 4(c)-(d).

6.1.2 Matrix element measurements

The matrix element measurements for ρ and ϕ production are presented as a function of Q^2 in Figs. 31 and 32, as a function of W for ρ production in Fig. 33, as a function of $|t|$ for ρ and ϕ production in Figs. 34 and 35, and finally as a function of the mass $m_{\pi\pi}$ for ρ production in Fig. 36; for ρ production, the data are presented in two ($|t|$, $m_{\pi\pi}$) or three (W) intervals of Q^2.

The present measurements as a function of Q^2 and $|t|$ confirm with increased precision the previous H1 results [4, 5, 7] and they are globally compatible with ZEUS measurements as a function of Q^2 [19, 24]. Measurements (not shown) of the matrix elements r^{04}_{00} and r^{04}_{1-1}, obtained from fits to the $\cos\theta$ and φ distributions as given by Eqs. (39-40) of Appendix A, are in agreement with those presented in Figs. 31 to 36. For the combinations $r^5_{00} + 2r^5_{11}$ and $r^1_{00} + 2r^1_{11}$ for ρ mesons, measurements from fits of Eq. (41) to the ϕ distribution, which give smaller errors than the projection method, are presented in Fig. 37.

[7] NPE trajectories are defined as containing for $t > 0$ poles with $P = (-1)^J$, P and J being the particle parity and spin, respectively.

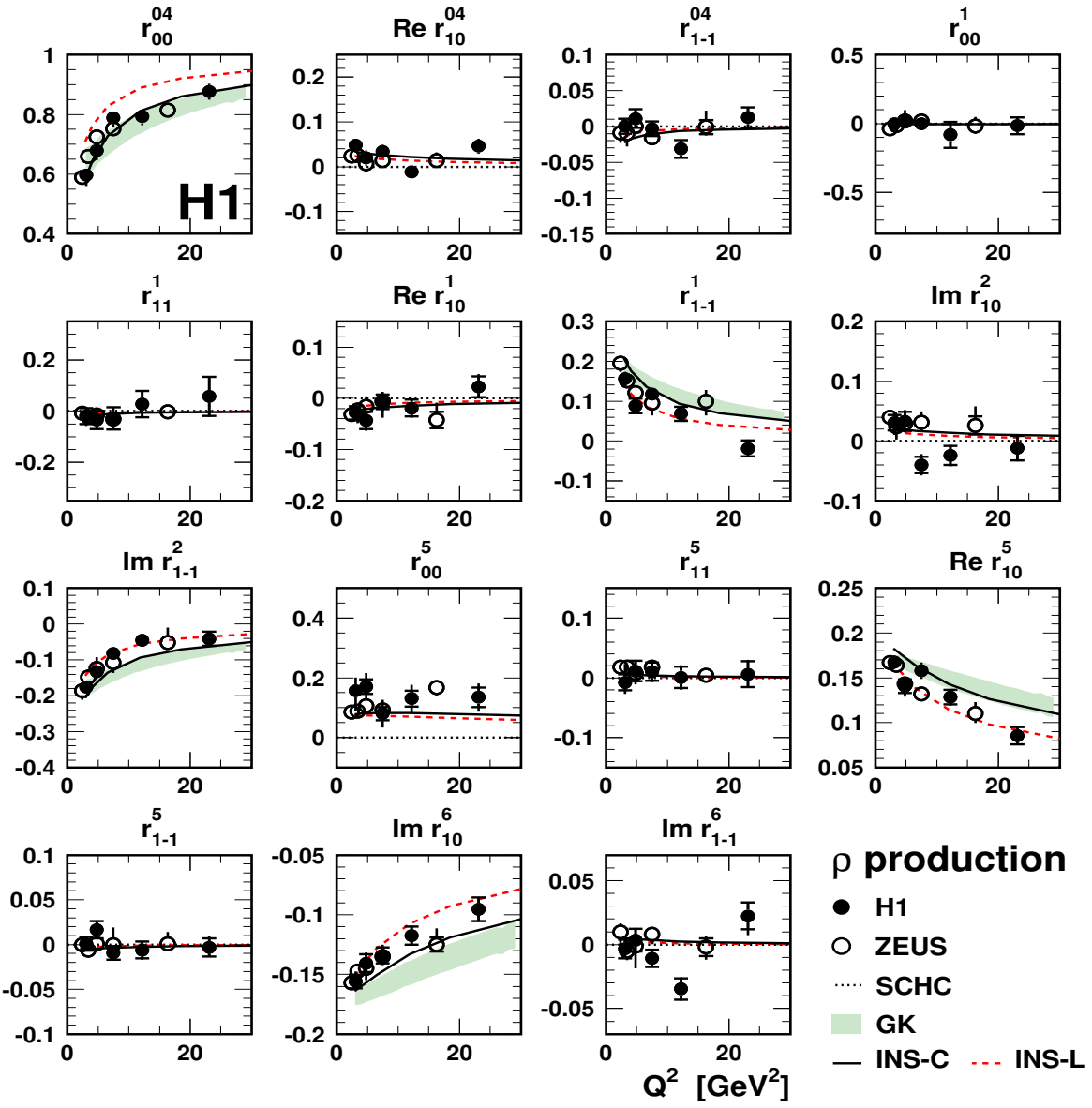

Figure 31: Spin density matrix elements for the diffractive electroproduction of ρ mesons, as a function of Q^2. The notag ($|t| \leq 0.5$ GeV^2) and tag ($|t| \leq 3$ GeV^2) samples are combined. ZEUS results [19] are also shown. Where appropriate, the dotted lines show the expected vanishing values of the matrix elements if only the SCHC amplitudes are non-zero. The shaded bands are predictions of the GK GPD model [61] for the elements which are non-zero in the SCHC approximation; the curves are predictions of the INS k_t-unintegrated model [65] for the compact (solid lines) and large (dashed lines) wave functions, respectively. The present measurements are given in Table 38.

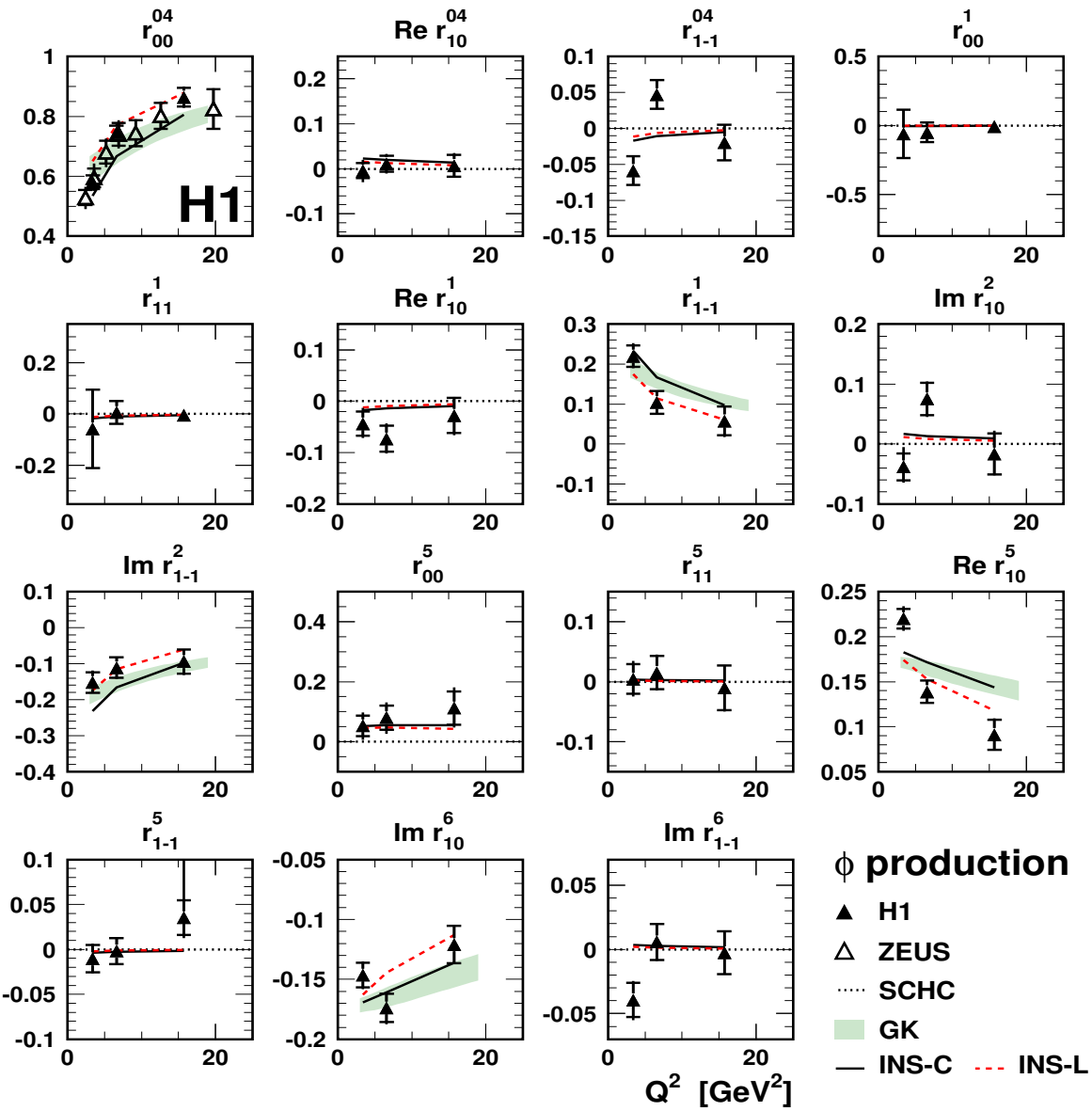

Figure 32: Same as Fig. 31, for ϕ mesons. ZEUS results [24] for the r_{00}^{04} matrix element are also shown. The present measurements are given in Table 39.

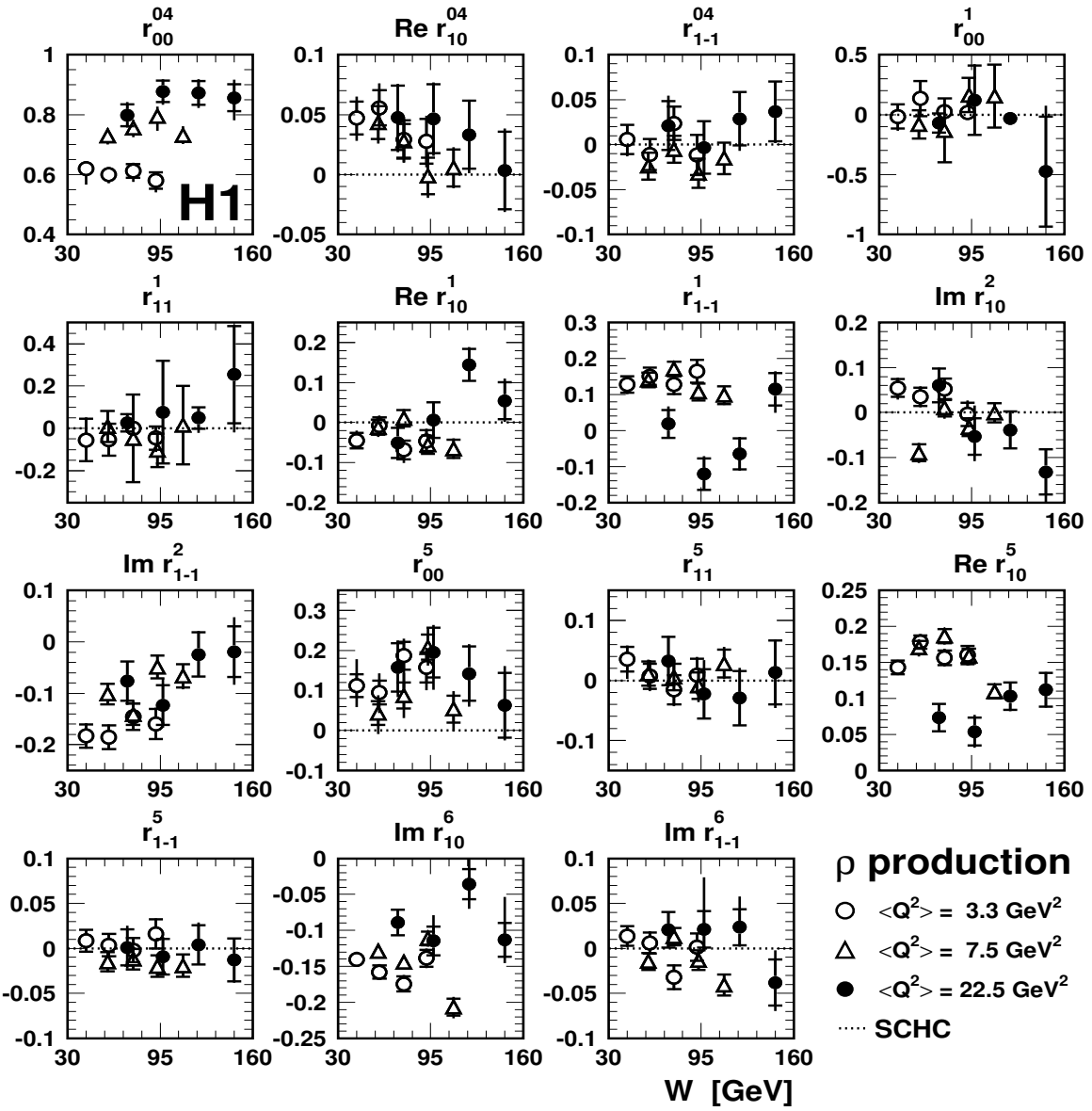

Figure 33: Spin density matrix elements for the diffractive electroproduction of ρ mesons, as a function of W for three intervals in Q^2: $2.5 \leq Q^2 < 5$ GeV^2, $5 \leq Q^2 < 15.5$ GeV^2 and $15.5 \leq Q^2 \leq 60$ GeV^2. The notag ($|t| \leq 0.5$ GeV^2) and tag ($|t| \leq 3$ GeV^2) samples are combined. Where appropriate, the dotted lines show the expected vanishing values of the matrix elements if only the SCHC amplitudes are non-zero. The measurements are given in Table 40.

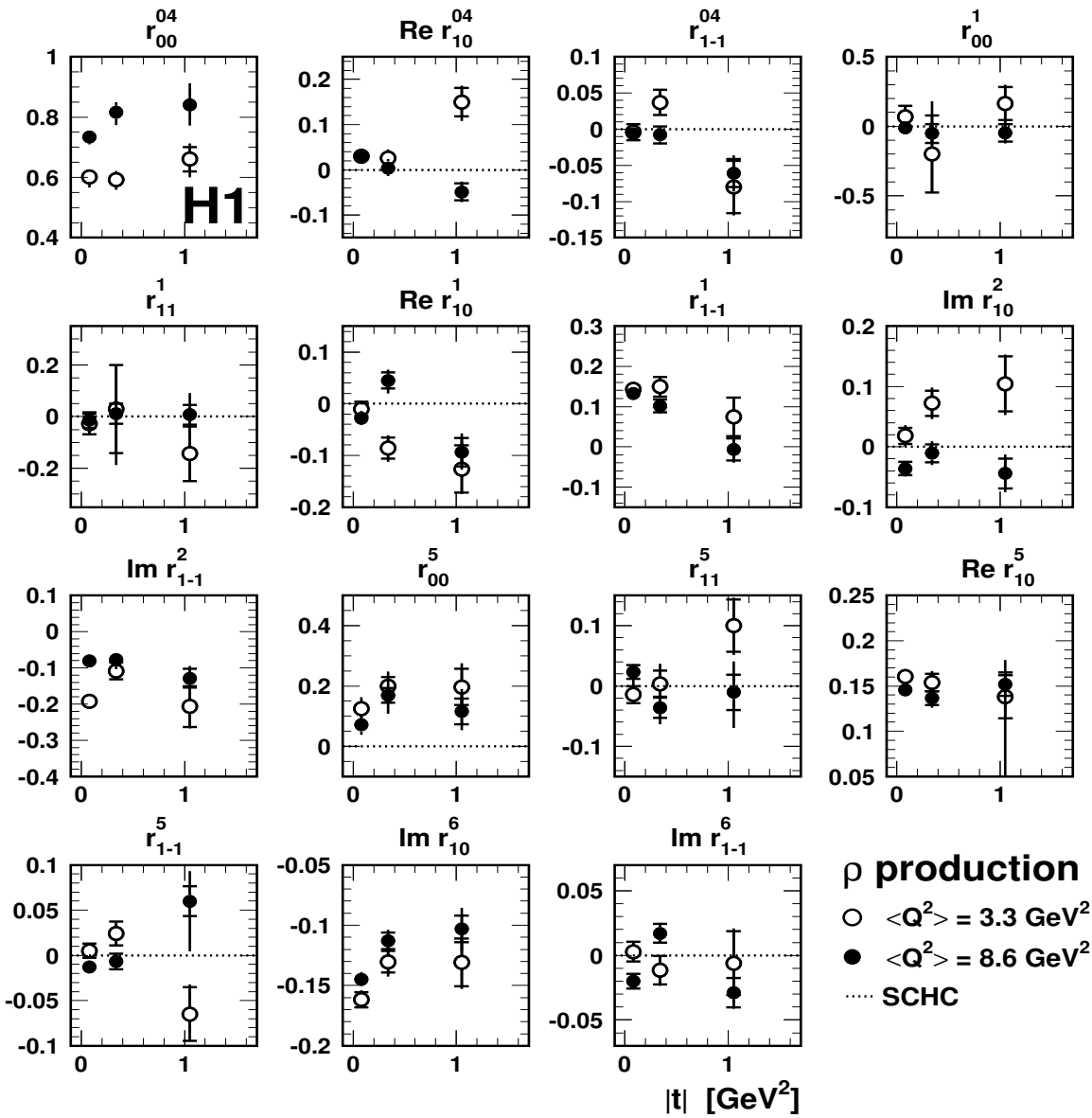

Figure 34: Same as Fig. 33, as a function of $|t|$, for two intervals in Q^2: $2.5 \leq Q^2 < 5$ GeV^2 and $5 \leq Q^2 \leq 60$ GeV^2. The measurements are given in Table 43.

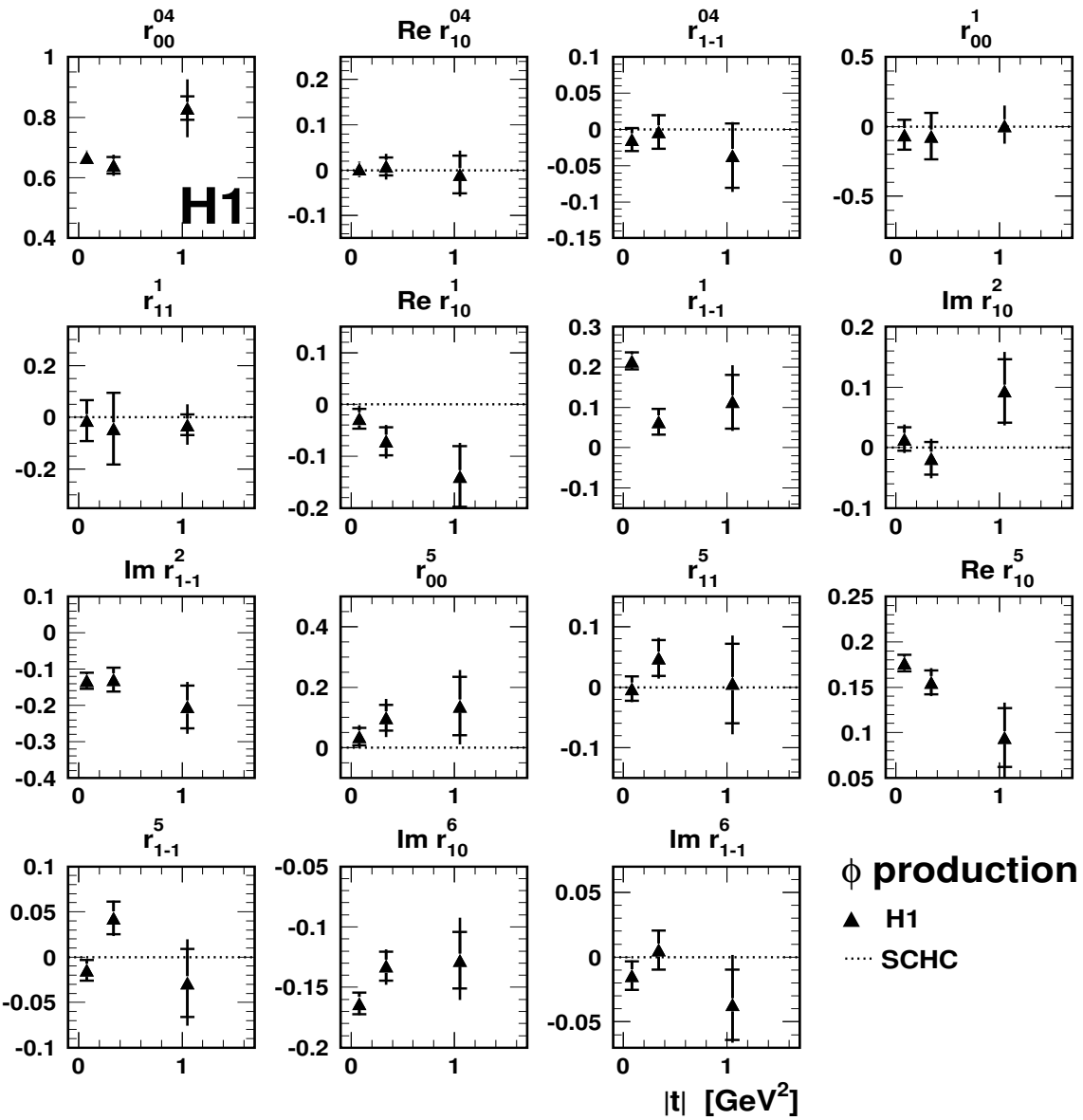

Figure 35: Same as Fig. 34, for ϕ mesons, with $2.5 \leq Q^2 \leq 60$ GeV^2. The measurements are given in Table 44.

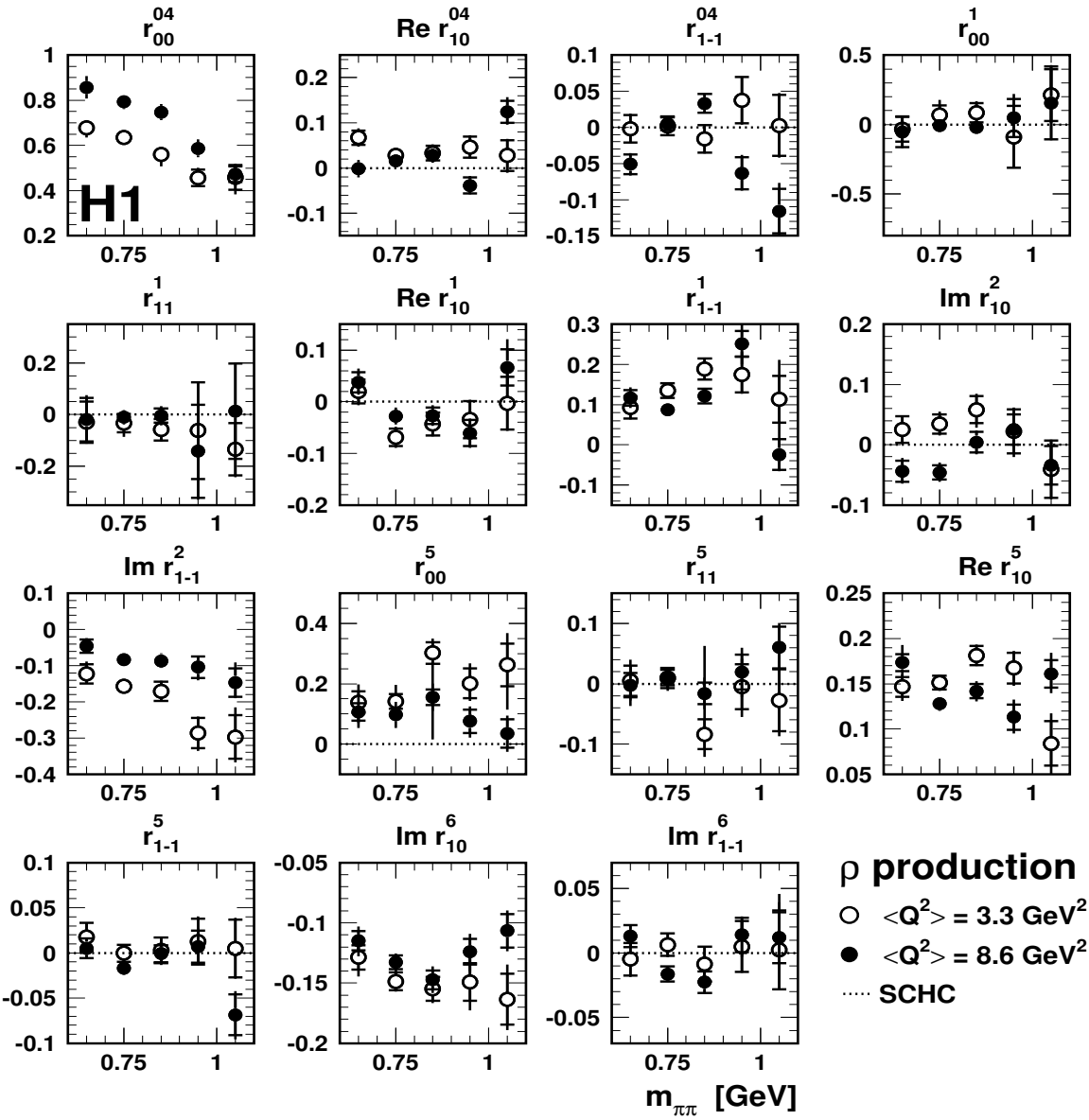

Figure 36: Same as Fig. 34, as a function of the mass $m_{\pi\pi}$. The measurements are given in Table 45.

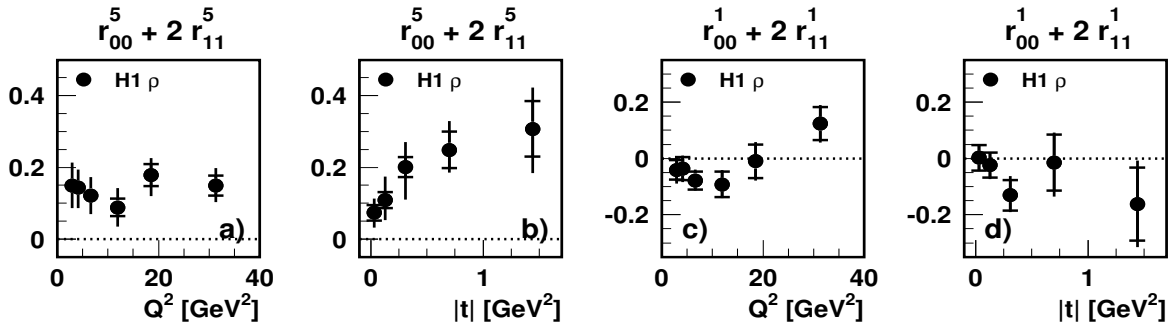

Figure 37: Measurements, as a function of Q^2 and $|t|$, of the ρ matrix element combinations $r^5_{00} + 2r^5_{11}$ and $r^1_{00} + 2r^1_{11}$, obtained from fits of Eq. (41) to the ϕ angle distributions. The notag ($|t| \leq 0.5$ GeV^2) and tag ($|t| \leq 3$ GeV^2) samples are combined. The dotted lines show the expected vanishing values of the matrix elements if only the SCHC amplitudes are non-zero. The measurements are given in Table 47.

6.1.3 Comparison with models

Figures 31 and 32 present, superimposed on the ρ and ϕ measurements, predictions of the GK GPD model [61] and of the INS k_t-unintegrated model [65] for two different wave functions; for the GK model, the SCHC approximation is used and only non-zero elements are shown.

For ρ production (Fig. 31), taking into account the experimental and theoretical uncertainties and the use of the SCHC approximation, the GK model [61] gives a description of the data which is reasonable in shape but does not describe the normalisation well. The INS model [65] reproduces the gross features of the Q^2 evolution but there are problems in the details. The model with the compact wave function describes the r^{04}_{00} matrix element evolution, but it fails for the other elements which are non-zero under SCHC (r^1_{1-1}, Im r^2_{1-1}, Re r^5_{10}, Im r^6_{10}); on the other hand, the model with the large wave function gives a rather good description of these four elements, but fails badly for r^{04}_{00}. In addition, both wave functions predict too low values for r^5_{00}, also in the regime with $Q^2 > 10$ GeV^2.

For ϕ mesons (Fig. 32) with less statistics, the picture is slightly different for the INS model [65], where the use of a large wave function gives a better description of all matrix elements, including r^{04}_{00}, than the compact wave function.

6.2 Nature of the exchange

6.2.1 Natural parity exchange

The observation at low energy [29, 30, 34] of dominant natural parity exchange (NPE) supports the attribution of the vacuum quantum numbers ($J^{PC} = 0^{++}$) to the pomeron; the recent observation by the HERMES collaboration [33] of the presence at low energy of a small contribution (about 6%) of unnatural parity exchange is attributed to quark exchange (π, a_1 or b_1 exchange).

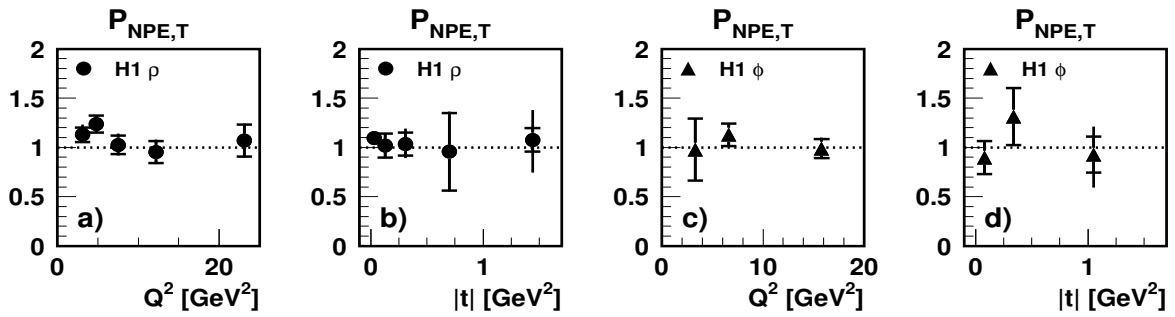

Figure 38: Asymmetry $P_{\rm NPE,T}$ between natural and unnatural parity exchange for transverse photons: (a)-(b) ρ mesons, as a function of Q^2 and $|t|$; (c)-(d) ϕ mesons. The dotted lines indicate the value 1 expected for NPE. The measurements are given in Table 48.

At high energy, the modeling of diffraction as two gluon exchange implies a NPE character, in particular in the GK GPD model [61].

With unpolarised beams and for a single value of the beam energies, the only accessible information about the parity of the exchange is the asymmetry $P_{\rm NPE,T} = (\sigma_T^N - \sigma_T^U) \,/\, (\sigma_T^N + \sigma_T^U)$ between natural (σ_T^N) and unnatural (σ_T^U) parity exchange for transverse photons, using Eq. (43) of Appendix A. Measurements of $P_{\rm NPE,T}$ as a function of Q^2 and $|t|$ for ρ and ϕ mesons are presented in Fig. 38. They are globally compatible with 1, which supports NPE for transverse photons. Natural parity exchange is assumed in the following.

6.2.2 Helicity conserving amplitudes; SCHC approximation

Inspection of Figs. 31 and 32 shows that, for both ρ and ϕ meson electroproduction, the five matrix elements listed in Eq. (44) of Appendix A (r^{04}_{00}, r^{1}_{1-1}, Im r^{2}_{1-1}, Re r^{5}_{10}, Im r^{6}_{10}), which contain products of the two helicity conserving amplitudes, T_{00} and T_{11}, are significantly different from zero, with the SCHC relations of Eq. (45) being approximately satisfied. In addition, with the significant exception of r^{5}_{00}, the other matrix elements are small or consistent with 0.

In the present kinematic domain, SCHC is thus a reasonable approximation, which can be used to obtain information on the transition amplitudes. In order to decrease the sensitivity to the SCHC violating amplitudes, which increase with $|t|$ (see sections 6.2.3 and 6.4), only events with $|t| \leq 0.5$ GeV^2 are used in the rest of this section.

ψ distributions; phase δ between the SCHC amplitudes Under SCHC, the angular distribution $W(\theta, \varphi, \phi)$ reduces to a function of the angles θ and $\psi = \phi - \varphi$, Eq. (47), which allows the extraction in this approximation of the cross section ratio $R = \sigma_L/\sigma_T$ and of the phase δ between the T_{00} and T_{11} amplitudes.

Measurements of $\cos\delta$ obtained from two-dimensional fits of Eq. (47) with R left free are presented in Fig. 39 as a function of Q^2 for ρ and ϕ production ($|t| \leq 0.5$ GeV^2). They are in

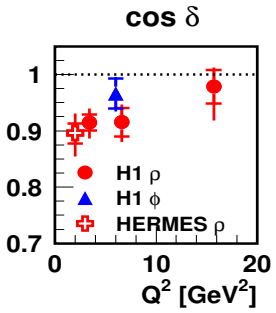

Figure 39: Cosine of the phase δ between the T_{00} and T_{11} helicity conserving amplitudes for ρ and ϕ production with $|t| \leq 0.5$ GeV^2, measured as a function of Q^2 from two-dimensional fits of Eq. (47), in the SCHC approximation. The HERMES [33] measurement on protons is also shown. The dotted line indicates the value 1 which corresponds to amplitudes in phase. The present measurements are given in Table 49.

agreement with the measurements obtained with R fixed to the values measured in the SCHC approximation using the r^{04}_{00} matrix element and Eq. (28).

The measurements of $\cos\delta$ are close to 1, indicating that the transverse and longitudinal amplitudes are nearly in phase. For ρ production with $Q^2 < 10$ GeV^2, $\cos\delta$ differs however significantly from 1, as is also observed for Q^2 around 2 GeV^2 in the low energy measurement by HERMES [33]. An indication of an increase of $\cos\delta$ toward 1 at high Q^2 may be present in the data. An interpretation of a value of $\cos\delta$ different from 1 at high energy in terms of a W dependence of σ_L/σ_T will be given in section 6.4.3.

6.2.3 Helicity flip amplitudes

A significant violation of SCHC is observed in Figs. 31 and 32 through the non-zero value of the r^5_{00} matrix element, for ρ and for ϕ mesons (see also Fig. 37 for the $r^5_{00} + 2r^5_{11}$ combination measurement for ρ mesons). The r^5_{00} matrix element is proportional to the product $\mathrm{Re}\,(T_{00}T^\dagger_{01})$ of T_{00}, the leading SCHC amplitude, and T_{01}, the helicity flip amplitude describing the transition from a transverse photon to a longitudinal VM (see Eq. 60 of Appendix B). In Figs. 34 and 36, non-zero values, with Q^2 dependent strengths, are also observed in ρ production for the matrix elements Re r^{04}_{10}, Re r^1_{10} and Im r^2_{10}, which contain the product $\mathrm{Re}\,(T_{11}T^\dagger_{01})$ of T_{01} and the second SCHC amplitude T_{11}. The data tend to support the relation $\mathrm{Im}\, r^2_{10} = -\mathrm{Re}\, r^1_{10}$ of Eq. (49). Other matrix elements are, within errors, consistent with 0 when integrated over t.

These findings confirm the previous H1 observation [4, 7] in ρ production that the T_{01} helicity flip amplitude is significantly different from 0 in the present Q^2 domain and is dominant among the SCHC violating amplitudes, supporting the hierarchy (see for instance [48])

$$|T_{00}| > |T_{11}| > |T_{01}| > |T_{10}|\ ,\ |T_{-11}|. \tag{27}$$

Note that helicity violation as such is not a signature for hard processes. When integrated over $|t|$, the T_{01} amplitude in the present kinematic domain is larger for low Q^2 than for large Q^2, as

shown by the r^5_{00} matrix element measurement in Fig. 36. At low energy and for $\langle Q^2 \rangle$ around 0.5 GeV^2, the T_{01} amplitude is non-zero, with $|T_{01}| \,/\, \sqrt{|T_{00}|^2 + |T_{11}|^2} = 15$ to 20% for W about 2.5 GeV [29] and 11 to 14% for $10 \leq W \leq 16$ GeV [30].

The r^5_{00} matrix element increases with $|t|$, as observed in Fig. 34 (see also Fig. 37). This is expected on quite general grounds for helicity flip amplitudes, as will be discussed in section 6.4.

6.3 Cross section ratio $R = \sigma_L/\sigma_T$

The cross section ratio $R = \sigma_L/\sigma_T$ is one of the most important observables in the study of light VM production, since its dependence on the kinematic variables Q^2, W, $|t|$ and, for ρ mesons, $m_{\pi\pi}$ is sensitive to the interaction dynamics, including effects related to the interacting dipole size or depending on the VM wave function.

In the SCHC approximation, R can be calculated from the r^{04}_{00} matrix element:

$$R_{SCHC} = \frac{T^2_{00}}{T^2_{11}} = \frac{1}{\varepsilon}\,\frac{r^{04}_{00}}{1 - r^{04}_{00}}. \tag{28}$$

In view of the observed violation of SCHC, a better approximation takes into account the dominant helicity flip amplitude T_{01} and uses in addition the measurement of r^5_{00}:

$$R_{SCHC+T_{01}} = \frac{T^2_{00}}{T^2_{11} + T^2_{01}} = \frac{1}{\varepsilon}\,\frac{r^{04}_{00} - \varepsilon(r^5_{00})^2 + \sqrt{(r^{04}_{00})^2 - 2\varepsilon(r^5_{00})^2}}{2 - 2r^{04}_{00} + \varepsilon(r^5_{00})^2}, \tag{29}$$

where NPE is assumed and the amplitudes are taken to be in phase. As expected, the effect of this improved approximation is mostly significant at large $|t|$ values, in view of the increase with $|t|$ of the helicity flip amplitudes: the corresponding measurement of R is lower than that obtained in the SCHC approximation by about 0.05 for $|t| = 0.1$ GeV^2 and about 0.30 for $|t| = 1$ GeV^2, independently of Q^2. Integrated over t, this makes a 7% difference.

Measurements of R are presented in Figs. 40 and 41 as a function of Q^2 for ρ and ϕ meson production, and in Fig. 42 as a function of W, $|t|$ and $m_{\pi\pi}$ for ρ mesons in different domains in Q^2. For the present measurements, the improved approximation of Eq. (29) is used; the general features of the kinematic variable dependences discussed below are similar when the SCHC approximation of Eq. (28) is used.

Q^2 dependence The measurements of R presented in Fig. 40 show a strong increase with Q^2, which is tamed at large Q^2, a feature already noted in previous H1 [4] and ZEUS [19] publications.

For ρ production, the GK GPD model [61], the MRT model [45] and the INS model [65] with the compact wave function give a good description of the measurements, whereas the KMW [59] predictions are too high and the INS model with the large wave function is ruled out; the predictions of the MPS model [62] (not shown) are very similar to those of KMW up to 10 GeV^2, and then slightly lower. For ϕ production, the KMW model gives a good description

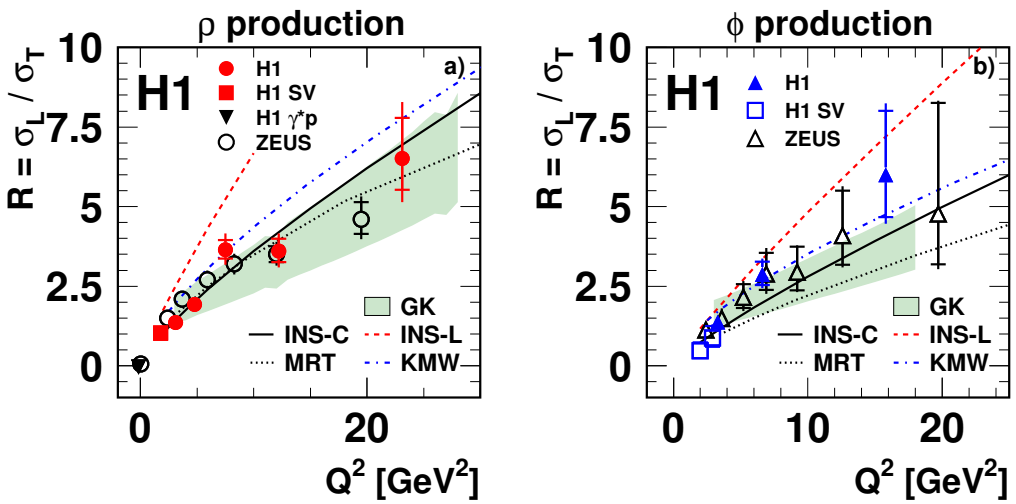

Figure 40: Q^2 dependence of the ratio $R = \sigma_L/\sigma_T$ of the longitudinal to transverse cross sections measured using Eq. (29) for (a) ρ meson production; (b) ϕ production. Measurements of R in the SCHC approximation, for ρ photoproduction by H1 [3] and ZEUS [17] and for ρ and ϕ electroproduction by ZEUS [17, 19, 24] are also shown. The superimposed curves are predictions of the models of GK [61] (shaded bands), INS [65] with the compact (solid lines) and the large (dashed lines) wave functions, MRT with the CTEQ6.5M PDF parameterisation [45] (dotted lines) and KMW [59] (dash-dotted lines). The present measurements are given in Table 50.

while the MRT predictions are too low; within the quoted uncertainty, the GK model describes the data; for the INS model, the large wave function gives a slightly better description than the compact wave function; the predictions of the MPS model (not shown) are again similar to those of KMW, although slightly higher at low Q^2.

R measurements for ρ, ϕ and J/ψ mesons are presented as a function of the scaling variable Q^2/M_V^2 in Fig. 41. The improved approximation, Eq. (29), is used for the present data whereas the SCHC approximation is used for the other data, which makes little difference for the t integrated measurements. A smooth and common behaviour is observed for the three VMs over the full Q^2/M_V^2 range and the full energy range, from the fixed target experiments to the HERA collider measurements.

The data are close to a law $R = Q^2/M_V^2$, represented by the dotted line. However, they lie systematically below the line, and the trend is toward a slower increase of R with increasing Q^2. These features will be confronted with a pQCD prediction in section 6.4.2.

***W* dependence** The W dependence of R is presented for ρ meson production in Fig. 42(a) for three intervals in Q^2. Because of the strong correlation in detector acceptance between W and Q^2, the lever arm in W for each domain in Q^2 is rather limited.

As discussed in section 2, the onset of hard diffraction, characterised by a strong W dependence, is expected to be delayed for transverse amplitudes compared to longitudinal amplitudes. A harder W dependence is thus expected for σ_L than for σ_T, resulting in an increase of R with

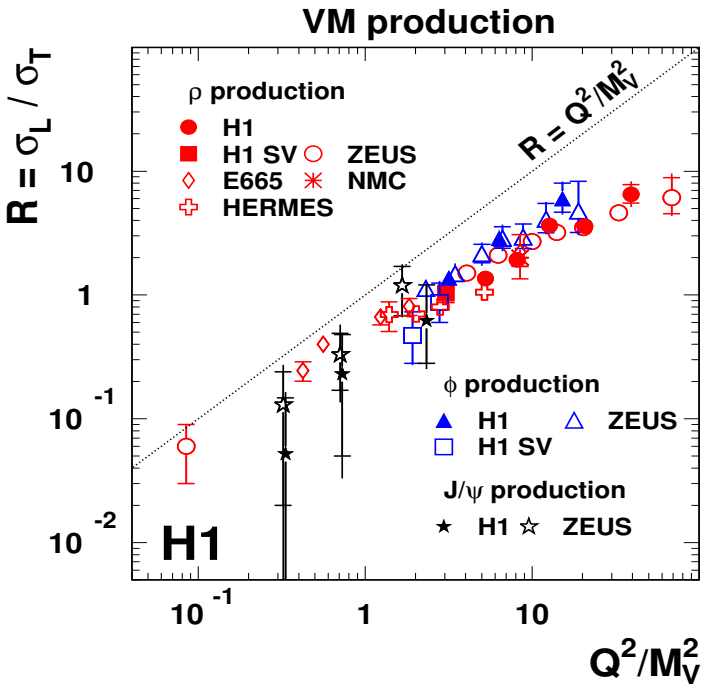

Figure 41: Ratio $R = \sigma_L/\sigma_T$ as a function of the variable Q^2 $/M_V^2$. Electroproduction measurements of ρ mesons by fixed target experiments (NMC [31], E665 [32] and HERMES [33]), of ρ and ϕ mesons by ZEUS [19, 24] and of J/ψ mesons by H1 and ZEUS [12, 26] are also shown. The dotted line represents the scaling behaviour $R = Q^2/M_V^2$.

W. In view of the limited precision, no significant conclusion can be drawn from the present measurements.

***t* dependence; $b_L - b_T$ slope difference** Figure 42(b) presents the measurement of R as a function of $|t|$ for ρ mesons, in two bins in Q^2: $2.5 \leq Q^2 < 5$ GeV^2 and $5 \leq Q^2 \leq 60$ GeV^2. For exponentially falling t distributions, this can be translated into a measurement of the difference between the longitudinal and transverse t slopes, through the relation $R(t) = \sigma_L(t)/\sigma_T(t) \propto e^{-(b_L - b_T)|t|}$. Measurements of the slope difference $b_L - b_T$ extracted from a fit of the t dependence of R are given in Table 12 (for completeness, the result for ϕ production in one bin in t is also given in spite of the large errors). The errors are dominated by the systematic uncertainty on the ρ' background subtraction. A slight indication (1.5σ) is found for a negative value of $b_L - b_T$ in the higher bin in Q^2. The use of the SCHC approximation of Eq. (28) instead of the improved approximation of Eq. (29) for the measurement of R does not affect the measurements of $b_L - b_T$.

A difference between the b slopes is expected to indicate a difference between the transverse size of the dominant dipoles for longitudinal and transverse amplitudes (see e.g. [65]). The indication for a negative value of $b_L - b_T$ in the higher bin in Q^2 is consistent with the expectation that σ_L reaches a harder QCD regime than σ_T, since a harder regime is characterised by a smaller

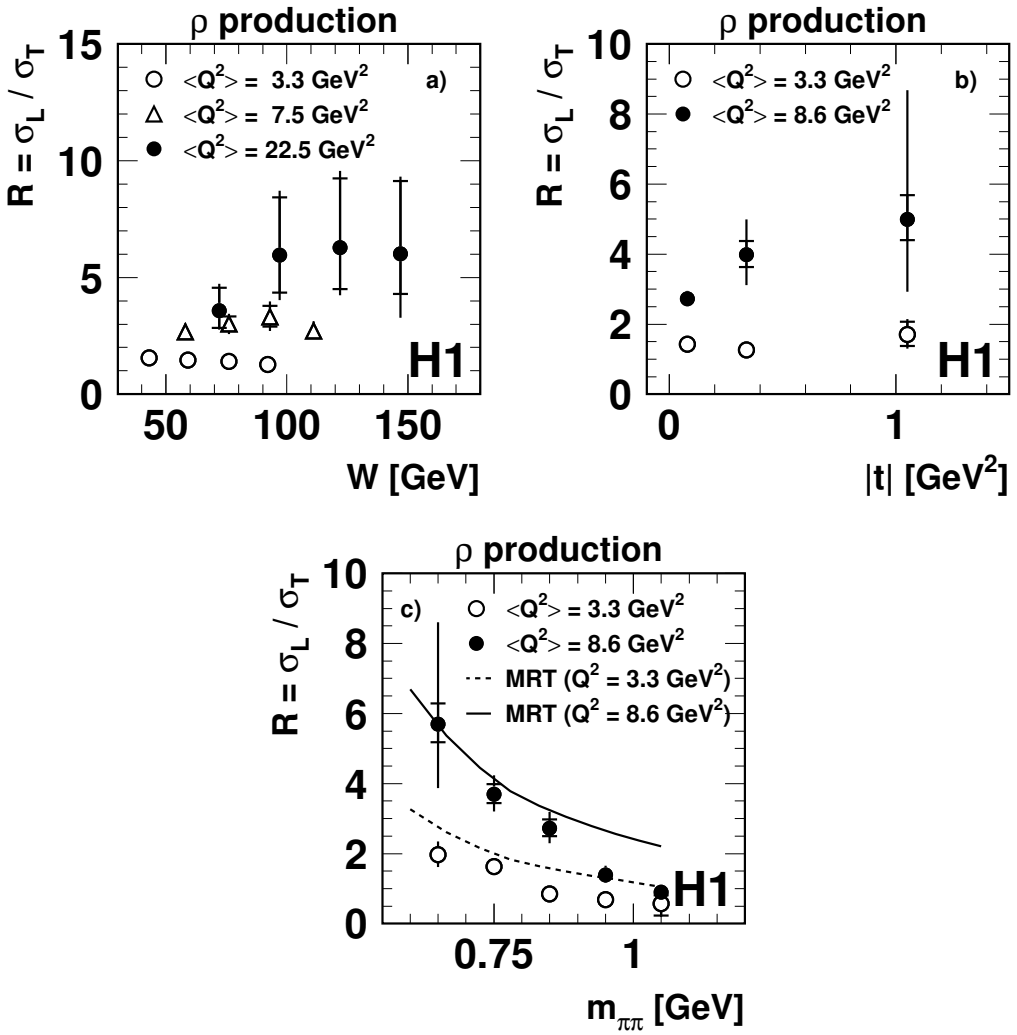

Figure 42: Dependence, for ρ meson production, of the ratio $R = \sigma_L/\sigma_T$ of the longitudinal to the transverse cross sections, determined using Eq. (29), on (a) W; (b) $|t|$; (c) $m_{\pi\pi}$, separately for $2.5 \leq Q^2 < 5$ GeV^2 and for $5 \leq Q^2 \leq 60$ GeV^2; for W, the latter bin is divided into $5 \leq Q^2 < 15.5$ and $15.5 \leq Q^2 \leq 60$ GeV^2. The curves in (c) are from the MRT model [107]. The measurements are given in Tables 51-53.

$\langle Q^2 \rangle$ (GeV^2)	$b_L - b_T$ (GeV^{-2})
ρ production	
3.3	$-0.03 \pm 0.27\ ^{+0.19}_{-0.17}$
8.6	$-0.65 \pm 0.14\ ^{+0.41}_{-0.51}$
ϕ production	
5.3	$-0.16 \pm 0.56^{+0.46}_{-1.10}$

Table 12: Difference between the longitudinal and transverse slopes, $b_L - b_T$, of the t distributions for ρ (two bins in Q^2) and ϕ meson production, calculated from the t dependence of the cross section ratio $R = \sigma_L/\sigma_T$ obtained using Eq. (29).

value of the diffractive b slope. Conversely, the absence of a $|t|$ dependence of R in the lower Q^2 range is consistent with the interpretation of b slope measurements in section 5.6.2, where it was suggested that not only the transverse amplitudes are dominated by large dipoles, but also that large dipoles may also be present in the longitudinal amplitudes ("finite size" effects) for moderate values of the scale $(Q^2+M_V^2)/4$.

$m_{\pi\pi}$ dependences A striking decrease of the cross section ratio R with the increase of the $m_{\pi\pi}$ mass, which was also reported by ZEUS [19], is observed in Fig. 42(c). This strong effect is not expected in calculations where the ρ meson is treated as a particle with well defined mass and wave function.

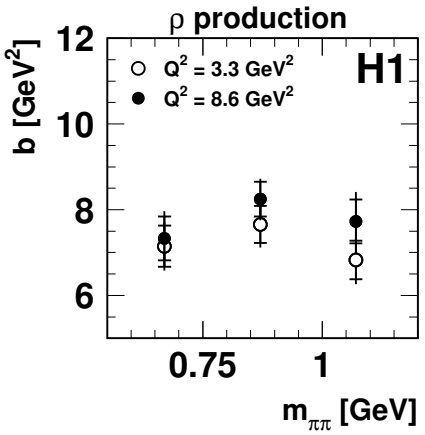

Figure 43: Dependence of the exponential t slope for ρ elastic production as a function of the mass $m_{\pi\pi}$, for $Q^2 = 3.3$ and 8.6 GeV^2. The measurements are given in Table 54.

A simple interpretation of the $m_{\pi\pi}$ dependence follows from the formal Q^2/M^2 dependence of the cross section ratio, if the mass M is understood as the dipion mass rather than the nominal resonance mass. Such an interpretation is in line with the open quark approach of the MRT

parton-hadron duality model [45], and is qualitatively supported by the calculations superimposed to the data in Fig. 42(c) [107]. The mass dependence of R expected from the interference of resonant ρ and non-resonant $\pi\pi$ production, discussed in [99], is small compared to that observed here and should decrease with Q^2.

The b slopes of the $|t|$ distributions do not show any significant dependence on the mass (see Fig. 43), which indicates that the $m_{\pi\pi}$ dependence of R can not be explained by an hypothetic kinematic selection of dipoles with specific size, related either to transverse or longitudinal amplitudes. All this suggests that the VM wave function plays a limited role in the description of VM diffractive production.

6.4 Helicity amplitude ratios and phases

The measurements of the spin density matrix elements presented in Figs. 31 to 36 give access to the ratios and relative phases of the helicity amplitudes, which are extracted and discussed in this section.

6.4.1 Kinematic variable dependences

Following the IK analysis [48], four amplitude ratios can be measured from global fits to the 15 matrix element measurements, assuming NPE and taking all amplitudes as purely imaginary. The ratios are calculated relative to the dominant T_{00} amplitude.

The fit results are presented in Figs. 44 to 47 for ρ and ϕ meson production as a function of Q^2, $1/Q$ and $|t|$, and for ρ mesons as a function of the $m_{\pi\pi}$ invariant mass. Negative values are allowed for the amplitude ratios, corresponding to opposite phases.

Q^2 dependences A strong decrease with Q^2 of the T_{11}/T_{00} amplitude ratio is observed for both VMs (Fig. 44), which is related to the increase with Q^2 of the cross section ratio R (Fig. 40). For the first time, a Q^2 dependence of the T_{01}/T_{00} ratio is also observed for ρ meson production (Figs. 44 and 45). This dependence is also visible in the comparison of the two Q^2 ranges in Figs. 46 and 47. Figure 45 shows consistency with a linear increase with $1/Q$ of the amplitude ratios T_{11}/T_{00} and T_{01}/T_{00} for ρ production and T_{11}/T_{00} for ϕ production.

t dependences The t dependence of the amplitudes, empirically parameterised as exponentially falling, is mainly determined by the proton and VM form factors. It is a reasonable assumption that these form factors affect in a similar way all amplitudes and that their effects cancel in matrix elements and in amplitude ratios [48]. The study of the t dependence of the amplitude ratios thus gives access, in the reaction dynamics, to features specific to the different amplitudes. Note, however, that this line of reasoning neglects the different t dependences for transverse and longitudinal amplitudes, related to different dipole sizes.

For all ratios of the helicity amplitudes shown in Fig. 46, $|t|$ dependences are observed, with varying strengths. For the first time, a decrease with $|t|$ of the ratio of amplitudes T_{11}/T_{00} is

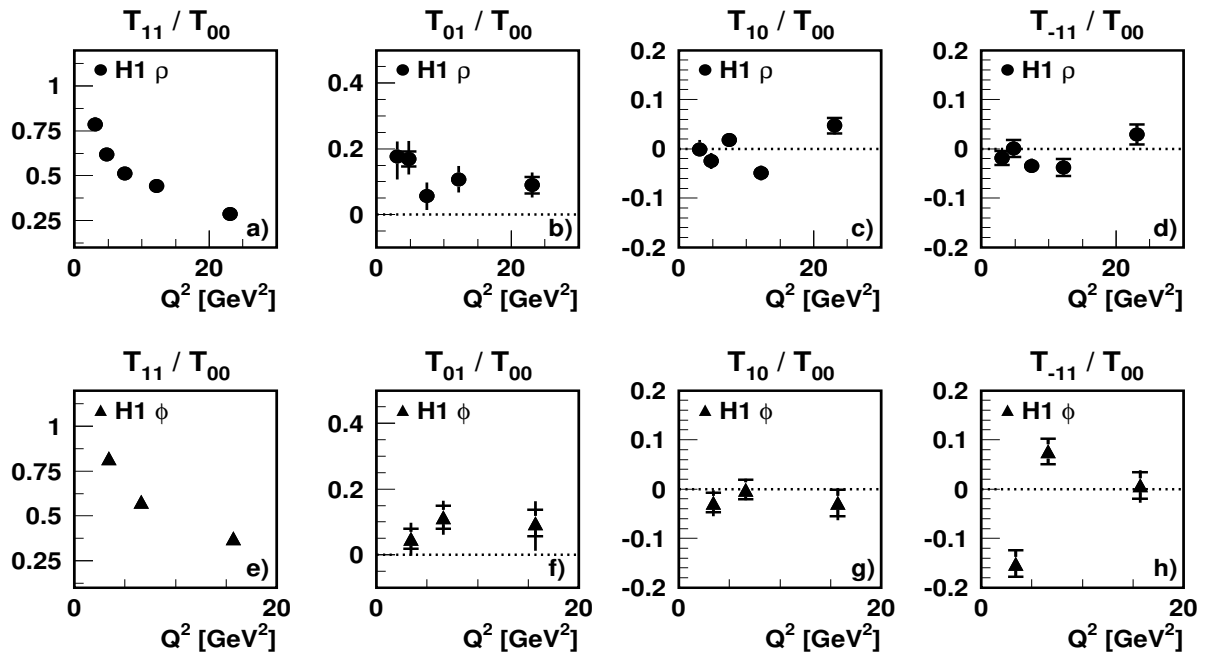

Figure 44: Ratios of the helicity amplitudes, calculated from global fits to the measurements of the 15 spin density matrix elements, as a function of Q^2: (a)-(d) ρ meson production; (e)-(h) ϕ production. NPE is assumed and all amplitudes are taken as purely imaginary. Where appropriate, the dotted lines show the expected null value of the ratio if the non-SCHC amplitudes are vanishing. The measurements are given in Table 55.

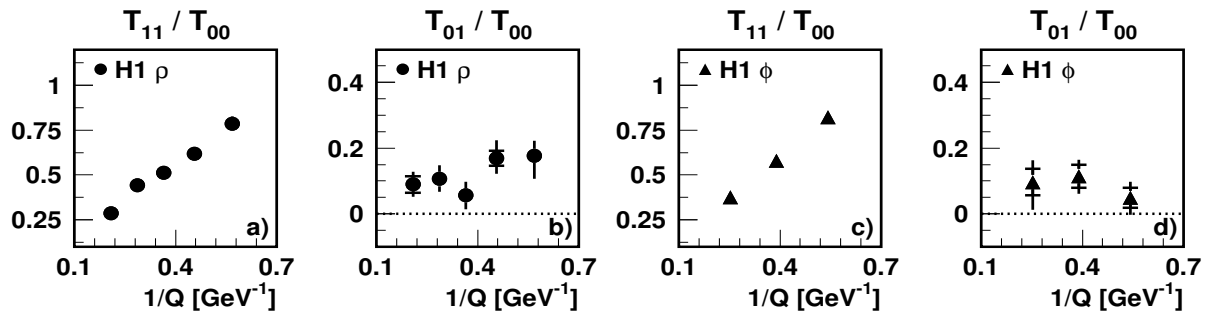

Figure 45: Ratios of the helicity amplitudes T_{11}/T_{00} and T_{01}/T_{00}, as in Fig. 44, presented as a function of $1/Q$: (a)-(b) ρ meson production; (c)-(d) ϕ production.

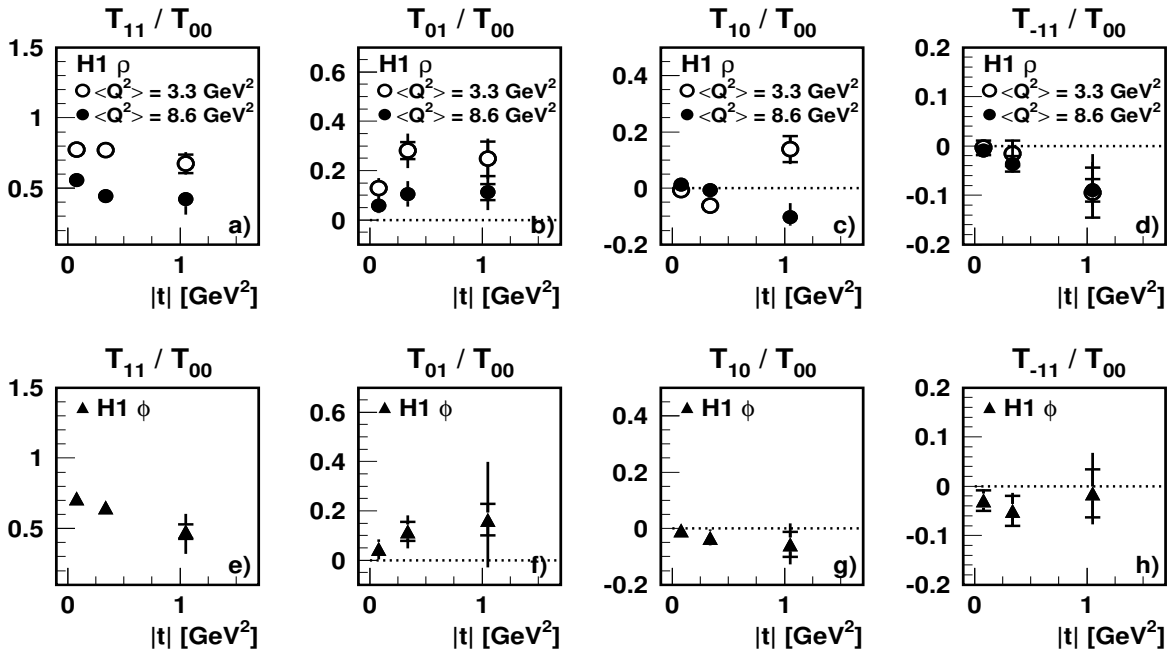

Figure 46: Same as Fig. 44, as a function of $|t|$: (a)-(d) ρ meson production, for two bins in Q^2: $2.5 \leq Q^2 < 5$ GeV^2 (open circles) and $5 \leq Q^2 \leq 60$ GeV^2 (closed circles); (e)-(h) ϕ production. The measurements are given in Table 56.

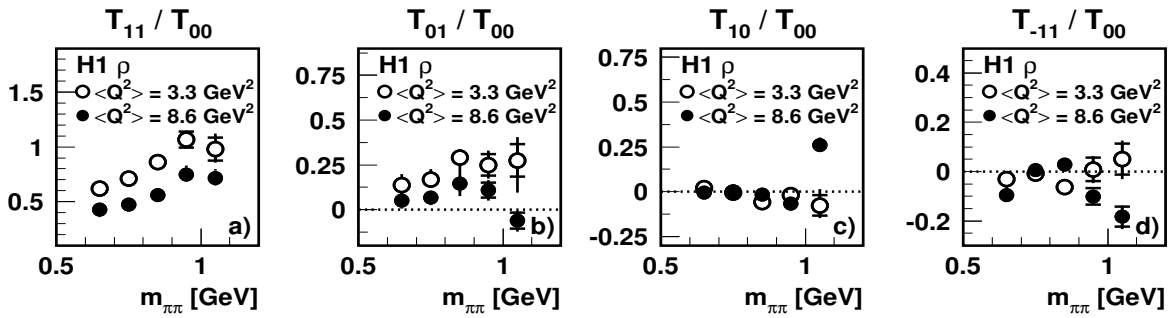

Figure 47: Same as Fig. 46 for ρ meson production, as a function of the mass $m_{\pi\pi}$. The measurements are given in Table 57.

observed, both for ρ and for ϕ production (Figs. 46(a) and (e)). For ρ production, t dependences are also observed in the three other ratios. The increase with $|t|$ of the normalised T_{01} helicity flip amplitude, which could be deduced from the behaviour of the r^5_{00} matrix element, is confirmed in Fig. 46(b) for ρ mesons in both domains in Q^2. For the second single flip amplitude, T_{10}, an increase of the strength of the ratio to T_{00}, with negative values for $|t| \gtrsim 0.3$ GeV^2, is observed in Fig. 46(c) for ρ production at large Q^2. Finally, non-zero values are found in Fig. 46(d) for the ratio of the double flip T_{-11} to the T_{00} amplitude, with negative values of the ratio and intensity increasing with $|t|$ for both bins in Q^2.

The t dependence of the helicity flip amplitudes for light quarks can be explained as follows. In the case of the T_{01} amplitude, the virtual photon with transverse polarisation fluctuates into a quark and an antiquark which, given their opposite helicities, must be in an orbital momentum state with projection 1 onto the photon direction. During the hard interaction, the dipole size and the quark and antiquark helicities are unchanged, but a transverse momentum $k_t \simeq \sqrt{|t|}$ is transferred to the dipole, which modifies its line of flight and thus allows a change of the orbital momentum projection. The T_{01} amplitude, which describes the production of a longitudinal meson from a transverse photon, is thus proportional to $\sqrt{|t|}$. Similar reasons explain the t dependence of the T_{10} amplitude. Note that, at variance with the case of light VMs, for heavy VMs with a non-relativistic wave function ($z \simeq 1 - z \simeq 1/2$), the exchange of orbital momentum cannot take place, thus implying SCHC.

In the two-gluon exchange picture of diffraction for the double flip T_{-11} amplitude, the change by two units from the photon to the VM helicities requires in addition spin transfer by the exchanged gluons. The observation of a non-zero value for this amplitude may thus provide important information concerning gluon polarisation in the proton [108].

$\langle Q^2 \rangle$ (GeV^2)	$b_L - b_T$ (GeV^{-2})
ρ production	
3.3	$-0.06 \pm 0.22\ ^{+0.24}_{-0.11}$
8.6	$-0.53 \pm 0.10\ ^{+0.14}_{-0.57}$
ϕ production	
5.3	$-0.70 \pm 0.23\ ^{+0.58}_{-0.63}$

Table 13: Difference between the longitudinal and transverse slopes of the t distributions for ρ (two bins in Q^2) and for ϕ meson production, calculated from the t dependence of the cross section ratio $R = \sigma_L/\sigma_T$ obtained using fits to the amplitude ratios, Eq. (30).

The $|t|$ dependence of the T_{11} to T_{00} amplitude ratio may be understood as an indication of different transverse dipole sizes in transverse and longitudinal photon scattering, as discussed in section 6.3 for the t dependence of the cross section ratio R. This is substantiated by the calculation of the cross section ratio using the helicity amplitude ratios. The cross section ratio $R = \sigma_L/\sigma_T$ is indeed given, using Eqs. (88-89), as:

$$R = \frac{1 + 2\,(T_{10}/T_{00})^2}{(T_{11}/T_{00})^2 + (T_{01}/T_{00})^2 + (T_{-11}/T_{00})^2}. \tag{30}$$

Following the procedure of section 6.3, the difference between the longitudinal and transverse slopes are extracted from the t dependence of R. The results are given in Table 13. For ρ production, the same effect is observed as in Table 12, where the value of R was obtained only from the measurements of the r^{04}_{00} and r^{5}_{00} matrix elements using Eq. (29): a value of $b_L - b_T$ consistent with 0 for $Q^2 < 5$ GeV^2, and a negative value for $Q^2 > 5$ GeV^2. Errors are reduced due to the use of all amplitude ratios in the global fits, and the value of $b_L - b_T$ in the Q^2 range with $Q^2 > 5$ GeV^2 is 3σ away from 0. For ϕ production, the limited statistics do not allow to measure separately the slope difference in two bins in Q^2.

***W* and $m_{\pi\pi}$ dependences** No significant W dependence of the amplitude ratios is observed (not shown), which follows from the absence of W dependence of the matrix elements in Fig. 33. The strong $m_{\pi\pi}$ dependence of the σ_L/σ_T cross section ratio observed in Fig. 42(c) is confirmed in the ratio T_{11}/T_{00} of the dominant SCHC amplitudes, as seen in Fig. 47.

6.4.2 Comparison with a pQCD model

The IK calculations [48] provide a general framework in pQCD for interpreting the main features of the present data. The model gives predictions for the dependences of the helicity amplitude ratios in the variables Q^2, $|t|$ and M, which is a typical $q\bar{q}$ mass for the VM under study. In the MRT model [45], the Q^2 dependence of the gluon density $G(x, Q^2) \propto (Q^2/Q_0^2)^\gamma$, where γ is the gluon anomalous dimension, damps the end-point singularities. Taking all amplitudes as imaginary, the following dependences are predicted (see [48] for details):

$$T_{11}/T_{00} = \frac{M}{Q}\,\frac{1+\gamma}{\gamma} \tag{31}$$

$$T_{01}/T_{00} = \frac{\sqrt{|t|}}{Q}\,\frac{1}{\sqrt{2}\gamma} \tag{32}$$

$$T_{10}/T_{00} = -\frac{M\,\sqrt{|t|}}{Q^2}\,\frac{\sqrt{2}}{\gamma} \tag{33}$$

$$T_{-11}/T_{00} = \eta^0 + \eta^1, \tag{34}$$

$$\eta^0 = -\frac{\bar{\alpha}_S^2 |t|\, M}{\pi\,\alpha_S\, Q\, m_\rho^2}\,\frac{1}{4^\gamma\,\frac{\Gamma^2(\gamma+1)}{\Gamma(2\gamma+2)}\,xG(x, Q^2/4)} \tag{35}$$

$$\eta^1 = \frac{M\,|t|}{Q^3}\,\frac{2(\gamma+2)}{\gamma}. \tag{36}$$

For the present kinematic range, the model predicts the hierarchy described by the inequalities (27).

For the ratio of the SCHC amplitudes T_{11} and T_{00}, the model predicts the linear increase with $1/Q$ observed in Fig. 45. These amplitudes govern, up to the small helicity flip corrections, the cross section ratio, with in the SCHC approximation $R \simeq |T_{00}|^2/|T_{11}|^2$. The factor $(1+\gamma)/\gamma > 1$ in Eq. (31) damps the Q^2/M_V^2 increase of R predicted by formal calculations, which accounts for the observation in Fig. 41 that the data lie below the dotted line. Since the anomalous dimension γ decreases with Q^2, the factor $[\gamma/(1+\gamma)]^2$ also decreases with Q^2,

which is consistent with the taming of the R evolution in Figs. 40 and 41. The $|t|$ dependence of T_{11}/T_{00} observed in Fig. 46 is not predicted in Eq. (31) but, as discussed in the previous section, it may follow from the different transverse size of transverse and longitudinal dipoles, which is not considered in this paper since it deals with the purely perturbative domain. The dependence of T_{11}/T_{00} on the mass $m_{\pi\pi}$ observed in Fig. 47 is also not predicted explicitely by the model, which does not analyse the mass structure of the resonance, but it may follow from the M/Q dependence in Eq. (31), taking for M the di-pion mass.

The $|t|$ dependence of the T_{01}/T_{00} amplitude ratio observed in Fig. 46 is predicted in the perturbative domain by Eq. (32). The decrease with Q^2 of the T_{01}/T_{00} amplitude ratio observed for ρ mesons in Figs. 44 and 45 is also predicted by Eq. (32).

The increase with $|t|$ of the amplitude ratio T_{10}/T_{00} for ρ mesons observed in Fig. 46 for the higher domain in Q^2 and its negative values are predicted by Eq. (33).

Finally, the $|t|$ dependence observed in Fig. 46 of the T_{-11}/T_{00} amplitude ratio, which involves the T_{-11} double helicity flip amplitude, supports the predictions of Eqs. (34-36) and may constitute an important piece of observation on gluon polarisation in the proton. The amplitude ratio is found to be negative, both for $Q^2 < 5$ GeV^2 and $Q^2 > 5$ GeV^2, supporting a dominance of the η^0 over the η^1 contribution, at variance with the expectation of the model [48], but this parameterisation includes strong approximations [108].

6.4.3 Amplitude relative phases

In an extension of the fits performed in the previous section, the phases between the amplitudes can be left free. To ensure proper convergence, the number of fitted quantities has to be reduced. In view of their small values, the approximation is made to put to 0 the amplitudes T_{10} and T_{-11}. When the phase difference $\cos(\phi_{01} - \phi_{00})$ is left free, it is pushed to the bound 1; it is therefore fixed to this value in the fit[8]. Finally, the amplitude ratios T_{11}/T_{00} and T_{01}/T_{00} and the phase difference $\cos(\phi_{11} - \phi_{00})$ are left free.

Figure 48 shows the $\cos(\phi_{11}-\phi_{00})$ phase difference for the ρ and ϕ meson SCHC amplitudes as a function of Q^2, $|t|$ and $m_{\pi\pi}$; the amplitude ratios T_{11}/T_{00} and T_{01}/T_{00} obtained from the fits are compatible with those presented in the previous section. The average value is

$$\cos(\phi_{11} - \phi_{00}) = 0.936 \pm 0.016\ (\text{stat.})\ ^{+0.025}_{-0.038}\ (\text{syst.}), \tag{37}$$

which confirms the result of section 6.2.2 under the SCHC approximation (Fig. 39), that the dominant longitudinal and transverse amplitudes are nearly but not completely in phase.

The phase difference between the two dominant amplitudes, T_{00} and T_{11}, may provide some indirect information on the energy (W) dependence of the longitudinal and transverse amplitudes. The phase difference indeed reflects a difference in the ratio $\beta = \text{Re A} \ / \ \text{Im A}$ of the real to imaginary parts of the amplitudes A. The ratio β is in turn related to the $W \propto 1/x$ dependence of the amplitude, since β is given by the $\log 1/x$ derivative of the amplitude: $\beta = \tan(\pi\lambda/2)$, with $\lambda = \partial \ln A / \partial \ln(1/x)$. A phase difference at high energy may thus be an indication of a different W dependence of the transverse and longitudinal amplitudes.

[8]The observation that $\cos(\phi_{01}-\phi_{00})$ is close to 1 is at variance with calculations in [109], where an attempt was made in a GPD approach to estimate the size of the T_{01} amplitude within the handbag approach. The prediction in [109] that the amplitudes should be out of phase depends in fact strongly on a number of assumptions [110].

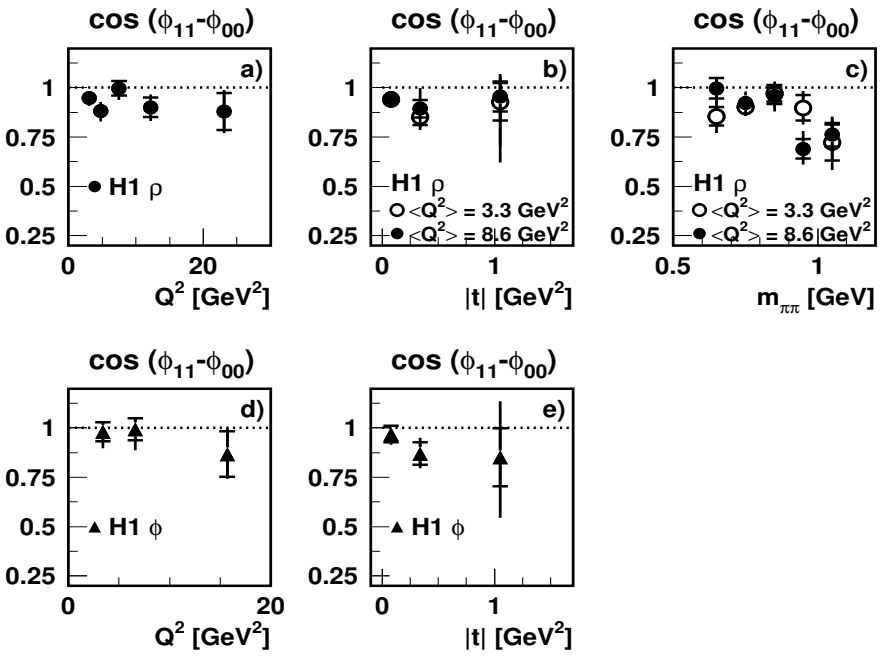

Figure 48: Phase difference between the T_{11} and T_{00} amplitudes, calculated from global fits to the measurements of the 15 spin density matrix elements (see text), (a)-(c) as a function of Q^2, $|t|$ and $m_{\pi\pi}$ for ρ meson production; (d)-(e) as a function of Q^2 and $|t|$ for ϕ production. For the $|t|$ and $m_{\pi\pi}$ dependences of ρ mesons, data are presented for two bins in Q^2: $2.5 \leq Q^2 < 5\ \mathrm{GeV}^2$ (open circles) and $5 \leq Q^2 \leq 60\ \mathrm{GeV}^2$ (closed circles). The dotted lines at 1 represent the case of amplitudes in phase. The measurements are given in Tables 55-57.

7 Summary and Conclusions

This paper reports on the measurement of diffractive ρ and ϕ meson electroproduction at high energy, both in the elastic and proton dissociative channels. The data were taken in the years 1996 to 2000 with the H1 detector at the ep collider HERA, in the kinematic domain $2.5 \leq Q^2 \leq 60\ \mathrm{GeV}^2$, $35 \leq W \leq 180$ GeV, $|t| \leq 3\ \mathrm{GeV}^2$ and $M_Y < 5\ \mathrm{GeV}$.

The total, longitudinal and transverse $\gamma^* p$ cross sections are measured as a function of the scaling variable $Q^2 + M_V^2$. They roughly follow power laws, and are well described by empirical parameterisations allowing the power to linearly depend on $Q^2 + M_V^2$. The ϕ to ρ total cross section ratios are found to be independent of $Q^2 + M_V^2$ and consistent for elastic and proton dissociative scattering, with a value close to but slightly lower than the ratio expected from quark charge counting, $\phi : \rho = 2 : 9$. The measurements significantly differ from the formal predictions $n = 3$ and $n = 4$ for the $1/(Q^2+M_V^2)^n$ dependence of the longitudinal and transverse cross sections, respectively, which is attributed mainly to the increase with Q^2 of the gluon density at small x.

The $\gamma^* p$ cross sections increase with the photon–proton centre of mass energy W, which is parameterised in the Regge inspired form $\propto W^\delta$, where δ increases significantly with Q^2. This "hardening" of the W distribution is described in terms of the intercept $\alpha_{I\!P}(0)$ of the effective

Regge trajectory. For values of the scale $\mu^2 = (Q^2+M_V^2)/4$ up to about 3 GeV^2, the W dependence of ρ and ϕ production is slightly harder than the soft behaviour characteristic of hadron interactions and photoproduction, $\alpha_{I\!P}(0) = 1.08$ to 1.11. For the higher $(Q^2+M_V^2)/4$ range, values of $\alpha_{I\!P}(0)$ of the order of 1.2 to 1.3 are reached, compatible with J/ψ measurements. DVCS measurements show a similar behaviour as a function of the scale $\mu^2 = Q^2$.

The t dependences of the cross sections are well described as exponentially falling distributions $\propto e^{-b|t|}$, up to $|t|$ values of 0.5 GeV^2 for elastic production and 3 GeV^2 for proton dissociation. The t slopes are measured for all four channels, providing the first precise determination at HERA of the proton dissociative slopes for light VM electroproduction. The values of the t slopes are lower than those in photoproduction and they decrease with increasing scale, in a way which is common to light VMs and DVCS. Values of the t slopes comparable to those for J/ψ production, or slightly larger, are reached for a scale $(Q^2+M_V^2)/4 \gtrsim 5$ GeV^2, which suggests that light VM form factors are small and confirms that the dominant longitudinal amplitudes approach a perturbative behaviour for $(Q^2+M_V^2)/4$ around 3 to 5 GeV^2. The correlation between the W and t dependences of the cross sections is parameterised in the form of the slope α' of the effective pomeron trajectory. For ρ meson production, this slope is smaller than that in soft hadron-hadron interactions, albeit with large errors.

The ratio of the proton dissociative to elastic cross sections for $|t| = 0$ and the difference between the elastic and proton dissociative slopes are measured to be independent of Q^2. These observations support the relevance of the factorisation of the process into a hard scattering contribution at the photon vertex and a soft diffractive scattering at the proton vertex ("Regge factorisation"). The value measured for ρ and ϕ production for the slope difference, $b_{el.} - b_{p.\ diss.} \simeq 5.5$ GeV^{-2}, however, is larger than for J/ψ production.

Polarisation effects are studied through the measurement of 15 spin density matrix elements, which are normalised bilinear combinations of the complex helicity amplitudes $T_{\lambda_V \lambda_\gamma}$. The dependence on the kinematic variables and, for ρ mesons, on the dipion mass is measured. The main feature in the present domain is the dominance of the s-channel helicity conserving (SCHC) amplitudes, T_{00} and T_{11}, with $T_{00} > T_{11}$. In addition, a significant breaking of SCHC is manifest through the non-zero value of the r^5_{00} matrix element, especially at large $|t|$ values.

The ratio $R = \sigma_L/\sigma_T$ of the longitudinal to transverse cross sections increases strongly with Q^2, as predicted in pQCD, with a scaling behaviour as a function of Q^2/M_V^2 for the different VMs. The linear dependence $R = Q^2/M_V^2$ predicted at LO, however, is damped for large values of Q^2. No W dependence of R is observed within errors. For t, an indication of the dependence of R is found for ρ meson production with $Q^2 > 5$ GeV^2. This can be interpreted as a difference between the longitudinal and transverse t slopes, $b_L - b_T$, which differs from zero by 1.5σ, with dominant systematic errors. A strong $m_{\pi\pi}$ dependence of R is observed for ρ meson production, both for Q^2 smaller and larger than 5 GeV^2. This behaviour may be interpreted as following from the general Q^2/M^2 dependence of VM production, if the mass M is understood as the dipion mass rather than the nominal resonance mass.

The ratio of the helicity amplitudes is measured from global fits to the 15 matrix elements. Several features expected in pQCD are observed for the first time. A decrease with increasing Q^2 is found for the amplitude ratio T_{01}/T_{00}, which supports the higher twist nature of the helicity flip amplitudes. The amplitude ratio T_{11}/T_{00} is observed to decrease with increasing $|t|$,

which may be related to different transverse sizes of transverse and longitudinal dipoles. This is substantiated by the non-zero value of the slope difference $b_L - b_T$ obtained from the measurement of R from global fits of the helicity amplitudes, with a 3σ significance. At large Q^2, the amplitude ratio T_{10}/T_{00} which involves the second single flip amplitude is found to exhibit a $|t|$ dependence. Finally, a non-zero value at large $|t|$ is found for the ratio T_{-11}/T_{00} which involves the double flip amplitude, an observation which may provide information on gluon polarisation in the proton. The phase between the T_{00} and T_{11} amplitudes is measured to be non-zero, which may suggest different W dependences of the transverse and longitudinal amplitudes.

The general features of the kinematic dependences of the cross sections and of the spin density matrix elements are understood qualitatively in QCD. In particular, the W and t dependences indicate that "hard", perturbative QCD features become dominant in the longitudinal cross section in the present kinematic domain, for $(Q^2+M_V^2)/4 \gtrsim 3-5\ \mathrm{GeV}^2$. The measurements are globally described by models using GPDs or a dipole approach, which differ in detail but agree on the gross features.

The study of VM production at HERA thus provides new insights for the understanding of QCD and the interplay of soft and hard diffraction.

Acknowledgements

We are grateful to the HERA machine group whose outstanding efforts have made this experiment possible. We thank the engineers and technicians for their work in constructing and maintaining the H1 detector, our funding agencies for financial support, the DESY technical staff for continual assistance, and the DESY directorate for the hospitality which they extend to the non-DESY members of the collaboration. We thank A. Bruni, J.-R. Cudell, M. Diehl, S.V. Goloskokov, D.Yu. Ivanov, I. Ivanov, R. Kirschner, P. Kroll, G. Soyez, M. Strikman, T. Teubner and G. Watt for useful discussions and for providing us with the predictions of their calculations.

Appendices

A Matrix elements; properties of the exchange

Matrix elements In the formalism of [106], the spin density matrix elements are normalised sums of products of two helicity amplitudes $T_{\lambda_\rho \lambda_{N'}, \lambda_\gamma \lambda_N}$ (see the definitions in Appendix B). They are given in the form r^i_{jk}, where the notation $^{(04)}$ of the upper index $^{(i)}$ denotes the combination of unpolarised transverse and longitudinal photons[9], the notations $^{(1)}$ and $^{(2)}$ are used for VM production by transverse photons with orthogonal linear polarisations, and $^{(5)}$ and $^{(6)}$ for the interference between VM production by transverse and longitudinal photons. The lower indices $_{(j,k)}$ refer to the VM helicities λ_V of the pair of amplitudes.

Angular distribution In the absence of longitudinal beam polarisation, 15 independent components of the spin density matrix can be measured (8 additional matrix elements are accessible with a longitudinally polarised lepton beam). They enter in the normalised angular distribution $W(\theta, \varphi, \phi)$:

$$
\begin{aligned}
W(\theta,\varphi,\phi) \;=\; & \frac{3}{4\pi}\;\Big\{\;\frac{1}{2}(1-r^{04}_{00})+\frac{1}{2}(3\,r^{04}_{00}-1)\;\cos^2\theta \\
- \;& \sqrt{2}\,\mathrm{Re}\,r^{04}_{10}\;\sin 2\theta\cos\varphi - r^{04}_{1-1}\;\sin^2\theta\cos 2\varphi \\
- \;& \varepsilon\;\cos 2\phi\,\Big(r^1_{11}\;\sin^2\theta + r^1_{00}\;\cos^2\theta - \sqrt{2}\,\mathrm{Re}\,r^1_{10}\;\sin 2\theta\cos\varphi \\
& \qquad\qquad - r^1_{1-1}\;\sin^2\theta\cos 2\varphi\,\Big) \\
- \;& \varepsilon\;\sin 2\phi\,\Big(\sqrt{2}\,\mathrm{Im}\,r^2_{10}\;\sin 2\theta\sin\varphi + \mathrm{Im}\,r^2_{1-1}\;\sin^2\theta\sin 2\varphi\Big) \\
+ \;& \sqrt{2\varepsilon\,(1+\varepsilon)}\;\cos\phi\;\Big(\,r^5_{11}\;\sin^2\theta + r^5_{00}\;\cos^2\theta \\
& \qquad\qquad -\sqrt{2}\,\mathrm{Re}\,r^5_{10}\;\sin 2\theta\cos\varphi - r^5_{1-1}\;\sin^2\theta\cos 2\varphi\,\Big) \\
+ \;& \sqrt{2\varepsilon\,(1+\varepsilon)}\;\sin\phi\;\Big(\sqrt{2}\,\mathrm{Im}\,r^6_{10}\;\sin 2\theta\sin\varphi \\
& \qquad\qquad +\mathrm{Im}\,r^6_{1-1}\;\sin^2\theta\sin 2\varphi\,\Big)\;\Big\}\,. \qquad (38)
\end{aligned}
$$

Measurement of the matrix elements The matrix elements are measured as projections of the normalised angular distribution, Eq. (38), onto orthogonal functions of the θ, φ and ϕ angles, with one specific function corresponding to each matrix element (see Appendix C of [106]). In practice, each matrix element is measured as the average value of the corresponding function, taken over all events in the data sample.

[9] The separation of the $^{(0)}$ and $^{(4)}$ components is only possible through measurements with different polarisation parameters ε, i.e. with different beam energies in the same detector configuration. In this case, 18 matrix elements in total can be measured.

Alternatively, fits to the projections of the angular distribution $W(\theta, \varphi, \phi)$ onto each of the three angles provide measurements of the matrix elements r^{04}_{00} and r^{04}_{1-1} and of the combinations $(r^5_{00} + 2r^5_{11})$ and $(r^1_{00} + 2r^1_{11})$:

$$W(\theta) \propto 1 - r^{04}_{00} + (3\, r^{04}_{00} - 1)\, \cos^2\theta \tag{39}$$

$$W(\varphi) \propto 1 - 2r^{04}_{1-1}\, \cos 2\varphi \tag{40}$$

$$W(\phi) \propto 1 + \sqrt{2\varepsilon(1+\varepsilon)} \cos\phi\, (r^5_{00} + 2r^5_{11}) - \varepsilon\, \cos 2\phi\, (r^1_{00} + 2r^1_{11}). \tag{41}$$

Natural parity exchange Natural parity exchange (NPE) in the t channel implies the following relations between amplitudes[10]:

$$T_{-\lambda_V \lambda_{N'}, -\lambda_\gamma \lambda_N} = (-1)^{\lambda_V - \lambda_\gamma}\, T_{\lambda_V \lambda_{N'}, \lambda_\gamma \lambda_N}. \tag{42}$$

For unnatural parity exchange, an additional factor (-1) appears in the right hand side of Eq. (42).

Under NPE and integrating over the nucleon polarisations, the number of independent $T_{\lambda_V \lambda_\gamma}$ amplitudes is reduced from 9 to 5: two helicity conserving amplitudes (T_{00} and $T_{11} = T_{-1-1}$), two single helicity flip amplitudes ($T_{01} = -T_{0-1}$ and $T_{10} = -T_{-10}$) and one double flip amplitude ($T_{-11} = T_{1-1}$).

In general, longitudinally polarised lepton beams are required to separate natural and unnatural parity exchange process. However, unpolarised beams allow the measurement of the asymmetry $P_{NPE,T}$ between natural (σ^N_T) and unnatural (σ^U_T) parity exchange for transverse photons:

$$P_{NPE,T} = \frac{\sigma^N_T - \sigma^U_T}{\sigma^N_T + \sigma^U_T} = 2 - r^{04}_{00} + 2r^{04}_{1-1} - 2r^1_{11} - 2r^1_{1-1}. \tag{43}$$

The measurement of the corresponding asymmetry for longitudinal photons requires different values of ε, i.e. different beam energies.

***s*-channel helicity conservation** In the approximation of s-channel helicity conservation (SCHC) [111], the helicity of the virtual photon (measured in the helicity frame defined in section 3.4) is retained by the final state VM (with the nucleon helicity also remaining unchanged). Single and double helicity flip amplitudes thus vanish ($T_{01} = T_{10} = T_{-11} = 0$) and only five matrix elements are non-zero:

$$r^{04}_{00}, \quad r^1_{1-1}, \quad \mathrm{Im}\, r^2_{1-1}, \quad \mathrm{Re}\, r^5_{10}, \quad \mathrm{Im}\, r^6_{10}; \tag{44}$$

Under SCHC and NPE, the following relations hold between these elements:

$$r^1_{1-1} = -\mathrm{Im}\, r^2_{1-1} = \frac{1}{2}\,(1 - r^{04}_{00}), \quad \mathrm{Re}\, r^5_{10} = -\mathrm{Im}\, r^6_{10}. \tag{45}$$

[10]More precisely, Eq. (42) implies that, for $|t| = |t|_{min}$, the trajectory exchanged in the t channel has natural parity.

In the case of SCHC, only two independent parameters are left, conveniently chosen as the cross section ratio $R = \sigma_L/\sigma_T$ and the phase δ between the T_{00} and T_{11} amplitudes, with

$$T_{00}\, T_{11}^{*} = |T_{00}|\, |T_{11}|\, e^{-i\delta}. \tag{46}$$

The angular distribution $W(\theta, \varphi, \phi)$ then reduces to a function of θ and $\psi = \phi - \varphi$, the angle between the electron scattering plane and the ρ meson decay plane, in the $\gamma^* p$ frame:

$$\begin{aligned} W(\cos\theta, \psi) &= \frac{3}{8\pi}\, \frac{1}{1+\varepsilon\, R}\, \Big\{ \sin^2\theta\, (1 + \varepsilon\, \cos 2\psi) \\ &+ 2\, \varepsilon\, R\, \cos^2\theta - \sqrt{2\varepsilon\, (1+\varepsilon)\, R}\, \cos\delta \sin 2\theta \cos\psi \Big\}. \end{aligned} \tag{47}$$

In the SCHC approximation, the cross section ratio R is obtained from the measurement of the matrix element r^{04}_{00}, as given by Eq. (28).

Dominant helicity flip amplitude T_{01} The precision of measurements performed in the SCHC approximation, especially at large $|t|$, can be improved by retaining the dominant helicity flip amplitude T_{01}. Five additional matrix elements are then non-zero, supplementing the five elements given in Eq. (44):

$$\mathrm{Re}\, r^{04}_{10}, \quad r^{1}_{00}, \quad \mathrm{Re}\, r^{1}_{10}, \quad \mathrm{Im}\, r^{2}_{10}, \quad r^{5}_{00}. \tag{48}$$

Under NPE, the following relations hold in addition to the SCHC relations (45):

$$\mathrm{Re}\, r^{04}_{10} = -\mathrm{Re}\, r^{1}_{10} = \mathrm{Im}\, r^{2}_{10}. \tag{49}$$

Assuming that the amplitudes are in phase, an improved approximation of the cross section ratio R is given by Eq. (29), which uses the matrix elements r^{04}_{00} and r^{5}_{00}.

B Definition of the matrix elements in terms of helicity amplitudes

The spin density matrix elements relevant for VM electroproduction with unpolarised lepton beam are given in terms of the helicity amplitudes $T_{\lambda_V \lambda_\gamma}$ [106] (natural parity exchange is not assumed):

$$r_{00}^{04} = \frac{1}{1+\varepsilon R}\left[\frac{1}{2N_T}\left(|T_{01}|^2+|T_{0-1}|^2\right)+\frac{\varepsilon R}{N_L}|T_{00}|^2\right] \quad (50)$$

$$\mathrm{Re}\, r_{10}^{04} = \frac{1}{1+\varepsilon R}\,\mathrm{Re}\left[\frac{1}{2N_T}\left(T_{11}T_{01}^{\dagger}+T_{1-1}T_{0-1}^{\dagger}\right)+\frac{\varepsilon R}{N_L}T_{10}T_{00}^{\dagger}\right] \quad (51)$$

$$r_{1-1}^{04} = \frac{1}{1+\varepsilon R}\left[\frac{1}{2N_T}\left(T_{11}T_{-11}^{\dagger}+T_{1-1}T_{-1-1}^{\dagger}\right)+\frac{\varepsilon R}{N_L}T_{10}T_{-10}^{\dagger}\right] \quad (52)$$

$$r_{00}^{1} = \frac{1}{1+\varepsilon R}\,\frac{1}{2N_T}\left(T_{0-1}T_{01}^{\dagger}+T_{01}T_{0-1}^{\dagger}\right) \quad (53)$$

$$r_{11}^{1} = \frac{1}{1+\varepsilon R}\,\frac{1}{2N_T}\left(T_{1-1}T_{11}^{\dagger}+T_{11}T_{1-1}^{\dagger}\right) \quad (54)$$

$$\mathrm{Re}\, r_{10}^{1} = \frac{1}{1+\varepsilon R}\,\frac{1}{2N_T}\,\mathrm{Re}\left(T_{1-1}T_{01}^{\dagger}+T_{11}T_{0-1}^{\dagger}\right) \quad (55)$$

$$r_{1-1}^{1} = \frac{1}{1+\varepsilon R}\,\frac{1}{2N_T}\left(T_{1-1}T_{-11}^{\dagger}+T_{11}T_{-1-1}^{\dagger}\right) \quad (56)$$

$$\mathrm{Im}\, r_{10}^{2} = \frac{1}{1+\varepsilon R}\,\frac{1}{2N_T}\,\mathrm{Re}\left(T_{1-1}T_{01}^{\dagger}-T_{11}T_{0-1}^{\dagger}\right) \quad (57)$$

$$\mathrm{Im}\, r_{1-1}^{2} = \frac{1}{1+\varepsilon R}\,\frac{1}{2N_T}\,\mathrm{Re}\left(T_{1-1}T_{-11}^{\dagger}-T_{11}T_{-1-1}^{\dagger}\right) \quad (58)$$

$$r_{00}^{5} = \frac{\sqrt{R}}{1+\varepsilon R}\,\frac{1}{\sqrt{2N_TN_L}}\left[\mathrm{Re}\left(T_{00}T_{01}^{\dagger}\right)-\mathrm{Re}\left(T_{00}T_{0-1}^{\dagger}\right)\right] \quad (59)$$

$$r_{11}^{5} = \frac{\sqrt{R}}{1+\varepsilon R}\,\frac{1}{\sqrt{2N_TN_L}}\left[\mathrm{Re}\left(T_{10}T_{11}^{\dagger}\right)-\mathrm{Re}\left(T_{10}T_{1-1}^{\dagger}\right)\right] \quad (60)$$

$$\mathrm{Re}\, r_{10}^{5} = \frac{\sqrt{R}}{1+\varepsilon R}\,\frac{1}{\sqrt{2N_TN_L}}\frac{1}{2}\mathrm{Re}\left(T_{10}T_{01}^{\dagger}+T_{11}T_{00}^{\dagger}-T_{10}T_{0-1}^{\dagger}-T_{1-1}T_{00}^{\dagger}\right) \quad (61)$$

$$r_{1-1}^{5} = \frac{\sqrt{R}}{1+\varepsilon R}\,\frac{1}{\sqrt{2N_TN_L}}\frac{1}{2}\left(T_{10}T_{-11}^{\dagger}+T_{11}T_{-10}^{\dagger}-T_{10}T_{-1-1}^{\dagger}-T_{1-1}T_{-10}^{\dagger}\right) \quad (62)$$

$$\mathrm{Im}\, r_{10}^{6} = \frac{\sqrt{R}}{1+\varepsilon R}\,\frac{1}{\sqrt{2N_TN_L}}\frac{1}{2}\mathrm{Re}\left(T_{10}T_{01}^{\dagger}-T_{11}T_{00}^{\dagger}+T_{10}T_{0-1}^{\dagger}-T_{1-1}T_{00}^{\dagger}\right) \quad (63)$$

$$\mathrm{Im}\, r_{1-1}^{6} = \frac{\sqrt{R}}{1+\varepsilon R}\,\frac{1}{\sqrt{2N_TN_L}}\frac{1}{2}\mathrm{Re}\left(T_{10}T_{-11}^{\dagger}-T_{11}T_{-10}^{\dagger}+T_{10}T_{-1-1}^{\dagger}-T_{1-1}T_{-10}^{\dagger}\right), \quad (64)$$

where R is the longitudinal to transverse cross section ratio,

$$R = \frac{N_L}{N_T}, \quad (65)$$

and

$$N_L = |T_{00}|^2+|T_{10}|^2+|T_{-10}|^2 \quad (66)$$

$$N_T = \frac{1}{2}\left[|T_{11}|^2+|T_{-1-1}|^2+|T_{01}|^2+|T_{0-1}|^2+|T_{-11}|^2+|T_{1-1}|^2\right]. \quad (67)$$

C Approximate relations

Assuming natural parity exchange and purely imaginary amplitudes, the spin density matrix elements relevant for VM electroproduction with unpolarised lepton beam are given in terms of amplitude ratios by [48, 106]

$$
\begin{aligned}
r^{04}_{00} &= B\,(\varepsilon+\beta^2) && (68)\\
\mathrm{Re}\, r^{04}_{10} &= B/2\,(2\varepsilon\delta+\beta\alpha-\beta\eta) && (69)\\
r^{04}_{1-1} &= B\,(\alpha\eta-\varepsilon\delta^2) && (70)\\
r^{1}_{00} &= -B\,\beta^2 && (71)\\
r^{1}_{11} &= B\,\alpha\eta && (72)\\
\mathrm{Re}\, r^{1}_{10} &= B/2\,\beta(\eta-\alpha) && (73)\\
r^{1}_{1-1} &= B/2\,(\alpha^2+\eta^2) && (74)\\
\mathrm{Im}\, r^{2}_{10} &= B/2\,\beta(\alpha+\eta) && (75)\\
\mathrm{Im}\, r^{2}_{1-1} &= B/2\,(\eta^2-\alpha^2) && (76)\\
r^{5}_{00} &= \sqrt{2}B\,\beta && (77)\\
r^{5}_{11} &= B/\sqrt{2}\,\delta(\alpha-\eta) && (78)\\
\mathrm{Re}\, r^{5}_{10} &= B/(2\sqrt{2})\,(2\beta\delta+\alpha-\eta) && (79)\\
r^{5}_{1-1} &= B/\sqrt{2}\,\delta(\eta-\alpha) && (80)\\
\mathrm{Im}\, r^{6}_{10} &= -B/(2\sqrt{2})\,(\alpha+\eta) && (81)\\
\mathrm{Im}\, r^{6}_{1-1} &= B/\sqrt{2}\,\delta(\alpha+\eta), && (82)
\end{aligned}
$$

where

$$
\begin{aligned}
\alpha &= T_{11}/T_{00} && (83)\\
\beta &= T_{01}/T_{00} && (84)\\
\delta &= T_{10}/T_{00} && (85)\\
\eta &= T_{-11}/T_{00} && (86)
\end{aligned}
$$

and

$$
\begin{aligned}
B &= \frac{1}{N_T+\varepsilon N_L} && (87)\\
N_T &= \alpha^2+\beta^2+\eta^2 && (88)\\
N_L &= 1+2\delta^2. && (89)
\end{aligned}
$$

References

[1] P. D. B. Collins, "An Introduction to Regge Theory and High-Energy Physics", Cambridge, 1977.

[2] M. L. Good and W. D. Walker, Phys. Rev. **120** (1960) 1857.

[3] S. Aid *et al.* [H1 Collaboration], Nucl. Phys. **B468** (1996) 3 [hep-ex/9602007].

[4] C. Adloff *et al.* [H1 Collaboration], Eur. Phys. J. **C13** (2000) 371 [hep-ex/9902019].

[5] C. Adloff *et al.* [H1 Collaboration], Phys. Lett. **B539** (2002) 25 [hep-ex/0203022].

[6] C. Adloff *et al.* [H1 Collaboration], Z. Phys. **C75** (1997) 607 [hep-ex/9705014].

[7] C. Adloff *et al.* [H1 Collaboration], Phys. Lett. **B483** (2000) 360 [hep-ex/0005010].

[8] F.D. Aaron *et al.* [H1 Collaboration], Phys. Lett. **B672** (2009) 219 [arXiv:0810.3096].

[9] F.D. Aaron *et al.*, [H1 Collaboration], Phys. Lett. **B659** (2008) 796 [arXiv:0709.4114]; F.D. Aaron *et al.*, [H1 Collaboration], DESY-09-109, accepted for publication by Phys. Lett. **B**, arXiv:0907.5289.

[10] S. Aid *et al.* [H1 Collaboration], Nucl. Phys. **B463** (1996) 3 [hep-ex/9601004].

[11] A. Aktas *et al.* [H1 Collaboration], Phys. Lett. **B 638** (2006) 422 [hep-ex/0603038].

[12] A. Aktas *et al.* [H1 Collaboration], Eur. Phys. J. **C46** (2006) 585 [hep-ex/0510016].

[13] A. Aktas *et al.* [H1 Collaboration], Phys. Lett. **B568** (2003) 205 [hep-ex/0306013].

[14] C. Adloff *et al.* [H1 Collaboration], Phys. Lett. **B541** (2002) 251 [hep-ex/0205107].

[15] C. Adloff *et al.* [H1 Collaboration], Phys. Lett. **B483** (2000) 23 [hep-ex/0003020].

[16] S. Chekanov *et al.* [ZEUS Collaboration], Phys. Lett. **B 573** (2003) 46 [hep-ex/0305028].

[17] J. Breitweg *et al.* [ZEUS Collaboration], Eur. Phys. J. **C14** (2000) 213 [hep-ex/9910038]; *idem*, Eur. Phys. J. **C2** (1998) 247 [hep-ex/9712020];
M. Derrick *et al.* [ZEUS Collaboration], Z. Phys. **C73** (1997) 253 [hep-ex/9609003]; *idem*, Z. Phys. **C69** (1995) 39 [hep-ex/9507011].

[18] J. Breitweg *et al.* [ZEUS Collaboration], Eur. Phys. J. **C6** (1999) 603 [hep-ex/9808020]; J. Breitweg *et al.* [ZEUS Collaboration], Eur. Phys. J. **C12** (2000) 393 [hep-ex/9908026].

[19] S. Chekanov *et al.* [ZEUS Collaboration], PMC Phys. **A1** (2007) 6 [arXiv:0708.1478].

[20] S. Chekanov *et al.* [ZEUS Collaboration], Eur. Phys. J. **C26** (2003) 389 [hep-ex/0205081].

[21] M. Derrick *et al.* [ZEUS Collaboration], Z. Phys. **C73** (1996) 73 [hep-ex/9608010].

[22] J. Breitweg *et al.* [ZEUS Collaboration], Phys. Lett. **B487** (2000) 273 [hep-ex/0006013].

[23] M. Derrick *et al.* [ZEUS Collaboration], Phys. Lett. **B 377** (1996) 259 [hep-ex/9601009].

[24] S. Chekanov *et al.* [ZEUS Collaboration], Nucl. Phys. **B 718** (2005) 3 [hep-ex/0504010].

[25] S. Chekanov *et al.* [ZEUS Collaboration], Eur. Phys. J. **C24** (2002) 345 [hep-ex/0201043].

[26] S. Chekanov *et al.* [ZEUS Collaboration], Nucl. Phys. **B 695** (2004) 3 [hep-ex/0404008].

[27] S. Chekanov *et al.* [ZEUS Collaboration], DESY-09-137, submitted to JHEP, arXiv:0910.1235.

[28] J. Breitweg *et al.* [ZEUS Collaboration], Phys. Lett. **B437** (1998) 432 [hep-ex/9807020];
S. Chekanov *et al.* [ZEUS Collaboration], Phys. Lett. **B680** (2009) 4 [arXiv:0903.4205].

[29] P. Joos *et al.* [DESY-Glasgow Collaboration], Nucl. Phys. **B113** (1976) 53.

[30] W.D. Shambroom *et al.* [CHIO Collaboration], Phys. Rev. **D26** (1982) 1.

[31] P. Amaudruz *et al.* [NMC Collaboration], Z. Phys **C54** (1992) 239;
M. Arneodo *et al.* [NMC Collaboration], Nucl. Phys. **B429** (1994) 503.

[32] M.R. Adams *et al.* [E665 Collaboration], Z. Phys **C74** (1997) 237.

[33] A. Airapetian *et al.* [HERMES Collaboration], Eur. Phys. J. **C17** (2000) 389;
K. Ackerstaff *et al.* [HERMES Collaboration], Eur. Phys. J. **C18** (2000) 303;
A. Airapetian *et al.* [HERMES Collaboration], Eur. Phys. J. **C62** (2009) 659 [arXiv:0901.0701].

[34] T.H. Bauer *et al.*, Rev. Mod. Phys. **50** (1978) 261.

[35] M. Derrick *et al.* [ZEUS Collaboration], Phys. Lett. **B315** (1993) 481;
T. Ahmed *et al.* [H1 Collaboration], Nucl. Phys. **B429** (1994) 477.

[36] J. Collins, L. Frankfurt and M. Strikman, Phys. Rev. **D56** (1997) 2982.

[37] A. Donnachie and P.V. Landshoff, Phys. Lett. **B185** (1987) 403;
idem, Nucl. Phys. **B311** (1989) 509.

[38] B.Z. Kopeliovich and B.G. Zakharov, Phys. Rev. **D44** (1991), 3466;
B.Z. Kopeliovich, J. Nemchik, N.N. Nikolaev and B.G. Zakharov, Phys. Lett. **B309** (1993) 179;
idem, Phys. Lett. **B324** (1994) 469.

[39] J. Nemchik, N.N. Nikolaev and B.G. Zakharov, Phys. Lett. **B341** (1994) 228.

[40] J. Nemchik, N.N. Nikolaev, E. Predazzi and B.G. Zakharov, Z. Phys. **C75** (1997) 71.

[41] M.G. Ryskin, Z. Phys. **C57** (1993) 89.

[42] S. Brodsky *et al.*, Phys. Rev. **D50** (1994) 3134.

[43] L. Frankfurt, W. Koepf and M. Strikman, Phys. Rev. **D54** (1996) 3194.

[44] H.G. Dosch, T. Gousset, G. Kulzinger and H.J. Pirner, Phys. Rev. **D55** (1997) 2602.

[45] A.D. Martin, M.G. Ryskin and T. Teubner, Phys. Rev. **D55** (1997) 4329.

[46] A.D. Martin, M.G. Ryskin and T. Teubner, Phys. Rev. **D62** (2000) 014022.

[47] E. Gotsman, E. Levin and U. Maor, Phys. Lett. **B425** (1998) 369.

[48] D.Yu. Ivanov and R. Kirschner, Phys. Rev. **D58** (1998) 114026.

[49] I. Royen and J.-R. Cudell, Nucl. Phys. **B545** (1999) 505;
I. Royen, Phys. Lett. **B513** (2001) 337.

[50] D. Schildknecht, G.A. Schuler and B. Surrow, Phys. Lett. **B449** (1999) 328;
G. Cvetic, D. Schildknecht, B. Surrow and M. Tentyukov, Eur. Phys. J. **C20** (2001) 77.

[51] M. McDermott, L. Frankfurt, V. Guzey and M. Strikman, Eur. Phys. J. **C16** (2000) 641.

[52] A.C. Caldwell and M.S. Soares, Nucl. Phys. **A696** (2001) 125.

[53] A. Donnachie, J. Gravelis and G. Shaw, Phys. Rev. **D63** (2001) 114013.

[54] L. Frankfurt and M. Strikman, Phys. Rev. **D66** (2002) 031502

[55] J.R. Forshaw and G. Shaw, JHEP **0412** (2004) 052.

[56] J.R. Forshaw, R. Sandapen and G. Shaw, Phys. Rev **D69** (2004) 094013;
idem, JHEP **0611** (2006) 025.

[57] D.Yu. Ivanov, A. Schaefer, L. Szymanowski and G. Krasnikov, Eur. Phys. J. **C34** (2004) 297;
D. Yu. Ivanov, L. Szymanowski and G. Krasnikov, JETP Lett. **80** (2004) 226.

[58] D.Yu. Ivanov, M.I. Kotsky and A. Papa, Eur. Phys. J. **C38** (2004) 195.

[59] H. Kowalski, L. Motyka and G. Watt, Phys. Rev. **D74** (2006) 074016.

[60] H.G. Dosch and E. Ferreira, Eur. Phys. J. **C51** (2007) 83.

[61] S.V. Goloskokov and P. Kroll, Eur. Phys. J. **C53** (2008) 367.

[62] C. Marquet, R. Peschanski and G. Soyez, Phys. Rev. **D76** (2007) 034011.

[63] N. Warkentin, M. Diehl, D.Yu. Ivanov and A. Schaefer, Eur. Phys. J. **A32** (2007) 273.

[64] L. Frankfurt, M. Strikman and C. Weiss, Ann. Rev. Nucl. Part. Sci. **55** (2005) 403.

[65] I.P. Ivanov, N.N. Nikolaev and A.A. Savin, Phys. Part. Nucl. **37** (2006) 1.

[66] M. Diehl, Phys. Rep. **388** (2003) 41;
A.V. Belitsky and A.V. Radyushkin, Phys. Rep. **418** (2005) 1.

[67] A.H. Mueller, Nucl. Phys. **B335** (1990) 115.

[68] N.N. Nikolaev and B.G. Zakharov, Z. Phys. **C49** (1991) 607;
idem, Z. Phys. **C53** (1992) 331.

[69] A.B. Zamolodchikov, B.Z. Kopeliovich and L.I. Lapidus, JETP Lett. **33** (1981) 595;
G. Bertsch, S.J. Brodsky, A.S. Goldhaber and J.R. Gunion, Phys. Rev. Lett. **47** (1981) 267.

[70] F.E. Low, Phys. Rev. **D12** (1975) 163;
S. Nussinov, Phys. Rev. Lett. **34** (1975) 1268.

[71] A.G. Shuvaev, K.J. Golec-Biernat, A.D. Martin and M.G. Ryskin, Phys. Rev. **D60** (1999) 014015.

[72] S. Munier, A.M. Staśto and A.H. Mueller, Nucl. Phys. **B603** (2001) 427.

[73] K.J. Golec-Biernat and M. Wüsthoff, Phys. Rev. **D59** (1999) 014017;
idem, Phys. Rev. **D60** (1999) 114023.

[74] E. Iancu, K. Itakura and S. Munier, Phys. Lett. **B590** (2004) 199.

[75] C. Adloff *et al.* [H1 Collaboration], Phys. Lett. **B520** (2001) 183 [hep-ex/0108035].

[76] A. Donnachie and P.V. Landshoff, Phys. Lett. **B437** (1998) 408;
idem, Phys. Lett. **B518** (2001) 63.

[77] J. Pumplin *et al.* [CTEQ Collaboration], JHEP **0207** (2002) 012 [hep-ph/0201195];
idem, JHEP **0702** (2007) 053 [hep-ph/0611254].

[78] A.D. Martin, W.J. Stirling and R.S. Thorne, Phys. Lett. **B636** (2006) 259 [hep-ph/0603143].

[79] J. Bartels, K.J. Golec-Biernat and K. Peters, Acta Phys. Polon. **B34** (2003) 3051.

[80] I. Abt *et al.* [H1 Collaboration], Nucl. Instr. Meth. **A386** (1997) 310 and 348;
R. D. Appuhn *et al.* [H1 SPACAL Group Collaboration], Nucl. Instr. Meth. **A386** (1997) 397.

[81] D. Pitzl *et al.*, Nucl. Instrum. Meth. **A454** (2000) 334.

[82] S. Bentvelsen, J. Engelen and P. Kooijman, in Proc. of the Workshop on Physics at HERA, W. Buchmüller and G. Ingelman ed., Hamburg (1992) 23;
K.C. Hoeger, *ibid.*, p 43.

[83] F. Jacquet and A. Blondel, DESY 79-048 (1979) 377.

[84] C. Amsler *et al.* [Particle Data Group], Phys. Lett. **667** (2008) 1.

[85] T. Abe, Comput. Phys. Comm. **136** (2001) 126.

[86] B. List and A. Mastroberardino, in Proc. of the Workshop on Monte Carlo Generators for HERA Physics, A.T. Doyle *et al.* ed., DESY-PROC-1999-02 (1999) 396.

[87] H. Fraas and D. Schildknecht, Nucl. Phys. **B14** (1969) 543.

[88] K. Goulianos, Phys. Rep. **101** (1983) 169.

[89] T. Sjöstrand, Comput. Phys. Comm. **82** (1994) 74.

[90] C. Collard, PhD Thesis, Université Libre de Bruxelles (ULB) (2002), appendix A, http://www-h1.desy.de/psfiles/theses/h1th-296.ps.

[91] M. Ross and L. Stodolsky, Phys. Rev. **149** (1966) 1172.

[92] A. Kwiatkowski, H.-J. Möhring and H. Spiesberger, Comput. Phys. Comm. **69** (1992), 155; *idem*, Proc. of the Workshop on Physics at HERA, W. Buchmüller and G. Ingelman ed., Hamburg (1992) 1294.

[93] GEANT 3, R. Brun *et al.*, CERN-DD/EE/84-1.

[94] V.M. Budnev *et al.*, Phys. Rep. **15** (1974) 181.

[95] L.N. Hand., Phys. Rev. **129** (1963) 1834.

[96] J.D. Jackson, Nuov. Cim. **34** (1964) 1644.

[97] P. Söding, Phys. Lett. **19** (1966) 702.

[98] M.G. Ryskin and Yu.M. Shabelski, Phys. Atom. Nucl. **62** (1999) 980 [Yad. Fiz. **62** (1999) 1047].

[99] M.G. Ryskin and Yu.M. Shabelski, Phys. Atom. Nucl. **61** (1998) 81 [Yad. Fiz. **61** (1998) 89];
Fig. 6 is corrected in: M.G. Ryskin and Yu.M. Shabelski, hep-ph/9704279 (1997).

[100] A. Bruni, X. Janssen and P. Marage, in Proc. of the HERA-LHC Workshop, Geneva, 2009 [hep-ph/0812.0539].

[101] I. Ivanov, private communication.

[102] A. Donnachie and P.V. Landshoff, Phys. Lett. **B296** (1992) 227;
J.-R. Cudell, K. Kang and S. Kim, Phys. Lett. **B395** (1997) 311.

[103] G.A. Jaroszkiewicz and P.V. Landshoff, Phys. Rev. **D10** (1974) 170;
A. Donnachie and P.V. Landshoff, Nucl. Phys. **B231** (1984) 189.

[104] D. Aston *et al.* [OMEGA Collaboration], Nucl. Phys. **B209** (1982) 56.

[105] A. Aktas *et al.* [H1 Collaboration], Eur. Phys. J. **C48** (2006) 749 [hep-ex/0606003].

[106] K. Schilling and G. Wolf, Nucl. Phys. **B61** (1973) 381.

[107] T. Teubner, private communication.

[108] D. Yu. Ivanov, private communication.

[109] S.V. Goloskokov and P. Kroll, Eur. Phys. J. **C42** (2005) 281.

[110] P. Kroll, private communication.

[111] F.J. Gilman *et al.*, Phys. Lett. **B31** (1970) 387.

Q^2 (GeV^2)	f_I			n		
3.3	-0.470	$\pm\ 0.049$	$^{+0.018}_{-0.017}$	1.73	$\pm\ 0.21$	$^{+0.07}_{-0.07}$
6.5	-0.270	$\pm\ 0.059$	$^{+0.019}_{-0.015}$	0.91	$\pm\ 0.24$	$^{+0.06}_{-0.08}$
11.9	-0.351	$\pm\ 0.095$	$^{+0.017}_{-0.020}$	1.27	$\pm\ 0.39$	$^{+0.09}_{-0.07}$
23.0	-0.100	$\pm\ 0.090$	$^{+0.009}_{-0.018}$	0.20	$\pm\ 0.37$	$^{+0.08}_{-0.04}$

Table 14: Q^2 dependence, for elastic ρ meson production, of the Söding skewing parameter f_I defined in Eq. (13) and of the Ross-Stodolsky parameter n defined in Eq. (6).

Q^2 (GeV^2)	$\sigma(\gamma^* p \to \rho p)$ (nb)		
2.65	563	$\pm\ 32$	$^{+59}_{-45}$
2.95	423	$\pm\ 24$	$^{+49}_{-34}$
3.30	383	$\pm\ 20$	$^{+43}_{-30}$
3.70	295	$\pm\ 17$	$^{+33}_{-25}$
4.15	232	$\pm\ 16$	$^{+27}_{-17}$
4.65	198	$\pm\ 13$	$^{+20}_{-19}$
5.20	154	$\pm\ 9$	$^{+17}_{-8}$
5.85	131	$\pm\ 9$	$^{+12}_{-7}$
6.55	102	$\pm\ 8$	$^{+8}_{-7}$
7.35	79.1	$\pm\ 6.4$	$^{+6.6}_{-3.6}$
8.20	56.5	$\pm\ 4.3$	$^{+5.5}_{-2.2}$
9.20	53.0	$\pm\ 3.9$	$^{+4.2}_{-3.7}$
10.3	39.3	$\pm\ 3.9$	$^{+4.2}_{-2.8}$
11.5	30.8	$\pm\ 2.9$	$^{+2.8}_{-2.5}$
12.9	25.8	$\pm\ 2.2$	$^{+2.7}_{-1.7}$
14.5	15.7	$\pm\ 1.3$	$^{+1.7}_{-1.2}$
16.5	12.5	$\pm\ 1.0$	$^{+1.3}_{-1.1}$
18.8	9.22	$\pm\ 0.82$	$^{+1.11}_{-0.80}$
21.7	5.99	$\pm\ 0.58$	$^{+0.67}_{-0.55}$
25.0	3.54	$\pm\ 0.42$	$^{+0.39}_{-0.31}$
29.3	2.24	$\pm\ 0.31$	$^{+0.31}_{-0.28}$
35.0	1.68	$\pm\ 0.27$	$^{+0.24}_{-0.21}$
46.0	0.742	$\pm\ 0.105$	$^{+0.101}_{-0.088}$

Table 15: Q^2 dependence of the $\gamma^* p$ cross section for elastic ρ meson production for $W = 75$ GeV. The overall normalisation uncertainty of 3.9% is not included in the systematic errors.

Q^2 (GeV^2)	$\sigma(\gamma^* p \to \rho Y)$ (nb)		
2.71	314	$\pm$ 32	$^{+45}_{-35}$
3.21	217	$\pm$ 20	$^{+29}_{-24}$
3.82	182	$\pm$ 16	$^{+26}_{-17}$
4.52	131	$\pm$ 13	$^{+17}_{-16}$
5.36	57.7	$\pm$ 6.2	$^{+6.8}_{-6.0}$
6.35	50.5	$\pm$ 5.7	$^{+6.5}_{-4.9}$
7.60	40.4	$\pm$ 4.6	$^{+5.1}_{-3.7}$
9.30	25.9	$\pm$ 2.3	$^{+3.0}_{-2.3}$
12.00	17.0	$\pm$ 1.8	$^{+2.3}_{-1.7}$
14.85	10.8	$\pm$ 1.4	$^{+1.2}_{-1.2}$
19.20	3.39	$\pm$ 0.45	$^{+0.53}_{-0.56}$
32.15	1.01	$\pm$ 0.12	$^{+0.16}_{-0.16}$

Table 16: Q^2 dependence of the $\gamma^* p$ cross section for proton dissociative ρ meson production for $W = 75$ GeV. The overall normalisation uncertainty of 4.6% is not included in the systematic errors.

Q^2 (GeV^2)	$\sigma(\gamma^* p \to \phi p)$ (nb)		
2.71	72.6	$\pm$ 8.5	$^{+10.6}_{-7.6}$
3.21	64.5	$\pm$ 6.2	$^{+8.3}_{-6.0}$
3.82	46.4	$\pm$ 4.5	$^{+5.2}_{-3.6}$
4.52	35.0	$\pm$ 4.0	$^{+4.1}_{-3.4}$
5.36	25.1	$\pm$ 2.7	$^{+2.6}_{-1.4}$
6.35	18.2	$\pm$ 2.0	$^{+1.9}_{-1.5}$
7.60	12.6	$\pm$ 1.5	$^{+1.2}_{-0.7}$
9.30	7.04	$\pm$ 0.90	$^{+0.78}_{-0.52}$
12.00	5.34	$\pm$ 0.63	$^{+0.56}_{-0.37}$
14.85	2.25	$\pm$ 0.38	$^{+0.30}_{-0.21}$
19.20	1.28	$\pm$ 0.24	$^{+0.17}_{-0.13}$
32.15	0.371	$\pm$ 0.076	$^{+0.049}_{-0.042}$

Table 17: Q^2 dependence of the $\gamma^* p$ cross section for elastic ϕ meson production for $W = 75$ GeV. The overall normalisation uncertainty of 4.7% is not included in the systematic errors.

Q^2 (GeV^2)	$\sigma(\gamma^* p \to \phi Y)$ (nb)		
3.3	33.4	$\pm$ 5.1	$^{+6.9}_{-4.2}$
6.6	8.04	$\pm$ 0.89	$^{+0.93}_{-1.04}$
11.9	2.66	$\pm$ 0.51	$^{+0.31}_{-0.33}$
18.6	0.779	$\pm$ 0.216	$^{+0.115}_{-0.141}$
31.3	0.273	$\pm$ 0.090	$^{+0.034}_{-0.038}$

Table 18: Q^2 dependence of the $\gamma^* p$ cross section for proton dissociative ρ meson production for $W = 75$ GeV. The overall normalisation uncertainty of 5.3% is not included in the systematic errors.

Q^2 (GeV^2)	$\sigma(\gamma^* p \to \phi p)/\sigma(\gamma^* p \to \rho p)$			$Q^2 + M^2$ (GeV^2)	$\sigma(\gamma^* p \to \phi p)/\sigma(\gamma^* p \to \rho p)$		
2.9	0.148	$\pm$ 0.012	$^{+0.011}_{-0.009}$	3.94	0.186	$\pm$ 0.015	$^{+0.014}_{-0.012}$
4.1	0.171	$\pm$ 0.014	$^{+0.009}_{-0.007}$	5.14	0.205	$\pm$ 0.017	$^{+0.011}_{-0.008}$
6.6	0.169	$\pm$ 0.011	$^{+0.007}_{-0.005}$	7.64	0.192	$\pm$ 0.013	$^{+0.008}_{-0.005}$
11.9	0.171	$\pm$ 0.018	$^{+0.007}_{-0.005}$	12.94	0.185	$\pm$ 0.019	$^{+0.007}_{-0.005}$
18.6	0.146	$\pm$ 0.025	$^{+0.009}_{-0.006}$	19.64	0.154	$\pm$ 0.027	$^{+0.010}_{-0.007}$
31.3	0.187	$\pm$ 0.047	$^{+0.010}_{-0.009}$	32.34	0.195	$\pm$ 0.049	$^{+0.010}_{-0.009}$

Table 19: Ratio of the ϕ to ρ elastic production cross sections for $W = 75$ GeV, as a function of Q^2 and of $(Q^2 + M_V^2)$. The overall normalisation uncertainty of 4.0% is not included in the systematic errors.

Q^2 (GeV^2)	$\sigma_L(\gamma^* p \to \rho p)$ (nb)			$\sigma_T(\gamma^* p \to \rho p)$ (nb)		
2.9	180	$\pm$ 11	$^{+23}_{-17}$	288	$\pm$ 26	$^{+29}_{-20}$
4.1	78.1	$\pm$ 5.5	$^{+10.2}_{-8.2}$	165	$\pm$ 17	$^{+17}_{-12}$
6.6	23.7	$\pm$ 1.6	$^{+3.1}_{-2.1}$	74.7	$\pm$ 6.9	$^{+5.6}_{-3.2}$
11.9	5.0	$\pm$ 0.6	$^{+0.7}_{-0.5}$	24.0	$\pm$ 3.4	$^{+2.3}_{-1.6}$
18.6	1.49	$\pm$ 0.25	$^{+0.30}_{-0.27}$	7.7	$\pm$ 1.8	$^{+0.9}_{-0.7}$
31.3	0.27	$\pm$ 0.06	$^{+0.05}_{-0.05}$	1.76	$\pm$ 0.49	$^{+0.20}_{-0.17}$

Table 20: Q^2 dependence of the longitudinal and transverse $\gamma^* p$ cross sections for elastic ρ meson production with $W = 75$ GeV. The overall normalisation uncertainty of 3.9% is not included in the systematic errors.

Q^2 (GeV^2)	$\sigma_L(\gamma^* p \to \phi p)$ (nb)			$\sigma_T(\gamma^* p \to \phi p)$ (nb)		
3.3	19.6	$\pm$ 2.4	$^{+2.9}_{-2.1}$	38.1	$\pm$ 7.3	$^{+4.1}_{-2.9}$
6.6	3.8	$\pm$ 0.5	$^{+0.6}_{-0.5}$	12.8	$\pm$ 2.6	$^{+1.1}_{-0.6}$
15.8	0.34	$\pm$ 0.10	$^{+0.07}_{-0.06}$	2.2	$\pm$ 1.0	$^{+0.3}_{-0.2}$

Table 21: Q^2 dependence of the longitudinal and transverse $\gamma^* p$ cross sections for elastic ϕ meson production with $W = 75$ GeV. The overall normalisation uncertainty of 4.7% is not included in the systematic errors.

Q^2 (GeV^2)	W (GeV)	$\sigma(\gamma^* p \to \rho p)$ (nb)		
3.3	41	308	$\pm$ 14	$^{+30}_{-16}$
3.3	54	294	$\pm$ 16	$^{+26}_{-17}$
3.3	67	346	$\pm$ 19	$^{+30}_{-21}$
3.3	80	416	$\pm$ 23	$^{+40}_{-27}$
3.3	93	397	$\pm$ 27	$^{+40}_{-25}$
6.6	48	72.6	$\pm$ 4.3	$^{+7.8}_{-4.2}$
6.6	64	97.2	$\pm$ 5.9	$^{+9.4}_{-5.5}$
6.6	80	99.3	$\pm$ 6.2	$^{+7.2}_{-5.0}$
6.6	96	120	$\pm$ 9	$^{+10}_{-6}$
6.6	114	115	$\pm$ 10	$^{+10}_{-6}$
11.9	59	25.3	$\pm$ 2.6	$^{+2.4}_{-1.3}$
11.9	77	33.1	$\pm$ 2.7	$^{+2.4}_{-1.5}$
11.9	95	32.1	$\pm$ 3.5	$^{+3.0}_{-1.8}$
11.9	113	27.5	$\pm$ 4.1	$^{+3.5}_{-1.9}$
11.9	131	34.9	$\pm$ 3.2	$^{+3.1}_{-2.3}$
19.5	61	6.5	$\pm$ 0.6	$^{+0.6}_{-0.4}$
19.5	83	9.6	$\pm$ 0.9	$^{+0.7}_{-0.5}$
19.5	105	9.3	$\pm$ 1.0	$^{+0.8}_{-0.5}$
19.5	127	9.8	$\pm$ 1.1	$^{+0.8}_{-0.6}$
19.5	149	16.9	$\pm$ 1.8	$^{+1.4}_{-1.0}$
35.6	71	1.2	$\pm$ 0.2	$^{+0.1}_{-0.1}$
35.6	97	2.0	$\pm$ 0.4	$^{+0.2}_{-0.1}$
35.6	116	2.3	$\pm$ 0.5	$^{+0.2}_{-0.1}$
35.6	139	3.4	$\pm$ 0.6	$^{+0.3}_{-0.2}$
35.6	165	2.9	$\pm$ 0.7	$^{+0.3}_{-0.2}$

Table 22: W dependence of the $\gamma^* p$ cross section for elastic ρ meson production, for several values of Q^2. The overall normalisation uncertainty of 3.9% is not included in the systematic errors.

Q^2 (GeV^2)	W (GeV)	$\sigma(\gamma^* p \to \rho Y)$ (nb)		
3.3	41	177	$\pm$ 17	$^{+25}_{-14}$
3.3	54	209	$\pm$ 20	$^{+23}_{-17}$
3.3	67	213	$\pm$ 21	$^{+27}_{-20}$
3.3	80	228	$\pm$ 26	$^{+29}_{-22}$
3.3	93	226	$\pm$ 33	$^{+29}_{-25}$
7.5	48	36.6	$\pm$ 2.8	$^{+4.9}_{-3.0}$
7.5	64	38.8	$\pm$ 4.2	$^{+5.1}_{-3.6}$
7.5	80	34.9	$\pm$ 3.7	$^{+4.3}_{-3.4}$
7.5	96	40.2	$\pm$ 4.3	$^{+4.4}_{-4.2}$
7.5	114	46.2	$\pm$ 5.2	$^{+5.0}_{-4.5}$
22.5	71	3.0	$\pm$ 0.4	$^{+0.3}_{-0.3}$
22.5	97	2.5	$\pm$ 0.5	$^{+0.4}_{-0.4}$
22.5	116	3.6	$\pm$ 0.7	$^{+0.4}_{-0.5}$
22.5	139	4.6	$\pm$ 0.8	$^{+0.5}_{-0.6}$
22.5	165	4.5	$\pm$ 1.0	$^{+0.5}_{-0.7}$

Table 23: W dependence of the $\gamma^* p$ cross section for proton dissociative ρ meson production, for several values of Q^2. The overall normalisation uncertainty of 4.6% is not included in the systematic errors.

Q^2 (GeV^2)	W (GeV)	$\sigma(\gamma^* p \to \phi p)$ (nb)		
3.3	41	41.2	$\pm$ 4.3	$^{+5.3}_{-2.9}$
3.3	54	55.1	$\pm$ 5.7	$^{+5.4}_{-3.7}$
3.3	67	49.2	$\pm$ 6.9	$^{+6.2}_{-4.4}$
3.3	80	57.5	$\pm$ 7.4	$^{+6.8}_{-4.6}$
3.3	93	69.6	$\pm$ 8.4	$^{+7.5}_{-5.2}$
6.6	48	13.2	$\pm$ 1.5	$^{+1.5}_{-0.9}$
6.6	64	13.0	$\pm$ 1.7	$^{+1.5}_{-1.0}$
6.6	80	20.5	$\pm$ 2.3	$^{+1.9}_{-1.1}$
6.6	96	14.7	$\pm$ 2.4	$^{+1.7}_{-1.0}$
6.6	114	23.3	$\pm$ 4.0	$^{+2.2}_{-1.6}$
15.8	71	2.3	$\pm$ 0.3	$^{+0.2}_{-0.1}$
15.8	97	2.5	$\pm$ 0.4	$^{+0.2}_{-0.2}$
15.8	116	3.9	$\pm$ 0.6	$^{+0.3}_{-0.2}$
15.8	139	4.4	$\pm$ 0.8	$^{+0.5}_{-0.3}$
15.8	165	7.6	$\pm$ 3.2	$^{+0.6}_{-0.4}$

Table 24: W dependence of the $\gamma^* p$ cross section for elastic ϕ meson production for several values of Q^2. The overall normalisation uncertainty of 4.7% is not included in the systematic errors.

Q^2 (GeV^2)	W (GeV)	$\sigma(\gamma^* p \to \phi Y)$ (nb)		
5.0	50	9.3	$\pm$ 1.6	$^{+1.6}_{-1.2}$
5.0	70	17.4	$\pm$ 2.3	$^{+2.2}_{-2.3}$
5.0	90	15.2	$\pm$ 2.5	$^{+1.9}_{-1.9}$
5.0	110	11.6	$\pm$ 2.9	$^{+1.7}_{-2.0}$
5.0	130	32.7	$\pm$ 11.7	$^{+6.3}_{-6.1}$
5.0	150	22.4	$\pm$ 13.7	$^{+6.1}_{-6.5}$

Table 25: W dependence of the $\gamma^* p$ cross section for proton dissociative ϕ meson production for $Q^2 = 5$ GeV^2. The overall normalisation uncertainty of 5.3% is not included in the systematic errors.

Q^2 (GeV^2)	δ			$\alpha_{I\!P}(0)$		
$\gamma^* p \to \rho p$						
3.3	0.40	$\pm$ 0.08	$^{+0.06}_{-0.06}$	1.10	$\pm$ 0.02	$^{+0.02}_{-0.02}$
6.6	0.57	$\pm$ 0.10	$^{+0.05}_{-0.07}$	1.14	$\pm$ 0.02	$^{+0.01}_{-0.02}$
11.9	0.28	$\pm$ 0.15	$^{+0.05}_{-0.05}$	1.07	$\pm$ 0.04	$^{+0.01}_{-0.01}$
19.5	0.77	$\pm$ 0.15	$^{+0.05}_{-0.05}$	1.19	$\pm$ 0.04	$^{+0.01}_{-0.01}$
35.6	1.17	$\pm$ 0.26	$^{+0.04}_{-0.04}$	1.29	$\pm$ 0.07	$^{+0.01}_{-0.01}$
$\gamma^* p \to \phi p$						
3.3	0.53	$\pm$ 0.17	$^{+0.09}_{-0.09}$	1.13	$\pm$ 0.04	$^{+0.02}_{-0.02}$
6.6	0.52	$\pm$ 0.21	$^{+0.07}_{-0.08}$	1.13	$\pm$ 0.05	$^{+0.02}_{-0.02}$
15.8	1.09	$\pm$ 0.34	$^{+0.08}_{-0.08}$	1.27	$\pm$ 0.08	$^{+0.02}_{-0.02}$
$\gamma^* p \to \rho Y$						
3.3	0.32	$\pm$ 0.17	$^{+0.08}_{-0.09}$	1.17	$\pm$ 0.04	$^{+0.04}_{-0.04}$
7.5	0.17	$\pm$ 0.14	$^{+0.07}_{-0.09}$	1.12	$\pm$ 0.04	$^{+0.07}_{-0.07}$
22.5	0.58	$\pm$ 0.29	$^{+0.10}_{-0.13}$	1.23	$\pm$ 0.07	$^{+0.07}_{-0.07}$
$\gamma^* p \to \phi Y$						
5.0	0.50	$\pm$ 0.24	$^{+0.16}_{-0.20}$	1.20	$\pm$ 0.06	$^{+0.07}_{-0.08}$

Table 26: Q^2 dependence of the parameters δ and $\alpha_{I\!P}(0)$, for elastic and proton dissociative ρ and ϕ meson production, computed from the W dependence of the cross section using Eqs. (16-18). The values of $\alpha_{I\!P}(0)$ are obtained using the measured values of $\langle t \rangle$ and the measurements of α' for ρ production given in Table 11.

Q^2 (GeV^2)	$\|t\|$ (GeV^2)	dσ/dt ($\gamma^* p \to \rho p$) (nb/GeV^2)		
3.3	0.025	2156	$\pm$ 82	$^{+202}_{-141}$
3.3	0.075	1379	$\pm$ 73	$^{+132}_{-90}$
3.3	0.125	858	$\pm$ 54	$^{+96}_{-65}$
3.3	0.175	665	$\pm$ 48	$^{+72}_{-60}$
3.3	0.250	346	$\pm$ 27	$^{+46}_{-38}$
3.3	0.350	234	$\pm$ 25	$^{+35}_{-28}$
3.3	0.450	61.2	$\pm$ 13.9	$^{+18.8}_{-16.4}$
6.6	0.025	604	$\pm$ 31	$^{+44}_{-21}$
6.6	0.075	392	$\pm$ 24	$^{+35}_{-16}$
6.6	0.125	214	$\pm$ 18	$^{+19}_{-12}$
6.6	0.175	198	$\pm$ 16	$^{+15}_{-9}$
6.6	0.250	99.1	$\pm$ 9.0	$^{+10.0}_{-8.4}$
6.6	0.350	50.0	$\pm$ 7.2	$^{+8.7}_{-5.6}$
6.6	0.450	31.5	$\pm$ 5.5	$^{+5.8}_{-4.7}$
11.5	0.025	181	$\pm$ 18	$^{+14}_{-10}$
11.5	0.075	123	$\pm$ 12	$^{+11}_{-8}$
11.5	0.125	89.8	$\pm$ 10.6	$^{+9.5}_{-5.4}$
11.5	0.175	61.4	$\pm$ 9.8	$^{+7.3}_{-6.0}$
11.5	0.250	44.0	$\pm$ 8.0	$^{+5.0}_{-4.5}$
11.5	0.350	22.0	$\pm$ 5.0	$^{+2.3}_{-2.3}$
11.5	0.450	8.58	$\pm$ 3.02	$^{+2.06}_{-1.35}$
17.4	0.025	51.1	$\pm$ 3.8	$^{+4.8}_{-3.9}$
17.4	0.075	35.6	$\pm$ 3.5	$^{+3.6}_{-2.8}$
17.4	0.125	24.3	$\pm$ 2.9	$^{+2.6}_{-2.2}$
17.4	0.175	26.4	$\pm$ 3.4	$^{+2.7}_{-2.4}$
17.4	0.250	12.3	$\pm$ 1.4	$^{+2.0}_{-1.2}$
17.4	0.350	8.48	$\pm$ 1.40	$^{+1.16}_{-1.04}$
17.4	0.450	3.87	$\pm$ 0.91	$^{+0.95}_{-0.64}$
33.0	0.025	6.52	$\pm$ 0.93	$^{+0.87}_{-0.77}$
33.0	0.075	4.90	$\pm$ 0.78	$^{+0.73}_{-0.62}$
33.0	0.125	4.43	$\pm$ 0.71	$^{+0.56}_{-0.50}$
33.0	0.175	2.59	$\pm$ 0.56	$^{+0.52}_{-0.32}$
33.0	0.250	2.28	$\pm$ 0.39	$^{+0.28}_{-0.28}$
33.0	0.350	1.85	$\pm$ 0.52	$^{+0.29}_{-0.24}$
33.0	0.450	0.660	$\pm$ 0.272	$^{+0.164}_{-0.127}$

Table 27: t dependences of the $\gamma^* p$ cross section for elastic ρ meson production for several values of Q^2. The overall normalisation uncertainty of 3.9% is not included in the systematic errors.

Q^2 (GeV^2)	$\lvert t\rvert$ (GeV^2)	$\mathrm{d}\sigma/\mathrm{dt}$ ($\gamma^* p \to \rho Y$) (nb/GeV^2)		
3.3	0.100	379	$\pm$ 32	$^{+47}_{-48}$
3.3	0.300	214	$\pm$ 19	$^{+28}_{-19}$
3.3	0.500	149	$\pm$ 16	$^{+21}_{-15}$
3.3	0.700	74.1	$\pm$ 11.3	$^{+11.1}_{-8.0}$
3.3	0.900	71.8	$\pm$ 13.7	$^{+11.0}_{-8.0}$
3.3	1.100	29.1	$\pm$ 8.4	$^{+6.0}_{-4.3}$
3.3	1.300	30.8	$\pm$ 12.4	$^{+6.6}_{-4.0}$
3.3	1.500	14.8	$\pm$ 4.5	$^{+2.7}_{-2.9}$
3.3	1.800	8.65	$\pm$ 2.29	$^{+1.78}_{-1.78}$
3.3	2.250	2.85	$\pm$ 1.32	$^{+0.94}_{-1.02}$
3.3	2.750	0.807	$\pm$ 0.653	$^{+0.258}_{-0.406}$
6.6	0.100	76.5	$\pm$ 7.6	$^{+7.5}_{-7.2}$
6.6	0.300	58.7	$\pm$ 7.6	$^{+8.8}_{-5.2}$
6.6	0.500	25.0	$\pm$ 3.5	$^{+3.3}_{-2.6}$
6.6	0.700	30.4	$\pm$ 4.9	$^{+4.0}_{-3.0}$
6.6	0.900	13.1	$\pm$ 1.9	$^{+2.1}_{-1.7}$
6.6	1.100	7.63	$\pm$ 1.48	$^{+1.23}_{-1.19}$
6.6	1.300	6.98	$\pm$ 1.37	$^{+1.30}_{-0.86}$
6.6	1.500	5.12	$\pm$ 1.13	$^{+0.69}_{-0.54}$
6.6	1.800	3.01	$\pm$ 0.64	$^{+0.59}_{-0.52}$
6.6	2.250	1.71	$\pm$ 0.42	$^{+0.39}_{-0.36}$
6.6	2.750	0.620	$\pm$ 0.278	$^{+0.182}_{-0.222}$
15.8	0.100	9.88	$\pm$ 1.13	$^{+1.32}_{-1.33}$
15.8	0.300	4.33	$\pm$ 0.64	$^{+0.57}_{-0.70}$
15.8	0.500	4.87	$\pm$ 0.78	$^{+0.71}_{-0.56}$
15.8	0.700	2.32	$\pm$ 0.35	$^{+0.33}_{-0.33}$
15.8	0.900	1.45	$\pm$ 0.27	$^{+0.28}_{-0.24}$
15.8	1.100	1.89	$\pm$ 0.43	$^{+0.23}_{-0.35}$
15.8	1.300	0.882	$\pm$ 0.216	$^{+0.225}_{-0.093}$
15.8	1.500	0.613	$\pm$ 0.193	$^{+0.093}_{-0.611}$
15.8	1.800	0.426	$\pm$ 0.108	$^{+0.096}_{-0.095}$
15.8	2.250	0.370	$\pm$ 0.089	$^{+0.095}_{-0.089}$
15.8	2.750	0.417	$\pm$ 0.245	$^{+0.037}_{-1.058}$

Table 28: t dependences of the $\gamma^* p$ cross section for proton dissociative ρ meson production for several values of Q^2. The overall normalisation uncertainty of 4.6% is not included in the systematic errors.

Q^2 (GeV^2)	$\lvert t\rvert$ (GeV^2)	dσ/dt ($\gamma^* p \to \phi p$) (nb/GeV^2)		
3.3	0.025	431	$\pm$ 34	$^{+40}_{-25}$
3.3	0.075	209	$\pm$ 24	$^{+24}_{-22}$
3.3	0.125	120	$\pm$ 21	$^{+24}_{-16}$
3.3	0.175	85.4	$\pm$ 17.1	$^{+15.2}_{-9.6}$
3.3	0.250	64.6	$\pm$ 10.5	$^{+9.0}_{-7.4}$
3.3	0.350	27.5	$\pm$ 7.4	$^{+5.8}_{-3.6}$
3.3	0.450	27.4	$\pm$ 7.1	$^{+5.4}_{-4.5}$
6.6	0.025	93.1	$\pm$ 10.4	$^{+7.8}_{-3.9}$
6.6	0.075	77.7	$\pm$ 9.1	$^{+6.8}_{-3.4}$
6.6	0.125	34.1	$\pm$ 6.1	$^{+3.1}_{-2.6}$
6.6	0.175	24.9	$\pm$ 5.0	$^{+2.8}_{-1.7}$
6.6	0.250	21.2	$\pm$ 3.8	$^{+2.7}_{-2.7}$
6.6	0.350	8.77	$\pm$ 2.37	$^{+1.54}_{-1.00}$
6.6	0.450	6.41	$\pm$ 2.12	$^{+1.29}_{-1.26}$
15.8	0.025	8.24	$\pm$ 1.14	$^{+1.09}_{-0.89}$
15.8	0.075	10.7	$\pm$ 1.4	$^{+1.3}_{-1.1}$
15.8	0.125	3.89	$\pm$ 0.85	$^{+0.59}_{-0.42}$
15.8	0.175	3.96	$\pm$ 0.80	$^{+0.48}_{-0.56}$
15.8	0.250	2.32	$\pm$ 0.47	$^{+0.39}_{-0.29}$
15.8	0.350	0.702	$\pm$ 0.296	$^{+0.188}_{-0.140}$
15.8	0.450	0.349	$\pm$ 0.278	$^{+0.160}_{-0.150}$

Table 29: t dependences of the $\gamma^* p$ cross section for elastic ϕ meson production for several values of Q^2. The overall normalisation uncertainty of 4.7% is not included in the systematic errors.

Q^2 (GeV^2)	$\lvert t\rvert$ (GeV^2)	dσ/dt ($\gamma^* p \to \phi Y$) (nb/GeV^2)		
5.0	0.150	58.2	$\pm$ 11.8	$^{+9.0}_{-6.1}$
5.0	0.500	23.1	$\pm$ 5.5	$^{+4.1}_{-2.6}$
5.0	1.100	6.17	$\pm$ 2.76	$^{+2.28}_{-1.25}$
5.0	2.250	0.681	$\pm$ 0.418	$^{+0.285}_{-0.301}$

Table 30: t dependence of the $\gamma^* p$ cross section for proton dissociative ϕ meson production for $Q^2 = 5$ GeV^2. The overall normalisation uncertainty of 5.3% is not included in the systematic errors.

Q^2 (GeV^2)	b (GeV^{-2})		
$\gamma^* p \to \rho p$			
3.3	7.82	$\pm$ 0.33	$^{+0.33}_{-0.33}$
6.6	7.57	$\pm$ 0.35	$^{+0.30}_{-0.31}$
11.5	6.72	$\pm$ 0.53	$^{+0.23}_{-0.25}$
17.4	5.86	$\pm$ 0.40	$^{+0.26}_{-0.33}$
33.0	4.87	$\pm$ 0.66	$^{+0.21}_{-0.22}$
$\gamma^* p \to \phi p$			
3.3	8.28	$\pm$ 0.80	$^{+0.49}_{-0.65}$
6.6	7.17	$\pm$ 0.73	$^{+0.36}_{-0.34}$
15.8	7.08	$\pm$ 0.71	$^{+0.38}_{-0.34}$
$\gamma^* p \to \rho Y$			
3.3	2.29	$\pm$ 0.12	$^{+0.12}_{-0.12}$
6.6	1.91	$\pm$ 0.26	$^{+0.13}_{-0.13}$
15.8	1.70	$\pm$ 0.15	$^{+0.42}_{-0.10}$
$\gamma^* p \to \phi Y$			
5.0	2.21	$\pm$ 0.37	$^{+0.48}_{-0.13}$

Table 31: Q^2 dependence of the b slope parameters of the exponentially falling $|t|$ distributions of ρ and ϕ elastic and proton dissociative production.

Q^2 (GeV^2)	m_{2g} (GeV)		
$\gamma^* p \to \rho p$			
3.3	0.59	$\pm$ 0.01	$^{+0.01}_{-0.01}$
6.6	0.60	$\pm$ 0.02	$^{+0.01}_{-0.01}$
11.5	0.65	$\pm$ 0.03	$^{+0.01}_{-0.01}$
17.4	0.71	$\pm$ 0.03	$^{+0.02}_{-0.02}$
33.0	0.80	$\pm$ 0.06	$^{+0.02}_{-0.02}$
$\gamma^* p \to \phi p$			
3.3	0.57	$\pm$ 0.03	$^{+0.02}_{-0.02}$
6.6	0.63	$\pm$ 0.04	$^{+0.02}_{-0.02}$
15.8	0.64	$\pm$ 0.04	$^{+0.02}_{-0.02}$

Table 32: Parameter m_{2g} of the two-gluon form factor of the FS model [54], extracted from fits of Eq. (20) to the t distributions of ρ and ϕ elastic production cross sections.

$\lvert t\rvert$ (GeV^2)	W (GeV)	$\sigma(\gamma^* p \to \rho Y)$ (nb)		
$Q^2 = 3.3$ GeV^2				
0.08	45	1451	$\pm$ 51	$^{+124}_{-56}$
0.08	65	1677	$\pm$ 66	$^{+123}_{-75}$
0.08	87	2030	$\pm$ 82	$^{+173}_{-102}$
0.32	45	393	$\pm$ 24	$^{+45}_{-29}$
0.32	65	433	$\pm$ 30	$^{+48}_{-37}$
0.32	87	453	$\pm$ 33	$^{+55}_{-44}$
0.69	45	95.1	$\pm$ 9.4	$^{+16.1}_{-13.5}$
0.69	65	110	$\pm$ 13	$^{+20}_{-17}$
0.69	87	124	$\pm$ 19	$^{+22}_{-17}$
1.45	45	14.5	$\pm$ 2.5	$^{+3.2}_{-2.7}$
1.45	65	9.0	$\pm$ 1.8	$^{+2.7}_{-2.4}$
1.45	87	8.3	$\pm$ 2.1	$^{+2.3}_{-2.2}$
$Q^2 = 8.6$ GeV^2				
0.08	65	261	$\pm$ 14	$^{+23}_{-11}$
0.08	79	261	$\pm$ 11	$^{+17}_{-10}$
0.08	104	320	$\pm$ 14	$^{+22}_{-13}$
0.32	65	64.8	$\pm$ 5.9	$^{+6.4}_{-3.8}$
0.32	79	72.8	$\pm$ 5.3	$^{+6.0}_{-5.3}$
0.32	104	82.1	$\pm$ 5.6	$^{+8.7}_{-5.9}$
0.69	65	16.5	$\pm$ 1.7	$^{+3.1}_{-2.6}$
0.69	79	17.5	$\pm$ 1.6	$^{+3.0}_{-2.5}$
0.69	104	17.3	$\pm$ 1.7	$^{+3.6}_{-3.2}$
1.47	65	2.8	$\pm$ 0.5	$^{+0.8}_{-0.8}$
1.47	79	1.5	$\pm$ 0.3	$^{+0.9}_{-0.8}$
1.47	104	2.3	$\pm$ 0.4	$^{+1.0}_{-0.9}$

Table 33: W dependence of the $\gamma^* p$ cross sections for ρ meson production in four bins in $|t|$, for $Q^2 = 3.3$ GeV^2 and $Q^2 = 8.6$ GeV^2. The notag ($|t| \leq 0.5$ GeV^2) and tag ($|t| \leq 3$ GeV^2) samples are combined. The overall normalisation uncertainty of 4% is not included in the systematic errors.

t (GeV^2)	$\alpha_{I\!P}(t)$		
Q^2= 3.3 GeV^2			
-0.08	1.12	$\pm$ 0.02	$^{+0.01}_{-0.01}$
-0.32	1.05	$\pm$ 0.04	$^{+0.02}_{-0.02}$
-0.69	1.10	$\pm$ 0.06	$^{+0.03}_{-0.02}$
-1.45	0.76	$\pm$ 0.12	$^{+0.06}_{-0.07}$
Q^2= 8.6 GeV^2			
-0.08	1.12	$\pm$ 0.04	$^{+0.01}_{-0.01}$
-0.32	1.12	$\pm$ 0.06	$^{+0.01}_{-0.01}$
-0.69	1.02	$\pm$ 0.07	$^{+0.04}_{-0.04}$
-1.48	0.93	$\pm$ 0.16	$^{+0.10}_{-0.15}$

Table 34: t dependence of $\alpha_{I\!P}(t)$ for ρ meson production, for two values of Q^2.

Q^2 (GeV^2)	$\frac{\sigma_{tot,\text{p. diss.}}}{\sigma_{tot,\text{el.}}}(\rho)$			$\frac{\mathrm{d}\sigma_{\text{p. diss.}}/\mathrm{d}t}{\mathrm{d}\sigma_{\text{el.}}/\mathrm{d}t}(\mathrm{t}=0)(\rho)$		
2.9	0.58	$\pm$ 0.04	$^{+0.12}_{-0.08}$	0.169	$\pm$ 0.017	$^{+0.011}_{-0.015}$
4.1	0.65	$\pm$ 0.05	$^{+0.07}_{-0.06}$	0.191	$\pm$ 0.019	$^{+0.014}_{-0.016}$
6.6	0.53	$\pm$ 0.03	$^{+0.02}_{-0.06}$	0.133	$\pm$ 0.021	$^{+0.009}_{-0.011}$
11.9	0.58	$\pm$ 0.05	$^{+0.09}_{-0.07}$	0.147	$\pm$ 0.022	$^{+0.041}_{-0.016}$
18.6	0.45	$\pm$ 0.05	$^{+0.04}_{-0.05}$	0.131	$\pm$ 0.021	$^{+0.042}_{-0.019}$
31.3	0.57	$\pm$ 0.09	$^{+0.04}_{-0.06}$	0.198	$\pm$ 0.044	$^{+0.062}_{-0.030}$

Table 35: Q^2 dependences, for $W = 75$ GeV, of the ratios of proton dissociative ($M_Y < 5$ GeV) to elastic ρ meson production cross sections integrated over t and for $t = 0$. The overall normalisation uncertainty of 2.4% is not included in the systematic errors.

Q^2 (GeV^2)	$\frac{\sigma_{tot,\text{p. diss.}}}{\sigma_{tot,\text{el.}}}(\phi)$			$\frac{\mathrm{d}\sigma_{\text{p. diss.}}/\mathrm{d}t}{\mathrm{d}\sigma_{\text{el.}}/\mathrm{d}t}(\mathrm{t}=0)(\phi)$		
3.3	0.58	$\pm$ 0.09	$^{+0.09}_{-0.04}$	0.155	$\pm$ 0.039	$^{+0.037}_{-0.006}$
6.6	0.48	$\pm$ 0.06	$^{+0.07}_{-0.10}$	0.148	$\pm$ 0.034	$^{+0.034}_{-0.015}$
15.8	0.47	$\pm$ 0.08	$^{+0.02}_{-0.07}$	0.146	$\pm$ 0.038	$^{+0.034}_{-0.015}$

Table 36: Q^2 dependences, for $W = 75$ GeV, of the ratios of proton dissociative ($M_Y < 5$ GeV) to elastic ϕ meson production cross sections integrated over t and for $t = 0$. The overall normalisation uncertainty of 2.4% is not included in the systematic errors.

Q^2 (GeV^2)	$b_{el.} - b_{p.\ diss.}$ (GeV^{-2})		
ρ			
3.3	5.52	$\pm$ 0.40	$^{+0.26}_{-0.26}$
6.6	5.74	$\pm$ 0.62	$^{+0.22}_{-0.25}$
15.8	4.76	$\pm$ 0.48	$^{+0.19}_{-0.65}$
ϕ			
5.0	5.81	$\pm$ 1.15	$^{+0.16}_{-0.70}$

Table 37: Slope differences $b_{el.} - b_{p.\ diss.}$ between elastic and proton dissociative scattering for ρ and ϕ meson production as a function of Q^2.

$\langle Q^2 \rangle$ (GeV^2)	3.1	4.8	7.5	12.2	23.1
r^{04}_{00}	$0.597 \pm 0.013\ ^{+0.014}_{-0.034}$	$0.680 \pm 0.017\ ^{+0.017}_{-0.028}$	$0.789 \pm 0.013\ ^{+0.018}_{-0.029}$	$0.793 \pm 0.016\ ^{+0.018}_{-0.023}$	$0.877 \pm 0.019\ ^{+0.019}_{-0.020}$
Re r^{04}_{10}	$0.049 \pm 0.009\ ^{+0.010}_{-0.010}$	$0.019 \pm 0.012\ ^{+0.012}_{-0.013}$	$0.034 \pm 0.010\ ^{+0.011}_{-0.010}$	$-0.011 \pm 0.012\ ^{+0.009}_{-0.009}$	$0.046 \pm 0.014\ ^{+0.008}_{-0.009}$
r^{04}_{1-1}	$0.000 \pm 0.011\ ^{+0.004}_{-0.004}$	$0.011 \pm 0.013\ ^{+0.002}_{-0.003}$	$-0.003 \pm 0.010\ ^{+0.002}_{-0.002}$	$-0.031 \pm 0.013\ ^{+0.003}_{-0.004}$	$0.012 \pm 0.014\ ^{+0.002}_{-0.004}$
r^{1}_{00}	$-0.001 \pm 0.029\ ^{+0.035}_{-0.012}$	$0.021 \pm 0.024\ ^{+0.015}_{-0.028}$	$0.001 \pm 0.039\ ^{+0.020}_{-0.013}$	$-0.081 \pm 0.095\ ^{+0.016}_{-0.018}$	$-0.015 \pm 0.061\ ^{+0.026}_{-0.011}$
r^{1}_{11}	$-0.019 \pm 0.031\ ^{+0.006}_{-0.021}$	$-0.034 \pm 0.036\ ^{+0.010}_{-0.005}$	$-0.028 \pm 0.044\ ^{+0.011}_{-0.011}$	$0.027 \pm 0.051\ ^{+0.015}_{-0.013}$	$0.058 \pm 0.077\ ^{+0.014}_{-0.018}$
Re r^{1}_{10}	$-0.029 \pm 0.013\ ^{+0.014}_{-0.010}$	$-0.043 \pm 0.017\ ^{+0.011}_{-0.012}$	$-0.007 \pm 0.014\ ^{+0.013}_{-0.010}$	$-0.019 \pm 0.017\ ^{+0.010}_{-0.009}$	$0.023 \pm 0.021\ ^{+0.013}_{-0.011}$
r^{1}_{1-1}	$0.157 \pm 0.015\ ^{+0.008}_{-0.008}$	$0.088 \pm 0.018\ ^{+0.005}_{-0.008}$	$0.117 \pm 0.014\ ^{+0.006}_{-0.007}$	$0.068 \pm 0.017\ ^{+0.006}_{-0.006}$	$-0.019 \pm 0.021\ ^{+0.008}_{-0.009}$
r^{2}_{10}	$0.031 \pm 0.013\ ^{+0.011}_{-0.016}$	$0.033 \pm 0.016\ ^{+0.010}_{-0.009}$	$-0.040 \pm 0.014\ ^{+0.012}_{-0.011}$	$-0.024 \pm 0.016\ ^{+0.007}_{-0.008}$	$-0.012 \pm 0.020\ ^{+0.012}_{-0.009}$
Im r^{2}_{1-1}	$-0.176 \pm 0.015\ ^{+0.010}_{-0.006}$	$-0.133 \pm 0.018\ ^{+0.005}_{-0.007}$	$-0.083 \pm 0.014\ ^{+0.003}_{-0.004}$	$-0.045 \pm 0.016\ ^{+0.003}_{-0.005}$	$-0.041 \pm 0.020\ ^{+0.009}_{-0.006}$
r^{5}_{00}	$0.156 \pm 0.019\ ^{+0.040}_{-0.065}$	$0.171 \pm 0.025\ ^{+0.038}_{-0.035}$	$0.080 \pm 0.022\ ^{+0.040}_{-0.041}$	$0.130 \pm 0.026\ ^{+0.039}_{-0.039}$	$0.135 \pm 0.033\ ^{+0.032}_{-0.034}$
r^{5}_{11}	$-0.008 \pm 0.014\ ^{+0.028}_{-0.014}$	$0.011 \pm 0.017\ ^{+0.008}_{-0.014}$	$0.010 \pm 0.015\ ^{+0.010}_{-0.009}$	$0.001 \pm 0.018\ ^{+0.009}_{-0.010}$	$0.006 \pm 0.022\ ^{+0.010}_{-0.009}$
Re r^{5}_{10}	$0.168 \pm 0.006\ ^{+0.004}_{-0.005}$	$0.141 \pm 0.008\ ^{+0.004}_{-0.005}$	$0.158 \pm 0.007\ ^{+0.006}_{-0.007}$	$0.128 \pm 0.008\ ^{+0.005}_{-0.005}$	$0.085 \pm 0.010\ ^{+0.003}_{-0.004}$
r^{5}_{1-1}	$0.001 \pm 0.008\ ^{+0.002}_{-0.002}$	$0.017 \pm 0.010\ ^{+0.002}_{-0.004}$	$-0.009 \pm 0.007\ ^{+0.003}_{-0.003}$	$-0.006 \pm 0.009\ ^{+0.003}_{-0.005}$	$-0.003 \pm 0.010\ ^{+0.007}_{-0.004}$
r^{6}_{10}	$-0.156 \pm 0.006\ ^{+0.006}_{-0.005}$	$-0.141 \pm 0.007\ ^{+0.005}_{-0.004}$	$-0.134 \pm 0.007\ ^{+0.006}_{-0.005}$	$-0.117 \pm 0.008\ ^{+0.004}_{-0.004}$	$-0.095 \pm 0.010\ ^{+0.003}_{-0.003}$
r^{6}_{1-1}	$-0.003 \pm 0.007\ ^{+0.001}_{-0.003}$	$0.003 \pm 0.009\ ^{+0.004}_{-0.002}$	$-0.011 \pm 0.007\ ^{+0.003}_{-0.002}$	$-0.035 \pm 0.008\ ^{+0.004}_{-0.004}$	$0.022 \pm 0.010\ ^{+0.002}_{-0.011}$

Table 38: Spin density matrix elements for the diffractive electroproduction of ρ mesons, as a function of Q^2. The notag ($|t| \leq 0.5$ GeV^2) and tag ($|t| \leq 3$ GeV^2) samples are combined.

$\langle Q^2 \rangle$ (GeV^2)	3.3	6.6	15.8
r^{04}_{00}	$0.581 \pm 0.023\ ^{+0.014}_{-0.015}$	$0.746 \pm 0.024\ ^{+0.017}_{-0.016}$	$0.864 \pm 0.031\ ^{+0.019}_{-0.016}$
Re r^{04}_{10}	$-0.004 \pm 0.017\ ^{+0.018}_{-0.020}$	$0.011 \pm 0.018\ ^{+0.012}_{-0.013}$	$0.007 \pm 0.024\ ^{+0.014}_{-0.011}$
r^{04}_{1-1}	$-0.059 \pm 0.020\ ^{+0.008}_{-0.004}$	$0.047 \pm 0.020\ ^{+0.004}_{-0.003}$	$-0.020 \pm 0.025\ ^{+0.006}_{-0.002}$
r^{1}_{00}	$-0.060 \pm 0.174\ ^{+0.011}_{-0.013}$	$-0.049 \pm 0.070\ ^{+0.018}_{-0.018}$	$-0.008 \pm 0.018\ ^{+0.020}_{-0.026}$
r^{1}_{11}	$-0.059 \pm 0.153\ ^{+0.008}_{-0.010}$	$0.006 \pm 0.044\ ^{+0.012}_{-0.009}$	$-0.004 \pm 0.014\ ^{+0.015}_{-0.011}$
Re r^{1}_{10}	$-0.044 \pm 0.023\ ^{+0.021}_{-0.015}$	$-0.073 \pm 0.025\ ^{+0.017}_{-0.013}$	$-0.028 \pm 0.034\ ^{+0.013}_{-0.018}$
r^{1}_{1-1}	$0.220 \pm 0.027\ ^{+0.018}_{-0.013}$	$0.104 \pm 0.029\ ^{+0.009}_{-0.007}$	$0.058 \pm 0.036\ ^{+0.010}_{-0.017}$
r^{2}_{10}	$-0.038 \pm 0.023\ ^{+0.024}_{-0.014}$	$0.075 \pm 0.027\ ^{+0.011}_{-0.014}$	$-0.017 \pm 0.034\ ^{+0.019}_{-0.012}$
Im r^{2}_{1-1}	$-0.152 \pm 0.028\ ^{+0.019}_{-0.009}$	$-0.111 \pm 0.029\ ^{+0.008}_{-0.016}$	$-0.094 \pm 0.034\ ^{+0.005}_{-0.016}$
r^{5}_{00}	$0.053 \pm 0.034\ ^{+0.027}_{-0.033}$	$0.080 \pm 0.040\ ^{+0.030}_{-0.036}$	$0.112 \pm 0.055\ ^{+0.041}_{-0.034}$
r^{5}_{11}	$0.004 \pm 0.025\ ^{+0.018}_{-0.015}$	$0.015 \pm 0.028\ ^{+0.011}_{-0.012}$	$-0.010 \pm 0.037\ ^{+0.009}_{-0.013}$
Re r^{5}_{10}	$0.220 \pm 0.011\ ^{+0.009}_{-0.008}$	$0.139 \pm 0.012\ ^{+0.005}_{-0.004}$	$0.091 \pm 0.017\ ^{+0.006}_{-0.003}$
r^{5}_{1-1}	$-0.010 \pm 0.015\ ^{+0.008}_{-0.005}$	$-0.002 \pm 0.015\ ^{+0.003}_{-0.004}$	$0.035 \pm 0.019\ ^{+0.082}_{-0.012}$
r^{6}_{10}	$-0.147 \pm 0.010\ ^{+0.005}_{-0.006}$	$-0.174 \pm 0.012\ ^{+0.005}_{-0.006}$	$-0.121 \pm 0.016\ ^{+0.004}_{-0.005}$
r^{6}_{1-1}	$-0.039 \pm 0.013\ ^{+0.006}_{-0.009}$	$0.006 \pm 0.014\ ^{+0.004}_{-0.005}$	$-0.003 \pm 0.017\ ^{+0.003}_{-0.003}$

Table 39: Spin density matrix elements for the diffractive electroproduction of ϕ mesons, as a function of Q^2. The notag ($|t| \leq 0.5$ GeV^2) and tag ($|t| \leq 3$ GeV^2) samples are combined.

$\langle Q^2 \rangle$ = 3.3 GeV^2				
$\langle W \rangle$ (GeV)	43	59	76	92
r^{04}_{00}	$0.619 \pm 0.021\ ^{+0.012}_{-0.048}$	$0.600 \pm 0.021\ ^{+0.012}_{-0.020}$	$0.612 \pm 0.023\ ^{+0.014}_{-0.029}$	$0.580 \pm 0.028\ ^{+0.014}_{-0.027}$
Re r^{04}_{10}	$0.580 \pm 0.028\ ^{+0.014}_{-0.027}$	$0.729 \pm 0.019\ ^{+0.016}_{-0.020}$	$0.755 \pm 0.019\ ^{+0.020}_{-0.024}$	$0.795 \pm 0.021\ ^{+0.023}_{-0.045}$
r^{04}_{1-1}	$0.795 \pm 0.021\ ^{+0.023}_{-0.045}$	$0.731 \pm 0.021\ ^{+0.021}_{-0.021}$	$0.798 \pm 0.037\ ^{+0.024}_{-0.018}$	$0.878 \pm 0.036\ ^{+0.018}_{-0.027}$
r^{1}_{00}	$0.878 \pm 0.036\ ^{+0.018}_{-0.027}$	$0.872 \pm 0.040\ ^{+0.023}_{-0.032}$	$0.856 \pm 0.045\ ^{+0.041}_{-0.059}$	$0.047 \pm 0.014\ ^{+0.012}_{-0.013}$
r^{1}_{11}	$0.047 \pm 0.014\ ^{+0.012}_{-0.013}$	$0.056 \pm 0.015\ ^{+0.014}_{-0.010}$	$0.029 \pm 0.016\ ^{+0.010}_{-0.010}$	$0.028 \pm 0.019\ ^{+0.010}_{-0.011}$
Re r^{1}_{10}	$0.028 \pm 0.019\ ^{+0.010}_{-0.011}$	$0.043 \pm 0.014\ ^{+0.011}_{-0.011}$	$0.028 \pm 0.014\ ^{+0.012}_{-0.012}$	$-0.001 \pm 0.015\ ^{+0.012}_{-0.010}$
r^{1}_{1-1}	$-0.001 \pm 0.015\ ^{+0.012}_{-0.010}$	$0.006 \pm 0.015\ ^{+0.008}_{-0.007}$	$0.047 \pm 0.027\ ^{+0.009}_{-0.010}$	$0.047 \pm 0.029\ ^{+0.009}_{-0.011}$
r^{2}_{10}	$0.047 \pm 0.029\ ^{+0.009}_{-0.011}$	$0.033 \pm 0.028\ ^{+0.008}_{-0.015}$	$0.004 \pm 0.032\ ^{+0.013}_{-0.012}$	$0.006 \pm 0.016\ ^{+0.003}_{-0.009}$
Im r^{2}_{1-1}	$0.006 \pm 0.016\ ^{+0.003}_{-0.009}$	$-0.011 \pm 0.017\ ^{+0.005}_{-0.002}$	$0.024 \pm 0.019\ ^{+0.004}_{-0.002}$	$-0.012 \pm 0.022\ ^{+0.003}_{-0.006}$
r^{5}_{00}	$-0.012 \pm 0.022\ ^{+0.003}_{-0.006}$	$-0.024 \pm 0.015\ ^{+0.002}_{-0.004}$	$-0.005 \pm 0.015\ ^{+0.004}_{-0.003}$	$-0.032 \pm 0.016\ ^{+0.004}_{-0.003}$
r^{5}_{11}	$-0.032 \pm 0.016\ ^{+0.004}_{-0.003}$	$-0.015 \pm 0.018\ ^{+0.004}_{-0.005}$	$0.021 \pm 0.027\ ^{+0.020}_{-0.017}$	$-0.003 \pm 0.029\ ^{+0.002}_{-0.024}$
Re r^{5}_{10}	$-0.003 \pm 0.029\ ^{+0.002}_{-0.024}$	$0.029 \pm 0.030\ ^{+0.006}_{-0.020}$	$0.037 \pm 0.033\ ^{+0.006}_{-0.012}$	$-0.015 \pm 0.100\ ^{+0.018}_{-0.064}$
r^{5}_{1-1}	$-0.015 \pm 0.100\ ^{+0.018}_{-0.064}$	$0.134 \pm 0.147\ ^{+0.022}_{-0.030}$	$0.025 \pm 0.041\ ^{+0.035}_{-0.018}$	$0.018 \pm 0.040\ ^{+0.077}_{-0.012}$
r^{6}_{10}	$0.018 \pm 0.040\ ^{+0.077}_{-0.012}$	$-0.082 \pm 0.118\ ^{+0.019}_{-0.011}$	$-0.130 \pm 0.266\ ^{+0.020}_{-0.013}$	$0.163 \pm 0.143\ ^{+0.023}_{-0.027}$
r^{6}_{1-1}	$0.163 \pm 0.143\ ^{+0.023}_{-0.027}$	$0.154 \pm 0.263\ ^{+0.032}_{-0.012}$	$-0.071 \pm 0.080\ ^{+0.021}_{-0.014}$	$0.120 \pm 0.291\ ^{+0.081}_{-0.036}$

Table 40: Spin density matrix elements for the diffractive electroproduction of ρ mesons as a function of W, for $2.5 \leq Q^2 < 5$, $5 \leq Q^2 < 15.5$ and $15.5 \leq Q^2 \leq 60$ GeV^2. The notag ($|t| \leq 0.5$ GeV^2) and tag ($|t| \leq 3$ GeV^2) samples are combined.

$\langle Q^2 \rangle$ = 7.5 GeV^2				
$\langle W \rangle$ (GeV)	58	76	93	111
r^{04}_{00}	$0.729 \pm 0.019\ ^{+0.016}_{-0.020}$	$0.755 \pm 0.019\ ^{+0.020}_{-0.024}$	$0.795 \pm 0.021\ ^{+0.023}_{-0.045}$	$0.731 \pm 0.021\ ^{+0.021}_{-0.021}$
Re r^{04}_{10}	$0.731 \pm 0.021\ ^{+0.021}_{-0.021}$	$0.798 \pm 0.037\ ^{+0.024}_{-0.018}$	$0.878 \pm 0.036\ ^{+0.018}_{-0.027}$	$0.872 \pm 0.040\ ^{+0.023}_{-0.032}$
r^{04}_{1-1}	$0.872 \pm 0.040\ ^{+0.023}_{-0.032}$	$0.856 \pm 0.045\ ^{+0.041}_{-0.059}$	$0.047 \pm 0.014\ ^{+0.012}_{-0.013}$	$0.056 \pm 0.015\ ^{+0.014}_{-0.010}$
r^{1}_{00}	$0.056 \pm 0.015\ ^{+0.014}_{-0.010}$	$0.029 \pm 0.016\ ^{+0.010}_{-0.010}$	$0.028 \pm 0.019\ ^{+0.010}_{-0.011}$	$0.043 \pm 0.014\ ^{+0.011}_{-0.011}$
r^{1}_{11}	$0.043 \pm 0.014\ ^{+0.011}_{-0.011}$	$0.028 \pm 0.014\ ^{+0.012}_{-0.012}$	$-0.001 \pm 0.015\ ^{+0.012}_{-0.010}$	$0.006 \pm 0.015\ ^{+0.008}_{-0.007}$
Re r^{1}_{10}	$0.006 \pm 0.015\ ^{+0.008}_{-0.007}$	$0.047 \pm 0.027\ ^{+0.009}_{-0.010}$	$0.047 \pm 0.029\ ^{+0.009}_{-0.011}$	$0.033 \pm 0.028\ ^{+0.008}_{-0.015}$
r^{1}_{1-1}	$0.033 \pm 0.028\ ^{+0.008}_{-0.015}$	$0.004 \pm 0.032\ ^{+0.013}_{-0.012}$	$0.006 \pm 0.016\ ^{+0.003}_{-0.009}$	$-0.011 \pm 0.017\ ^{+0.005}_{-0.002}$
r^{2}_{10}	$-0.011 \pm 0.017\ ^{+0.005}_{-0.002}$	$0.024 \pm 0.019\ ^{+0.004}_{-0.002}$	$-0.012 \pm 0.022\ ^{+0.003}_{-0.006}$	$-0.024 \pm 0.015\ ^{+0.002}_{-0.004}$
Im r^{2}_{1-1}	$-0.024 \pm 0.015\ ^{+0.002}_{-0.004}$	$-0.005 \pm 0.015\ ^{+0.004}_{-0.003}$	$-0.032 \pm 0.016\ ^{+0.004}_{-0.003}$	$-0.015 \pm 0.018\ ^{+0.004}_{-0.005}$
r^{5}_{00}	$-0.015 \pm 0.018\ ^{+0.004}_{-0.005}$	$0.021 \pm 0.027\ ^{+0.020}_{-0.017}$	$-0.003 \pm 0.029\ ^{+0.002}_{-0.024}$	$0.029 \pm 0.030\ ^{+0.006}_{-0.020}$
r^{5}_{11}	$0.029 \pm 0.030\ ^{+0.006}_{-0.020}$	$0.037 \pm 0.033\ ^{+0.006}_{-0.012}$	$-0.015 \pm 0.100\ ^{+0.018}_{-0.064}$	$0.134 \pm 0.147\ ^{+0.022}_{-0.030}$
Re r^{5}_{10}	$0.134 \pm 0.147\ ^{+0.022}_{-0.030}$	$0.025 \pm 0.041\ ^{+0.035}_{-0.018}$	$0.018 \pm 0.040\ ^{+0.077}_{-0.012}$	$-0.082 \pm 0.118\ ^{+0.019}_{-0.011}$
r^{5}_{1-1}	$-0.082 \pm 0.118\ ^{+0.019}_{-0.011}$	$-0.130 \pm 0.266\ ^{+0.020}_{-0.013}$	$0.163 \pm 0.143\ ^{+0.023}_{-0.027}$	$0.154 \pm 0.263\ ^{+0.032}_{-0.012}$
r^{6}_{10}	$0.154 \pm 0.263\ ^{+0.032}_{-0.012}$	$-0.071 \pm 0.080\ ^{+0.021}_{-0.014}$	$0.120 \pm 0.291\ ^{+0.081}_{-0.036}$	$-0.032 \pm 0.033\ ^{+0.028}_{-0.026}$
r^{6}_{1-1}	$-0.032 \pm 0.033\ ^{+0.028}_{-0.026}$	$-0.474 \pm 0.458\ ^{+0.300}_{-0.051}$	$-0.055 \pm 0.101\ ^{+0.031}_{-0.009}$	$-0.054 \pm 0.076\ ^{+0.012}_{-0.013}$

Table 41: Spin density matrix elements for the diffractive electroproduction of ρ mesons as a function of W, for $2.5 \leq Q^2 < 5$, $5 \leq Q^2 < 15.5$ and $15.5 \leq Q^2 \leq 60$ GeV^2, continued from table 40.

$\langle Q^2 \rangle$ = 22.5 GeV^2				
$\langle W \rangle$ (GeV)	72	97	122	147
r_{00}^{04}	$0.798 \pm 0.037\ ^{+0.024}_{-0.018}$	$0.878 \pm 0.036\ ^{+0.018}_{-0.027}$	$0.872 \pm 0.040\ ^{+0.023}_{-0.032}$	$0.856 \pm 0.045\ ^{+0.041}_{-0.059}$
Re r_{10}^{04}	$0.856 \pm 0.045\ ^{+0.041}_{-0.059}$	$0.047 \pm 0.014\ ^{+0.012}_{-0.013}$	$0.056 \pm 0.015\ ^{+0.014}_{-0.010}$	$0.029 \pm 0.016\ ^{+0.010}_{-0.010}$
r_{1-1}^{04}	$0.029 \pm 0.016\ ^{+0.010}_{-0.010}$	$0.028 \pm 0.019\ ^{+0.010}_{-0.011}$	$0.043 \pm 0.014\ ^{+0.011}_{-0.011}$	$0.028 \pm 0.014\ ^{+0.012}_{-0.012}$
r_{00}^{1}	$0.028 \pm 0.014\ ^{+0.012}_{-0.012}$	$-0.001 \pm 0.015\ ^{+0.012}_{-0.010}$	$0.006 \pm 0.015\ ^{+0.008}_{-0.007}$	$0.047 \pm 0.027\ ^{+0.009}_{-0.010}$
r_{11}^{1}	$0.047 \pm 0.027\ ^{+0.009}_{-0.010}$	$0.047 \pm 0.029\ ^{+0.009}_{-0.011}$	$0.033 \pm 0.028\ ^{+0.008}_{-0.015}$	$0.004 \pm 0.032\ ^{+0.013}_{-0.012}$
Re r_{10}^{1}	$0.004 \pm 0.032\ ^{+0.013}_{-0.012}$	$0.006 \pm 0.016\ ^{+0.003}_{-0.009}$	$-0.011 \pm 0.017\ ^{+0.005}_{-0.002}$	$0.024 \pm 0.019\ ^{+0.004}_{-0.002}$
r_{1-1}^{1}	$0.024 \pm 0.019\ ^{+0.004}_{-0.002}$	$-0.012 \pm 0.022\ ^{+0.003}_{-0.006}$	$-0.024 \pm 0.015\ ^{+0.002}_{-0.004}$	$-0.005 \pm 0.015\ ^{+0.004}_{-0.003}$
r_{10}^{2}	$-0.005 \pm 0.015\ ^{+0.004}_{-0.003}$	$-0.032 \pm 0.016\ ^{+0.004}_{-0.003}$	$-0.015 \pm 0.018\ ^{+0.004}_{-0.005}$	$0.021 \pm 0.027\ ^{+0.020}_{-0.017}$
Im r_{1-1}^{2}	$0.021 \pm 0.027\ ^{+0.020}_{-0.017}$	$-0.003 \pm 0.029\ ^{+0.002}_{-0.024}$	$0.029 \pm 0.030\ ^{+0.006}_{-0.020}$	$0.037 \pm 0.033\ ^{+0.006}_{-0.012}$
r_{00}^{5}	$0.037 \pm 0.033\ ^{+0.006}_{-0.012}$	$-0.015 \pm 0.100\ ^{+0.018}_{-0.064}$	$0.134 \pm 0.147\ ^{+0.022}_{-0.030}$	$0.025 \pm 0.041\ ^{+0.035}_{-0.018}$
r_{11}^{5}	$0.025 \pm 0.041\ ^{+0.035}_{-0.018}$	$0.018 \pm 0.040\ ^{+0.077}_{-0.012}$	$-0.082 \pm 0.118\ ^{+0.019}_{-0.011}$	$-0.130 \pm 0.266\ ^{+0.020}_{-0.013}$
Re r_{10}^{5}	$-0.130 \pm 0.266\ ^{+0.020}_{-0.013}$	$0.163 \pm 0.143\ ^{+0.023}_{-0.027}$	$0.154 \pm 0.263\ ^{+0.032}_{-0.012}$	$-0.071 \pm 0.080\ ^{+0.021}_{-0.014}$
r_{1-1}^{5}	$-0.071 \pm 0.080\ ^{+0.021}_{-0.014}$	$0.120 \pm 0.291\ ^{+0.081}_{-0.036}$	$-0.032 \pm 0.033\ ^{+0.028}_{-0.026}$	$-0.474 \pm 0.458\ ^{+0.300}_{-0.051}$
r_{10}^{6}	$-0.474 \pm 0.458\ ^{+0.300}_{-0.051}$	$-0.055 \pm 0.101\ ^{+0.031}_{-0.009}$	$-0.054 \pm 0.076\ ^{+0.012}_{-0.013}$	$0.001 \pm 0.028\ ^{+0.014}_{-0.021}$
r_{1-1}^{6}	$0.001 \pm 0.028\ ^{+0.014}_{-0.021}$	$-0.045 \pm 0.055\ ^{+0.012}_{-0.035}$	$0.009 \pm 0.074\ ^{+0.011}_{-0.012}$	$-0.047 \pm 0.206\ ^{+0.010}_{-0.014}$

Table 42: Spin density matrix elements for the diffractive electroproduction of ρ mesons as a function of W, for $2.5 \leq Q^2 < 5$, $5 \leq Q^2 < 15.5$ and $15.5 \leq Q^2 \leq 60$ GeV^2, continued from table 40.

$\langle\lvert t\rvert\rangle$ (GeV^2)	0.08	0.34	1.05
$\langle Q^2\rangle = 3.3$ GeV^2			
r^{04}_{00}	$0.602 \pm 0.014\ ^{+0.011}_{-0.031}$	$0.593 \pm 0.020\ ^{+0.019}_{-0.029}$	$0.660 \pm 0.040\ ^{+0.033}_{-0.045}$
Re r^{04}_{10}	$0.030 \pm 0.009\ ^{+0.011}_{-0.012}$	$0.026 \pm 0.014\ ^{+0.013}_{-0.009}$	$0.150 \pm 0.032\ ^{+0.017}_{-0.028}$
r^{04}_{1-1}	$-0.004 \pm 0.011\ ^{+0.002}_{-0.004}$	$0.037 \pm 0.017\ ^{+0.006}_{-0.002}$	$-0.080 \pm 0.036\ ^{+0.010}_{-0.015}$
r^{1}_{00}	$0.070 \pm 0.077\ ^{+0.020}_{-0.014}$	$-0.198 \pm 0.277\ ^{+0.259}_{-0.025}$	$0.163 \pm 0.119\ ^{+0.067}_{-0.076}$
r^{1}_{11}	$-0.028 \pm 0.040\ ^{+0.006}_{-0.011}$	$0.029 \pm 0.171\ ^{+0.025}_{-0.132}$	$-0.144 \pm 0.106\ ^{+0.015}_{-0.015}$
Re r^{1}_{10}	$-0.010 \pm 0.014\ ^{+0.008}_{-0.006}$	$-0.086 \pm 0.020\ ^{+0.015}_{-0.017}$	$-0.126 \pm 0.045\ ^{+0.028}_{-0.016}$
r^{1}_{1-1}	$0.143 \pm 0.016\ ^{+0.006}_{-0.009}$	$0.149 \pm 0.024\ ^{+0.011}_{-0.013}$	$0.075 \pm 0.048\ ^{+0.010}_{-0.022}$
r^{2}_{10}	$0.018 \pm 0.013\ ^{+0.012}_{-0.012}$	$0.072 \pm 0.021\ ^{+0.016}_{-0.016}$	$0.104 \pm 0.046\ ^{+0.017}_{-0.025}$
Im r^{2}_{1-1}	$-0.192 \pm 0.015\ ^{+0.007}_{-0.006}$	$-0.108 \pm 0.023\ ^{+0.016}_{-0.008}$	$-0.207 \pm 0.056\ ^{+0.018}_{-0.022}$
r^{5}_{00}	$0.125 \pm 0.020\ ^{+0.032}_{-0.060}$	$0.199 \pm 0.030\ ^{+0.038}_{-0.047}$	$0.197 \pm 0.060\ ^{+0.051}_{-0.033}$
r^{5}_{11}	$-0.014 \pm 0.014\ ^{+0.024}_{-0.007}$	$0.004 \pm 0.022\ ^{+0.025}_{-0.028}$	$0.100 \pm 0.043\ ^{+0.017}_{-0.022}$
Re r^{5}_{10}	$0.160 \pm 0.006\ ^{+0.003}_{-0.004}$	$0.154 \pm 0.010\ ^{+0.008}_{-0.009}$	$0.138 \pm 0.024\ ^{+0.015}_{-0.207}$
r^{5}_{1-1}	$0.005 \pm 0.008\ ^{+0.001}_{-0.003}$	$0.024 \pm 0.013\ ^{+0.003}_{-0.005}$	$-0.065 \pm 0.030\ ^{+0.014}_{-0.006}$
r^{6}_{10}	$-0.162 \pm 0.006\ ^{+0.005}_{-0.004}$	$-0.130 \pm 0.009\ ^{+0.008}_{-0.009}$	$-0.131 \pm 0.020\ ^{+0.012}_{-0.010}$
r^{6}_{1-1}	$0.003 \pm 0.008\ ^{+0.002}_{-0.002}$	$-0.012 \pm 0.011\ ^{+0.004}_{-0.004}$	$-0.006 \pm 0.025\ ^{+0.011}_{-0.004}$
$\langle Q^2\rangle = 8.6$ GeV^2			
r^{04}_{00}	$0.734 \pm 0.011\ ^{+0.014}_{-0.022}$	$0.817 \pm 0.014\ ^{+0.031}_{-0.040}$	$0.841 \pm 0.016\ ^{+0.069}_{-0.067}$
Re r^{04}_{10}	$0.030 \pm 0.008\ ^{+0.009}_{-0.008}$	$0.004 \pm 0.011\ ^{+0.016}_{-0.014}$	$-0.049 \pm 0.019\ ^{+0.014}_{-0.013}$
r^{04}_{1-1}	$-0.006 \pm 0.008\ ^{+0.001}_{-0.001}$	$-0.008 \pm 0.012\ ^{+0.004}_{-0.006}$	$-0.061 \pm 0.019\ ^{+0.015}_{-0.016}$
r^{1}_{00}	$-0.009 \pm 0.032\ ^{+0.008}_{-0.007}$	$-0.052 \pm 0.067\ ^{+0.049}_{-0.023}$	$-0.046 \pm 0.063\ ^{+0.070}_{-0.042}$
r^{1}_{11}	$-0.013 \pm 0.030\ ^{+0.004}_{-0.004}$	$0.012 \pm 0.039\ ^{+0.026}_{-0.026}$	$0.008 \pm 0.038\ ^{+0.074}_{-0.073}$
Re r^{1}_{10}	$-0.028 \pm 0.011\ ^{+0.009}_{-0.007}$	$0.045 \pm 0.016\ ^{+0.014}_{-0.020}$	$-0.094 \pm 0.027\ ^{+0.024}_{-0.020}$
r^{1}_{1-1}	$0.133 \pm 0.012\ ^{+0.004}_{-0.005}$	$0.102 \pm 0.016\ ^{+0.010}_{-0.010}$	$-0.007 \pm 0.027\ ^{+0.018}_{-0.019}$
r^{2}_{10}	$-0.036 \pm 0.011\ ^{+0.007}_{-0.008}$	$-0.011 \pm 0.015\ ^{+0.013}_{-0.013}$	$-0.044 \pm 0.025\ ^{+0.019}_{-0.018}$
Im r^{2}_{1-1}	$-0.081 \pm 0.011\ ^{+0.002}_{-0.003}$	$-0.077 \pm 0.016\ ^{+0.006}_{-0.022}$	$-0.129 \pm 0.026\ ^{+0.022}_{-0.017}$
r^{5}_{00}	$0.071 \pm 0.017\ ^{+0.029}_{-0.028}$	$0.169 \pm 0.024\ ^{+0.051}_{-0.055}$	$0.115 \pm 0.042\ ^{+0.062}_{-0.046}$
r^{5}_{11}	$0.023 \pm 0.012\ ^{+0.005}_{-0.006}$	$-0.036 \pm 0.017\ ^{+0.020}_{-0.021}$	$-0.010 \pm 0.029\ ^{+0.042}_{-0.052}$
Re r^{5}_{10}	$0.146 \pm 0.005\ ^{+0.003}_{-0.003}$	$0.137 \pm 0.008\ ^{+0.008}_{-0.008}$	$0.152 \pm 0.013\ ^{+0.023}_{-0.021}$
r^{5}_{1-1}	$-0.013 \pm 0.006\ ^{+0.002}_{-0.003}$	$-0.007 \pm 0.009\ ^{+0.004}_{-0.004}$	$0.060 \pm 0.016\ ^{+0.029}_{-0.053}$
r^{6}_{10}	$-0.145 \pm 0.005\ ^{+0.003}_{-0.003}$	$-0.113 \pm 0.007\ ^{+0.006}_{-0.007}$	$-0.103 \pm 0.011\ ^{+0.014}_{-0.015}$
r^{6}_{1-1}	$-0.020 \pm 0.006\ ^{+0.001}_{-0.002}$	$0.017 \pm 0.007\ ^{+0.003}_{-0.003}$	$-0.029 \pm 0.012\ ^{+0.002}_{-0.005}$

Table 43: Spin density matrix elements for the diffractive electroproduction of ρ mesons as a function of $|t|$, for $2.5 \leq Q^2 < 5$ and $5 \leq Q^2 \leq 60$ GeV^2. The notag ($|t| \leq 0.5$ GeV^2) and tag ($|t| \leq 3$ GeV^2) samples are combined.

$\langle\lvert t\rvert\rangle$ (GeV^2)	0.08	0.34	1.05
r_{00}^{04}	$0.667 \pm 0.019\ ^{+0.012}_{-0.011}$	$0.641 \pm 0.027\ ^{+0.021}_{-0.021}$	$0.830 \pm 0.039\ ^{+0.087}_{-0.088}$
Re r_{10}^{04}	$0.002 \pm 0.014\ ^{+0.010}_{-0.012}$	$0.008 \pm 0.020\ ^{+0.020}_{-0.021}$	$-0.010 \pm 0.041\ ^{+0.033}_{-0.026}$
r_{1-1}^{04}	$-0.014 \pm 0.016\ ^{+0.004}_{-0.002}$	$-0.003 \pm 0.023\ ^{+0.010}_{-0.006}$	$-0.036 \pm 0.044\ ^{+0.012}_{-0.024}$
r_{00}^{1}	$-0.058 \pm 0.108\ ^{+0.005}_{-0.007}$	$-0.069 \pm 0.166\ ^{+0.037}_{-0.020}$	$0.007 \pm 0.032\ ^{+0.140}_{-0.127}$
r_{11}^{1}	$-0.012 \pm 0.079\ ^{+0.005}_{-0.002}$	$-0.044 \pm 0.138\ ^{+0.020}_{-0.015}$	$-0.029 \pm 0.040\ ^{+0.068}_{-0.065}$
Re r_{10}^{1}	$-0.028 \pm 0.019\ ^{+0.016}_{-0.009}$	$-0.071 \pm 0.027\ ^{+0.016}_{-0.020}$	$-0.139 \pm 0.059\ ^{+0.026}_{-0.025}$
r_{1-1}^{1}	$0.215 \pm 0.021\ ^{+0.009}_{-0.007}$	$0.064 \pm 0.032\ ^{+0.010}_{-0.013}$	$0.114 \pm 0.067\ ^{+0.060}_{-0.031}$
r_{10}^{2}	$0.014 \pm 0.019\ ^{+0.015}_{-0.013}$	$-0.018 \pm 0.027\ ^{+0.017}_{-0.019}$	$0.094 \pm 0.053\ ^{+0.037}_{-0.021}$
Im r_{1-1}^{2}	$-0.132 \pm 0.022\ ^{+0.007}_{-0.008}$	$-0.129 \pm 0.033\ ^{+0.008}_{-0.013}$	$-0.204 \pm 0.060\ ^{+0.036}_{-0.045}$
r_{00}^{5}	$0.037 \pm 0.029\ ^{+0.025}_{-0.026}$	$0.099 \pm 0.042\ ^{+0.046}_{-0.048}$	$0.138 \pm 0.097\ ^{+0.071}_{-0.081}$
r_{11}^{5}	$-0.002 \pm 0.020\ ^{+0.009}_{-0.010}$	$0.049 \pm 0.030\ ^{+0.015}_{-0.018}$	$0.006 \pm 0.066\ ^{+0.044}_{-0.053}$
Re r_{10}^{5}	$0.176 \pm 0.009\ ^{+0.003}_{-0.004}$	$0.155 \pm 0.013\ ^{+0.009}_{-0.008}$	$0.094 \pm 0.032\ ^{+0.021}_{-0.030}$
r_{1-1}^{5}	$-0.015 \pm 0.011\ ^{+0.003}_{-0.003}$	$0.043 \pm 0.018\ ^{+0.006}_{-0.009}$	$-0.028 \pm 0.038\ ^{+0.030}_{-0.029}$
r_{10}^{6}	$-0.163 \pm 0.009\ ^{+0.003}_{-0.004}$	$-0.132 \pm 0.012\ ^{+0.007}_{-0.009}$	$-0.128 \pm 0.023\ ^{+0.026}_{-0.023}$
r_{1-1}^{6}	$-0.014 \pm 0.011\ ^{+0.004}_{-0.003}$	$0.005 \pm 0.015\ ^{+0.005}_{-0.003}$	$-0.037 \pm 0.027\ ^{+0.027}_{-0.012}$

Table 44: Spin density matrix elements for the diffractive electroproduction of ϕ mesons as a function of $|t|$. The notag ($|t| \leq 0.5$ GeV^2) and tag ($|t| \leq 3$ GeV^2) samples are combined.

$\langle Q^2 \rangle = 3.3$ GeV^2					
$\langle m_{\pi^+\pi^-} \rangle$ (GeV)	0.65	0.75	0.85	0.95	1.05
r_{00}^{04}	$0.677 \pm 0.021\ ^{+0.029}_{-0.037}$	$0.635 \pm 0.017\ ^{+0.012}_{-0.021}$	$0.559 \pm 0.023\ ^{+0.013}_{-0.046}$	$0.456 \pm 0.037\ ^{+0.024}_{-0.012}$	$0.458 \pm 0.055\ ^{+0.027}_{-0.051}$
Re r_{10}^{04}	$0.067 \pm 0.016\ ^{+0.013}_{-0.012}$	$0.028 \pm 0.012\ ^{+0.011}_{-0.013}$	$0.033 \pm 0.016\ ^{+0.011}_{-0.012}$	$0.046 \pm 0.023\ ^{+0.013}_{-0.010}$	$0.027 \pm 0.034\ ^{+0.014}_{-0.016}$
r_{1-1}^{04}	$-0.002 \pm 0.019\ ^{+0.009}_{-0.003}$	$0.002 \pm 0.013\ ^{+0.002}_{-0.002}$	$-0.016 \pm 0.019\ ^{+0.005}_{-0.007}$	$0.038 \pm 0.032\ ^{+0.008}_{-0.010}$	$0.003 \pm 0.042\ ^{+0.014}_{-0.014}$
r_{00}^{1}	$-0.033 \pm 0.091\ ^{+0.026}_{-0.033}$	$0.068 \pm 0.070\ ^{+0.084}_{-0.017}$	$0.084 \pm 0.070\ ^{+0.045}_{-0.054}$	$-0.089 \pm 0.223\ ^{+0.061}_{-0.029}$	$0.212 \pm 0.186\ ^{+0.060}_{-0.077}$
r_{11}^{1}	$-0.029 \pm 0.079\ ^{+0.027}_{-0.027}$	$-0.033 \pm 0.035\ ^{+0.011}_{-0.041}$	$-0.058 \pm 0.042\ ^{+0.025}_{-0.019}$	$-0.062 \pm 0.187\ ^{+0.015}_{-0.034}$	$-0.135 \pm 0.101\ ^{+0.030}_{-0.037}$
Re r_{10}^{1}	$0.020 \pm 0.023\ ^{+0.009}_{-0.013}$	$-0.069 \pm 0.017\ ^{+0.011}_{-0.011}$	$-0.043 \pm 0.022\ ^{+0.009}_{-0.009}$	$-0.035 \pm 0.036\ ^{+0.014}_{-0.014}$	$-0.003 \pm 0.051\ ^{+0.038}_{-0.018}$
r_{1-1}^{1}	$0.093 \pm 0.028\ ^{+0.011}_{-0.010}$	$0.135 \pm 0.019\ ^{+0.005}_{-0.007}$	$0.188 \pm 0.026\ ^{+0.011}_{-0.008}$	$0.175 \pm 0.045\ ^{+0.033}_{-0.021}$	$0.113 \pm 0.058\ ^{+0.080}_{-0.057}$
r_{10}^{2}	$0.025 \pm 0.022\ ^{+0.009}_{-0.010}$	$0.034 \pm 0.016\ ^{+0.013}_{-0.010}$	$0.058 \pm 0.023\ ^{+0.013}_{-0.020}$	$0.022 \pm 0.036\ ^{+0.015}_{-0.023}$	$-0.041 \pm 0.047\ ^{+0.012}_{-0.016}$
Im r_{1-1}^{2}	$-0.122 \pm 0.027\ ^{+0.021}_{-0.010}$	$-0.156 \pm 0.017\ ^{+0.009}_{-0.006}$	$-0.171 \pm 0.027\ ^{+0.011}_{-0.007}$	$-0.286 \pm 0.042\ ^{+0.017}_{-0.026}$	$-0.297 \pm 0.060\ ^{+0.056}_{-0.037}$
r_{00}^{5}	$0.139 \pm 0.036\ ^{+0.046}_{-0.059}$	$0.142 \pm 0.024\ ^{+0.049}_{-0.034}$	$0.302 \pm 0.036\ ^{+0.032}_{-0.284}$	$0.202 \pm 0.049\ ^{+0.044}_{-0.032}$	$0.263 \pm 0.071\ ^{+0.079}_{-0.130}$
r_{11}^{5}	$0.005 \pm 0.025\ ^{+0.025}_{-0.021}$	$0.010 \pm 0.017\ ^{+0.006}_{-0.013}$	$-0.084 \pm 0.025\ ^{+0.145}_{-0.028}$	$-0.005 \pm 0.037\ ^{+0.028}_{-0.034}$	$-0.027 \pm 0.051\ ^{+0.041}_{-0.031}$
Re r_{10}^{5}	$0.147 \pm 0.011\ ^{+0.009}_{-0.011}$	$0.151 \pm 0.007\ ^{+0.003}_{-0.005}$	$0.181 \pm 0.011\ ^{+0.006}_{-0.004}$	$0.167 \pm 0.017\ ^{+0.008}_{-0.009}$	$0.084 \pm 0.025\ ^{+0.022}_{-0.034}$
r_{1-1}^{5}	$0.018 \pm 0.016\ ^{+0.004}_{-0.009}$	$0.000 \pm 0.009\ ^{+0.002}_{-0.002}$	$0.003 \pm 0.014\ ^{+0.003}_{-0.008}$	$0.013 \pm 0.025\ ^{+0.011}_{-0.007}$	$0.005 \pm 0.032\ ^{+0.010}_{-0.010}$
r_{10}^{6}	$-0.129 \pm 0.010\ ^{+0.009}_{-0.012}$	$-0.149 \pm 0.007\ ^{+0.005}_{-0.004}$	$-0.155 \pm 0.010\ ^{+0.006}_{-0.007}$	$-0.149 \pm 0.016\ ^{+0.013}_{-0.018}$	$-0.163 \pm 0.021\ ^{+0.020}_{-0.015}$
r_{1-1}^{6}	$-0.005 \pm 0.013\ ^{+0.002}_{-0.005}$	$0.006 \pm 0.009\ ^{+0.002}_{-0.004}$	$-0.009 \pm 0.013\ ^{+0.002}_{-0.004}$	$0.005 \pm 0.020\ ^{+0.003}_{-0.005}$	$0.002 \pm 0.031\ ^{+0.031}_{-0.007}$

Table 45: Spin density matrix elements for the diffractive electroproduction of ρ mesons as a function of $m_{\pi\pi}$, for $2.5 \leq Q^2 < 5$ and $5 \leq Q^2 \leq 60$ GeV^2. The notag ($|t| \leq 0.5$ GeV^2) and tag ($|t| \leq 3$ GeV^2) samples are combined.

$\langle Q^2 \rangle = 8.6$ GeV^2					
$\langle m_{\pi^+\pi^-} \rangle$ (GeV)	0.65	0.75	0.85	0.95	1.05
r_{00}^{04}	$0.857 \pm 0.012\ ^{+0.048}_{-0.049}$	$0.793 \pm 0.012\ ^{+0.019}_{-0.030}$	$0.747 \pm 0.016\ ^{+0.032}_{-0.032}$	$0.586 \pm 0.027\ ^{+0.031}_{-0.028}$	$0.473 \pm 0.035\ ^{+0.021}_{-0.026}$
Re r_{10}^{04}	$-0.002 \pm 0.013\ ^{+0.015}_{-0.014}$	$0.016 \pm 0.009\ ^{+0.011}_{-0.010}$	$0.028 \pm 0.012\ ^{+0.009}_{-0.012}$	$-0.039 \pm 0.018\ ^{+0.012}_{-0.009}$	$0.125 \pm 0.024\ ^{+0.021}_{-0.015}$
r_{1-1}^{04}	$-0.051 \pm 0.014\ ^{+0.007}_{-0.008}$	$0.005 \pm 0.009\ ^{+0.002}_{-0.001}$	$0.033 \pm 0.013\ ^{+0.002}_{-0.004}$	$-0.063 \pm 0.022\ ^{+0.012}_{-0.010}$	$-0.116 \pm 0.031\ ^{+0.024}_{-0.025}$
r_{00}^{1}	$-0.053 \pm 0.109\ ^{+0.022}_{-0.036}$	$-0.008 \pm 0.025\ ^{+0.026}_{-0.010}$	$-0.020 \pm 0.037\ ^{+0.031}_{-0.022}$	$0.047 \pm 0.137\ ^{+0.105}_{-0.033}$	$0.156 \pm 0.263\ ^{+0.074}_{-0.052}$
r_{11}^{1}	$-0.019 \pm 0.084\ ^{+0.042}_{-0.032}$	$-0.009 \pm 0.022\ ^{+0.016}_{-0.018}$	$-0.004 \pm 0.028\ ^{+0.024}_{-0.026}$	$-0.141 \pm 0.180\ ^{+0.025}_{-0.054}$	$0.013 \pm 0.184\ ^{+0.041}_{-0.040}$
Re r_{10}^{1}	$0.038 \pm 0.020\ ^{+0.017}_{-0.014}$	$-0.028 \pm 0.012\ ^{+0.012}_{-0.010}$	$-0.027 \pm 0.016\ ^{+0.012}_{-0.010}$	$-0.061 \pm 0.025\ ^{+0.012}_{-0.014}$	$0.066 \pm 0.035\ ^{+0.042}_{-0.009}$
r_{1-1}^{1}	$0.117 \pm 0.020\ ^{+0.017}_{-0.016}$	$0.087 \pm 0.013\ ^{+0.004}_{-0.008}$	$0.121 \pm 0.018\ ^{+0.009}_{-0.008}$	$0.251 \pm 0.032\ ^{+0.128}_{-0.039}$	$-0.024 \pm 0.039\ ^{+0.040}_{-0.016}$
r_{10}^{2}	$-0.044 \pm 0.017\ ^{+0.014}_{-0.010}$	$-0.046 \pm 0.012\ ^{+0.012}_{-0.010}$	$0.004 \pm 0.017\ ^{+0.009}_{-0.011}$	$0.025 \pm 0.025\ ^{+0.004}_{-0.010}$	$-0.034 \pm 0.032\ ^{+0.021}_{-0.009}$
Im r_{1-1}^{2}	$-0.046 \pm 0.018\ ^{+0.013}_{-0.006}$	$-0.084 \pm 0.012\ ^{+0.004}_{-0.005}$	$-0.087 \pm 0.018\ ^{+0.010}_{-0.008}$	$-0.104 \pm 0.030\ ^{+0.012}_{-0.020}$	$-0.146 \pm 0.039\ ^{+0.039}_{-0.019}$
r_{00}^{5}	$0.106 \pm 0.029\ ^{+0.042}_{-0.044}$	$0.098 \pm 0.019\ ^{+0.038}_{-0.041}$	$0.155 \pm 0.026\ ^{+0.037}_{-0.038}$	$0.075 \pm 0.039\ ^{+0.031}_{-0.038}$	$0.035 \pm 0.047\ ^{+0.034}_{-0.039}$
r_{11}^{5}	$-0.002 \pm 0.020\ ^{+0.025}_{-0.028}$	$0.010 \pm 0.013\ ^{+0.011}_{-0.012}$	$-0.016 \pm 0.018\ ^{+0.020}_{-0.019}$	$0.019 \pm 0.029\ ^{+0.029}_{-0.029}$	$0.060 \pm 0.035\ ^{+0.020}_{-0.022}$
Re r_{10}^{5}	$0.173 \pm 0.010\ ^{+0.017}_{-0.016}$	$0.128 \pm 0.006\ ^{+0.004}_{-0.005}$	$0.142 \pm 0.008\ ^{+0.008}_{-0.008}$	$0.113 \pm 0.014\ ^{+0.014}_{-0.011}$	$0.161 \pm 0.015\ ^{+0.018}_{-0.015}$
r_{1-1}^{5}	$0.005 \pm 0.011\ ^{+0.005}_{-0.005}$	$-0.017 \pm 0.007\ ^{+0.003}_{-0.003}$	$-0.001 \pm 0.009\ ^{+0.003}_{-0.003}$	$0.007 \pm 0.018\ ^{+0.010}_{-0.007}$	$-0.068 \pm 0.023\ ^{+0.013}_{-0.015}$
r_{10}^{6}	$-0.115 \pm 0.008\ ^{+0.009}_{-0.010}$	$-0.133 \pm 0.006\ ^{+0.004}_{-0.004}$	$-0.147 \pm 0.008\ ^{+0.008}_{-0.007}$	$-0.124 \pm 0.011\ ^{+0.010}_{-0.012}$	$-0.107 \pm 0.014\ ^{+0.009}_{-0.010}$
r_{1-1}^{6}	$0.013 \pm 0.009\ ^{+0.003}_{-0.003}$	$-0.016 \pm 0.006\ ^{+0.002}_{-0.001}$	$-0.023 \pm 0.008\ ^{+0.002}_{-0.004}$	$0.014 \pm 0.013\ ^{+0.005}_{-0.010}$	$0.012 \pm 0.020\ ^{+0.019}_{-0.009}$

Table 46: Spin density matrix elements for the diffractive electroproduction of ρ mesons as a function of $m_{\pi\pi}$, for $2.5 \leq Q^2 < 5$ and $5 \leq Q^2 \leq 60$ GeV^2, continued from table 45.

$\langle Q^2 \rangle$ (GeV^2)	$r^5_{00} + 2r^5_{11}$			$r^1_{00} + 2r^1_{11}$		
2.9	0.149	$\pm$ 0.018	$^{+0.062}_{-0.060}$	-0.041	$\pm$ 0.034	$^{+0.029}_{-0.034}$
4.1	0.144	$\pm$ 0.019	$^{+0.046}_{-0.055}$	-0.036	$\pm$ 0.041	$^{+0.023}_{-0.025}$
6.6	0.122	$\pm$ 0.016	$^{+0.049}_{-0.049}$	-0.078	$\pm$ 0.032	$^{+0.023}_{-0.014}$
11.9	0.088	$\pm$ 0.024	$^{+0.049}_{-0.047}$	-0.093	$\pm$ 0.045	$^{+0.024}_{-0.018}$
18.5	0.178	$\pm$ 0.031	$^{+0.037}_{-0.049}$	-0.010	$\pm$ 0.059	$^{+0.034}_{-0.034}$
31.3	0.149	$\pm$ 0.028	$^{+0.041}_{-0.037}$	0.123	$\pm$ 0.059	$^{+0.030}_{-0.032}$
$\langle \lvert t \rvert \rangle$ (GeV^2)	$r^5_{00} + 2r^5_{11}$			$r^1_{00} + 2r^1_{11}$		
0.03	0.074	$\pm$ 0.022	$^{+0.032}_{-0.036}$	0.003	$\pm$ 0.045	$^{+0.004}_{-0.013}$
0.13	0.109	$\pm$ 0.022	$^{+0.062}_{-0.052}$	-0.024	$\pm$ 0.044	$^{+0.017}_{-0.024}$
0.31	0.200	$\pm$ 0.028	$^{+0.064}_{-0.086}$	-0.131	$\pm$ 0.054	$^{+0.041}_{-0.028}$
0.70	0.249	$\pm$ 0.051	$^{+0.063}_{-0.038}$	-0.015	$\pm$ 0.099	$^{+0.040}_{-0.067}$
1.44	0.308	$\pm$ 0.077	$^{+0.086}_{-0.096}$	-0.162	$\pm$ 0.129	$^{+0.086}_{-0.080}$

Table 47: Q^2 and $|t|$ dependences of the matrix element combinations $r^5_{00} + 2r^5_{11}$ and $r^1_{00} + 2r^1_{11}$, obtained from fits of Eq. (41) to the ϕ distribution, for ρ meson electroproduction. The notag ($|t| \leq 0.5$ GeV^2) and tag ($|t| \leq 3$ GeV^2) samples are combined.

$\langle Q^2 \rangle$ (GeV^2)	$P_{\mathrm{NPE,T}}$			$\langle \lvert t \rvert \rangle$ (GeV^2)	$P_{\mathrm{NPE,T}}$		
ρ production							
3.1	1.13	$\pm$ 0.07	$^{+0.07}_{-0.03}$	0.03	1.10	$\pm$ 0.06	$^{+0.05}_{-0.02}$
4.8	1.24	$\pm$ 0.09	$^{+0.04}_{-0.03}$	0.13	1.02	$\pm$ 0.12	$^{+0.03}_{-0.03}$
7.5	1.03	$\pm$ 0.10	$^{+0.06}_{-0.05}$	0.31	1.03	$\pm$ 0.12	$^{+0.11}_{-0.08}$
12.2	0.95	$\pm$ 0.11	$^{+0.05}_{-0.05}$	0.70	0.96	$\pm$ 0.39	$^{+0.11}_{-0.09}$
23.1	1.07	$\pm$ 0.16	$^{+0.06}_{-0.05}$	1.44	1.08	$\pm$ 0.12	$^{+0.28}_{-0.31}$
ϕ production							
3.3	0.98	$\pm$ 0.31	$^{+0.04}_{-0.05}$	0.08	0.90	$\pm$ 0.17	$^{+0.02}_{-0.02}$
6.6	1.13	$\pm$ 0.11	$^{+0.04}_{-0.05}$	0.34	1.31	$\pm$ 0.29	$^{+0.06}_{-0.05}$
15.8	0.99	$\pm$ 0.10	$^{+0.06}_{-0.05}$	1.05	0.93	$\pm$ 0.18	$^{+0.22}_{-0.28}$

Table 48: Asymmetry $P_{\mathrm{NPE,T}}$ between natural and unnatural parity exchange for transverse photons, as a function of Q^2 and $|t|$, for ρ and ϕ meson production.

$\langle Q^2 \rangle$ (GeV^2)	$\cos\delta$		
ρ production			
3.3	0.914	$\pm$ 0.014	$^{+0.021}_{-0.024}$
6.6	0.915	$\pm$ 0.026	$^{+0.018}_{-0.024}$
15.8	0.978	$\pm$ 0.030	$^{+0.016}_{-0.052}$
ϕ production			
5.3	0.966	$\pm$ 0.027	$^{+0.012}_{-0.018}$

Table 49: Cosine of the phase δ between the T_{00} and T_{11} helicity conserving amplitudes for ρ and ϕ meson production, measured as a function of Q^2 from two-dimensional fits to Eq. (47), in the SCHC approximation ($|t| \leq 0.5$ GeV^2)

$\langle Q^2 \rangle$ (GeV^2)	$R = \sigma_L/\sigma_T$		
ρ production			
3.1	1.36	$^{+0.08}_{-0.08}$	$^{+0.11}_{-0.13}$
4.8	1.92	$^{+0.16}_{-0.15}$	$^{+0.15}_{-0.12}$
7.5	3.65	$^{+0.31}_{-0.27}$	$^{+0.41}_{-0.38}$
12.2	3.60	$^{+0.38}_{-0.34}$	$^{+0.39}_{-0.37}$
23.1	6.52	$^{+1.27}_{-0.98}$	$^{+1.23}_{-0.96}$
ϕ production			
3.3	1.37	$^{+0.14}_{-0.13}$	$^{+0.09}_{-0.09}$
6.6	2.87	$^{+0.40}_{-0.34}$	$^{+0.28}_{-0.26}$
15.8	6.01	$^{+2.00}_{-1.33}$	$^{+1.00}_{-0.78}$

Table 50: Q^2 dependence of the ratio $R = \sigma_L/\sigma_T$ of the longitudinal to transverse cross sections, for ρ and ϕ meson production.

$\langle W \rangle$ (GeV)	$R = \sigma_L/\sigma_T$		
$\langle Q^2 \rangle = 3.3$ GeV^2			
43	1.56	$^{+0.15}_{-0.14}$	$^{+0.11}_{-0.08}$
59	1.46	$^{+0.14}_{-0.13}$	$^{+0.09}_{-0.08}$
76	1.40	$^{+0.16}_{-0.15}$	$^{+0.10}_{-0.08}$
92	1.27	$^{+0.17}_{-0.15}$	$^{+0.10}_{-0.11}$
$\langle Q^2 \rangle = 7.5$ GeV^2			
58	2.67	$^{+0.28}_{-0.24}$	$^{+0.22}_{-0.18}$
76	3.00	$^{+0.34}_{-0.29}$	$^{+0.29}_{-0.30}$
93	3.31	$^{+0.47}_{-0.41}$	$^{+0.46}_{-0.45}$
111	2.72	$^{+0.32}_{-0.28}$	$^{+0.26}_{-0.22}$
$\langle Q^2 \rangle = 22.5$ GeV^2			
72	3.59	$^{+0.98}_{-0.74}$	$^{+0.59}_{-0.37}$
97	5.96	$^{+2.48}_{-1.60}$	$^{+1.19}_{-1.05}$
122	6.27	$^{+2.98}_{-1.76}$	$^{+1.41}_{-1.02}$
147	6.01	$^{+3.13}_{-1.71}$	$^{+1.08}_{-2.14}$

Table 51: W dependence of the ratio $R = \sigma_L/\sigma_T$ of the longitudinal to transverse cross sections for ρ meson production, for $2.5 \leq Q^2 < 5$ GeV^2, $5 \leq Q^2 < 15.5$ GeV^2 and $15.5 \leq Q^2 \leq 60$ GeV^2.

$\langle \lvert t \rvert \rangle$ (GeV^2)	$R = \sigma_L/\sigma_T$		
$\langle Q^2 \rangle = 3.3$ GeV^2			
0.08	1.43	$^{+0.09}_{-0.09}$	$^{+0.08}_{-0.08}$
0.34	1.26	$^{+0.13}_{-0.12}$	$^{+0.16}_{-0.16}$
1.05	1.70	$^{+0.37}_{-0.32}$	$^{+0.24}_{-0.23}$
$\langle Q^2 \rangle = 8.6$ GeV^2			
0.08	2.73	$^{+0.16}_{-0.15}$	$^{+0.15}_{-0.15}$
0.34	3.98	$^{+0.40}_{-0.35}$	$^{+0.92}_{-0.79}$
1.05	4.99	$^{+0.69}_{-0.59}$	$^{+3.63}_{-1.98}$

Table 52: $|t|$ dependence of the ratio $R = \sigma_L/\sigma_T$ of the longitudinal to transverse cross sections for ρ meson production, for $2.5 \leq Q^2 < 5$ GeV^2 and $5 \leq Q^2 \leq 60$ GeV^2.

$\langle m_{\pi^+\pi^-} \rangle$ (GeV)	$R = \sigma_L/\sigma_T$		
$\langle Q^2 \rangle = 3.3$ GeV^2			
0.65	1.97	$^{+0.21}_{-0.19}$	$^{+0.32}_{-0.30}$
0.75	1.62	$^{+0.13}_{-0.12}$	$^{+0.11}_{-0.13}$
0.85	0.85	$^{+0.14}_{-0.15}$	$^{+0.12}_{-0.09}$
0.95	0.69	$^{+0.14}_{-0.15}$	$^{+0.05}_{-0.10}$
1.05	0.57	$^{+0.24}_{-0.34}$	$^{+0.14}_{-0.19}$
$\langle Q^2 \rangle = 8.6$ GeV^2			
0.65	5.70	$^{+0.59}_{-0.52}$	$^{+2.85}_{-1.75}$
0.75	3.70	$^{+0.28}_{-0.26}$	$^{+0.46}_{-0.43}$
0.85	2.72	$^{+0.25}_{-0.23}$	$^{+0.40}_{-0.36}$
0.95	1.39	$^{+0.17}_{-0.15}$	$^{+0.20}_{-0.17}$
1.05	0.90	$^{+0.14}_{-0.12}$	$^{+0.08}_{-0.06}$

Table 53: $m_{\pi\pi}$ dependence of the ratio $R = \sigma_L/\sigma_T$ of the longitudinal to transverse cross sections for ρ meson production, for $2.5 \leq Q^2 < 5$ GeV^2 and $5 \leq Q^2 \leq 60$ GeV^2.

$\langle m_{\pi^+\pi^-} \rangle$ (GeV)	$b_{\gamma^* p \to \rho p}$ (GeV^{-2})		
$\langle Q^2 \rangle = 3.3$ GeV^2			
0.67	7.33	$\pm$ 0.51	$^{+0.38}_{-0.36}$
0.87	8.25	$\pm$ 0.40	$^{+0.26}_{-0.29}$
1.07	7.73	$\pm$ 0.51	$^{+0.46}_{-0.42}$
$\langle Q^2 \rangle = 9.0$ GeV^2			
0.67	7.15	$\pm$ 0.48	$^{+0.27}_{-0.30}$
0.87	7.65	$\pm$ 0.43	$^{+0.30}_{-0.32}$
1.07	6.83	$\pm$ 0.45	$^{+0.27}_{-0.35}$

Table 54: Dependence of the exponential t slope for ρ elastic production, as a function of the mass $m_{\pi\pi}$, for two domains in Q^2: $2.5 \leq Q^2 < 5$ GeV^2 and $5 \leq Q^2 \leq 60$ GeV^2

$\langle Q^2 \rangle$ (GeV^2)	T_{11}/T_{00}	T_{01}/T_{00}	T_{10}/T_{00}	T_{-11}/T_{00}	$\cos(\phi_{11} - \phi_{00})$
ρ production					
3.1	$0.786 \pm 0.019\ ^{+0.036}_{-0.020}$	$0.177 \pm 0.019\ ^{+0.042}_{-0.068}$	$-0.002 \pm 0.011\ ^{+0.016}_{-0.005}$	$-0.019 \pm 0.014\ ^{+0.002}_{-0.005}$	$0.949 \pm 0.024\ ^{+0.028}_{-0.034}$
4.8	$0.619 \pm 0.021\ ^{+0.033}_{-0.018}$	$0.169 \pm 0.022\ ^{+0.051}_{-0.042}$	$-0.025 \pm 0.014\ ^{+0.008}_{-0.009}$	$0.001 \pm 0.017\ ^{+0.002}_{-0.005}$	$0.882 \pm 0.035\ ^{+0.028}_{-0.038}$
7.5	$0.511 \pm 0.015\ ^{+0.017}_{-0.011}$	$0.056 \pm 0.018\ ^{+0.038}_{-0.038}$	$0.018 \pm 0.010\ ^{+0.006}_{-0.005}$	$-0.034 \pm 0.014\ ^{+0.004}_{-0.005}$	$0.997 \pm 0.038\ ^{+0.007}_{-0.046}$
12.2	$0.444 \pm 0.018\ ^{+0.015}_{-0.008}$	$0.106 \pm 0.022\ ^{+0.035}_{-0.034}$	$-0.049 \pm 0.013\ ^{+0.006}_{-0.007}$	$-0.038 \pm 0.017\ ^{+0.009}_{-0.010}$	$0.900 \pm 0.049\ ^{+0.043}_{-0.049}$
23.1	$0.287 \pm 0.020\ ^{+0.006}_{-0.005}$	$0.090 \pm 0.025\ ^{+0.030}_{-0.029}$	$0.047 \pm 0.016\ ^{+0.003}_{-0.009}$	$0.029 \pm 0.020\ ^{+0.007}_{-0.005}$	$0.879 \pm 0.094\ ^{+0.056}_{-0.054}$
ϕ production					
3.4	$0.823 \pm 0.033\ ^{+0.024}_{-0.019}$	$0.049 \pm 0.031\ ^{+0.039}_{-0.041}$	$-0.027 \pm 0.020\ ^{+0.015}_{-0.019}$	$-0.151 \pm 0.027\ ^{+0.011}_{-0.007}$	$0.982 \pm 0.048\ ^{+0.011}_{-0.070}$
6.6	$0.580 \pm 0.029\ ^{+0.014}_{-0.014}$	$0.115 \pm 0.035\ ^{+0.035}_{-0.041}$	$-0.001 \pm 0.020\ ^{+0.010}_{-0.009}$	$0.076 \pm 0.026\ ^{+0.005}_{-0.003}$	$0.993 \pm 0.057\ ^{+0.003}_{-0.091}$
15.7	$0.375 \pm 0.035\ ^{+0.019}_{-0.014}$	$0.097 \pm 0.041\ ^{+0.052}_{-0.073}$	$-0.028 \pm 0.027\ ^{+0.013}_{-0.024}$	$0.008 \pm 0.027\ ^{+0.014}_{-0.023}$	$0.867 \pm 0.115\ ^{+0.069}_{-0.051}$

Table 55: Ratios of the helicity amplitudes (taken to be purely imaginary) and phase difference between the T_{11} and T_{00} amplitudes (the amplitude ratios T_{10}/T_{00} and T_{-11}/T_{00} and the phase difference $\phi_{01} - \phi_{00}$ are taken to be 0) for ρ and ϕ meson production, computed from global fits to the measurements of the 15 spin density matrix elements, as a function of Q^2 (NPE is assumed).

$\langle\lvert t\rvert\rangle$ (GeV^2)	T_{11}/T_{00}	T_{01}/T_{00}	T_{10}/T_{00}	T_{-11}/T_{00}	$\cos(\phi_{11}-\phi_{00})$
ρ production					
$\langle Q^2\rangle = 3.3$ GeV^2					
0.08	$0.773 \pm 0.020\ ^{+0.032}_{-0.015}$	$0.128 \pm 0.020\ ^{+0.037}_{-0.057}$	$-0.007 \pm 0.012\ ^{+0.015}_{-0.004}$	$-0.004 \pm 0.015\ ^{+0.003}_{-0.005}$	$0.939 \pm 0.026\ ^{+0.019}_{-0.029}$
0.34	$0.769 \pm 0.031\ ^{+0.042}_{-0.033}$	$0.281 \pm 0.034\ ^{+0.060}_{-0.062}$	$-0.062 \pm 0.019\ ^{+0.012}_{-0.010}$	$-0.015 \pm 0.026\ ^{+0.011}_{-0.009}$	$0.851 \pm 0.040\ ^{+0.047}_{-0.053}$
1.05	$0.673 \pm 0.067\ ^{+0.048}_{-0.040}$	$0.248 \pm 0.070\ ^{+0.043}_{-0.043}$	$0.138 \pm 0.046\ ^{+0.013}_{-0.027}$	$-0.095 \pm 0.051\ ^{+0.036}_{-0.015}$	$0.929 \pm 0.094\ ^{+0.088}_{-0.293}$
$\langle Q^2\rangle = 8.6$ GeV^2					
0.08	$0.559 \pm 0.013\ ^{+0.018}_{-0.012}$	$0.059 \pm 0.014\ ^{+0.028}_{-0.028}$	$0.012 \pm 0.009\ ^{+0.005}_{-0.005}$	$-0.009 \pm 0.011\ ^{+0.002}_{-0.001}$	$0.947 \pm 0.026\ ^{+0.023}_{-0.031}$
0.34	$0.445 \pm 0.016\ ^{+0.029}_{-0.010}$	$0.104 \pm 0.020\ ^{+0.050}_{-0.046}$	$-0.007 \pm 0.012\ ^{+0.010}_{-0.007}$	$-0.037 \pm 0.016\ ^{+0.034}_{-0.008}$	$0.894 \pm 0.044\ ^{+0.094}_{-0.089}$
1.05	$0.422 \pm 0.021\ ^{+0.029}_{-0.107}$	$0.113 \pm 0.033\ ^{+0.056}_{-0.064}$	$-0.103 \pm 0.019\ ^{+0.046}_{-0.022}$	$-0.090 \pm 0.023\ ^{+0.070}_{-0.025}$	$0.955 \pm 0.076\ ^{+0.087}_{-0.241}$
ϕ production					
0.08	$0.713 \pm 0.024\ ^{+0.018}_{-0.016}$	$0.046 \pm 0.025\ ^{+0.030}_{-0.033}$	$-0.007 \pm 0.016\ ^{+0.007}_{-0.008}$	$-0.029 \pm 0.021\ ^{+0.009}_{-0.003}$	$0.969 \pm 0.042\ ^{+0.004}_{-0.033}$
0.34	$0.650 \pm 0.036\ ^{+0.020}_{-0.013}$	$0.117 \pm 0.039\ ^{+0.052}_{-0.056}$	$-0.033 \pm 0.025\ ^{+0.016}_{-0.011}$	$-0.050 \pm 0.031\ ^{+0.020}_{-0.009}$	$0.869 \pm 0.057\ ^{+0.056}_{-0.045}$
1.05	$0.478 \pm 0.053\ ^{+0.113}_{-0.147}$	$0.164 \pm 0.065\ ^{+0.225}_{-0.183}$	$-0.056 \pm 0.044\ ^{+0.059}_{-0.056}$	$-0.015 \pm 0.049\ ^{+0.067}_{-0.040}$	$0.851 \pm 0.146\ ^{+0.245}_{-0.270}$

Table 56: Ratios of the helicity amplitudes (taken to be purely imaginary) and phase difference between the T_{11} and T_{00} amplitudes (the amplitude ratios T_{10}/T_{00} and T_{-11}/T_{00} and the phase difference $\phi_{01}-\phi_{00}$ are taken to be 0), computed from global fits to the measurements of the 15 spin density matrix elements, as a function of $|t|$, separately for $2.5 \leq Q^2 < 5$ GeV^2 and $5 \leq Q^2 \leq 60$ GeV^2 for ρ meson production and for $2.5 \leq Q^2 \leq 60$ GeV^2 for ϕ production (NPE is assumed).

$\langle m_{\pi^+\pi^-}\rangle$ (GeV)	T_{11}/T_{00}	T_{01}/T_{00}	T_{10}/T_{00}	T_{-11}/T_{00}	$\cos(\phi_{11}-\phi_{00})$
$\langle Q^2\rangle = 3.3$ GeV^2					
0.65	$0.618 \pm 0.029\ ^{+0.026}_{-0.019}$	$0.138 \pm 0.034\ ^{+0.049}_{-0.055}$	$0.020 \pm 0.021\ ^{+0.007}_{-0.006}$	$-0.031 \pm 0.025\ ^{+0.015}_{-0.006}$	$0.855 \pm 0.047\ ^{+0.078}_{-0.070}$
0.75	$0.711 \pm 0.023\ ^{+0.022}_{-0.018}$	$0.166 \pm 0.024\ ^{+0.056}_{-0.037}$	$-0.006 \pm 0.014\ ^{+0.004}_{-0.010}$	$-0.007 \pm 0.018\ ^{+0.006}_{-0.006}$	$0.902 \pm 0.033\ ^{+0.022}_{-0.034}$
0.85	$0.861 \pm 0.036\ ^{+0.052}_{-0.020}$	$0.292 \pm 0.035\ ^{+0.032}_{-0.212}$	$-0.058 \pm 0.020\ ^{+0.075}_{-0.008}$	$-0.062 \pm 0.026\ ^{+0.010}_{-0.006}$	$0.971 \pm 0.042\ ^{+0.019}_{-0.057}$
0.95	$1.066 \pm 0.073\ ^{+0.040}_{-0.038}$	$0.250 \pm 0.060\ ^{+0.053}_{-0.049}$	$-0.018 \pm 0.035\ ^{+0.012}_{-0.019}$	$0.009 \pm 0.048\ ^{+0.023}_{-0.027}$	$0.898 \pm 0.065\ ^{+0.055}_{-0.056}$
1.05	$0.981 \pm 0.106\ ^{+0.091}_{-0.066}$	$0.275 \pm 0.090\ ^{+0.093}_{-0.155}$	$-0.077 \pm 0.057\ ^{+0.073}_{-0.043}$	$0.050 \pm 0.063\ ^{+0.043}_{-0.051}$	$0.722 \pm 0.091\ ^{+0.084}_{-0.106}$
$\langle Q^2\rangle = 8.6$ GeV^2					
0.65	$0.429 \pm 0.015\ ^{+0.032}_{-0.069}$	$0.050 \pm 0.022\ ^{+0.038}_{-0.038}$	$-0.006 \pm 0.013\ ^{+0.010}_{-0.009}$	$-0.095 \pm 0.017\ ^{+0.028}_{-0.011}$	$0.997 \pm 0.052\ ^{+0.006}_{-0.055}$
0.75	$0.472 \pm 0.013\ ^{+0.019}_{-0.009}$	$0.069 \pm 0.015\ ^{+0.036}_{-0.039}$	$0.001 \pm 0.009\ ^{+0.007}_{-0.004}$	$0.006 \pm 0.012\ ^{+0.004}_{-0.009}$	$0.923 \pm 0.034\ ^{+0.048}_{-0.058}$
0.85	$0.558 \pm 0.019\ ^{+0.020}_{-0.021}$	$0.145 \pm 0.023\ ^{+0.038}_{-0.038}$	$-0.017 \pm 0.013\ ^{+0.006}_{-0.009}$	$0.028 \pm 0.017\ ^{+0.007}_{-0.014}$	$0.959 \pm 0.041\ ^{+0.061}_{-0.069}$
0.95	$0.746 \pm 0.041\ ^{+0.071}_{-0.022}$	$0.110 \pm 0.041\ ^{+0.037}_{-0.042}$	$-0.066 \pm 0.027\ ^{+0.014}_{-0.014}$	$-0.101 \pm 0.033\ ^{+0.011}_{-0.007}$	$0.690 \pm 0.049\ ^{+0.077}_{-0.064}$
1.05	$0.717 \pm 0.052\ ^{+0.062}_{-0.043}$	$-0.062 \pm 0.045\ ^{+0.037}_{-0.040}$	$0.261 \pm 0.038\ ^{+0.022}_{-0.008}$	$-0.183 \pm 0.041\ ^{+0.019}_{-0.029}$	$0.761 \pm 0.059\ ^{+0.072}_{-0.065}$

Table 57: Ratios of the helicity amplitudes (taken to be purely imaginary) and phase difference between the T_{11} and T_{00} amplitudes (the amplitude ratios T_{10}/T_{00} and T_{-11}/T_{00} and the phase difference $\phi_{01}-\phi_{00}$ are taken to be 0), computed from global fits to the measurements of the 15 spin density matrix elements, as a function of $m_{\pi\pi}$ separately for $2.5 \leq Q^2 < 5$ GeV^2 and $5 \leq Q^2 \leq 60$ GeV^2 for ρ meson production and for $2.5 \leq Q^2 \leq 60$ GeV^2 for ϕ production (NPE is assumed).